High Resolution Experimental Studies and Numerical Analysis of Fine Bubble Ozone Disinfection Contactors

A Thesis

Submitted to the Faculty

of

Drexel University

by

Timothy A. Bartrand

in partial fulfillment of the

requirements for the degree

of

Doctor of Philosophy

Nove

Dedications

This dissertation is dedicated to my wife, Carolyn Davis, and my daughter, Olivia Bartrand. Few people in my station in life have the opportunity to devote time and effort to a dissertation. That is because they don't have a wife and daughter like mine. Thank you both for the support, the fun, the trips to the lab and office, the loan of parts of the house to act as my office and, above all, the love you've given during this process. May I do the same for you both.

Ackowledgements

During my dissertation studies, my work was funded by the L.D. Betz Endowment for Environmental Engineering, the Koerner Family Fellowship, the Philadelphia Water Department, the Steven Geigerich Schoarship, and the Northeast Chemical Association. I am deeply grateful for the support of these organizations.

I received technical support from many during the execution of my work. Without the help of the individuals I mention below, this work would surely have faltered. My greatest thanks are due to my advisors, Professor Charles Haas and Professor Bakhtier Farouk. Their assistance to me went beyond technical assistance. They showed me, through example and in discussions, what research should and could be. They also shared their knowledge of proposal writing and project development with me. If, in the future, I should succeed at these endeavors it will be by following their examples. I am grateful for the oversight and improvements in my dissertation provided by my other committee members, Prof. Raj Mutharasan, Prof. Wen Shieh and Dr. Jin Wen.

Others who helped me in my research at Drexel are Blaise Tobia (College of Media, Arts and Design), who helped develop the lighting scheme I used in experiments, Gary Burlingame, Philadelphia Water Department, who always opened his door to me when I called, Nicole Charlton, Philadelphia Water Department, who provided a tour and data of the Philadelphia Water Department's pilot reactors, Dr. Patrick Gurian, for assistance with statistics, Dr. Guibo Xie, for assistance with chemistry, and, last but not

least, Professor Joseph Martin, for helping me find a perfect bubble column reactor and for good conversations about engineering and beyond.

Kim DiGiovanni, Russell Goodman, Dr. Domenico Santoro, Joanna Pope, Mark Weir, Arun Kumar and Shamia Hoque all helped in experimental data acquisition. Thanks to them for their efforts and the cheerful way in which they offered them.

The Civil, Architectural and Environmental staff, Barbara Interlandi, Sharon Stokes, Ken Holmes and Amanda Gonzales, are to be commended for their willingness to help students and the collegial way they worked with them.

Finally, I acknowledge the help and camaraderie of my fellow graduate students not yet mentioned, Dr. Dennis Greene, Dr. Bariş Kaymak, Dr. Lijie Li, Jason Marie, Dr. Rob Ryan and Jade Blackwell. These students and those mentioned above made my graduate studies richer and more enjoyable than I could have expected.

Table of Contents

LIST OF TABLES

LIST OF FIGURES

ABSTRACT

Countercurrent flow hydrodynamics and mass transfer were explored using computational fluid dynamics (CFD) analyses, tracer studies and a novel mass transfer visualization technique. In concert, these techniques yielded a comprehensive description of countercurrent hydrodynamics and mass transfer.

In the laboratory bubble column reactor in which experimental studies were performed, liquid flowed upward with gas bubbles in the core of the bubble plume and downward outside the bubble plume near the cylinder walls at all gas flow rates. CFD predicted a large recirculating flow near the sparger. Well-mixed conditions were observed in a zone termed the entrance length, located near the sparger. Mass transfer visualization experiments allowed estimation of the entrance region length. The entrance region increased as a function of gas flow rate and ranged from a value of about 22% (for the lowest gas to liquid flow ratio experiment) to nearly 40% (for the highest gas to liquid flow ratio experiment.

To demonstrate its utility as a design tool or for troubleshooting underperforming full scale reactors, CFD was used to predict hydrodynamics, *Cryptosporidium parvum* inactivation and bromate formation in a full scale reactor. Despite being relatively crude the CFD model identified flowfield features conducive to bromate formation or deleterious to *C. parvum* inactivation. Specifically, in chambers in which ozone is applied, large recirculating flows were predicted. Water detained in these recirculating flows have relatively long detention times and contribute to bromate formation in waters with sufficient bromide content.

The current study demonstrates that, even in a simple tall right circular cylindrical bubble column, hydrodynamics plays a major role in contact of ozone with microorganisms and substances that form bromate. Both experimental and analytical studies identified significant spatial variations in mixing and mass transfer in the relatively simple bubble column reactor. These findings indicate that CFD could be more widely used as a component of pilot scale studies of ozone bubble contactor reactors or in design of full scale contactors. Given current computer prices and speeds, CFD analysis is appropriate for plants with capacities which are smaller than the very large capacity plants for which CFD is presently used.

I INTRODUCTION

Thorough, efficient water disinfection requires sustained, uniform contact between pathogenic organisms suspended in the water and dissolved disinfectant. The most frequent way of assessing the extent of disinfectant-pathogen contact is through estimation of "*Ct,*" where *C* is the disinfectant residual and *t* is the contact time between disinfectant and organisms.

The disinfectant residual is seldom uniform or steady. Chemical disinfectants react and decay. Mixing of disinfectant with pathogen-laden water may be incomplete. In ultraviolet disinfection processes, shielding or variations in distance between pathogens and the UV source may result in non-uniform contact between disinfectant and microorganisms. To account for spatial and temporal variations in disinfectant-organism contact and disinfectant residual, estimates for "*Ct*" are made using conservative estimates for contact time and disinfectant concentration, such as the time required for 10% of a conservative tracer to exit the reactor in a pulse tracer experiment (T_{10}) and the disinfectant residual at the reactor discharge or discharge from individual chambers in the reactor (Lev and Regli 1992a; Lev and Regli 1992b).

Beyond having to account for uneven contact between organisms and disinfectant, regulatory agencies must also apply safety factors to estimated *Ct* values to account for uncertainty in inactivation rate models and for the influence of water matrix constituents and varying water quality properties on inactivation rate. For example, given the wide variation in observed *Cryptosporidium parvum* inactivation rates, disinfection goals up to 1 log-unit higher than desired disinfection goals may be required to ensure actual

inactivation is within 95% confidence bounds of predicted inactivation (Finch et al., 2001).

There are drawbacks to the protective design approach to disinfection process design criteria described above – disinfection byproduct (DBP) formation and excessive energy consumption and chemical dosing. Depending on the composition of the water that is disinfected and the disinfectant used, byproducts that pose chronic human health risks may be formed during disinfection. Chlorine-based disinfectants produce trihalomethanes (THMs) and haloacetic acids (HAAs) among other byproducts. THMs and HAAs are regulated under the Disinfectant and Disinfectant Byproducts rule (US EPA Office of Water 2001) and numerous community public water treatment facilities have been out of compliance with these regulations since their promulgation (US EPA 2005).

As will be described in Chapter 2, ozone produces fewer and lower concentrations of DBPs than chlorine, except in waters high in bromide (Br^-). In those waters, depending on the pH, ammonia concentration, temperature, alkalinity and dissolved organic carbon concentration, bromate (BrO_3^-), a suspected human carcinogen, may be formed. The US EPA's current maximum contaminant level (MCL) for bromate is 10 μg/L.

Microbial inactivation and DBP formation processes occur at the same time scale, as illustrated in Figure 1. Taking *Ct* to indicate a level of disinfection, the plot shows exposure to *Cryptosporidium parvum* oocysts and bromate commensurate with a range of disinfection levels. The dashed curve showing reduction in *Cryptosporidium parvum* is

based on an inactivation rate model derived from batch studies of *Cryptosporidium* inactivated in filtered water (Finch et al., 2001). The bromate formation curve was developed based on regression analysis of bromate formation rate data and is drawn for filtered water with a relatively high (170 μg/L) initial bromide ion concentration (Song et al., 1996). Recalling that the current MCL for bromate is 10 μg/L, achieving a design reduction in *Cryptosporidium parvum* of 2 logs using only ozone disinfection is not possible without exceeding the bromate MCL unless steps are taken to enhance inactivation or retard bromate formation. If appropriate safety factors protective of microbiological quality are employed, bromate concentration will exceed the MCL by an even greater amount.

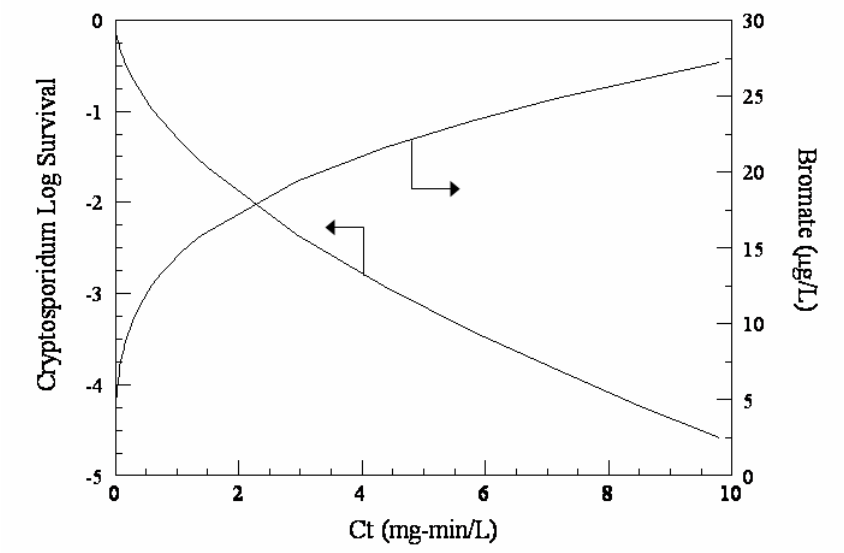

Figure 1: Inactivation and DBP Formation for a Hypothetical Water

In chlorine-based disinfection, chemical disinfectant is introduced to the treatment train as a solution and is mixed with process water prior to introduction to the disinfection processes. After the disinfectant demand of the raw water is satisfied, the rate of decay of active forms of chlorine is slow relative to typical retention times in disinfection processes and the chlorine concentration does not vary significantly in the reactor. In ozone disinfection, water enters the reactor with no ozone and ozone is dissolved into process water in early stages of the disinfection process. There is often significant ozone demand in the early portion of an ozonation process. For example, in a pilot study of ozonation of Central Arizona Project (CAP) water, identical ozone doses were applied to two identical cylindrical contactors arranged in series and operating in countercurrent mode. When the contact time in the cylinders was large (above 7.5 minutes) the increase in ozone residual between the intake and discharge in the second column was double that of the first column (Nieminski 1990). The rate of decay of ozone is also significantly higher than that of chlorine disinfectants, especially for water at temperatures above 20°C or that are slightly basic (Rakness 2005). Thus, ozone concentration varies more widely than that of chlorine in disinfection processes.

Because the number of pathogens present in treated drinking water is very low, regulating disinfection processes based on detection of pathogens in reasonably sized samples is not possible. Rather, the United States Environmental Protection Agency grants “disinfection credits” for well-operated filtration processes, disinfection and, in recent amendments to the safe drinking water act, demonstration of high source water quality and protection (42 U.S.C. 300g-1(b)(7)(C)(iv)). Plants receive “*Ct* credit” based on measured or estimated hydraulic characteristics of unit process operations and based

on batch kinetic studies of their disinfectant's decay rate in the plant's water. *Ct* credit for disinfection processes is established based on measurement of disinfectant dose at the reactor discharge and intermediate locations and on either measured residence time distributions (RTDs) or using hydraulic models such as continuously stirred tank reactors (CSTRs) for assessing reactor hydraulics. The *Ct* required to achieve a desired reduction in microbial concentration depends on the disinfectant, the microorganism, water properties (primarily pH and temperature) and constituents, initial microbial density, and possibly other factors. Log credit awarded by EPA for *Cryptosporidium* inactivation by ozone is presented in Table 1.

Table 1: Ct Values for Cryptosporidium Inactivation by Ozone (40 CFR 141.730)

Log credit	**Water Temperature (°C)**									
	0.5	**1**	**2**	**3**	**5**	**7**	**10**	**15**	**20**	**25**
0.5	12	12	10	9.5	7.9	6.5	4.9	3.1	2.0	1.2
1.0	24	23	21	19	16	13	9.6	6.2	3.9	2.5
1.5	36	35	31	29	24	20	15	9.3	5.9	3.7
2.0	48	46	42	38	32	26	20	12	7.8	4.9
2.5	60	58	52	48	40	33	25	16	9.8	6.2
3.0	72	69	63	57	47	39	30	19	12	7.4

The current conservative approach to disinfection is evident in the assessment and assignment of treatment plant Ct described above. Table 2 provides an overview of the disinfection/byproduct tradeoff. Source waters carry with them varying loads of

pathogenic organisms and chemical compounds and have diverse physical properties. Given these complexities, establishing an optimal reactor design that provides sufficient disinfection and minimizes disinfection byproduct formation is clearly a formidable task that will require significant experimental studies and modeling.

Table 2: Summary of Disinfection Impacts (United States Environmental Protection Agency 1999)

Disinfection parameter	**Typical impact on pathogen inactivation**	**Typical impact on DBP formation**
Disinfectant type	Depends on inactivation efficacy	Depends on disinfectant reactivity
Disinfectant strength	The stronger the disinfectant, the faster the disinfection process.	The stronger the disinfectant, the greater the production of DBPs.
Disinfectant dose	Increasing the disinfectant dose increases the disinfection rate	Increasing the disinfectant dose typically increases the rate of DBP formation
Type of organism	Susceptibility to disinfection varies according to pathogen group. In general, protozoa are more resistant to disinfectants than bacteria and viruses.	None.
Contact time	Increasing the contact time decreases the disinfectant dose required for a given level of inactivation	Increasing the contact time with an equivalent disinfectant dose increases the formation of DBPs.
pH	pH may affect the disinfectant form and, in-turn, the efficiency of the disinfectant.	The impact of pH varies with DBP. For ozonated water containing bromide ion, high pH favors the formation of bromate ion and low pH favors formation of brominated organic byproducts.
Temperature	Increasing temperature increases the rate of disinfection.	Increasing temperature typically promotes faster oxidation kinetics and, hence, increases DBP formation.
Turbidity	Particles responsible for turbidity can surround and shield pathogenic microorganisms from disinfectants.	Increased turbidity may be associated with increased NOM, which represents an increased amount of DBP precursors for the formation of DBPs when disinfectant is applied.

Disinfection parameter	Typical impact on pathogen inactivation	Typical impact on DBP formation
Dissolved organics	Dissolved organics can interfere with disinfection by creating demand and reducing the amount of disinfectant available for pathogen inactivation.	Increased dissolved organics will represent a larger amount of DBP precursor for the formation of DBPs when the disinfectant is applied.

I.1 Objectives and Study Overview

The current study provides detailed quantitative information on the mixing and mass transfer processes for dissolution of ozone in countercurrent flow and demonstrates use of a detailed model for design and analysis of ozone bubble contactors. These detailed measurements and analyses are intended to allow more precise prediction of ozone mass transfer, microbial disinfection and chemical byproduct formation and can be used to strike a balance allowing management of acute risk of microbial infection and management of chronic risks associated with disinfection byproducts.

As described in the following chapter, many mass transfer relations for dissolution of gases from bubbles have uncertain applicability at conditions differing from those in which the data from which they were developed were collected. Specifically, many relations found in the literature were developed for co-current bubble contactors or are theoretical relations developed without concern over the interactions between the liquid flow field and bubble plume and their impacts on mass transfer. None of the mass transfer studies described in the literature review included an assessment of axial variations in mass transfer. Mass transfer studies and mass transfer relations drawn from the literature are described in detail in section II.1.1.5. Given the marked difference

in the distribution of bubbles and their momentum near the sparger compared with their distribution and momentum away from the sparger, these axial variations are expected to be significant and should be explored.

I.1.1 Objectives

The goal of the present work was to quantify the influence of non-ideal hydrodynamics on mass transfer and contact of dissolved ozone with pathogens in countercurrent bubbly flow. The objectives of this work were to:

- Quantify dispersion (inclusive of axial variations) in a laboratory countercurrent flow bubble column reactor using experimental residence time distribution studies and computational fluid dynamic (CFD) modeling and relate the dispersion to reactor operating conditions and geometry;
- Use a novel visualization technique for observing ozone mass transfer (inclusive of axial variations) in the bubble column and determine whether axial variations in mass transfer significantly impact the ability of engineers to scale up countercurrent flow reactors;
- Validate a CFD model for ozone mass transfer in countercurrent flow and assess the accuracy of the mass transfer model in predicting mass transfer in countercurrent flow; and
- Demonstrate the ability of the validated CFD model to simultaneously predict *Cryptosporidium parvum* inactivation and bromate formation in a full-scale reactor

and identify advantages and disadvantages of CFD compared with design models currently used in ozone bubble contactor design and Ct credit assessments.

I.1.2 Overview

To achieve these objectives, two sets of experiments were performed and a CFD model of countercurrent ozone mass transfer, inclusive of relevant chemistry and microbial inactivation, was developed and exercised. The two sets of laboratory experiments were

- tracer studies performed to quantify mixing and hydrodynamics in countercurrent gas-liquid flow and
- ozone mass transfer visualization studies performed to enable estimation of mass transfer rate and identify spatial variations in mass transfer.

The CFD model was developed using the commercial CFD code CFX (ANSYS Inc. 2004) and was validated using data taken in both the tracer studies and mass transfer visualization studies. Results from CFD studies were compared with those of experimental studies, providing explanation for trends observed. Finally, a CFD model was developed and executed for simultaneous prediction of *Cryptosporidium parvum* inactivation and bromate formation in a full scale reactor.

I.2 When and Why Ozone is Used in Water Treatment

I.2.1 Ozone Use in Potable Water Disinfection

In general, potable water[1] disinfectants are strong oxidants and may serve multiple purposes in the water treatment process. These may include (United States Environmental Protection Agency 1999):

- Inactivation of pathogenic organisms;
- Control of aquatic nuisance species;
- Oxidation of iron and manganese;
- Removal of compounds causing tastes and odors;
- Improvement of coagulation (and subsequent filtration);
- Removal of color;
- Prevention of algal growth in sedimentation basins and filters; and
- Prevention of biological regrowth in distribution systems.

Thus, selection of a chemical for water disinfection may be guided by its use in other processes in water treatment as well as its ability to kill pathogenic organisms.

Chlorine remains the most widely used disinfectant in the United States. As of 2000, The United States Environmental Protection Agency reports that 68.7% of

---

[1] In the remainder of this thesis, all processes will be assumed to be for potable water treatment and the modifier “potable water” will be omitted.

community water systems (systems providing service connections and year-round service to at least 15 connections or 25 people, inclusive of those required to disinfect and those exempt) use chlorine downstream of filtration (for those plants employing filtration) (United States Environmental Protection Agency 2000). This percentage includes plants using one or more disinfectants in conjunction with chlorine. Only 0.4% of plants report using ozone downstream of filtration, though 3.5% of reporting plants use ozone for predisinfection or oxidation upstream of filtration.

However, as American utilities strive to meet disinfection and disinfection byproduct goals required by the Stage 1 Disinfectants and Disinfection Byproducts Rule and Long Term 2 Enhanced Surface Water Treatment Rule (LT2SWTR), plants are assessing ozone disinfection as an alternative, particularly for *Cryptosporidium parvum* inactivation and for disinfection byproduct minimization.

I.2.2 Advantages and Disadvantages of Ozone as a Disinfectant

The impetuses for recent increases in the number of U.S. water treatment plants incorporating ozone disinfection into treatment are concerns over chlorine-resistant organisms and disinfection byproducts. Specifically, ozone is the only chemical disinfectant that inactivates *Cryptosporidium parvum* at doses and contact times realizable in treatment plants and does not produce the halogen-substitute byproducts typical of water treated with chlorine. The advantages and disadvantages of ozone disinfection (compared with other schemes) are summarized in Table 3 (US EPA Office of Water 1999).

Table 3: Advantages and Disadvantages of Ozone as a Disinfectant

Advantages	Disadvantages
▪ More effective than chlorine, chlorine dioxide, chloramines for inactivation of viruses, *Cryptosporidium parvum* and *Giardia* ▪ Efficient chemical disinfectant requiring relatively short contact time ▪ In the absence of bromide, halogen-substitute DBPs are not formed. ▪ Ozone is a strong oxidant and controls odor, color and taste	▪ Produces disinfection byproducts including products of bromide (primarily bromate), aldehydes, ketones and others. ▪ High capital and operating costs ▪ Ozone is corrosive and toxic ▪ Ozone provides no residual ▪ Ozone decays rapidly at high pH and warm temperatures

I.3 Ozone Contactor Design

I.3.1 Typical Reactor Designs and Design Parameters

Gaddis (1999) lists potential gas-liquid contactors (excluding surface contactors which would be inappropriate for ozonated water) as bubble columns, stirred vessels, jet loop reactors and impinging stream reactors. Among these, the bubble column has the lowest volumetric mass transfer coefficient but offers the advantages of simple design and operation, high interfacial transfer area (to account for a much higher liquid film resistance to mass transfer than gas film resistance) and, when well-designed, a greater propensity toward plug flow hydraulics. Thus, ozone contactors are often bubble columns. Shah, Kelkar et al. (1982) state that bubble contactors are well suited for slow liquid phase reactions (such as microbial inactivation by dissolved ozone gas) due to high

transport rates between phases, high interfacial area, large liquid holdup and the absence of moving parts.

A schematic diagram showing typical ozone bubble contactor configuration is found in Figure 2 (based on Cockx et al., 1999). Countercurrent and co-cocurrent flow may be encountered, though countercurrent contact between bubbles and liquid is more common (Rakness 2005). Industrial ozone bubble contactors are typically on the order of 4 m tall and employ baffling as shown in Figure 2 to promote uniform contact between the phases and distribution of ozone in the untreated water. Off gas from industrial bubble contactors is collected and either destroyed or recycled and reinjected into the water.

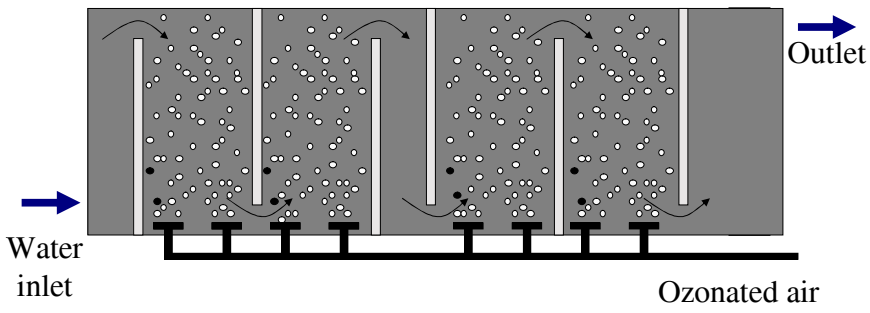

Figure 2: Schematic Diagram of a Full Scale Ozone Bubble Contactor

The bubble contactor design features that determine contactor performance and over which engineers have control are (Do-Quang et al., 2000):

- Contactor geometry;
- Gas/water flow rates:

- Gas/water flow ratio; and
- Diffuser positions.

The choice of these design and operating parameters determines bubble contactor performance and is manifested in gas holdup distribution, liquid phase mixing, mass transfer coefficients, bubble size distribution and coalescence (Sanyal et al., 1999).

Geometric features of contactors demonstrated to significantly improve hydraulic performance (increase the ratio of T_{10} to hydraulic residence time) are addition of baffles (especially double baffles), use of spargers that produce fine bubbles, and uniform distribution of spargers along the contactor bottom (Henry and Freeman 1995; Do-Quang et al., 2000). Design features that have shown only minor influence on reactor hydraulics performance are addition of corner fillets and wall foils.

I.3.2 Reactor Design and Scale-up

With the possible exception of CFD analyses, there are no models or fundamental theories capable of a priori, dependable prediction of liquid phase mass transfer coefficients or gas phase holdups for multiphase flow reactors (Nauman 2001). Factors such as non-ideal reactor hydrodynamics, variations in liquid or gas composition and quality, and transient operation influence mass transfer rate. So full scale ozone bubble contactor reactor designs are based on measurements taken in bench scale semi-batch or batch experiments performed in well-stirred reactors or on measurements in continuous flow pilot systems.

To the extent possible, engineers are advised to design pilot and bench scale reactors that physically resemble full scale reactors (Langlais et al., 1991), giving rise to a

chicken and egg dilemma. Scale-up of semi-batch systems can be done effectively – Rakness (2005) reports nearly identical predicted and realized performance for a full scale ozone contactor designed based on semi-batch data. One possible explanation for this agreement is that the chambers in the full-scale contactor perform as continuously stirred tank reactors (CSTRs) and that the hydrodynamics closely resemble those in semi-batch experiments. The positive side of this agreement is that the full scale contactor achieved design goals. The negative side is that, if the chambers are behaving as CSTRs, ozone transfer and inactivation are less than they would be if the contactor had been designed with hydraulics closer to plug flow.

Often, in pilot studies gas phase ozone concentration is measured only at the reactor intake and in the off-gas and ozone mass transfer is quantified via the transferred dose or the transfer efficiency (100% × transfer dose/applied dose) (Langlais et al., 1991; Rakness 2005). Because ozone contactors are invariably designed with relatively low gas to liquid flow ratios, transfer efficiency is almost always very high (> 95%). Commonly, design engineers simply assume that transfer efficiency of typical bubble contactors is in the range 90% to 95% (Schulz et al., 2003). Such gross mass transfer data and assumptions provide no information on where in the reactor the mass transfer occurs and provide no guidance on the optimal liquid phase depth, despite the goal of setting full scale reactor depth to ensure high transfer efficiency and minimize ozone production costs (Langlais et al., 1991).

I.3.3 *Ct* Credit

As described above, utilities demonstrate compliance with water disinfection regulations by obtaining "*Ct*" credits based on design and operation of bubble contactors, not through direct measurement of reduction in microbial loads in the process stream. A description of how *Ct* is calculated follows. This discussion is important because meeting *Ct* requirements is the primary design goal for engineers designing ozone bubble column reactors. For the work presented in this dissertation to be of practical use in the water treatment industry, it must be applicable within the framework of the current regulatory system or it must present alternative methods for ensuring adequate disinfection.

The US EPA has approved assessment of *Ct* in ozone bubble contactors via one of four prescribed models (described below) or via a site specific evaluation (US EPA Office of Water 2003; Rakness 2005). The models allowable for claiming *Ct* credit in ozone bubble contactors are:

- The T_{10} method,
- segregated flow analysis (SFA);
- completely stirred tank reactor (CSTR) analysis; or
- extended CSTR analysis.

Guidelines for selection of Ct calculation method from EPA's guidance for compliance with the Long Term 2 Enhanced Surface Water Treatment Rule (LT2ESWTR) are presented in Table 4.

Table 4: Guidelines for Selection of Ct Calculation Method

	Section description	Terminology	Method for calculating log inactivation	Restrictions
No tracer data	*Chambers where ozone is added*			
	First chamber	First dissolution chamber	No log inactivation credit is recommended	None
	Other Chambers	Co-current or counter-current dissolution chambers	CSTR method in each chamber w/ a measured effluent residual concentration	No credit given to a dissolution chamber unless detectable ozone residual is measured upstream of the chamber
	Reactive Chambers			
	≥ 3 consecutive reactive chambers	Extended CSTR zone	Extended CSTR method in each chamber	Detectable ozone residual should be present in at least 3 chambers in zone, measured via in-situ sample ports. Otherwise, apply CSTR method individually to each chamber with a measured O_3 residual
	< 3 Consecutive chambers	CSTR reactive chambers	CSTR method in each chamber with a measured ozone residual concentration	None
With tracer data	*Chambers where ozone is added*			
	First chamber	First dissolution chamber	No log inactivation credit is recommended	None
	Other Chambers	Co-current or counter-current dissolution chambers	T_{10} or CSTR method in each chamber	No credit is given to a dissolution chamber unless a detectable ozone residual is measured upstream of the chamber
	Reactive chambers			
	≥ 3 consecutive reactive chambers	Extended CSTR zone	Extended CSTR method in each chamber	Detectable ozone residual should be present in at least 3 chambers in zone, measured via in-situ sample ports. Otherwise, apply the T_{10} - CSTR method individually to each chamber with a measured O_3 residual
	< 3 Consecutive chambers	CSTR reactive chambers	CSTR method in each chamber with a measured ozone residual concentration	None

The compliance guidance for the LT2ESWTR has been withdrawn pending revision, though the draft guidance (US EPA Office of Water 2003) is referenced in this dissertation. The LT2ESWTR allows calculation of Ct using the extended CSTR method (described below) in addition to the methods allowed under the Surface Water Treatment Rule (SWTR) (US EPA Office of Drinking Water 1991).

I.3.3.1 The T_{10} Method

In the T_{10} method, conservative estimates for the residence time of fluid elements in the reactor and the average ozone concentration in the elements during their residence are made and Ct is the product of the estimates. T_{10}, the time required 10% of a conservative tracer introduced as a pulse at the reactor inlet to exit the reactor, has been shown to provide a conservative estimate of the time fluid elements spend in a reactor, whether flow in the reactor approaches that in a CSTR or that of an advection-dispersion-reaction model (Lev and Regli 1992b). Since the ozone concentration varies from chamber to chamber in a multi-chamber reactor (such as the one depicted in Figure 2), it is necessary to estimate the T_{10} for individual chambers separately. In the absence of tracer data for individual chambers, it is assumed that the T_{10} of individual chambers scales with the overall system T_{10} according to

$$T_{10,\text{subunit}} = \left(\frac{V_{\text{subunit}}}{V_{\text{system}}} \right) T_{10,\text{system}} \quad (1)$$

where V_{subunit} is the volume of the subunit and V_{system} is volume of the overall system. According to the authors, equation 1 provides a reasonable estimate of subunit T_{10} for subunits whose volume is less than 50% the total reactor volume.

Because ozone undergoes autodecomposition in water, ozone concentration is not constant in contactors and the average ozone concentration in subunits of the reactor must be estimated for use in Ct calculations. The mode of operation (countercurrent two-phase flow, co-current two phase flow or reactive segment [with no ozone application]) in a given reactor subunit dictates the way the average ozone concentration is calculated. It is assumed that, because of ozone demand and decay, no significant ozone residual is achieved in the first chamber of an ozone bubble contactor in which ozone is applied. In subsequent chambers, the following guidelines apply (Lev and Regli 1992a):

$$C_{avg} = \begin{cases} 0 & \text{First dissolution chamber} \\ C_{out}/s & \text{Countercurrent operation; } 2 \le s \le 3 \\ \frac{1}{2}\left(C_{out} + C_{in}\right) \quad \text{or} \quad C_{out} & \text{Cocurrent operation} \\ C_{out} & \text{Reactive segments} \end{cases} \tag{2}$$

In equation 2, C_{avg} is the average ozone concentration in a subunit, C_{out} is ozone concentration at the subunit discharge, C_{in} is the ozone concentration at the subunit inlet and s is a safety factor. When ozone decomposition rate is high, the safety factor approaches the value 3; when decomposition rate is low, it approaches 2.

I.3.3.2 CSTR Analysis

The CSTR analysis (described below) is appropriate for

- reactors whose flow approaches that of a CSTR,
- reactors with only one chamber and for which T_{10} / HDT < 0.33 *and* required inactivation level for *Giardia* greater than or equal to 2.5 logs, and

- reactors for which there are no tracer data (U.S. EPA Office of Drinking Water 1991).

Assuming disinfectant and microorganisms are homogenously distributed within a reactor chamber and that inactivation of microorganisms is first order with respect to microorgansism concentration and disinfectant concentration (Chick kinetics), the Ct that achieves a survival ratio of N/N_0 (concentration of surviving organisms divided by concentration of organisms introduced to the chamber) is given by

$$C \times (\mathrm{HDT}) = \frac{1 - (N/N_0)}{2.303 k (N/N_0)} \tag{3}$$

In equation 3, HDT is the theoretical hydraulic detention time (chamber volume ÷ volumetric flow rate) and *k* is the inactivation rate constant (assuming first order kinetics with respect to microorganism density and disinfectant concentration) for the microorgansism of interest. At present, the two organisms believed most resistant to disinfection are *Giardia* and *Cryptosporidium* and *Ct* is calculated for one or both of those organisms. The inactivation rate constant may be determined via batch kinetic studies (the preferable method) or drawn from tables of inactivation rate constants published by the EPA.

I.3.3.3 Segregated Flow Analysis

In the segregated flow analysis (SFA), it is assumed that the inactivation achieved in a reactor is proportional to two probabilities: the probability that a microorganism remains in the reactor for a specified time and the probability that the microorganism is

inactivated if exposed to disinfectant for the specified time. The segregated flow model is illustrated in Figure 3.

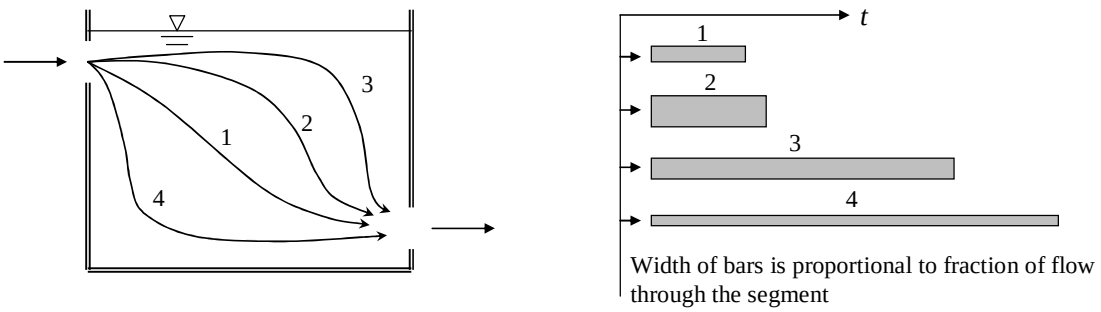

Figure 3: Segregated Flow Analysis Illustration

The probability distribution for water (and microorganism) residence times, $E(t)$, is determined via tracer studies and residence time distribution analyses (Danckwerts 1953; Haas et al., 1997). The probability of inactivation over a time period, t, is calculated using a modified form of Chick's law (Trussell and Chao 1977):

$$\frac{N}{N_0} = 10^{-kCt} \tag{4}$$

Note that in equation 4 that the ozone residual concentration, C, is assumed constant with respect to time. The EPA's guidance does not provide explicit instructions on the value of ozone concentration for use in equation 4.

The overall probability of organism survival is then

$$\frac{N}{N_0} = \sum_{i=1}^{n} E(t_i) \times 10^{-k(Ct)_i} \tag{5}$$

where *n* is the number of segments into which the flow was divided. Equation 5 may be used to determine the concentration, *C*, required to achieve a desired level of disinfection.

I.3.3.4 Extended CSTR Analysis

In the extended CSTR method, three or more consecutive reactive chambers (chambers without ozone addition) can be analyzed as consecutive CSTRs (US EPA Office of Water 2003). In the ozone bubble contactor shown in Figure 4 (based on the example of the extended CSTR method provided by Rakness (2005)), the reaction zone over which the extended CSTR method may be used to estimate inactivation is comprised of all the chambers downstream of chamber 1 (in which ozone is applied). Each of the chambers is treated as a CSTR. Three sample points, S1, S2 and S3 are shown. The ozone residual is measured at each o those sample points and used in estimation of the ozone decay rate and average residual in each chamber. The advantages of the extended CSTR method are that it requires very little experimental data and that it accounts for ozone decay more systematically than the other Ct analyses.

The ozone decay rate, k^*, in the reactor is estimated based on the difference in ozone residual measurements made at sample ports 1 and 2 and between sample ports 1 and 3. Sample location one should be at least one chamber downstream of the discharge of a chamber in which ozone is applied. This ensures that most of the ozone demand has been exerted and measured differences in ozone concentration are due to autodecomposition.

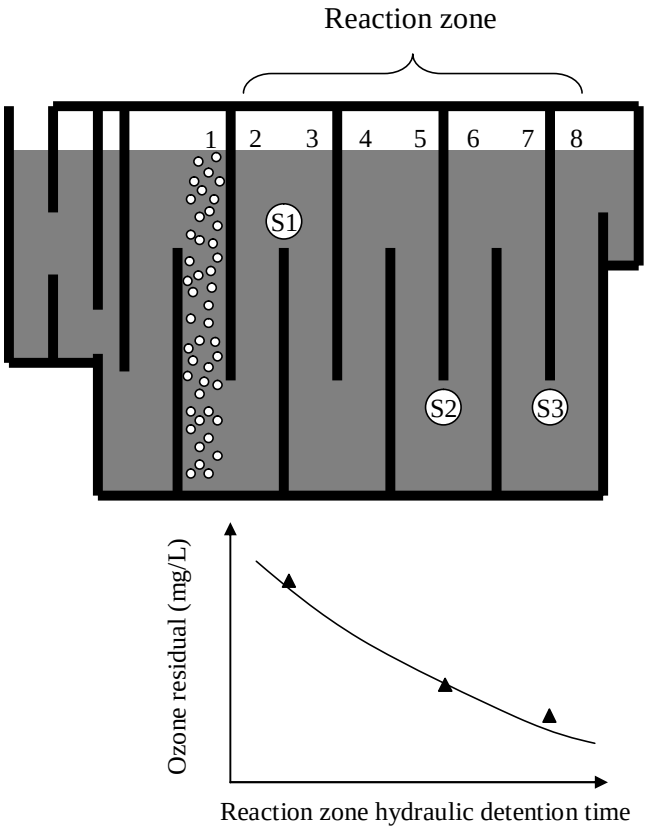

Figure 4: Extended CSTR Method Illustration

Assuming all chambers are CSTRs, the decay rate between sample locations i and j is given by

$$k^*_{i-j} = \frac{n_{i-j}}{(\mathrm{HDT})_{i-j}}\left[\left(\frac{C_i}{C_j}\right)^{(1/n_{i-j})} - 1\right] \quad (6)$$

where k^*_{i-j} is the apparent ozone decay rate based on measurements i and j, n_{i-j} is the number of chambers between sample points i and j, $(\mathrm{HDT})_{i-j}$ is the net theoretical hydraulic detention time between sample points i and j, and C_i and C_j are the ozone

residual concentrations measured at sample points i and j. Equation 6 is evaluated between sample points 1 and 2 and between sample points 1 and 3. The average decay rate, k^*_{avg}, is the average of k^*_{1-2} and k^*_{1-3}, provided neither value differs from the average by more than 20%.

The ozone concentration at the inlet to the reaction zone is estimated based on the concentrations measured at the three sample points. First, an inlet concentration is estimated based on the average decay constant and the measured ozone concentration at each sample point:

$$C_{\text{in},1} = C_1 \times \left(1 + k^*_{avg} \frac{V_{0\to1}}{n_{0\to1} \times Q}\right)^{n_{0\to1}} \tag{7}$$

$$C_{\text{in},2} = C_2 \times \left(1 + k^*_{avg} \frac{V_{0\to2}}{n_{0\to2} \times Q}\right)^{n_{0\to2}} \tag{8}$$

$$C_{\text{in},3} = C_3 \times \left(1 + k^*_{avg} \frac{V_{0\to3}}{n_{0\to3} \times Q}\right)^{n_{0\to3}} \tag{9}$$

In equations 7-9, $C_{\text{in},i}$ is the reaction zone inlet concentration estimated based on the concentration measured at sample location i, C_i is the concentration measured at sample location i, $V_{0\to i}$ is the reactor volume between the reaction zone inlet and sample location i, $n_{0\to i}$ is the number of chambers between the reaction zone inlet and sample location i, and Q is the volumetric flow rate. Concentration at the intake to the reaction zone is then

$$C_{in} = \frac{C_{\text{in},1} + C_{\text{in},2} + C_{\text{in},3}}{3} \tag{10}$$

The characteristic concentration for each chamber is calculated via the expression

$$C_i = \frac{C_{in}}{\left(1 + k^*_{avg} \frac{\mathrm{HDT}_{0\to i}}{n_{0\to i}}\right)^{n_{0\to i}}} \tag{11}$$

and the Ct for each chamber is the product of the hydraulic detention time and the characteristic concentration for that chamber. The overall Ct for the reaction zone is the sum of the Cts of the chambers in the reaction zone.

I.3.4 Roles for CFD within the Regulatory Framework

The models used to determine regulatory compliance are low-fidelity (zero-dimensional) and were developed to be easy to use and very conservative in their estimation of level of disinfection. Notwithstanding the presence of a CFD approach in the current regulation, there are several roles CFD might play in the ozone contactor design and benchmarking processes.

First, CFD models can provide detailed information on hydrodynamics that cannot be deduced from tracer studies or from sampling from a small number of positions in the reactor. This includes the situation where the reactor does not yet exist. Where tracer studies might identify that short-circuiting is occurring, CFD could be used in determining where the short-circuiting occurs. Where sampling such as that performed in the extended CSTR analysis can provide information on ozone concentration at strategic points, CFD can be used to predict concentration profiles anywhere in the reactor and more accurately quantify the variations in concentration throughout the reactor. CFD

might be used to inform the choice of sample locations, enabling engineers to avoid regions of backflow or other regions where the concentration might not be representative of reactor performance.

Second, CFD could be used as a component of the design process, supplementing and guiding the more intelligent conduct of expensive and time-consuming experimentation. If, through tracer analysis or other means, engineers determine a reactor has an unusually short T_{10}, they may opt to alter the reactor design to improve hydraulics and achieve a higher Ct. A validated CFD could be used to predict performance of reactors with modifications such as baffle additions, inlet or discharge reconfigurations or modified sparger placement.

Finally, as is demonstrated in the dissertation, CFD can be used for modeling multiphase reacting flows. This ability will enable design engineers to progress beyond models in which the ozone transfer efficiency is assumed. Improved modeling and understanding will yield reactor designs that improve bubble-liquid contact and mixing and promote more uniform ozone concentration in the process water.

I.4 CFD in Water and Wastewater Treatment Operations Analysis

Computational fluid dynamics (CFD) is being used more frequently in the water treatment and wastewater treatment engineering due to improvement in commercially-available CFD codes (especially improved physics and chemistry submodels) and because personal computers now have sufficient speed and memory to permit modeling of realistic water treatment processes.

In water treatment, CFD has been used to

- assess design modifications for improved clarifier performance (Adams and Rodi 1990; Lyn et al., 1992; Zhou et al., 1994; Brouckaert and Buckley 1999; Craig et al., 2002),
- simulate and troubleshoot flocculation processes (Ducoste and Clark 1999; Lainé et al., 1999; Liu et al., 2004),
- model the performance of a static mixer (Jones et al., 2002),
- simulate hydrodynamics and microbial inactivation in pilot and full scale chlorine contact chambers (Falconer and Ismail 1997; Wang and Falconer 1998; Greene et al., 2001),
- simulate multiphase flow in flotation processes (Sarrot et al., 2005);
- assess ozone contactor hydraulics, mass transfer and microbial inactivation (Henry and Freeman 1995; Murrer et al., 1995; Cockx et al., 1999; Do-Quang et al., 1999; Cockx et al., 2001; Huang et al., 2002; Ta and Hague 2004) and
- assess mixing in water storage tanks and reservoirs (Ta and Brignal 1998).

This list of applications will certainly grow as researchers develop and validate CFD models for water treatment applications and the environmental engineering community realizes benefits from CFD studies.

CFD has allowed engineers to perform relatively inexpensive testing and can be used to assist in reactor scale-up and design (e.g., in design of a UV disinfection reactor (Valade et al., 2003)). As noted in a previous study (Brouckaert and Buckley 1999), treatment processes in water and wastewater treatment plants are often carried out in

large vessels prone to non-uniform flow or other non-ideal flow characteristics. Examples of non-ideal processes that may take place in typical unit operations are:

- Short circuiting or dead zones in reactors;
- Poor mixing of reagents (e.g., coagulants) in flow streams;
- Inefficient settling in clarifiers operated at loadings different from design values;
- Stratification in membrane reactors;
- Stratification or short-circuiting in reservoirs and storage tanks.

Experimental determination of flow conditions in water and wastewater reactors and appurtenances is costly given the size of reactors and the likelihood that units would have to be taken off-line to facilitate measurements. Thus, CFD appears to meet a need currently not addressed in the water treatment industry.

I.5 Need for the Current Study

As illustrated in the literature review below, current design methodology for ozone contactors relies on simplified, calibrated models that are applicable over a relatively narrow range of reactor designs and operating conditions. So the current study was formulated to assess the ability of CFD to model operation of ozone bubble contactors accurately, inclusive of all significant hydrodynamics, chemistry and biology, using only submodels for turbulence (mixing), mass transfer, chemistry and microbial inactivation that are independent of reactor geometry or operating conditions. Such a capability would be a great benefit to engineers assessing the performance of pilot scale

reactors and designing full-scale reactors in which hydrodynamics may differ significantly from those encountered at the pilot scale.

Despite an extensive literature related to bubble columns, relatively few studies have been conducted on the behavior and modeling of countercurrent bubble flows and the performance of countercurrent bubble columns and even fewer have considered mass transfer; to date the majority of published studies on bubble contactor operation have focused on hydrodynamics and have analyzed columns of bubbles injected into a non-flowing liquid column or cocurrent flow. The work performed in this study was developed to advance the state of CFD analysis of bubble columns by adding the complexities of countercurrent flow, mass transfer, reaction and microbial inactivation. These additions are significant since the objective of a bubble column is to produce efficient mass transfer between phases and contact between disinfectant and pathogenic organisms and because many industrial bubble columns are run in countercurrent mode.

Just as a systematic study has been made of CFD submodels for momentum exchange between phases, so should there be a systematic study of mass transfer models. The CFD studies identified in the literature survey of this proposal present no strong justification for their selection of mass transfer submodel and the scientific community will benefit from a thorough review of the sensitivity of CFD simulations to choice of mass transfer relation and guidance in selecting a relation for a given design and operating condition.

I.6 Significance of the Proposed Work

I.6.1 Advancement of Knowledge

The current work is intended to yield three important contributions to the technical literature:

- Rigorous verification and validation of CFD countercurrent hydrodynamics and mass transfer submodels for ozone bubble contactor simulations;
- Detailed experimental and modeling investigation of interphase ozone mass transfer and mass transfer models; and
- Demonstration of simultaneous prediction of microbial inactivation and bromate formation with a CFD model that does not need to be "calibrated" with experimental data.

The majority of bubble contactor CFD studies published to date have entailed modeling hydrodynamics of bubble columns with either stagnant water or cocurrent flow. In the few studies published that included interphase mass transfer, countercurrent flow and microbial inactivation, researchers have not provided justification for their selection of bubble drag, interphase mass transfer or microbial inactivation models. Validation of submodels is an important step in demonstrating the utility of CFD in design of water treatment unit operations and will boost the confidence of the water utility community in CFD analyses.

Since bubble column hydrodynamics has been addressed in other studies, the mass transfer studies proposed herein will likely yield the greatest immediate benefit to

the scientific community. As described in detail below, mass transfer in bubble columns is complex and varies with water depth within a given reactor operating at known water and gas flow rates. The experimental work described below was designed to allow visualization of the mass transfer process and yield quantitative and qualitative data on the influence of phase distribution and mixing on the mass transfer rate. The experiments were novel and, arguably, were a significant improvement over pilot reactor mass transfer studies that have been performed in the past.

The CFD simulations of interphase mass transfer provide further details on interphase mass transfer physics and, most important, demonstrate that CFD is a better design tool than currently-used models and scale-up laws. CFD offers two benefits to the other approaches:

- Use of first principles in development of the model and
- characterization of the problem in sufficient detail to account for the influence of reactor geometry on reactor performance.

These benefits allow CFD to be used in more phases of the design process, even including the design of pilot facilities. Whereas lower-fidelity models such as the one-dimensional advection-dispersion-reaction model and completely stirred tank reactor (CSTR) model require calibration and cannot be used for reactors whose geometry differs from those to which the models were calibrated, CFD may be applied to any geometry.

Prediction of microbial inactivation and bromate formation in a full scale reactor with a CFD model is significant both because it will be the first such study in a published

work and because it will demonstrate a methodology for achieving an illusive public health goal – balancing acute microbial risk with long term risk from DBP consumption.

A final, incremental advancement in scientific knowledge is provided in simulation of microbial inactivation in continuous flow reactors. The microbial inactivation modeling performed builds upon the work performed by Greene (2003). However, this work further develops a procedure for including microbial inactivation in CFD simulations of continuous flow reactors and may expose alternatives or modifications to the *Ct* approach to reactor design leading to reduced deleterious byproduct formation.

I.6.2 Value to Industry

Compared with engineers from other disciplines, environmental engineers have been slow to adopt CFD as a design and analysis tool, though in the past 3-4 years the number of publications of CFD studies related to water and wastewater unit operations has increased dramatically. Validation and experience with CFD such as demonstrated in this dissertation should increase the confidence of the engineering community in CFD analyses and demonstrate the utility of CFD to water utilities choosing between experimental programs and CFD studies. CFD cannot replace careful experimentation in water treatment. It can, however, be used in concert with experimentation to shorten design cycle time, improve design of extant reactors, troubleshoot underperforming reactors and explore novel reactor designs. This study can act as another stone in the

foundation of studies that will make CFD a more attractive tool to environmental engineers.

An additional value to industry of the current work is improved understanding of ozone transfer in bubble contactors. According to calculations and experiments made in this study and the observations made in past studies (Mariñas et al., 1993), the most intense ozone transfer in bubble column reactors often takes place over a relatively small vertical portion of the reactor. Most ozone contactors are designed for nearly 100% ozone mass transfer efficiency (i.e., 100% of the applied dose transfer to the water). This design philosophy is necessitated by the expense of generating ozone and a lack of design relations capable of accurately predicting mass transfer rates in arbitrary geometries. The insights into mass transfer drawn from the work reported in this thesis may suggest reactor designs that are consistent with the processes occurring in countercurrent flow mass transfer and achieve acceptable ozone transfer efficiencies with reduced bromate formation.

The proposed work can contribute to the development and evaluation of the models the U.S. EPA current allows for utilities wishing to claim inactivation credit for ozone bubble contactors. Current guidelines do not allow inactivation credit for the first chamber in which ozone is introduced into a bubble contactor. The assumption is that ozone demand and decay in the first dissolution chamber are so high that no significant accumulation of dissolved ozone occurs. CFD analyses, as performed in this study, could allow detailed knowledge of ozone distribution in the first dissolution chamber and assessment of this guideline. In addition, CFD calculations can be compared with results

from CSTR, extended CSTR and segmented flow models of ozone bubble contactors. These comparisons will provide information that will help utilities make appropriate choices for modeling to claim inactivation credit and will provide information to U.S. EPA on whether the segmented flow model is appropriate for ozone bubble contactors and how best to apply it.

II LITERATURE SURVEY

This chapter surveys studies of bubble column reactor hydrodynamics and performance, ozone disinfection and byproduct formation, modeling studies apropos to ozone bubble contactors and ozone bubble column reactor design and scale up.

First, a description of phenomena occurring in bubble column reactors in general and ozone bubble contactors in specific is presented. Next, models for the physical and chemical phenomena occurring in ozone bubble contactors are reviewed. This review is merited since these models are employed in CFD simulations and because CFD simulations may provide a means to estimate some of the parameters commonly used in reactor design.

Significant processes that occur in diffused ozone bubble column reactors are:

- Gas injection and bubble dynamics
  - Introduction of gas into liquid stream
  - Evolution of bubble shape and acceleration to terminal velocity
  - Bubble breakup, collision and agglomeration
- Mixing
  - Large length scale liquid phase turbulence related to the reactor intake, discharge and geometry and exchange of momentum between the bubble plume and liquid outside the bubble plume
  - Small length scale liquid phase turbulence related to dissipation of turbulence and hydrodynamics of bubble wakes

- Mass transfer
    - Dissolution of gaseous ozone molecules through chemical and physical barriers at the bubble surface and into the liquid phase
    - Diffusion (penetration) of dissolved ozone into liquid adjacent to the bubble surface
    - Exchange of liquid at the bubble surface with liquid from the bulk liquid phase
    - Exchange of ozone-rich liquid in the bubble plume with ozone-poor liquid outside the bubble plume.
- Chemical reaction and microbial inactivation
    - Ozone demand
    - Ozone decay
    - Bromate and disinfection byproduct (DBP) formation
    - Microbial inactivation.

Studies that provide insight into or quantification of these processes are summarized below. The data and relations presented are drawn from a rich literature on bubble column reactors. The vast majority of published studies describe performance of pilot scale cylindrical bubble column reactors operated in either co-current mode (with the liquid and gas phases flowing in the same direction) or with non-flowing liquid phase. Because bubble column reactor performance is strongly dependent on column geometry (especially diameter to height ratio) and operating conditions (especially gas to liquid

volumetric flow ratio), the studies summarized below should be applied to countercurrent bubble column flow only after consideration of mode of operation and scale.

After description of phenomena occurring in diffused bubble ozone contactors, models that have been developed for bubble column reactors and ozonation processes are summarized. Models differ in spatial dimensionality (0, 1 2 and 3 dimensional models), type (empirical, stochastic and deterministic) and in the physics, chemistry and biology included. Particular attention is paid to the application of computational fluid dynamics (CFD) to bubble column reactors and to ozone bubble contactors.

II.1 Bubble Column Reactor Phenomena

Figure 5 is an illustration of the interrelated processes that occur in bubble columns (Heijnen and Van't Riet 1984). As indicated in the diagram, flow and mass transfer in bubble columns are related to the choice of sparger, liquid properties, gas properties, bubble column operating conditions and bubble column geometry. Bubble columns may be operated in co-current mode (with bulk gas and liquid flows in the same direction), countercurrent mode (with liquid and gas phase bulk flows in opposite directions) and without net liquid flow. Note that, even in the absence of net liquid flow, bubbles produce large- and small-scale liquid motions in bubble columns. Dispersion, hold-up and mass transfer differ significantly for bubble columns undergoing these three modes of operation.

For all three modes of operation, changing the ratio of gas flow rate to liquid flow rate changes the interactions between bubbles and between the phases. For relatively low

gas flow rates and liquid flow rates less than the bubble terminal rise velocity, bubbles tend to be small, non-interacting and dispersed and flow is in the “ideal bubbly flow” or “dispersed flow” regime. In this regime, bubbles tend to be monodisperse and there is not significant breakup or coalescence of bubbles.

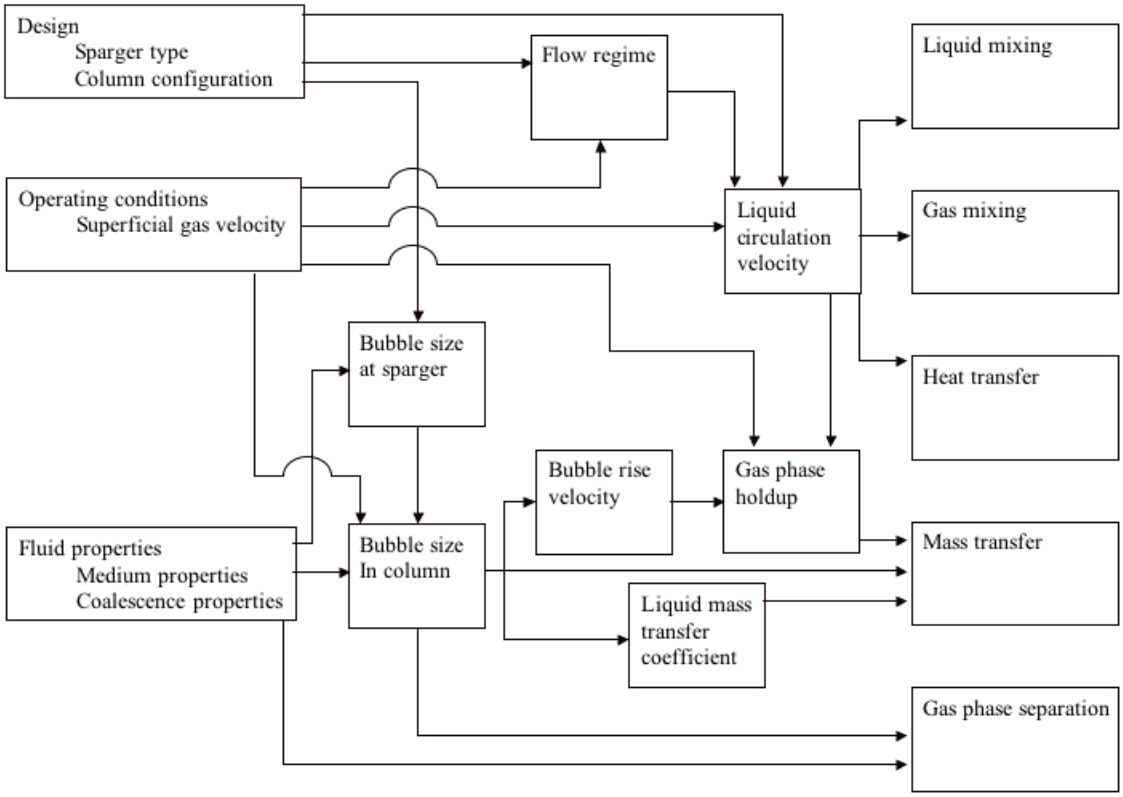

Figure 5: Interrelated Processes in a Bubble Column (adapted from Heijnen and Van't Riet (1984))

II.1.1 Countercurrent Two-phase Flow Modeling

Depending upon the relative velocity of the phases in a countercurrent bubble column, three flow regimes are possible: bubble flow (also called ideal bubbly flow);

churn turbulent flow; and bubble down flow (Uchida et al., 1989). Bubbly flow is characterized by a narrow, monomodal distribution of bubble diameter and negligible break-up or coalescence (Olmos et al., 2003). Churn turbulent flow and the transition region between bubbly flow and churn turbulent flow are also termed heterogeneous flow. Homogeneous and heterogeneous bubble flows are illustrated in Figure 6. Other regimes (churn turbulent and slug flow) may be encountered at very high gas flow rates, but are not depicted in Figure 6 because it is unlikely they would be encountered in typical ozone contactor bubble column operation.

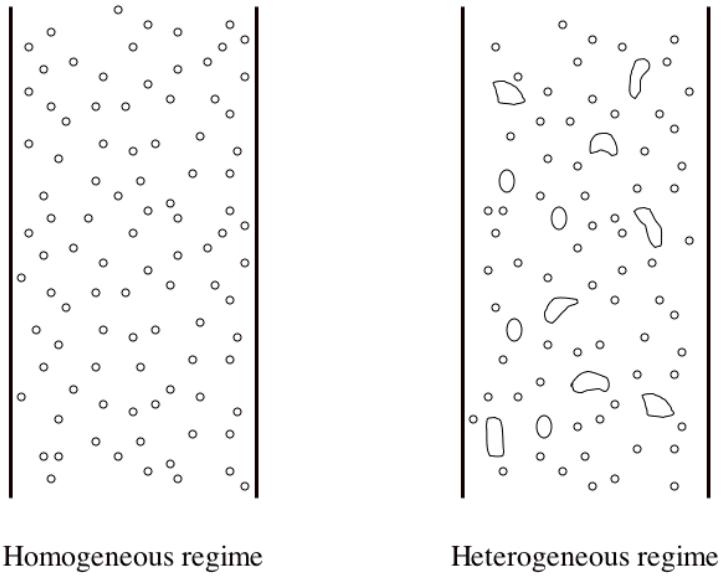

Figure 6: Illustration of Homogeneous and Heterogeneous Bubbly Flow (Camarasa et al., 1999)

Bubble column flow regimes are shown schematically in Figure 7 (adapted from Uchida, Tsuyutani et al. (1989)). The trends depicted in Figure 7 are based on

experimental data collected for a single bubble column (4.6 cm inner diameter) operated in countercurrent mode over a range of gas to liquid flow ratios. Data were collected for air bubbled into water and glycerol solutions of 5%, 10% and 15%.

The transition from bubble flow (ideal bubbly flow) to churn turbulent flow occurred in a well-defined band (depicted with dashed lines) of gas-liquid flow ratios for the liquids studied. The transition from bubble flow to bubble downflow was, not surprisingly, strongly dependent on liquid composition (and surface tension, which influences bubble shape and surface mobility) and temperature. The family of solid curves drawn on Figure 7 indicates the transition associated with the liquids tested. Transition occurred earliest (at the lowest gas flow rate) for the 15% glycerol solution and latest (at the highest gas flow rate) for the lowest-temperature water tested.

Based on their results, Uchida, Tsuyutani et al. determined that the boundary between churn turbulent flow and other flow regimes was insensitive to the composition and properties of the liquid phase and dependent mainly on reactor design and choice of sparger. The boundary between ideal bubbly flow and bubble down flow was strongly dependent on the composition of the liquid phase. This may be due to differences in properties in the liquid phase and/or differences in bubble properties and tendency to coalesce. Lockett and Kirkpatrick (1975) suggest that the transition from ideal bubbly flow to churn turbulent may be related to liquid circulation due to spatial variations in gas phase holdup at a given axial location or the presence of large bubbles. Flooding (not shown on Figure 7) is unlikely for the flow conditions typically encountered in bubble

columns and likely plays no role in the transition from ideal bubbly flow to churn turbulent flow.

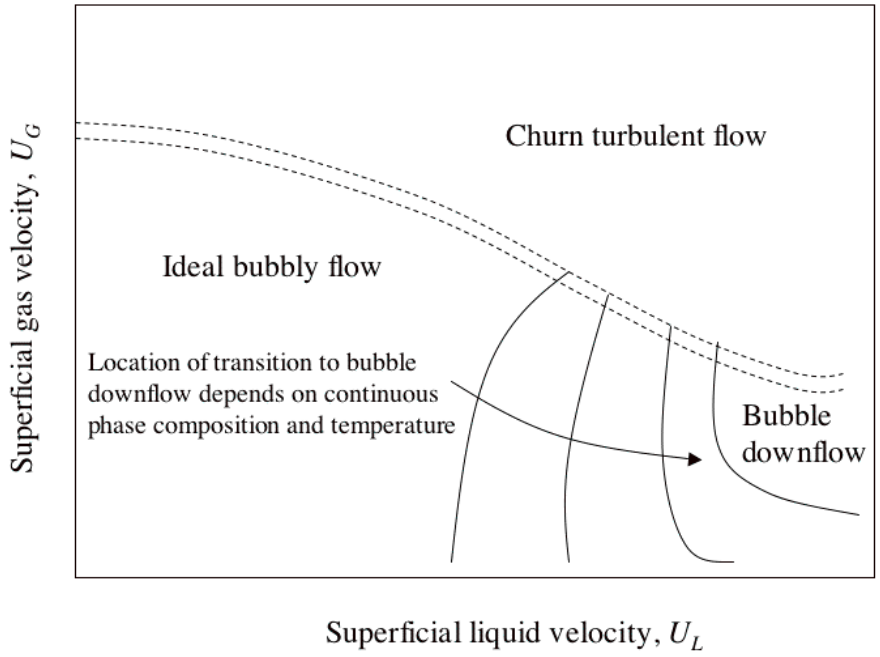

Figure 7: Countercurrent Bubble Column Flow Regimes Schematic Diagram (adapated from Uchida, Tsuyutani et al. (1989)

Ruzicka, Drahoš et al. (2001) quantified the effect of liquid depth and bubble column diameter (for cylindrical columns) on the critical gas hold-up (column volume occupied by gas divided by column volume) at which transition from homogeneous bubbly flow to heterogeneous regime occurs. Although their work was done in bubble columns with stagnant liquids, it can be assumed that transition from ideal to churn turbulent flow in countercurrent bubble columns is also dependent on column diameter

and liquid depth. In general, the authors found that increasing the column diameter caused transition to heterogeneous bubble flow at lower void ratios and increasing liquid depth in the column caused transition to heterogeneous bubble flow at lower void ratios. In reviewing bubble column transition literature, Ruzicka et al. found the effect of column diameter on transition was due to turbulence scale, intensity of circulations, back-mixing, dispersion, wall friction and turbulent viscosity. The dependence of liquid depth on critical void ratio was attributed to the relative importance of the flow regions at the top and bottom of the column (compared with the region in the middle of the column).

As described by Camarasa, Vial et al. (1999), the behavior and modeling of liquid-solid two phase systems is significantly different from that of gas-liquid two-phase systems. In gas-liquid two-phase systems, the properties of the dispersed phase (bubble shape and size, distribution of bubbles in the column, influence of bubbles on each other) depend on reactor geometry and operating conditions and the physico-chemical properties of the continuous phase. According to Camarasa, this coupling of dispersed phase properties with continuous phase behavior precludes *a priori* bubble column reactor design given current knowledge of processes in bubble columns. Based on these considerations, hydrodynamics and mass transfer are likely fundamentally different in cocurrent bubble columns, countercurrent bubble columns and bubble columns in which gas is introduced into non-flowing liquids. Specifically, liquid-phase dispersion, circulation in the bubble column and bubble breakup and coalescence differ significantly between the column configurations.

Cocurrent bubble column flow has been studied in greater depth than counter current bubble column flow. For example, Deckwer, Burckhart et al. (1974) performed cocurrent flow experiments in bubble columns of 15 cm and 20 cm and employing different spargers. The experiments were conducted with air bubbled into tap water and various salt and molasses solutions. The primary objective of these studies was development of relations to predict oxygen mass transfer. Based on measured gas phase holdup and analysis of samples taken at an unspecified number of axial locations in the reactor, the authors concluded that, for the cocurrent configuration employed,

- there was little or no axial variation in oxygen mass transfer rate in the columns;
- the mass transfer rate was influenced more by sparger type than column dimensions;
- for the liquids studied, the mass transfer rate, $k_L a$, varied roughly linearly with gas velocity
- addition of electrolytes to the solution appeared to reduce bubble size (increasing specific surface area, a) but decrease mass transfer coefficient, k_L, resulting in a slightly lower overall mass transfer rate.

II.1.1.1 Bubble Size and Interfacial Area

The shape of bubbles and the drag they impart on the water depends upon the water surface tension (which may, in turn, depend on the concentration of impurities in the feed water), the manner in which they are injected into the water (gas flow rate and diffuser type), the flow rate of the water column, and the temperature. Moore (1959)

suggests that bubble shape is the dominant feature in determining bubble drag and rise velocity in the flow regimes normally encountered in bubble column flows.

Bubble size is largely a function of sparger type, aqueous phase properties and gas velocity. Though it is convenient to work with a characteristic bubble diameter in performing calculations, it should be remembered that there is variation in bubble diameter at a given axial station in a contactor and that bubbles change size in the contactor, often having significantly different average diameter near the sparger compared with mean diameter in the rest of the bubble column.

The two processes integral to determining bubble size are injection and coalescence. Injection of gas into a liquid column may be via nozzles, porous discs or two-phase injectors (Heijnen and Van't Riet 1984). The type of sparger largely determines the size of bubble introduced to the liquid while the behavior and possible coalescence of bubbles in the liquid column is mainly a function of aqueous phase properties. Pure liquids tend to cause bubbles with more mobile surfaces that have a greater tendency to coalesce. Less pure waters tend to produce smaller, more rigid bubbles.

For relatively large-diameter bubble columns, interfacial area is usually approximated by (Roustan et al., 1996):

$$a = \frac{6}{d_b}\frac{\varepsilon_g}{1-\varepsilon_g} \tag{12}$$

where a is specific surface area (net surface area per reactor volume), d_b is effective bubble diameter (diameter of a spherical bubble whose volume is the same as that of the

bubble) and ε_g is gas phase holdup (i.e., the gas phase volume divided by the total reactor volume). For very small gas holdup, interfacial area can be approximated by

$$a = \frac{6\varepsilon_g}{d_b} \tag{13}$$

For smaller-diameter columns, the column geometry may influence gas holdup and Akita and Yoshida (Akita and Yoshida 1974) propose the relation

$$ad_c = \frac{1}{3}\left(\frac{gd_c^2\rho_L}{\sigma}\right)^{0.5}\left(\frac{gd_c^3}{\nu_L^2}\right)^{0.1}\varepsilon_g^{1.13} = \frac{1}{3}B_o^{0.5}G_a^{0.1}\varepsilon_g^{1.13} \tag{14}$$

where d_c is column diameter, g is gravitational acceleration, ρ_L is liquid phase density, σ is surface tension, ν_L is liquid phase kinematic viscosity, B_o is Bond number and G_a is Galileo number. The Akita-Yoshida relation was developed based on analysis of data from a 2.5 m high rectangular cross section bubble column outfitted with a porous plate sparger.

Many relations have been proposed for bubble diameter, some of which are presented in Table 5. These relations must be used with care. First, the relations predict a single diameter bubble though in reality spargers discharge bubbles with a range of diameters. Second, small differences in sparger manufacture, fouling of sparger or corrosion may significantly alter discharge bubble diameter. Finally, relations are generally derived for bubbles either at the sparger discharge or far enough into the liquid column that coalescence and other changes are complete and a uniform, steady diameter is established. Choosing just one of these locations as representative is a simplification.

Gas phase holdup is another important design variable because it relates to the overall transfer area, because it provides an indication of the bubble flow regime in which the column is operating and because it is relatively easy to measure. As with relations for bubble diameter, numerous relations have been developed for gas phase holdup. Gas phase holdup relations that have been proposed in the scientific literature and are applicable to ozone bubble contactor operation are summarized in Table 6. Because many of these relations were developed based on empirical measurements care should be taken to understand the conditions for which the relations were developed before they are used.

.

Table 5: Summary of Bubble Diameter Relations

Expression	Source	Sparger	Location	Notes
$d_b = \begin{cases} 0.0287\, d_o^{1/2} R_{eo}^{1/3} & R_{eo} \le 2100 \\ 0.0071\, R_{eo}^{-0.05} & 10{,}000 \le R_{eo} \le 50{,}000 \end{cases}$	Leibson in Benitez (2002)	Any with spacing between nozzles > 3 d_o	Sparger	Based on air-water system data. Units of and d_o are m.
$d_b = \begin{cases} 1.7\left(\dfrac{\sigma\, d_o}{\Delta\rho\, r}\right)^{1/3} & \text{Single bubble regime} \\ 1.17(U_g^{\,o})\, d_o^{0.8} g^{-0.2} & \text{Continuous chain regime} \\ 4\text{ mm} < d_b < 6\text{ mm} & \text{Jet regime} \end{cases}$	Heijnen and Van't Riet (1984)	Nozzle	Sparger	In SI units. Single bubble, continuous chain and jet regime correspond to conditions at low, medium and high gas flow rates, respectively.
$d_b = \begin{cases} 0.0061\left(U_g^{\,o} d_o\right)^{0.1} d_0^{0.08}\left(\dfrac{\sigma}{\sigma_w}\right)^{0.38} & \text{Coalescing} \\ 0.0104\left(U_g^{\,o} d_o\right)^{0.1} d_0^{-0.07}\left(\dfrac{\sigma}{\sigma_w}\right)^{0.0.41} & \text{Non-coalescing} \end{cases}$	Heijnen and Van't Riet (1984)	Porous disc	Sparger	SI units. The ratio σ/σ_w is the liquid surface tension to pure water surface tension ratio
$0.5\text{ mm} < d_b < 1.0\text{ mm}$ Non-coalescing media $4.0\text{ mm} < d_b < 6.0\text{ mm}$ Coalescing media	Heijnen and Van't Riet (1984)	Injector/ ejector	Sparger	

Expression	Source	Sparger	Location	Notes
$d_b = 4.15\frac{\sigma^{0.6}\varepsilon_g^{0.5}}{\left(\frac{\wp}{v_b}\right)\rho_L^{0.2}} + 9.0\times10^{-4}\,\text{m}$ $\wp = Q_g P_{atm} \ln\left(\frac{P_{atm}}{P_{sparger}}\right)$ $v_b = \left(\frac{2\sigma}{\rho_L d_b} + 0.5 g\, d_b\right)^{1/2}$	Dudley (1995)	Any	Column	$\wp$ is gas power input, v_b is bubble free rise velocity. Developed for turbine contactor but widely used for bubble columns
$d_b = 2.15\times10^{-3}\left(\rho_L\, g U_g\right)^{0.16}$	Bín, Duczmal et al. (2001)	Porous plates	Column	Based on experimental data for large bubbles in a bubble column. SI units, bubble diameter in mm.

Table 6: Summary of Gas Phase Holdup Relations

Expression	Source	Notes
$\frac{\varepsilon_g}{(1-\varepsilon_g)^4} = \alpha \left(\frac{d_c^2 \rho_L g}{\sigma}\right)^{1/8} \left(\frac{g d_c^3}{\nu_L^2}\right)^{1/12} \frac{U_g}{\sqrt{g d_c}}$	Akita and Yoshida (1973)	According to Deckwer and Schumpe (1993) this relation provides a "reliable conservative estimate" of gas hold-up. For pure liquids and non-electrolyte solutions $\alpha=0.2$ and for salt solutions $\alpha=0.25$.
$U_g(1-\varepsilon_g) - U_L \varepsilon_g = V_b \varepsilon_g (1-\varepsilon_g)^{2.39}$	Lockett and Kirkpatrick (1975)	Developed for 5 mm air bubbles in disperse bubbly flow ($\varepsilon_g < 0.3$).
$\varepsilon_g = 0.672 f \left(\frac{U_g \mu}{\sigma}\right)^{0.578} \left(\frac{\mu_L^4 g}{\rho_L \sigma^3}\right)^{-0.131} \left(\frac{\rho_g}{\rho_L}\right)^{0.062} \left(\frac{\mu_g}{\mu_L}\right)^{0.107}$	Hikita, Asai et al. (1980)	According to Deckwer and Schumpe (1993), this relation provides slightly better holdup estimates than the Akita Yoshida relation because variations in gas phase properties are accounted for. The value of f is 1 for non-electrolyte solutions and is a function of strength for salt solutions.
$\varepsilon_g = 1.07 \left(\frac{U_g^2}{g d_c}\right)$	Kawase and Moo-Young (1987)	Based on theoretical relations developed for Newtonian and non-Newtonian continuous phase. The relation shown is for air bubbles rising in water at 20°C
$\frac{U_g}{\varepsilon_g} = 0.175 B_o^{-1/8} G_a^{-1/12} R_{es}^{1/2} (g d_c)^{1/2} + 3.5\times10^{-3} B_o^{3/4} R_{es}^{2/7} (1+0.85\varepsilon_g)(U_L + U_g)$ $R_{es} = \frac{d_b U_s}{\nu_L}$ $U_s = \frac{U_g}{\varepsilon_g} - \frac{U_L}{1-\varepsilon_L}$	Uchida, Tsuyutani et al. (1989)	Developed for countercurrent bubble flow in a variety of gas-liquid systems. This is the only relation identified that directly accounts for the difference between countercurrent and other bubble columns.
$\varepsilon_g = \frac{U_g}{0.3 + 2U_g}$	Langlais, Reckhow et al. (1991)	Assumes bubbles are free-moving and non-coalescent. Based on work by Hughmark.

Expression	Source	Notes
$\varepsilon_g = C U_g^x$ C / x / Sparger / Column diameter 3.61 / 0.91 / Porous plate / 0.15 m 4.25 / 0.99 / Membrane / 0.15 m 3.66 / 0.83 / Perforated Plate / 0.15 m 3.43 / 1.03 / Porous plate / 0.2 m 3.12 / 1.05 / Membrane / 0.2 m 2.2 / 1.06 / Porous plate / 0.2 m	Bouaifi, Hebrard et al. (2001)	Given the clear dependence of gas holdup on column geometry and sparger type, this relation does not appear general. Units of superficial gas velocity in this relation are cm/s.

II.1.1.2 Interphase Momentum Transfer

In his comprehensive article on bubble behavior, Moore (1959) described bubble behavior (shape, rise velocity and drag) for bubbles in various liquids and with various shapes. The parameters governing bubble drag and terminal velocity include liquid properties (viscosity, density, surface tension, temperature), gas properties (viscosity, density, surface tension), bubble diameter (which is largely a function of sparger type and the tendency of bubbles to coalesce) and local acceleration due to gravity. Gas properties are generally unimportant in determining bubble drag and rise speed. The remaining parameters can be grouped and described via the dimensionless parameters, listed in Table 7. Among the parameters making up the dimensionless quantities in Table 7, the only one over which designers have substantial control is the bubble diameter.

Table 7: Dimensionless Parameters Associated with Bubble Drag and Terminal Rise Speed

Name	Formula	Description
Morton number	$M_o = \frac{g\mu^4\Delta\rho}{\rho_L^2\sigma^3}$	Morton number is solely a function of liquid properties. Liquid to liquid variations are largely due to differences in viscosity, since surface tension is less variable. Low Morton number fluids are those with $M_o < 10^{-8}$ and high Morton number fluids are those with $M_o > 10^{-3}$. Pure water has $M_o = O(10^{-10})$. The precise value depends upon the temperature and purity of the water. In most cases contaminated water has a higher Morton number (due to the presence of surface active agents and lower surface tension) than pure water.
Reynolds number	$R_e = \frac{d_b V_b}{\nu_L}$	The ratio of inertial forces to viscous forces. For bubbles, the characteristic length is the effective bubble diameter, defined as the diameter of a sphere whose volume is the same as that of the bubble. The characteristic velocity is the bubble terminal rise velocity.

Name	Formula	Description
Weber number	$W_e = \frac{d_b \rho V_b^2}{\sigma}$	The ratio of hydrodynamic forces to surface tension forces. Where surface tension forces dominate (low Weber number), bubble shape is that which minimizes surface tension forces and is spherical. Where hydrodynamic forces dominate, the bubble assumes a shape to minimize drag.
Eötvös number	$E_o = \frac{g \Delta\rho d_b^2}{\sigma}$	The ratio of gravitational forces to surface tension forces.

The significance of the bubble diameter and shape in determining bubble drag and rise velocity is illustrated in Figure 8 (Moore 1959). For small bubble diameters (generally less than 2 mm for air bubbles in water), bubbles are spherical and rise rectilinearly. As bubble diameter increases, hydrodynamic forces play an increasing role in determining bubble shape and bubbles assume ellipsoidal then oblate shapes. As bubble diameter is further increased, bubble shape fluctuates and trajectories become zigzag or spiral as bubbles ascend. In this Weber number range, the bubble rise speed decreases significantly. At what is presumed to be a critical Weber number (Moore 1959), the trailing edge of the bubble becomes unstable in shape and bubbles assume a spherical cap (mushroom-like) shape. In this regime, the leading (upward) edge of the bubble has a stable hemispheric shape and a well-defined boundary layer. The rear surface fluctuates in shape and the local flow field is dominated by turbulent eddies.

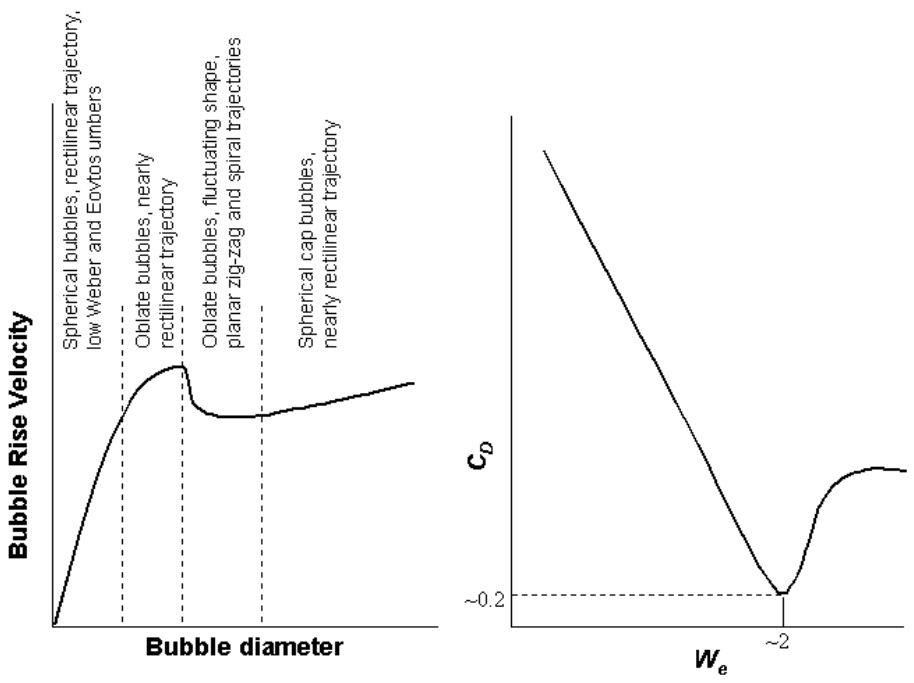

Figure 8: Bubble Rise Velocity and Discharge Coefficient Schematics (Moore 1959)

Based on the forgoing, care must be used in choosing a drag coefficient relation consistent with the bubble shape (Weber number regime) encountered in a bubble contactor. Numerous relations have been proposed and used. The most commonly used relations describing drag and terminal bubble speed of dispersed bubbles in a liquid medium are presented in Table 8 and Table 9.

Table 8: Summary of Bubble Drag Relations

Relation	Source	Notes
$C_D = \frac{24}{R_e}$	Various	Stokes relation for a sphere rising steadily at low Reynolds number.
$C_D = \frac{24}{R_e}\left(1+0.15R_e^{0.687}\right)$	Schiller and Naumann (in Clift, Grace et al. (1978))	For spherical bubbles rising in the viscous regime ($R_e < 800$) and widely dispersed in a liquid.
$C_D = \begin{cases} \frac{32}{R_e} & \text{Spherical bubbles, high } R_e \\ \frac{6}{18^{3/5}} M^{1/5} W^{-3/5} & \text{Non-spherical bubbles} \\ 2.6 & \text{Spherical cap bubbles} \end{cases}$	Moore (1959)	Theoretically based relations for single bubbles rising in stagnant liquids.
$C_D = \begin{cases} \frac{24}{R_e} & \text{Stokes regime} \\ \frac{24}{R_e}\left(1+0.1R_e^{0.75}\right) & \text{Viscous regime} \\ \frac{2}{3} E_o^{1/2} \left\{ \frac{1+17.67\left[f(\varepsilon_g)\right]^{6/7}}{18.67\, f(\varepsilon_g)} \right\}^2 & \text{Distorted particle regime} \\ \frac{8}{3}\left(1-\varepsilon_g\right)^2 & \text{Churn turbulent regime} \end{cases}$ $f(\varepsilon_g) = \sqrt{1-\varepsilon_g}\left(\frac{\mu_c}{\mu_m}\right)$	Ishii and Zuber (1979)	For groups of bubbles in all flow regimes. Relations are theoretical and validated via comparison with data collected by many researchers. Relations for drag in the distorted particle and churn turbulent regimes are reported valid to gas holdups of 0.95. Reynolds number based on bubble diameter and speed of the bubbles relative to the liquid phase.

Relation	**Source**	**Notes**
$C_D = \frac{24}{R_e} + 5.48\,R_e^{-0.573} + 0.36$	Ihme in Clift, Grace et al. (1978).	For rigid spheres with $R_e < 10^4$.
$C_D = \frac{4}{3}\frac{g\,d_b}{v_b^2}\frac{\Delta\rho}{\rho_L}$ $v_b = \frac{\mu_L}{\rho_L\,d_b} M_o^{-0.149}\left(J - 0.857\right)$ $J = \begin{cases} 0.94\,\Omega^{0.751} & 2 < \Omega < 59.3 \\ 3.42\,\Omega^{0.441} & \Omega > 59.3 \end{cases}$ $\Omega = \frac{4}{3} E_o\, M_o^{-0.149}\left(\frac{\mu_L}{\mu_{\text{ref}}}\right)$	Grace (in Clift, Grace et al. (1978))	For distorted air bubbles rising in water. Reference viscosity is that of pure water at specified temperature and pressure and can be taken as 0.0009 kg m^{-1} s^{-1}. Valid over the range of Ω specified.

Table 9: Summary of Bubble Terminal Speed Relations

Expression	Source	Notes
$V_B = \begin{cases} \dfrac{2R_{e,B}^2(\rho_L-\rho_G)g}{9\mu_L} & R_{e,B} < 2 \\ 0.33\, g^{0.76} \nu_L^{-0.52} R_{e,B}^{1.28} & 2 < R_{e,B} < 4.02\, M_1^{-0.214} \\ 1.35\left(\dfrac{\sigma}{\rho_L R_{e,B}}\right)^{0.5} & 4.02\, M_1^{-0.214} < R_{e,B} < 3.10\, M_1^{-0.25} \\ 1.18\left(\dfrac{g\sigma}{\rho_L}\right)^{0.25} & 3.10\, M_1^{-0.25} < R_{e,B} \end{cases}$ *where* $R_{e,B} = \dfrac{\rho_L V_B d_{B,e}}{\mu_L}$	Peebles and Garber (1953)	The variable $d_{B,e}$ is the effective bubble diameter (the diameter of the sphere that has the same volume as the bubble) and the variable M is the Morton number.
$V_B = \dfrac{\mu_L}{\rho_L d_b} M_o^{-0.149}(J - 0.857)$ $J = \begin{cases} 0.94\Omega^{0.747} & 2 < \Omega \le 59.3 \\ 3.42\Omega^{0.441} & \Omega > 59.3 \end{cases}$ $\Omega = \dfrac{4}{3} E_o M_o^{-0.149}$	Clift, Grace et al. (1978)	For single ellipsoidal bubbles rising in contaminated water. Validate for $M_o < 10^{-3}$, $E_o < 40$, $R_e > 0.1$ and aqueous viscosity not significantly different from that of pure water.
$V_B = \sqrt{2}\left(\dfrac{\sigma g \Delta\rho}{\rho_L^2}\right)^{1/4}(1-\varepsilon_g)^{1.75}$	Ishii and Zuber (1979)	For bubbles in liquids in the distorted particle regime.
$V_B = \left[\left(\dfrac{0.574}{\varepsilon_g}\right)\dfrac{U_g}{(g d_c)^{0.5}}\right]^{2.5}$	Viswanathan and Rao (in Kawase and Moo-Young (1987)	Theoretically-derived relation that includes dependence on column diameter.
$V_B = \begin{cases} 210 d_b \dfrac{1.004}{\mu_L} & 0.5 < d_b < 1.8\,\text{mm} \\ \left(20 + 33.8 e^{-4.88 d_b}\right)\dfrac{1.004}{\mu_L} & 1.8 < d_b < 4\,\text{mm} \end{cases}$	Mariñas, Liang et al. (1993)	Empirical relation based on observations of the rise of single bubbles in stagnant liquids. Units of V_B, d_b and μ_L are cm/s, cm and centipoise, respectively.
$V_B = \sqrt{\dfrac{2\sigma}{\rho d_b} + 0.5 g d_b}$	Winkler (in Dudley (1995))	

II.1.1.3 Bubble-Induced Turbulence

Bubbles generate turbulence in their wakes, the practical results of which are altered drag on other bubbles and changes in mixing. Sato and Sekoguchi (Sato and Sekoguchi 1975) proposed a turbulence model that accounts for the fact that bubbles in a shear flow (such as in a turbulent eddy) generate their own turbulence due to form drag. The authors proposed that instantaneous fluid velocity in a bubble-laden flow can be expressed as:

$$\vec{V} = \overline{V} + \vec{V}' + \vec{V}'' \tag{15}$$

where $\vec{V}$ is local instantaneous fluid velocity, $\vec{V}'$ is fluctuating velocity component (instantaneous turbulence velocity) inherent in the liquid and independent of the existence of bubbles and $\vec{V}''$ is a fluctuating velocity component caused by the motion of the bubble relative to the surrounding fluid. As with single-phase turbulence modeling, the velocity expression is introduced into the liquid phase momentum equation and the resulting equation is averaged. This procedure produces an additional viscosity term in the momentum equation:

$$\mu_{\text{eff}} = \mu_L + \mu_T + \mu_{B,T} \tag{16}$$

where μ_{eff} is effective viscosity, μ_{L} is liquid molecular viscosity, μ_{T} is turbulent viscosity and $\mu_{\text{T,B}}$ is bubble-induced turbulent viscosity. This relation is available as an option in the commercial CFD code that has been used in numerical simulations in this work.

II.1.1.4 Mixing

II.1.1.4.1 Large Scale Hydrodynamics and Mixing

Mixing is critically important in ozone bubble columns. Small scale mixing (dispersion) renews bubble surfaces with low ozone content liquid and promotes mass transfer. Dispersion also carries water with high dissolved ozone concentration into water with low ozone concentration

Mixing in ozone bubble contactors depends on the gas and liquid flow rates in the contactor and the contactor geometry (Schulz and Bellamy 2000). Properly designed and mixed operations do not have significant "channeling (short-circuiting)" or temporal variations in ozone residual at a given location for a given gas and liquid flow rate. Mixing in industrial ozone facilities is most often assessed based on the coefficient of variation of time series of ozone residual at the reactor discharge. A coefficient of variation less than 5% is thought to indicate sufficient mixing and that short-circuiting or other non-ideal hydrodynamic processes are not significant (Schulz and Bellamy 2000).

When mixing in an ozone bubble contactor is believed to be inadequate, the most common remedial actions are:

- addition of ozonated air or oxygen at a lower ozone concentration and a higher gas flow rate;
- ensuring a dense coverage of diffusers in chambers where gas is introduced;
- supplemental mixing with diffused air or water jets;
- improvement of intake or discharge hydraulics.

Because design data and guidelines for implementing these changes are not available, experience is the only guide to effective choice and design of appurtenances for enhancing mixing.

Large scale mixing phenomena determine how well the phases are distributed in a reactor and the likelihood of short-circuiting or backmixing in the reactor. Bubble plumes tend to migrate to walls or toward each other, as shown in Figure 9 and Figure 10 (Freire et al., 2002). This effect, sometimes called the Coanda effect, arises because entrainment of liquid into the bubble plume is constrained on one side.

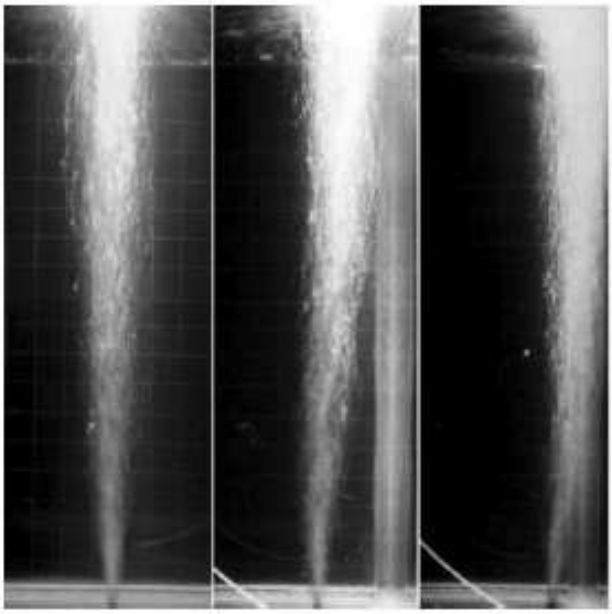

Figure 9: Migration of a Bubble Plume to a Wall (Freire et al., 2002)

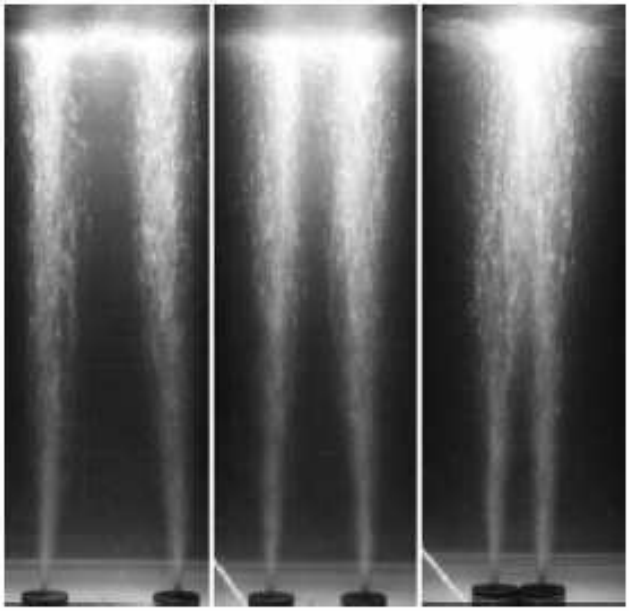

Figure 10: Migration of Bubble Plumes toward Each Other (Freire et al., 2002)

In ozone bubble contactors, bubble plume migration may occur, depending on sparger placement and gas to liquid flow ratio. Depending on the type of feed for the ozone generator (oxygen or air) and the design gas flow rates, rod and dome shaped diffusers may be used in full scale fine bubble contactors. Rod shaped diffusers are usually used when air is ozone generator feed gas and gas flow rates between 0.057 and 0.17 m^3/min (2 and 6 ft^3/min). Dome shaped diffusers are most often used when oxygen is the feed gas and gas flow rate is between 0.014 m^3/min and 0.17 m^3/min. A guideline for sparger spacing 4 ft^2 or less per diffuser (Rakness 2005).

Numerous studies have been made of large-scale mixing in bubble columns with non-flowing liquid phase (Grevet et al., 1982; Anderson and Rice 1989; Drahos et al., 1992; Burns and Rice 1997; Lapin et al., 2002) but only one (published in multiple parts) was identified that described or quantified large scale mixing in countercurrent flow

columns (Anderson and Rice 1989; Burns and Rice 1997). In columns with non-flowing liquid phase, bubble plumes entrain liquid as they rise, establishing regions of circulating flow outside the bubble plume. The size and arrangement of these circulations is dependent on the gas flow rate and the reactor geometry. Shallow bubble beds (height / diameter ≤ 2) with non-flowing liquid phase establish a single circulation cell outside the bubble plume. Bubble beds with larger height to diameter ratios establish multiple cells (Drahos et al., 1992).

In countercurrent flow in cylindrical reactors, liquid flow tends to be upward in the "core" of the bubble plume, and downward outside the bubble plume near the wall (Burns and Rice 1997). The presence of a strong liquid down flow outside the bubble plume reduces the amount of recirculation in the liquid phase. At high gas to liquid flow ratios (but below churn turbulent flow) the bubble plume tends to grow in diameter more slowly as it rises compared plumes at lower gas to liquid flow ratios.

For tall cylindrical bubble columns, minor misalignments of the centerline from vertical can result in drastic differences in liquid flow (Rice and Littlefield 1987). In the cited study, the authors filled a cylindrical bubble column with a solution of hydrochloric acid and a pH indicator, sparged air into the solution until steady state hydraulics were achieved, then pumped a strong solution of sodium hydroxide into bottom of the reactor. As the sodium hydroxide progressed upward in the reactor, the pH indicator changed color. Near the sparger the reactor behaved like a continuously stirred tank reactor (CSTR) and the progress of the line of neutralization could not be followed. Above the entrance region, the line of neutralization between the acidic and basic regions tended to be distinct and to rise steadily. The progress of the line of neutralization was recorded on

video tape. The rate of rise of the line of neutralization was computed from the video images and the liquid phase dispersion was calculated via fitting a one-dimensional axial dispersion model to observed rates. Two findings drawn from that study are of importance to the current study. First, minor vertical misalignments (less than 0.5°) of the column from true vertical resulted in major differences in dispersion. Second, an "entrance region" was determined to exist near the sparger. This entrance region behaved as a plug flow reactor. Regression was used to determine model parameters (dispersion and height of the entrance region) that best fit experimental data. Unfortunately the authors did not report the dependence of the height of the entrance region on gas flow rate.

II.1.1.4.2 Small Scale Hydrodynamics and Mixing

Bubbles give rise to liquid-phase hydrodynamic dispersion in bubble columns and dispersion, in turn, influences mass transfer rates. To date most analyses have approximated liquid dispersion in a bubble column via a single dispersion number (inverse of Peclet number) though dispersion likely varies axially in bubble columns. For example, in a study of cocurrent air-water flow in bubble columns, Deckwer, Burckhaart et al. (1974) found that dispersion was lower in the vicinity of the sparger compared with dispersion in the rest of the column. In a study of a bubble column with no net liquid flow, other authors determined the region near the sparger behaved as a CSTR (Rice and Littlefield 1987).

Lehrer (1984) identifies the following parameters as influencing dispersion:

- Gas and liquid flow rates;

- column dimensions;
- configuration of fluid injection; and
- properties of fluids.

Based on these observations, the author proposed a relation for axial dispersion of the form:

$$E_L = E_B B + \sum_{i=1}^{N} \left(E_K\right)_i - \sqrt{Q_b U_g} \tag{17}$$

where E_L is the axial dispersion, E_B is the contribution due to bubble form drag, B is a hindered motion factor which accounts for interactions between bubbles, E_K is the contribution due to fluid injection through sparger holes, N is the number of sparger holes, Q_g is gas volumetric flow rate and U_g is gas superficial velocity. This relation has limited applicability, given that for high gas flow rates the turbulent dispersion can decrease or even become negative.

A number of relations for liquid phase dispersion commonly cited in the literature are provided in Table 10. The conditions under which data supporting these relations were taken are provided in the notes. These conditions should be given careful attention given the importance of sparger type and reactor geometry in dispersion.

Table 10: Axial Dispersion Relations

Relation	Source	Notes
$E_L = 2.7\, d_c^{1.4} U_g^{0.3}$	Deckwer, Burckhart et al. (1974)	Developed for cocurrent flow of air in water, molasses and salt solutions in two cylindrical bubble columns of 15 and 20 cm diameter and 4.4 and 7.23 m water column heights. Units of column diameter, d_c, and superficial gas velocity, U_g, and liquid phase dispersion, E_L, are cm, cm/s and cm2/s, respectively.
$E_L = 0.90 d_c^{1.5} \left[H \left(U_g - \varepsilon_g U_s \right) \right]^{1/3}$	Field and Davidson (1980)	Developed for cocurrent gas-liquid flow with $U_g >> U_L$. In this equation U_s is slip velocity and units are m^2/s, m, m, m/s and m/s for E_L, d_c, H, U_g and U_s, respectively.
$E_L = 1.3134 g^{0.2} N^{0.2} Q_g^{0.6} \left[\tanh\left(\frac{0.168 g^{0.2} d_c}{N^{0.3} Q_g^{0.4}} \right) \right]^{1/2} - \sqrt{Q U_g}$	Lehrer (1984)	Theoretical relation developed based on energy imparted to the liquid stream by gas injection, bubble drag and friction on column walls.
$p_e^{-1} = \frac{4.88}{H} \left[0.00185 + 9.7 \frac{U_g^{1/2}}{U_L^{5/3}} \left(\frac{\nu_L}{d_b} \right)^{7/6} \right]$	Kim, Tomiak et al. (2002a)	Developed based on experimental observation in right circular cylindrical bubble columns. Units of column height, H, are m. Units of other variables must be dimensionally consistent.
$P_e = \frac{H}{d_c} \left[\frac{1.3 R_e^{0.1}}{1 + (1/235)(1 - \varepsilon_g)(R_e / F_r^{1/3})^{-2/3} G_a^{-0.6}} \right]$	Moustiri, Hebrard et al. (2001)	Developed for cocurrent gas-liquid flow in cylindrical columns. The authors found a pronounced effect of column diameter, fluid superficial velocities and bubble regime on dispersion.

II.1.1.5 Interphase Ozone Mass Transfer

The first step in the dissolution of an ozone molecule is transport of the molecule from the bulk gas phase (interior of a bubble) to the gas-liquid interface. As the ozone molecule approaches the interface, it encounters resistance to its transport. This resistance is a result of forces between gas and liquid molecules at the bubble surface and additional forces related to the accumulation of surface active agents at the bubble surface. These surface active agents accumulate as bubbles rise, explaining, in part, the dependence of mass transfer rate on bubble age or reactor height. Surface active agents are thought to produce interfacial resistance through formation of an energy barrier, formation of a physical "sieve" that blocks some gas molecules or by influencing small length scale hydrodynamics near the bubble surface (Goodridge and Robb 1965; Vasconcelos et al., 2002; Alves et al., 2005).

At the bubble length scale, features that influence mass transfer are the shape of the bubble, fluid motion on the length scale of the bubble diameter and proximity of other bubbles. As illustrated, to accurately predict mass transfer, one must account for bubble surface area (shape and effective diameter), gas phase hold-up, gas phase distribution, liquid phase dispersion and circulation and chemical properties at the bubble surface.

Along with mass transfer, there is momentum transfer between the gas and liquid phases. Momentum transfer results in enhanced turbulence and may lead to an increase in dispersion and mixing, though not necessarily. In bubble columns and other multiphase mass transfer operations, efficient mass transfer is facilitated by contacting the phases in such a way that the difference in concentration of the material that is

transferred is a maximum. So, countercurrent bubble columns (in which the liquid flows downward and the gas bubbles upward) are preferred over cocurrent configurations.

Since the early 20th century, numerous researchers have sought to identify the features that govern mass transfer between bubbles and liquids and have proposed relations to predict the rate of transfer. The features that may govern mass transfer have been identified as:

- The manner in which bubbles are introduced into the contactor;
- Liquid physical properties (viscosity, surface tension and dissolved ozone diffusivity;
- The superficial gas flow rate;
- The rate of dissolved ozone consumption in liquid phase reactions;
- The presence of surface-active contaminants;
- The contactor geometry (especially the ratio of the diffuser area to the contactor cross sectional area and diffuser height); and
- Bubble age.

Table 11 summarizes dimensionless parameters for characterizing bubble column mass transfer.

Table 11: Dimensionless Parameters Relevant to Bubble Column Mass Transfer

Dimensionless parameter	Formula
Bond number	$B_o = \frac{g\, d_c^3\, \rho_L}{\sigma}$
Froude number	$F_r = \frac{U_L^2}{g\, d_c}$
Galileo number	$G_a = \frac{g\, d_c^3}{\nu_L^2}$
Peclet number	$P_e = \frac{U_g d_B}{D_i}$
Reynolds number	$R_e = \frac{U_g d_b}{\nu_L}$
Schmidt number	$S_c = \frac{\nu_L}{D_i}$
Sherwood number	$S_h = \frac{k_L d_B}{D_i}$

In development of early models of the dissolution of gases, it was hypothesized that there are thin layers of stagnant fluid on both sides of the gas-liquid interface, as illustrated in Figure 11. In order for a gas molecule to diffuse from the bulk gas phase to the bulk liquid phase, it must first overcome the gas film resistance, the resistance of the surface layer and the liquid film resistance. The flow in the gas and liquid films is assumed laminar and flow in the bulk phases is usually assumed to be turbulent.

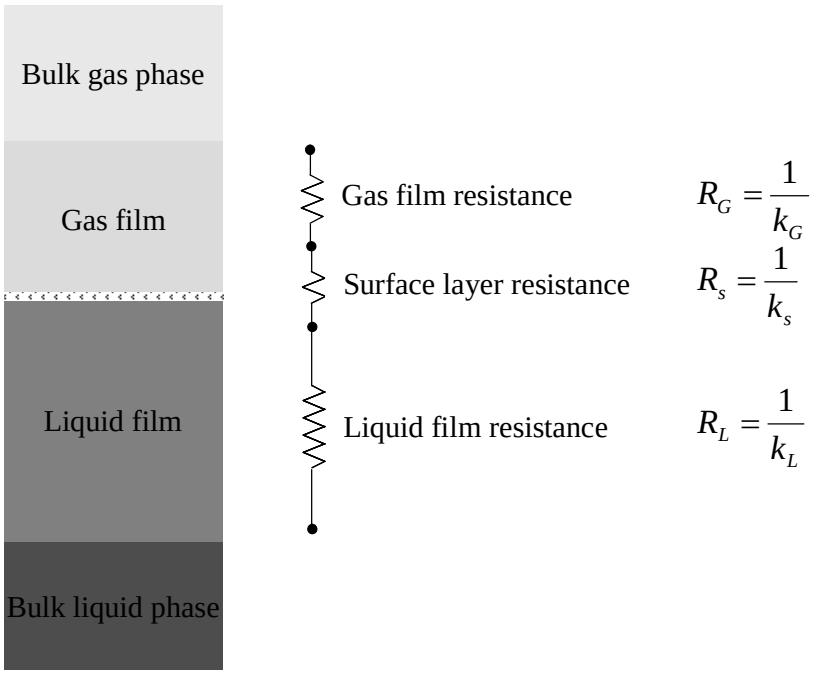

Figure 11: Schematic Diagram of the Two-Film Mass Transfer Model

Surface resistance depends upon the composition of the gas and liquid phases and the presence of surface active agents that accumulate at the gas-liquid interface. Surface active agents are hypothesized to offer resistance to gas diffusion via (Goodridge and Robb 1965):

- development of an energy barrier that impedes the progress of low-energy gas molecules;
- a sieving effect caused by the collision of gas molecules with surface agent agent molecules assembled at the gas-liquid interface;
- alteration of the hydrodynamics and size of the gas and liquid films adjacent to the gas-liquid interface.

Surface active agents alter mass transfer rates indirectly by influencing the nature of the bubble surface and consequently the bubble size, shape and tendency to break up or

coalesce with other bubbles. The presence of trace concentrations of surface active agents tends to change the mobility of bubbles surfaces (Clift et al., 1978; Alves et al., 2005), the effective bubble diameter and holdup observed at a given liquid and gas flow rate (Anderson and Quinn 1970). In studies of carbon dioxide sparged into distilled water, de-ionized water and tap water, bubble coalescence was significantly lower in tap water than in either de-ionized water or distilled water (Anderson and Quinn 1970). The authors attributed this finding to the presence in tap water of substances that decrease the mobility of bubbles and the possible presence in trace concentrations of coalescence-promoting substances (possibly from resins in deionizing filters) in distilled and deionized waters. For the ozone-water system, the Henry's law constant varies with pH and ionic strength as well as temperature (Bín 1995). The impact of surface active agents on mass transfer is profound – the rate of dissolution of gases into waters with very low ionic concentration is more than twice that into tap water (Alves et al., 2005).

Surface active agents (Vasconcelos et al., 2002; Alves et al., 2005) and microorganisms (Blanchard 1970; Wozniak et al., 1976) accumulate on bubble surfaces as bubbles rise through contaminated liquids. This accumulation explains the observed dependence of mass transfer on bubble age. In studies of bubble rise velocity and mass transfer rates of single bubbles, the rise velocity and mass transfer rate were both found to decrease as a function of time as surface active materials accumulated on the bubble surface. Liquid side mass transfer coefficient was found to lie between the value predicted by penetration theory (which assumes a completely mobile bubble surface and is described below)

$$k_L^{\text{mobile}} = 1.13\sqrt{\frac{u_s D}{d_b}} \tag{18}$$

and that predicted for a bubble with a rigid surface

$$k_L^{\text{rigid}} = 0.6\sqrt{\frac{u_s}{d_B}}\, D^{2/3} \nu^{-1/6} \tag{19}$$

In equations 17 and 18, u_s is slip velocity (relative velocity between the bubble and liquid), D is molecular diffusivity, d_B is bubble diameter and ν is dynamic viscosity of the liquid phase. The phenomenon of bacterial accumulation on bubble surfaces does not impact mass transfer, but does influence the transport of microorganisms and the uniformity of their contact with disinfectant.

Mass transfer models proposed after the two-film model recognized that the gas and liquid film are not likely to be stagnant. Rather, fresh liquid and gas are continuously exchanged between the films and bulk phases. The hydrodynamics related to the transport of ozone from bubbles to the bulk liquid phase are illustrated in Figure 12. At the bubble scale, gas phase circulation within the bubble influences the distribution of ozone in the gas phase, the shape of the bubble and the rate at which ozone is transported from the bulk gas phase to the gas-liquid interface. In the liquid phase, small scale turbulence present in the bubble wakes and generated via hydrodynamic dispersion transport liquid from the bulk phase to the bubble surface. Large scale fluid structures (with length scale equal to the bubble column diameter) advect dissolved gases away from the bubble plume and, in the case of uneven distribution of phases, into the liquid phase.

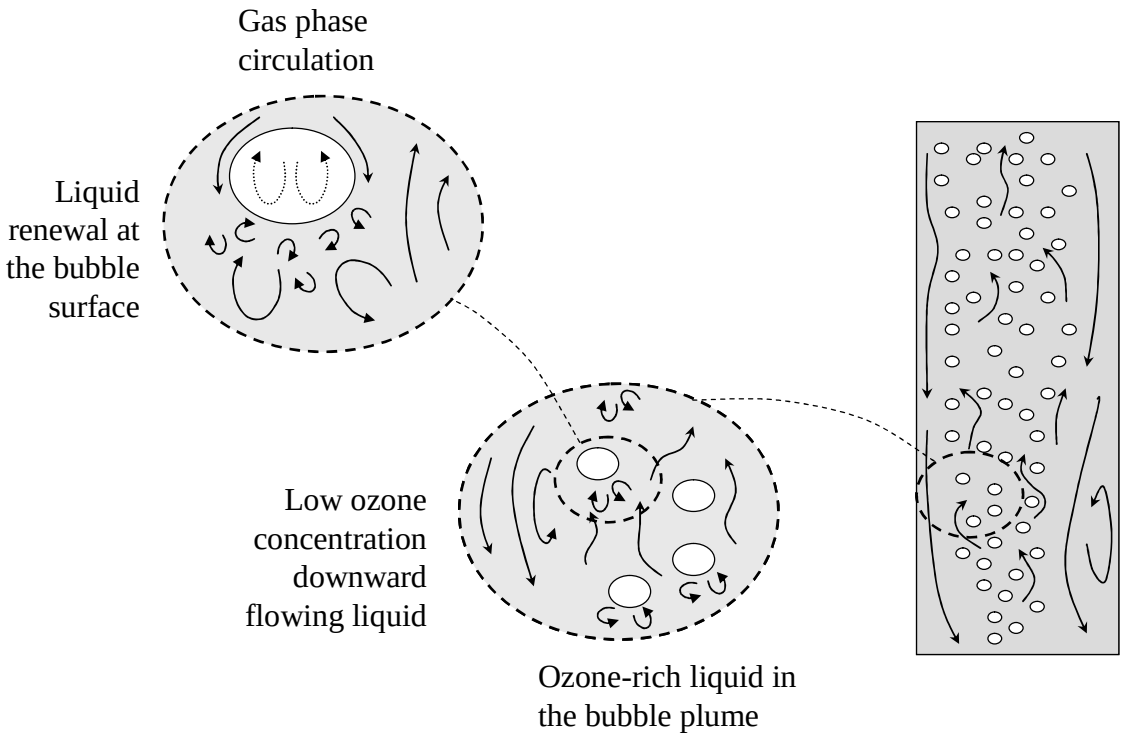

Figure 12: The Hydrodynamics of the Transport of Ozone from Gas Phase to the Bulk Liquid Phase

In the first mass transfer model proposed to account for realistic exchange of liquid between the bulk phase and film (called penetration theory), it was hypothesized that parcels of "fresh" liquid from the bulk phase are in contact with the interface for a characteristic time (Higbie 1935). During the contact time between the fluid parcel and interface, dissolved gases "penetrate" into the fluid parcel. Fluid parcels having longer contact times with the bubble surface experience greater depth of penetration of the dissolved gas into the fluid parcel. Dissolved gas penetrates into the fluid parcel fastest during initial contact of the parcel with the bubble surface when the dissolved gas concentration in the fluid parcel is low. After long contact times the dissolved gas concentration in the fluid parcel increases and the flux of dissolved gas into the fluid parcel decreases. Assuming negligible gas phase resistance to mass transfer, penetration

theory predicts the absorption rate for fluid parcels with a contact time of θ with the gas-liquid interface is given by

$$\psi(\theta) = \left(C^* - C_0\right)\sqrt{\frac{D}{\pi\,\theta}} \tag{20}$$

where C^* is gas phase concentration divided by Henry's law constant, C_0 is the initial dissolved gas concentration in the fluid parcel and D is the diffusivity of the dissolved gas in the liquid. Assuming the contact time between a fluid parcel and the bubble surface is equal to the bubble diameter divided by the slip velocity, Higbie's penetration theory predicts the liquid mass transfer coefficient is given in equation 18 (repeated below)

$$k_L = 1.13\sqrt{\frac{u_s\,D}{d_b}} \tag{18}$$

Since the penetration theory was proposed, researchers have proposed alternative mass transfer models in which the contact time between fluid parcels and the gas-liquid interface is not uniform. Danckwerts (1951) suggested that fluid parcels are exchanged randomly at the gas-liquid interface and that the overall mass transfer coefficient at a given time is the integrated mass transfer to all fluid parcels (with a distribution of contact times with the gas-liquid interface) at the interface. This model, in which parcels are renewed at the interface with some distribution of parcel contact times, is called the "surface renewal" model. These assumptions give rise to the mass transfer rate

$$k_L = \sqrt{D\,s} \tag{21}$$

where s is the random replacement rate for fluid particles at the interface (units of T^{-1}).

Although it may better reflect interface processes, relation 10 is used for predicting mass transfer rate less often than equation 7, perhaps because of the difficulty in estimating the replacement rate. Since the introduction of the surface renewal model, other investigators have developed mass transfer models using various distributions of parcel residence times at the interface. For example, a mass transfer model assuming the distribution of parcel residence times at the interface was given by the gamma distribution provided improvements in mass transfer prediction in turbulent pipe flow over predictions based on Danckwerts' model (Harriott 1962). Although the replacement rate for parcels is likely related to the distribution of eddy sizes in turbulent flow, no studies were found that related mass transfer coefficient to distribution of turbulent kinetic energy.

The most commonly used relations for mass transfer are presented in Table 12. The relations are presented as they were presented in original publications except where the original nomenclature conflicts with that used in this dissertation. The basis (theoretical, empirical and semi-empirical) for the relation and notes on the data on which the relations were developed are also presented. Among the relations in Table 12, the Hughmark relations (Hughmark 1967a; Hughmark 1967b) are most widely used and basic mass transfer text books present them as the de facto standard for bubble contactor design (Rakness et al., 1988; Benitez 2002). Although the Hughmark relations are convenient to use and have long records of accomplishment, care should be taken in choosing and using them – Hughmark's original papers presented several alternate relations appropriate for different flow regimes. The correct formula should be chosen and justification should be provided for that choice.

Calderbank and Moo-Young (1961) determined that the two most important parameters in determining interphase mass transfer between dispersed bubbles and a continuous liquid are diffusivity of the gas diffusing into the liquid and the size and flow regime of the bubble. In general, mass transfer rates from larger bubbles is greater than that from small bubbles, presumably because in large bubbles form drag predominates, while friction drag predominates for small bubbles. The hydrodynamics associated with friction drag present a barrier to penetration of dissolved gas into a continuous liquid, while turbulent wakes behind large bubbles disperse dissolved gases away from bubbles and bring low-concentration fluid in contact with the bubbles. Large diameter bubbles were considered those with a diameter greater than 2.5 mm. Motarjemi and Jameson (1978) validated the Calderbank and Moo-Young expressions for large and very small bubbles, but found that in the transition region between small and large bubbles, the mass transfer was significantly higher than that predicted by Calderbank and Moo-Young. Their finding led them to propose an optimal bubble size of 1 mm for oxygen transfer in air-tap water systems.

The debate over small and large bubble behavior should also consider the presence of surface-active contaminants in the water and their effect on bubble size, shape and behavior. Anderson and Quinn (1970) found a marked difference between gas phase holdup and bubble shape between experiments with air bubbled in distilled water and air bubbled in tap water. When bubbled in distilled water, air bubbles had a greater tendency to coalesce and form spherical cap bubbles. In concluding, the authors caution that trace amounts of contaminants may drastically change bubble column mass and momentum transfer behavior and that, in conducting tracer experiments, care should be

taken in choosing a tracer that does not have surface-active properties. Dudley (1995) states that surfactants reduce surface tension, resulting in greater specific surface area. However, surfactants also alter gas diffusivity in the aqueous phase and make bubble surfaces more rigid. The net result of the presence of surfactants is a net reduction in $k_L a$ in contaminated waters compared with transfer in pure water. Deckwer, Burckhart, et al. (1974), like Dudley, noted that while specific surface area increases as surfactants are introduced into the liquid phase, mass transfer coefficient, k_L, reduces. This is attributed to the formation of an electric double layer at the gas-liquid interface that impedes the diffusion of dissolved gas into the aqueous phase. Prior researchers have suggested mechanisms other than formation of an electric double layer to explain the way in which surfactants impede mass transfer (Goodridge and Robb 1965). These mechanisms including a "sieving effect" (physical entrapment of gas molecules by a thin surfactant film) or hydrodynamic effects such as change in mass transfer boundary layer thickness or local turbulence scale at the gas-liquid interface. In a recent study, it was suggested that the major influence surfactant have on mass transfer relates to the impact of surface active agents on bubble size and shape (Sardeing et al., 2006).

Dudley (1995) evaluated a number of mass transfer coefficient expressions developed using a theoretical basis or data from co-current and non-flowing liquid bubble columns (Calderbank and Moo-Young 1961; Motarjemi and Jameson 1978; Khudenko and Shpirt 1986; Öztürk et al., 1987; Kawase and Moo-Young 1992) against experimental mass transfer data collected in a 0.2 m diameter bubble column with a height of 4 m and non-flowing liquid phase. Two diffusers of differing diameter and unspecified type injected air into the columns. Liquid height, gas flow rate and liquid

composition were varied. The relation providing the best correlation with the experimental data was that of Kawase and Moo-Young (1992). Dudley recommends the Kawase relation for general use because of its good correlation with data and its theoretical basis.

Heijnen and Van't Riet (1984) suggest the use of the Higbie relation for bubbles of diameters larger than 2 mm in diameter. This suggestion is made based on analysis of mass transfer data from many sources but is questionable given the tendency of surfactants to make bubbles more rigid (more like small bubbles) and the conclusion of Calderbank and Moo-Young (1961) that the transition between small and large bubble behavior is for bubbles whose diameter is between 1 and 2.5 mm. The range of mass transfer coefficients expected in typical bubble columns for bubbles of average diameter greater than 2 mm is 2×10^{-4} m/s < k_L < 3×10^{-4} m/s. For bubbles of average diameter less than 0.8 mm the transfer coefficient is insensitive to bubble diameter and approximately 1×10^{-4} m/s.

Table 12: Summary of Mass Transfer Relations for Dispersed Bubbles in Continuous Liquids

Author	Relation	Basis[2]	Description
Higbie (in Motarjemi and Jameson (1978))	$k_L = \frac{2}{\sqrt{\pi}}\sqrt{\frac{D_i}{t_e}} = \frac{2}{\sqrt{\pi}}\sqrt{\frac{D_i U_s}{L_c}} = \frac{2}{\sqrt{\pi}}\sqrt{\frac{R_e S_c}{P_e}}$	T	Developed based on penetration theory. The variable t_e is the time to traverse one bubble diameter and corresponds roughly to the contact time between liquid fluid parcels and bubble surface. This relation was proposed based on an assumption that form drag predominates and bubble surface is mobile. The relation is most appropriately used for large bubbles.
Froessling (in Motarjemi and Jameson (1978))	$S_h = 0.6\ R_e^{1/2}\, S_c^{1/3}$	T	Developed from potential flow theory for small spherical rigid bubbles. This relation was proposed based on the assumption that friction drag predominates and mass transfer takes place through a laminar boundary surrounding the bubble. This relation is most appropriately used for small bubbles.
Calderbank and Moo-Young (1961)	$k_L = \begin{cases} 0.31\left(\frac{\Delta\rho}{\rho_L}\frac{gD_i}{S_c}\right)^{1/3} & \text{Bubble swarms, } d_B < 2.5 \text{ mm} \\ 0.42\left(\frac{\Delta\rho}{\rho_L}\frac{g^2 D_i^2}{S_c}\right)^{1/6} & \text{Bubble swarms, } d_B > 2.5 \text{ mm} \end{cases}$	E	Correlations developed based on historical data and data collected for a variety of gas-liquid systems and with a variety of diffusers. The units of k_L depend on the choice of units for g and D_i. Figures included in the paper indicate that small bubbles might be more-appropriately designated as those 1 mm or smaller in diameter.
Hughmark (1967b)	$S_h = \begin{cases} 2+0.6R_e^{1/2}S_c^{1/3} & 1 < R_e < 450;\quad S_c < 250 \\ 2+0.5R_e^{1/2}S_c^{0.42} & 1 < R_e < 17;\quad S_c > 250 \\ 2+0.4R_e^{1/2}S_c^{0.42} & 17 < R_e < 450;\quad S_c > 250 \\ 2+0.27\,R_e^{0.62}S_c^{1/3} & 450 < R_e < 10^4;\quad S_c < 250 \\ 2+0.175R_e^{0.62}S_c^{0.42} & 450 < R_e < 10^4;\quad S_c > 250 \end{cases}$	E	Developed based on mass transfer data from single, rigid spheres taken for a variety of species dissolving into a variety of liquids.

[2] Designations are: "T" for theoretical, "E" for empirical and "SE" for semi-empirical (based on calibrated models developed from the Buckingham pi theorem).

Author	Relation	Basis[2]	Description
Hughmark (1967a)	$S_h = 2 + a\left[R_e^{0.484} S_c^{0.339}\left(\frac{d_B g^{1/3}}{D_i^{2/3}}\right)^{0.072}\right]^b$ a=0.061, b=1.61 for individual gas bubbles a=0.0187, b=1.61 for bubbles in swarms	E	Developed based on bubble column data from numerous sources and with a variety of gas-liquid systems (CO_2-water, Air-Water, Air-glycerol, air-aqueous solutions). Sherwood number is based on bubble diameter and dissolved gaseous species diffusivity.

Author	Relation	Basis[2]	Description
Lochiel and Calderbank (1964)	For rigid bubbles (fixed shape): $S_h = \begin{cases} 0.99\,P_e^{1/3} & R_e < 1; \quad \text{spherical bubble} \\ 0.84\,R_e^{1/2}S_c^{1/3} & R_e >> 1; \quad \text{spherical bubble} \\ S_{h,sphere}E^2\left[\frac{2}{3}(1+k)\right]^{1/2}\Lambda & \text{All } R_e, \text{ oblate spheroids} \end{cases}$ For bubbles with mobile interfaces, $S_h = \begin{cases} 0.65\left(\frac{\mu_L}{\mu_L+\mu_G}\right)^{1/2}P_e^{1/2} & R_e < 1; \quad \text{spherical bubble} \\ 1.13\left(1-\frac{2.96}{R_e^{1/2}}\right)^{1/2}P_e^{1/2} & R_e >> 1; \quad \text{spherical bubble} \\ S_{h,sphere}\left[\frac{2}{3}(1+k)\right]^{1/2}\Lambda & \text{All } R_e, \text{ oblate spheroids} \end{cases}$ Where $\Lambda = \left(\frac{2E^{1/3}\sqrt{E^2-1}}{E\sqrt{E^2-1}+\ln\left(E+\sqrt{E^2-1}\right)}E^{1/6}\right)$ $k = -\frac{eE^2 - E\sin^{-1}e}{e - E\sin^{-1}e}$ $e = \sqrt{1-\frac{1}{E^2}}$	T	Theoretical relations developed for high Peclet and Schmidt number cases. Relationships were derived for single bubbles of known shape. Relationships were also developed for spherical cap shaped bubbles, but these are not presented here because spherical cap bubbles are unlikely to be encountered in ozone bubble contactors.

Author	Relation	Basis[2]	Description
Deckwer, Burckhart et al. (1974)	$k_L a = b_0 U_g^{b_1}$ where b_1=0.0086 and b_1 = 0.884 correspond to a 20 cm diameter bubble column of total height 7.23 m outfitted with 56 injector nozzles and b_1=0.0274 and b_1 = 0.8 correspond to a 15 cm diameter bubble column of total height 4.4 m outfitted with 56 porous plate injector.	E	Based on measurement of interfacial area and mass transfer in cocurrent flow bubble columns of varying diameter and injector type. Liquids in the bubble column were water, assorted salt solutions and molasses. Oxygen transfer was observed and it is assumed that air was the dispersed phase gas.
Akita and Yoshida (1974)	$S_h = 0.5\, S_c^{1/2} G_a^{1/2} B_o^{3/8}$	E	Mass transfer and specific surface area data were collected in three bubble columns. The columns had square cross sections and were 2.5 m tall. The cylinder side dimensions for the three columns were 7.7 cm, 15 cm, and 30 cm. Single orifice spargers were used for all three columns and porous plate and perforated plate spargers were used in the 15 cm column. Oxygen and air were employed as the dispersed gas phase fluid. Numerous liquids were used as the continuous fluid, including water, glycol solutions, glycerol solutions, methanol and sodium sulfite solution.
Jackson and Shen (1978)	$(k_L a)_{20} = \begin{cases} 2.37\, U_g^{1.07} H^{-0.45} & \text{Based on previous data} \\ 2.28\, U_g^{1.14} H^{-0.55} & \text{Based on 1.8m tank data} \\ 0.53\, U_g^{1.15} & \text{Data from all experiments} \end{cases}$	E	Based on air bubbled into deoxygenated water or mixed liquor. Three tanks (76 mm, 1.8 m and 3.6 m diameters) were used. A single nozzle injected gas into the 76 mm column. Four nipples were used as injection sites in the 1.8m diameter tank. Fifty-nine injection sites (holes drilled in pipe wall) were used in the 7.6 m diameter tank. H is liquid depth with no gas holdup and $(k_L a)_{20}$ is mass transfer coefficient at 20ºC in units of hr^{-1}.

Author	Relation	Basis[2]	Description
Khudenko and Shpirt (1986)	$k_L a = 0.041\,\alpha\,\gamma\left(\frac{h}{d_b}\right)^{0.67}\left(\frac{f}{W}\right)^{0.18}\left(\frac{U_g}{H}\right)$	SE	This relation was developed via dimensional analysis and calibration with experiments performed in rectangular tanks of three sizes. Liquid-gas systems were deoxygenated tap water and air. Two diffusers and several diffuser spacings were employed. The transfer parameter k_La has units of hr^{-1}. Variables α_1 and α_2 are corrections for the presence of contaminants and the deviation of temperature from 20ºC, respectively. H and h are the column height and aerator submergence depth. W is the width of the aeration tank.
Roustan, Duguet et al. (1987)	$k_L a = 0.0139\,U_g^{0.82}$	E	This expression was developed based on fitting an assumed power-law relation between transfer rate and superficial gas velocity to experimental data collected in a full-scale ozone contactor. The gas-liquid system observed was ozonated air – filtered water. Column height was 4.3 m and porous disc diffusers were used to introduce ozonated air into the contactor. Units of k_La corresponding to this relation are min^{-1} and U_g is superficial gas velocity (gas volumetric flow rate divided by reactor cross sectional area) in units of m/hr.
Öztürk, Schumpe et al. (1987)	$S_h = 0.62\,S_c^{0.5}\,B_o^{0.33}\,G_a^{0.29}\,F_r^{0.68}\left(\frac{\rho_g}{\rho_L}\right)^{0.04}$	E	Developed based on measurements in a cylindrical bubble column (diameter of 0.095 m, height of 0.85 m). A single gas distributor was used with 50 different gas-liquid systems. Carrying gases were air, nitrogen, carbon dioxide helium and hydrogen. Liquid phase was 17 pure organic liquids and 22 mixtures of organic liquids with water.
Uchida, Tsuyutani et al. (1989)	$\frac{k_L a\, d_c^2}{D_i} = 0.17\,S_c^{0.5}\,B_O^{0.62}\,G_A^{0.31}\,\varepsilon_g^{1.1}$ $= 0.17\,D_i^{0.5}\,d_c^{0.17}\,\nu_L^{-0.12}\,g^{0.93}\,\rho_L^{0.62}\,\gamma^{-0.62}\,\varepsilon_g^{1.1}$	E	Developed based on experimental measurement of oxygen transfer into deoxygenated liquids including distilled water, glycerol solutions, butanol solutions and aqueous solutions containing a surface active agent. A right circular cylindrical bubble column was operated in countercurrent mode with variable superficial gas velocities. A porous ball glass filter gas distributor and single nozzle were used for air injection. Units for k_La are sec^{-1}.

Author	Relation	Basis[2]	Description
Kawase and Moo-Young (1992)	$k_L = \begin{cases} 0.28\left(\frac{g D_i^2}{\nu_L}\right)^{1/3} & \text{Newtonian liquid, } d_B < 2.5 \text{ mm} \\ 0.47\left(\frac{g^2 D_i^3}{\nu}\right)^{1/6} & \text{Newtonian liquid, } d_B > 2.5 \text{ mm} \end{cases}$	T	Developed for rigid, small bubbles behaving as solid spheres and rising in Newtonian fluids. Trace amounts of contaminants may make small bubbles behave as rigid spheres. Relations developed in this study are similar to the empirical relations of (Calderbank and Moo-Young 1961) and provide theoretical backing for their use. The equations are dimensionally consistent. Relations are also developed for two-phase mass transfer in non-Newtonian liquids.
LeSauze, LaPlanche et al. (1993)	$k_L a = \alpha\, U_g^{\gamma}$ $(\alpha,\gamma) = \begin{cases} (0.06,\ 0.5) & R_e \geq 2100 \\ (0.06,\ 0.7) & R_e \geq 2100 \end{cases}$	E	Developed based on measurements in a pilot ozone contactor with circular cross section, 4.3 m height, 0.15 m diameter, a porous plate diffuser and undergoing countercurrent flow. Units of superficial gas velocity and k_La are m/s and s^{-1}, respectively.
Roustan, Wang et al. (1996)	$k_L a = \begin{cases} 0.105\, U_g^{0.564} & R_e = 680 \\ 0.055\, U_g^{0.564} & 1912 < R_e < 2986 \end{cases}$	E	Developed for countercurrent flow of ozonated air bubbles in a pilot ozone contactor (0.15 m diameter, 2.5m height) outfitted with a ceramic porous distributor. The predominant bubble shape was elliptical. Units of k_La and U_g (superficial gas velocity) are min^{-1} and m/hr, respectively.

II.1.2 Ozone Demand, Decomposition and Properties

When ozone is exposed to filtered water, there is a fast decrease in ozone concentration followed by a decrease that can be modeled with first order kinetics (Langlais et al., 1991; von Gunten 2003a). The stability of dissolved ozone is affected by pH, ultraviolet light, ozone concentration and the concentration of ozone scavengers. Because ozone decomposition kinetics are complex and because of the many factors that influence the chemistry of ozone decomposition, rate constants are typically determined experimentally for waters in batch experiments. Ozone decomposition is thought to be a bimolecular process involving ozone and hydroxyl radicals and with a rate expression given by:

$$-\frac{d[\mathrm{O_3}]}{dt} = k'[\mathrm{O_3}][\mathrm{OH^-}] \tag{22}$$

However, rate data are most often reported via a pseudo-first-order rate constant, k'_{O_3}, where

$$k_{O_3} = \frac{k'}{[\mathrm{OH^-}]} \tag{23}$$

Researchers (LeSauze et al., 1993) have developed expressions of the form

$$\log\left(k_{O_3}\right) = a + b\ \mathrm{pH} + c\ \log[\mathrm{TOC}] + d\ \log[\mathrm{TA}] \tag{24}$$

where *a, b, c,* and *d* are experimentally-determined constants and [TOC] and [TA] are concentrations of total organic carbon and total alkalinity.

Examples of rate constants and the conditions under which they were determined are found in Table 13. Depending upon the water quality, ozone half-life in water can range from the order of seconds to hours (von Gunten 2003a). Ozone decomposition is a strong function of temperature, with ozone decomposing much slower at low temperatures (below 10°C). Ozone plants operating in regions that undergo large seasonal variations in raw water temperature must install ozone-quenching units downstream of bubble contactors because low temperatures result in very high ozone residuals downstream of ozone contactors presenting potential corrosion or human health concerns. Conversely, high raw water temperatures necessitate application of high ozone doses to maintain desired ozone concentration in contactors.

Table 13: Ozone Decomposition Rate Constants

k_{O_3}	**Source**	**Conditions**
0.011 s^{-1}	Tang, Adu-Sarkodie et al. (2005)	Filter effluent from the ACWD treatment plant, Fremont, CA, at 20°C, pH 7.3, 3.5 mg/L TOC, total alkalinity 82 mg/L as $CaCO_3$.
0.0025 s^{-1}	Kim, Rennecker et al. (2002b)	Treated Ohio River water at 298 K (data are given as activation energy and frequency factor)
0.0017 - 0.018 s^{-1}	Roustan, Wang et al. (1996)	Tap water (source not given) with 12ºC < T <19ºC, 7.5 < pH < 8.1, 75 < [TA] < 150 mg/L and 0.8 < [TOC] < 6.0 mg/L
0.0045 – 0.019 s^{-1}	Mariñas, Liang et al. (1993)	Filtered treated water with 12ºC < T <25ºC and 8.3 < pH < 8.4

For mass transfer calculations, the most important ozone properties are ozone Henry's law constant and liquid phase molecular diffusivity. Ozone is considerably more soluble in water than oxygen or nitrogen. Ozone's Henry's law constant increases with temperature and pH and can be calculated using the expression:

$$K_H = 3.87 \times 10^{-7} \, [\mathrm{OH^-}]^{0.035} \exp\left(\frac{-2428}{T}\right) \tag{25}$$

where H is ozone Henry's law constant in atm/L/mol and T is temperature in K (Langlais et al., 1991). Molecular diffusivity also varies with temperature and can be calculated by

$$D_{O_3} = 1.10 \times 10^{-6} \exp\left(\frac{-1896}{T}\right) \tag{26}$$

where D_{O_3} has units of m^2/s and T has units of K (Johnson and Davis 1996).

II.1.3 Disinfection Byproduct Formation

Von Gunten (2003b) divides ozone's potential by-products into those formed in the absence of bromide and those formed in the presence of bromide. Among those formed in the absence of bromide, the predominant by-products are from the oxidation of natural organic matter (NOM) by ozone. The resulting products can be aldehydes, ketones, keto aldehydes, carboxylic acids, keto acids, hydroxy acids, alcohols and esters. The main concern with these products is that they are readily biodegradable and may promote biofouling in distribution systems. In the presence of bromide, disinfection byproducts may include bromate, a regulated potential human carcinogen, and

brominated compounds including trihalomethanes (THMs, presumed human carcinogens) and halogenated acetic acids (HAAs, also regulated and among which are presumed human carcinogens) (Westerhoff et al., 1998). The common ozone DBPs are illustrated in Figure 13.

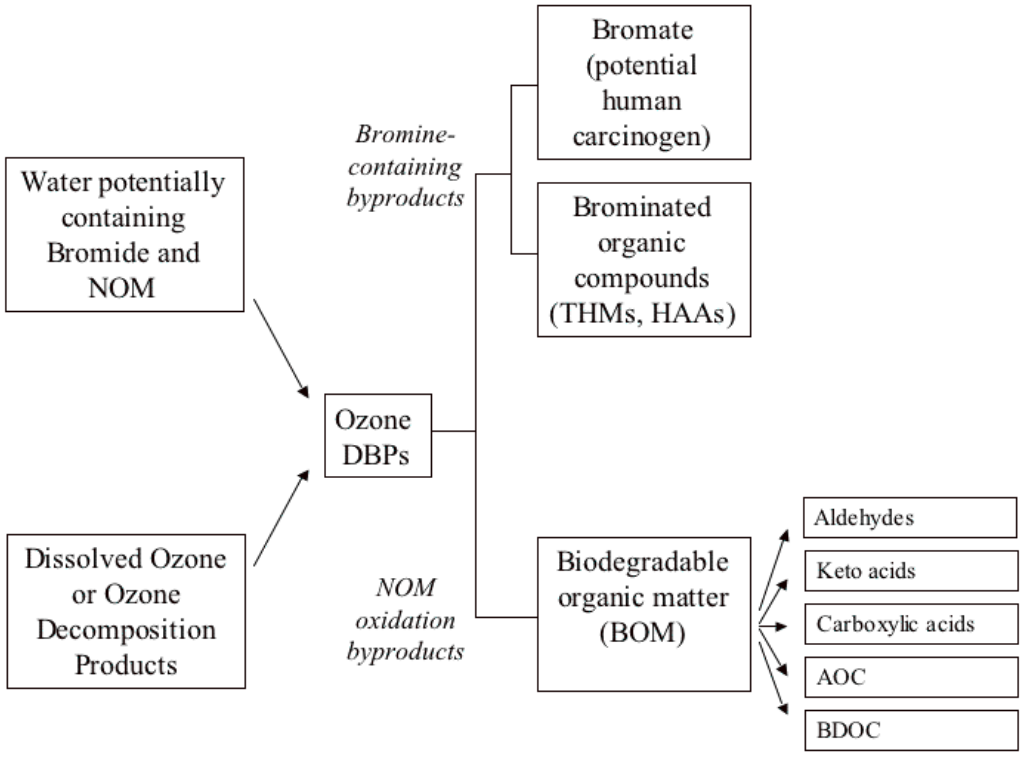

Figure 13: Significant Ozone Disinfection Byproducts (Song et al., 1997; United States Environmental Protection Agency 1999; von Gunten 2003b)

The most problematic ozone byproducts, are those formed in the presence of bromine, and particularly bromate. Bromide occurs naturally in water due to salt-water intrusion and special geological formations or due to human activity including coal

mining, potassium mining and chemical production (von Gunten 2003b).

When ozone oxidizes NOM in the presence of bromide, a number of bromo-organic byproducts may be formed. Concentrations of those compounds are usually far below levels of human health concern. Bromate, however, has been classified as a potential human carcinogen and the U.S. EPA has established a maximum contaminant level (MCL) of 10 μg/L for bromate in finished drinking water. In general, VonGunten states that bromate production is not a concern for waters with a bromide concentration less than 20μg/L. For waters with bromide in the 40 – 100 μg/L range, bromate production may exceed acceptable levels and minimization strategies may have to be employed. Above bromide concentrations of 100 μg/L, bromate production during ozonation will be very high.

Bromate forms in the presence of ozone via multiple pathways involving dissolved ozone and hydroxyl radicals. Numerous authors (e.g., von Gunten (2003b)) indicate that both ozone and hydroxyl radicals must be included in a credible bromate formation model and that "a simulation within a factor of two relative to the measured bromate concentration has to be considered satisfactory" in modeling. An illustration of the most significant pathways for bromate formation is shown in Figure 14. Note that the mechanisms shown do not include NOM. In general, NOM tends to decrease bromate formation by consuming bromide and ozone.

Roustan, Duguet et al. (1996) suggest that an approximate simplified bromate

formation model is:

$$O_3 + Br^- \xrightarrow{k_1} BrO^- + O_2 \quad k_1 = 160\,M^{-1}s^{-1} \text{ at } 20^\circ C$$

$$HOBr \leftrightarrow BrO^- + H^+ \quad pKa = 9.0 \text{ (or } 8.8) \text{ at } 20^\circ C$$

$$2\,O_3 + BrO^- \xrightarrow{k_2} 2O_2 + BrO_3^- \quad k_2 = 100\,M^{-1}s^{-1} \text{ at } 20^\circ C$$

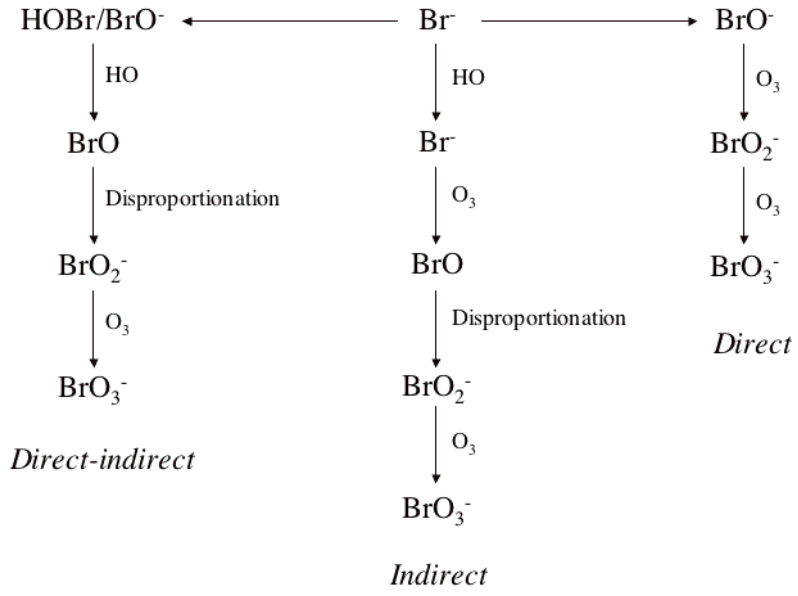

Figure 14: Bromate Formation Pathways (Song et al., 1997)

Applying the Roustan bromate formation mechanism in ideal plug flow reactor (PFR) and continuously stirred tank reactor (CSTR) models, the authors determined that at

similar operating conditions the two reactor types discharged similar bromate ion concentrations, but that to achieve a desired level of infection a CSTR requires a greater *Ct* than a PFR. The authors caution strongly that the proposed bromate formation model does not take into account hydroxyl radical formation and may yield misleading results.

Experimental investigations into the complex mechanism responsible for bromate formation led Song, Donohoe et al. (1996) to the following conclusions:

- increasing bromide, ozone dose, pH or inorganic carbon concentration increases bromate formation;
- Increasing dissolved organic carbon (DOC) or ammonia nitrogen tends to decrease bromate formation;
- Increasing contact time tends to increase bromate formation; and
- increasing temperature tends to promote bromate formation.

The order of importance of the parameters in bromate formation is shown in Table 14.

Strategies for minimizing bromate formation in ozone contactors include ammonia addition, pH reduction, hydroxyl radical scavenging or reduction of hypobromous acid. The most practical of these solutions are ammonia addition and pH depression (Pinkernell and Von Gunten 2001). In a study of concurrent inactivation and bromate minimization, Driedger, Staub et al. (2001) demonstrated the feasibility of bromate control while achieving target inactivation rates using both pH depression and

ammonia addition.

Table 14: Factors Influencing Bromate Formation

Order of importance for parameters that tend to increase bromate formation: pH > Ozone dose > Br^- > Inorganic Carbon
Order of importance for parameters that tend to decrease bromate formation: DOC > NH_3-N
Absolute effect on bromate formation: pH > Ozone dose > DOC > Br^- < NH_3-N ≈ Inorganic carbon

II.1.4 Microbial inactivation

Microorganisms respond differently to disinfectants and a number of models have been developed to describe their inactivation rate. The models are based on general behavior observed in disinfection experiments ("shoulders," "tailing") and an understanding of the mechanisms by which disinfectants inactivate microorganisms. The relations depend on kinematic parameters that are determined via statistical analysis of experimental data collected in batch reactors. The most commonly used models, corrected to account for first order disinfectant decay, are presented in Table 15 (Gyürék and Finch 1998). In all the expressions in Table 15 except the Chick expression, the degree of disinfection, *Ct*, includes changes in disinfectant concentration. In the Hom and Hom power law expressions for batch survival, γ is the incomplete gamma function,

defined as

$$\gamma(m,\, nk't) = \int_0^{nk't} e^{-z} z^{m-1} dz \qquad (27)$$

Haas and Joffe (1998) proposed a method for developing inactivation relations for use in continuous flow systems based on models developed for batch inactivation data. Greene, Haas et al. (2001) demonstrated this procedure in their CFD simulation of chlorine, chloramines and ozone disinfection of four microorganisms in a pilot scale single-phase contactor.

Current practice and regulatory requirements assess reactor performance in terms of "*Ct*" rather than by direct measurement of inactivation in water treatment. The *Ct* approach acknowledges that the survival of organisms depends on the concentration of disinfectant to which they are subjected (*C*) and the time over which they are subjected to the disinfectant (*t*). Because ozone decays and is consumed during the disinfection process, an average ozone concentration is used to calculate *Ct*. The contact time is chosen conservatively as T_{10}, the time for the first 10% of a conservative tracer to be discharged from the reactor following the step introduction of the tracer to the reactor inlet.

The *Ct* approach is practical given the difficulty of counting the myriad organisms present in drinking water and given the time required to produce accurate counts, but problematic given the variations encountered in disinfection process operations such as:

- variations in reactor hydraulics due to operation at off-design conditions;
- variations in water quality leading to changes in disinfectant demand or microbial sensitivity to the disinfectant;
- influence of initial microbial density on inactivation rate; or
- strain-to-strain variations in resistance to disinfection.

Table 15: Commonly-used Disinfection Models

Model name	Predicted batch survival function $\ln\left(\frac{N}{N_0}\right) =$	Kinetic parameters	Rate
Chick	$-kCt$	k	$-kCN$
Chick-Watson	$-\frac{kC_0^n}{nk^*}\left[1-\exp\left(-nk^*t\right)\right]$	k, n	$-kC^nN$
Hom	$\frac{mkC_0^n}{\left(nk'\right)^m}\gamma\left(m, nk't\right)$	k, n, m	$-mN\left(kC^n\right)^{1/m}\left[-\ln\left(\frac{N}{N_0}\right)\right]^{\left(1-\frac{1}{m}\right)}$
Power law	$-\frac{1}{x-1}\ln\left\{1+\frac{(x-1)kC_0^n}{nk^*}N_0^{x-1}\left[1-\exp\left(-nk't\right)\right]\right\}$	k, n, x	$-kC^nN^x$
Hom power law	$-\frac{1}{x-1}\ln\left\{1+(x-1)\frac{mkC_o^n}{\left(nk^*\right)^m}\gamma\left(m, nk't\right)N_0^{x-1}\right\}$	k, n, m, x	$-mkC^nN^x\left\{\frac{N^{1-x}-N_0^{1-x}}{(x-1)kC^n}\right\}^{\frac{m-1}{m}}$

Equally problematic is the tendency for the *Ct* approach, as it is currently implemented for ozone contactors, to overestimate the required ozone dose or contact time to achieve a given level of kill. Overestimating required ozone dose results in excess costs and the potential for forming more disinfection byproducts than if a lower ozone dose were used.

Ozone is the most potent chemical biocide studied by the U.S. EPA to date (Clark and Boutin 2001). A summary of inactivation data generated by several researchers for ozone disinfection is presented in Table 16. *Giardia muris* and *Cryptosporidium parvum* exhibit a temperature dependent lag phase when exposed to ozone (von Gunten 2003b).

Table 16: Summary of Ozone Inactivation Data (Clark and Boutin 2001)

Organism	**Ct** $\left(\frac{\text{mg min}}{\text{L}}\right)$	**Log Reduction**	**Conditions**
Indigenous aerobic bacterial endospores	19	3	Filtered Ohio River water at temperatures between 23.6 and 25.2ºC
Polio virus	1.2	2	Filtered Ohio River water at temperatures between 23.6 and 25.2ºC and pH 7.6
Giardia muris	1.9	2	Unknown water source, temperature of 5ºC and pH of 7
Giardia lamblia	0.55	2	Unknown water source, temperature of 5ºC and pH of 7
Giardia muris	0.75	2	Filtered Ohio River water, temperature between 23 and 24C and pH 7.65
Cryptosporidium parvum	5	2	Conditions not described

Organism	Ct $\left(\frac{\text{mg min}}{\text{L}}\right)$	Log Reduction	Conditions
Cryptosporidium parvum	6.56	2.5	Temperature of 25ºC, other conditions not described
Cryptosporidium parvum	4	1.4	Filtered Ohio River water, temperature between 23 and 24C and pH 7.65

The action of ozone on pathogenic organisms has been debated, with the debate fueled by a wide variation in published values for rate constants of organisms of interest in water treatment. In one camp are those who believe that direct action of ozone on microorganisms is the dominant mechanisms of inactivation. In the second, indirect action of ozone through generation of hydroxyl radicals is assumed to be the dominant mechanism in inactivation. Based on comparison of inactivation rates in the presence of dissolved ozone with inactivation rates for organisms exposed to known concentration of hydroxyl radicals, von Gunten (2003b) states that the predominant mechanism for inactivation is direct action of ozone, with hydroxyl radicals playing a minor role.

II.2 Experimental Investigations of Bubble Column Reactors

The many published experimental investigations of phenomena in bubble column reactors can be grouped into:

- mass transfer investigations and

- hydrodynamics investigations.

II.2.1 Experimental Measurement of Mass Transfer in Bubble Columns

To date, bubble column mass transfer investigations have involved measurement of dissolved gas concentration at discrete locations along the bubble column reactor. Experiments are performed for a range of gas and liquid flow rates and, in some cases, with different water qualities.

LeSauze (1993) performed tracer studies and estimated ozone mass transfer for a 4.2 m tall, 0.l5 m diameter bubble column. Ozone mass transfer rate estimates were based on analysis of samples drawn from sample ports located at the reactor top and bottom and three intermediate depths. The precise depths of the intermediate sample ports are not provided. Tracer and ozone mass transfer experiments were conducted at three superficial liquid flow rates (0.86, 1.42, and 1.97 cm/s), four superficial gas flow rates (0.076, 0.087, 0.203 and 0.48 m/s) and for influent gas-phase ozone concentration ranging from 0.463 to 2.142 g/m^3). Rather than use ozone residual data for developing a rate expression for ozone mass transfer, the authors used an empirical relation for ozone mass transfer from a prior study and assessed several combinations of ideal reactor models to determine the one which best fit measured ozone residual data. Based on their results, the authors suggested the following criteria be used in design of ozone contactors:

- for water disinfection, reactors approaching plug flow conditions yield continuous residual and optimal performance;

- for use of ozone in oxidation of dissolved matter, reactors hydraulics should approach complete mixed performance;
- for realistic reactors which must achieve both objectives, reactors should be designed in tow stages: a completely-mixed stage whose effluent is the ozone residual required for disinfection followed by a plug flow stage that facilitates contact between disinfectant and microorganisms.

To ascertain the influence of water quality on ozone mass transfer and disinfection performance, Owens (2000) measured the influent ozone concentration, effluent ozone concentration and ozone concentration for samples drawn from 4 equally-spaced intermediate ports in an ozone bubble column of 0.15 m diameter and 2.65 m height. The contactor was operated in countercurrent mode at a liquid flow rate of 6.4 L/min and a gas flow rate of 0.64 L/min. Ozone mass transfer rate was not estimated directly in this study; rather, *CT* values corresponding to the depths of each of the intermediate ports were determined by numerical integration of measured residual ozone concentrations and assuming liquid flow rate equal to superficial velocity. Bromate concentration was also measured in samples drawn from the influent, effluent and intermediate ports. The authors concluded that, for Ohio River water, there is a trade-off between the log removal of *Cryptosporidium parvum* oocysts and production of bromate.

In a study which compared ozone and peroxone (water with dissolved ozone gas and hydrogen peroxide) for pre-oxidation to improve filter performance (Tobiason et al., 1992), ozone dissolved into raw water in a 3.05 m tall, 30.5 cm diameter bubble column

run in countercurrent mode. Net ozone mass transfer was estimated based on gas phase measurements of ozone in the feed gas and off-gas. Experiments were performed at a liquid flow rate of 37.8 lpm and a gas flow rate of 16.5 slpm and at ozone doses ranging from 0 to 0.75 mg/L. No ozone mass transfer analyses were performed in this study. Both ozone and PEROXONE were found to extend filter runs when used in combination with coagulant doses typically used in treatment at the New Haven, CT drinking water treatment plant.

In another pilot study investigating the difference between ozone and PEROXONE, Scott (Scott et al., 1992) dissolved ozone into pilot plant filter effluent in four 5.2 m tall, 15.4 cm diameter cylindrical bubble columns arranged in series. Contact time (taken to be equal to the effluent ozone residual multiplied by T_{50}) was varied between 2.16 and 5.23 mg-min/L). As in other pilot studies, ozone mass transfer rate was not directly calculated. Ozone residual in the effluent was seen to vary "unpredictably" with given dose. The authors did not speculate as to the cause of these variations, though they advised use of measured residual rather than applied dose for estimating disinfection in ozone contactors. The variation seen in ozone residual has been observed in full scale contactors (Schulz and Bellamy 2000) and is likely related to hydrodynamics and sample acquisition.

II.2.2 High-Resolution Study of Bubble Column Hydrodynamics

Several experimental techniques have been employed for observation and quantification of hydrodynamics in bubble columns. Though techniques are available for

observation of bubble motion in an ensemble of bubbles, these techniques have most often been applied for measurement of liquid-phase motion. These techniques provide no direct measurement of mass transfer rate or dissolved gas concentration.

Particle image velocimetry (PIV) consists of laser sheeting, image recording and data processing (Chen and Fan 1992). Images can record the position of bubbles in the plane of the laser sheet and, when the liquid phase is seeded with visible particles, the position of the particles suspended in the liquid phase (Degaleesan et al., 2001). In image processing, procedures must be developed for distinguishing individual bubbles and particles and for tracking particles and bubbles from frame to frame. Because the liquid phase is usually seeded with visible particles, this technique has, to date, only been used in bubble columns with non-flowing liquid phase. Versions of PIV have been used to measure spatial variations in gas hold-up in a bubble column with non-flowing liquid phase (Delnoij et al., 1999), to measure spatial variations in gas hold-up and turbulence intensity in a two-phase system (Liu et al., 2005) and to make general observations of flow in a three-phase system with non-flowing liquid and solid phases (Chen and Fan 1992). PIV allows visualization of features that influence countercurrent mass transfer (back-mixing and non-uniform hold-up) but does not allow direct measurement of the effects of these phenomena on mass transfer.

Another experimental technique for quantifying hydrodynamics in bubble columns is the computer-automated radioactive particle tracking (CARPT) procedure. In contrast to PIV, CARPT experiments do not visualize flow on a single plane in the

bubble column. Rather, the positions of individual radioactive particles are tracked (in three dimensions) as they are carried by the liquid phase. The advantage of this technique over PIV is that it provides information on hydrodynamics in the entire reactor. CARPT has been used to investigate the flow field (presence of circulation and distribution of turbulence intensity) in bubble column reactors with non-flowing liquid phase (Degaleesan et al., 2001).

II.3 Ozone Contactor Modeling

II.3.1 CFD Models

Four researchers have published papers on CFD ozone bubble columns modeling studies. These studies are described below and summarized in Table 17.

In a study performed for the Metropolitan Water District of Southern California, Henry and Freeman (1995) developed a finite element model of a full-scale ozone contactor. The commercial code FIDAP (formerly licensed by Fluid Dynamics Inc., currently by Fluent Inc.) was used to perform a two-dimensional, two-phase simulation of a proposed full-scale contactor. Bubbles were assumed to have fixed diameters of 3 mm and were modeled via a Lagrangian approach. Details on gas boundary conditions are not provided.

The CFD model was used to simulate a tracer study and results were compared with experimental data. The authors report an average deviation of CFD study tracer E curve values (expectation) of 6.8% from experimental values. The E curve (also called

the exit age or residence time distribution curve) is a plot of measured or predicted tracer concentration as a function of time and normalized by intake tracer concentration. Plotted experimental and computational tracer curves indicate the CFD model significantly over-predicts dispersion. Having modeled tracer studies, the authors modeled potential design modifications to the ozone contactor including:

- Alternate water depth to contactor length ratios;
- Alternate baffle gap spacing to chamber length ratios;
- Addition of vanes, corner fillets and wall foils.

Sketches showing the baffle gap, vanes, fillets and wall foils are provided in Figure 15.

In general, greater water depths and wider baffle spacing gaps result in higher T_{10}:*HDT*. T_{10} is the time at which 10% of the tracer exits the contactor and *HDT* is the contactor hydraulic detention time. Higher T_{10}:*HDT* indicates more uniform contacting of water with dissolved ozone and is generally desirable. Addition of vertical vanes in the contactor (to direct flow passing through baffle gaps) had a pronounced effect on RTD, increasing predicted T_{10}:*HDT* by 8%. Fillets provided only minor improvement in hydraulic performance. Adding wall foils produced a 4.8% increase in predicted T_{10}:*HDT*.

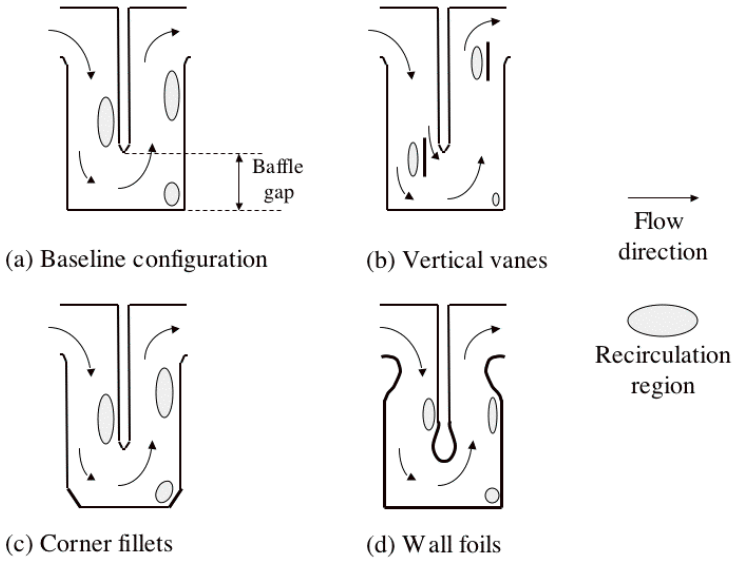

Figure 15: Ozone Contactor Design Modifications (Henry and Freeman 1995)

A progenitor to the commercial CFD code CFX was used to assess design modifications to a full-scale ozone contactor employed at the Alton Water Treatment Works, Anglian Water, UK (Murrer et al., 1995). The authors performed the study in the hopes of developing an alternative to expensive, time consuming and complicated experimental studies. A schematic diagram showing the contactor is found in Figure 16.

Few details of the CFD model are provided in the published results. The model was three-dimensional and two-phase, though details on treatment of multiphase momentum and mass transfer are not provided. The authors state that the model was calibrated via modifications and comparison with pulse tracer studies, though it is unclear what they take calibration to mean and what model parameters may have been adjusted.

Excellent correlation of simulated and experimental tracer curves is claimed without reference to any quantitative measure of correlation.

Following successful calibration of the CFD model, the authors extended the model to include ozone transfer between phases and ozone demand in the aqueous phase. A bench-scale experimental study was performed to ascertain bubble size, rise rate and growth rate. Employing these data, CFD simulations were able to predict ozone residual in the full scale reactor accurately. Finally, the authors predicted the reactor performance under varied operating conditions, with modified diffuser placement and with additional baffling in the final chamber of the contactor. The CFD model predicted significant improvement in reactor performance when the gas flow rate in the first bubble contacting chamber (see Figure 16) was higher than in the second and when a baffle was added to the last chamber in the reactor.

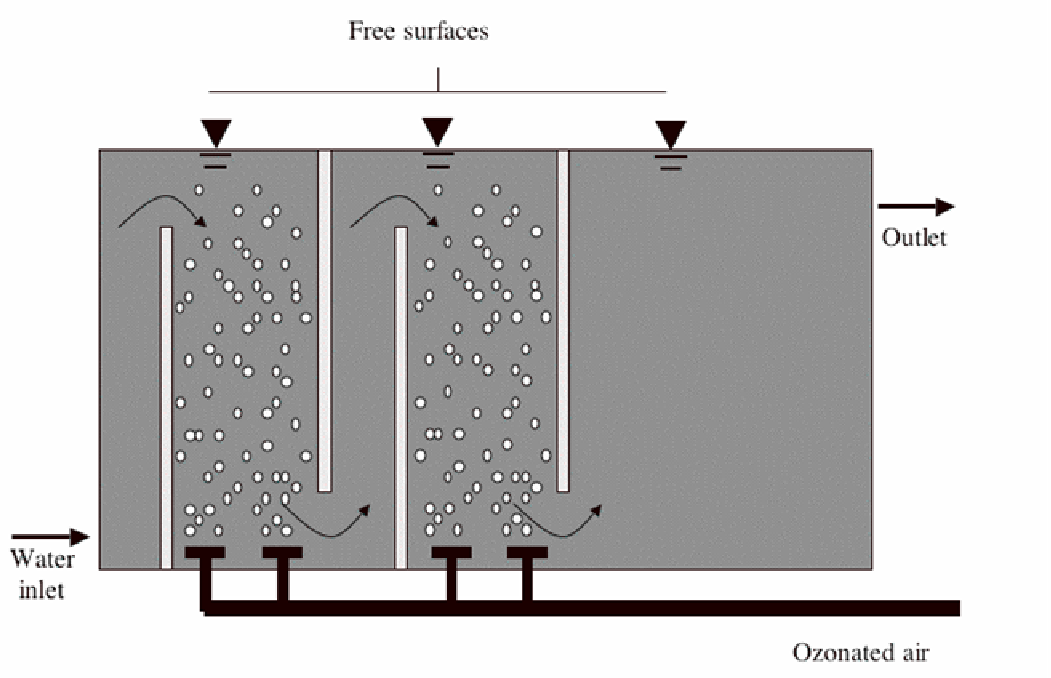

Figure 16: Murrer, Gunstead et al. (1995) Reactor Schematic

Cockx, Do-Quang et al. (1999) performed the most inclusive CFD study of an ozone contactor to date. In the study, CFD was used to simulate two-phase flow, ozone mass transfer and ozone decomposition in a full-scale bubble contactor. The contactor modeled was comprised of seven chambers whose combined volume is 350 m^3 and with a capacity of 53,000 m^3/day. A schematic diagram of the contactor is presented in Figure 17.

The authors used the finite volume CFD code ASTRID for analyses. An Eulerian-Eulerian treatment of two-phase flow was employed with provisions made for momentum and mass transfer between the phases. Momentum exchange between the

phases is calculated as

$$\overline{M}_L = a_p \frac{1}{2} \rho_l C_D V_r \left| V_r \right| \tag{28}$$

where $\overline{M}_L$ is the mean volumetric momentum transfer to the liquid phase from the gas phase for a control volume, a_p is projected volumetric interfacial area (L^2 projected surface area per L^3 reactor volume), ρ_l is liquid phase density, C_D is drag coefficient (described below) and V_r is the relative speed between the phases (the slip velocity). The authors assumed ellipsoidal bubbles with attendant volumetric interfacial area of

$$a_p = \frac{3}{2} \frac{\varepsilon_g}{b} \tag{29}$$

where ε_g is local volumetric gas fraction and b is the projected bubble diameter on a horizontal plane. Without explanation, the authors selected a drag coefficient of 1.0. Bubble diameter was assumed uniform and constant and equal to 3 mm. No mention is made of bubble-induced turbulence (Sato and Sekoguchi 1975) and it is assumed the authors did not account for that phenomenon.

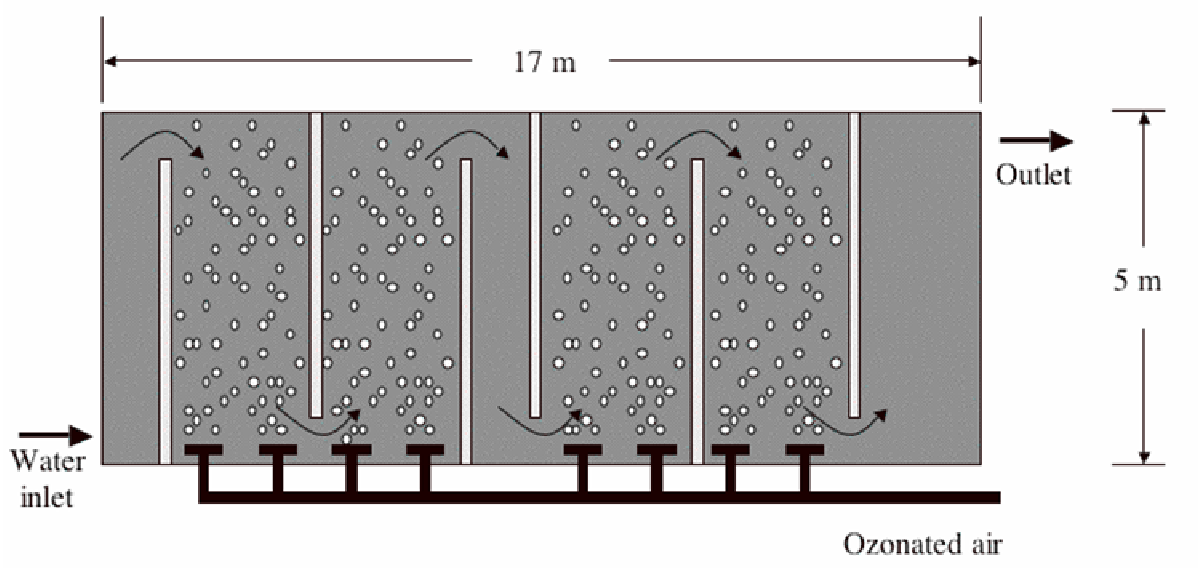

Figure 17: Reactor Schematic for Cockx CFD Study

Mass transfer of ozone between the gas and aqueous phases, given as

$$\overline{L}_l = k_L a\,(C_L^* - C_L) \tag{30}$$

where $\overline{L}_l$ is mean volumetric mass transfer to the liquid phase, k_L is the interphase transfer coefficient, a is volumetric interfacial area (L^2 bubble surface area per L^3 reactor volume), C_L^* is the saturation concentration of ozone corresponding to the gas-phase ozone partial pressure and C_L is mean local aqueous ozone concentration. Without providing insights into the reasons for their choice, the authors use the Higbie (Motarjemi and Jameson 1978) relation for mass transfer coefficient:

$$a = \frac{6\varepsilon_g}{d_b}; \qquad k_L = 2\sqrt{\frac{D_{O_3} V_b}{\pi d_b}} \tag{31}$$

where D_L is molecular diffusion (L^2/T) for dissolved ozone in water. Direct use of the Higbie relation is questionable, since it was developed for large bubbles with mobile surfaces in pure water. The influent water is assigned an instantaneous ozone demand of 0.24 mg/l and aqueous phase ozone decay is assumed to follow first order kinetics with a rate constant of 0.12 min^{-1}.

Cockx compared results from the resulting CFD model with experimental tracer study data and particle image velocimetry (PIV) data collected in a pilot study. The pilot study data are not reported. RTD curves for experimental and simulated tracer studies appear to agree well, through no statistical or quantitative measure of their agreement is presented. Based on apparent success in simulating tracer experiments, the authors simulated a modified reactor in which baffles were added to the chamber to inhibit short-circuiting and promote slug flow. In CFD simulations of the modified reactor, *Ct* (presumably at the reactor discharge) was increased 165%. In experiments (whose details are not described) *Ct* was improved 114%.

In the most recent published ozone contactor CFD study, Huang, Brouckaert et al. (2002) developed a model for a full-scale ozone contacting system. The ozone contactor modeled in that study is a retrofit of a chamber whose primary use is water disinfection. The contactor is located at the Wiggins Water Works, Durban, South Africa. It consists of a static mixer, located immediately upstream of the contactor, in which ozonated air is

injected into the water stream and all ozone is assumed dissolved into the aqueous phase. No data are presented to support the assumption that all ozone is transferred from the gas phase prior to introduction of the water/gas mixture into the contact chamber. Ozonated water is introduced into the contact chamber via an inlet located in the chamber bottom. The contact chamber is of serpentine design and water exits the contactor via a weir.

Huang used the commercial CFD code FLUENT for numerical analyses and used FLUENT's preprocessor, GAMBIT, for developing a mesh. A κ-ε turbulence model was employed and the presence of bubbles was approximated via augmented turbulence intensity of the inlet stream. Only heuristic justification was provided for approximating the gas phase in this manner. Inlet turbulence intensity was adjusted to provide the best match between computational and experimental tracer studies. The inlet (located on the contactor floor) was modeled as a Dirichlet boundary condition. The free surface was approximated as a horizontal rigid lid. The outlet weir was approximated as a submerged rectangular slot and a frictional loss coefficient was assigned to the weir to account for head loss over the weir.

Experimental tracer studies were performed for the contactor with and without gas injection. The presence of injected gas made a relatively minor difference in the shape of the tracer curves. Computational tracer studies were performed and turbulence intensity, defined as

$$I_T = \frac{\sqrt{\frac{2}{3}\kappa}}{\bar{V}} \tag{32}$$

was varied. In equation 1, I_T is turbulence intensity (dimensionless), κ is turbulent kinetic energy (L^2/T^2) and $\bar{V}$ is mean fluid speed (L/T).

The authors found that an inlet turbulence intensity ratio of 50% provided a better match between experimental and computational tracer curves than an inlet turbulence intensity ratio of 20%. This conclusion was based on qualitative comparison of experimental and simulated tracer curves. The authors state that the good agreement between simulated and experimental tracer studies validate their model and justify the simplifications employed, especially their simplified treatment of two-phase flow.

Table 17: Summary of Ozone Contactor CFD Studies

Author	Code and formulation	Two-phase model	Turbulence model	Mass transfer model	Ozone chemistry	Inactivation model
(Henry and Freeman 1995)	FIDAP/FE	Eulerian-Lagrangian	κ-ε	None	None	None
(Murrer et al., 1995)	CFX/FV	Eulerian-Eulerian	Unknown	Unknown	Demand	None
(Cockx et al., 1999) and (Do-Quang et al., 1999)	ASTRID/ FV	Eulerian-Eulerian	κ-ε	Higbie	Instanta-neous demand, 1st-order decay	Chick
(Huang et al., 2002)	FLUENT 5.5.14/FV	Modified influent turbulence intensity	κ-ε	None	None	None

II.3.2 Other Models

Ozone contactor modeling has historically been performed using one-dimensional axial dispersion models or tanks in series models. These models have provided insights into gross design principles and have provided a means for analyzing data collected in laboratory and pilot scale plants but do not have an obvious role in detailed investigation of bubble column phenomena or design of full scale contactors. Several ozone contactor models are described below, with emphasis on their successes and limitations.

LeSauze, LaPlanche et al. (1993) modeled countercurrent ozone mass transfer in a bubble column using three ideal reactor models and a fourth model in which portions of the reactor were modeled via different models. The ideal reactor models employed were a completely stirred tank reactor (CSTR) model, a plug flow reactor (PFR) model and an axial dispersion model. In the hybrid model the portion of the reactor near the sparger was modeled via an axial dispersion model with high dispersion, the middle portion of the reactor was modeled as a PFR and the top portion of the reactor was modeled via an axial dispersion model with a moderate level of dispersion. The hybrid model results provided the best match with data collected in an experimental bubble column.

Zhou and Smith (1994) developed an axial dispersion model of a countercurrent ozone bubble contactor and used the model to predict the performance of a bubble contactor for varying liquid and gas flow rates and feed gas ozone concentrations. Mass transfer coefficients were estimated via the Deckwer correlation (Table 12) and corrections were made for aqueous phase ozone decay. The authors made a limited

number of comparisons of model outputs with experimental data and described the data that would be required to perform more rigorous validation of the model.

Finally, Kim, Tomiak et al. (2002a) developed an axial dispersion model inclusive of ozone mass transfer, ozone demand, ozone decay and microbial inactivation. The resulting ordinary differential equations are presented below. Numerous assumptions were made in development of this modeling, including first-order ozone decay, second order reaction of ozone and natural organic matter (NOM), uniform steady bubble diameter, uniform axial dispersion in the bubble column and Chick-Watson inactivation kinetics (with n=1).

$$
\begin{aligned}
&P_e^{-1}\frac{d^2C_L}{dz^2}-\frac{dC_L}{dz}+N_S\left(\frac{C_g}{K_H}-C_L\right)-D_{a,O_3}C_L-D_{a,NOM}C_LC_{NOM}=0\\
&\frac{d\left(\frac{C_g}{K_H}\right)}{dz}-\frac{N_S}{S}\left(\frac{C_g}{K_H}-C_L\right)=0\\
&P_e^{-1}\frac{d^2C_{NOM}}{dz^2}-\frac{dC_{NOM}}{dz}-D_{a,NOM}C_LC_{NOM}=0\\
&P_e^{-1}\frac{d^2N}{dz^2}-\frac{dN}{dz}-D_{a,N}NC_L=0
\end{aligned}
\qquad (33)
$$

In these expressions, z height above the column bottom, C_L and C_g are liquid and gas phase ozone concentrations, $D_{a,I}$ is Damkhöler number for the reaction in which species i is consumed, N is number of microorganisms per unit volume, N_S is Stanton number and S is a stripping factor, defined as

$$S = \frac{m U_g}{U_L} \tag{34}$$

Auxiliary relations for bubble diameter, mass transfer coefficient, Henry's law constant and microbial inactivation rate were used to determine constants found in the above equations and the resulting equations were solved simultaneously.

The authors compared predicted ozone transfer and microbial inactivation to experimental data with generally favorable results. The authors cautioned strongly against general application of this model to other contactors without careful examination of parameter estimations. Application of this model to a full-scale reactor with three-dimensional flow patterns would be problematic. Specifically, several assumptions used in developing the axial dispersion model are invalid for the hydraulically-complex flows encountered in full-scale reactors. Questionable or invalid assumptions include uniform dispersion, uniform gas phase distribution in the reactor, and one-dimensional transport within the reactor.

II.4 Other Bubble Contactor CFD Studies

As recounted below, researchers have applied numerous techniques in developing CFD models for bubble contactors. In this section the major modeling choices for CFD simulation of bubble columns are presented and examples of studies using various types of models are described. The majority of the bubble contactor papers identified in the literature were analyses of bubble columns in which gas was bubbled through stagnant liquids and the authors were interested mainly in hydrodynamics, not mass transfer.

Several authors noted the lack of bubble column experimental data in the open literature for comparison with CFD simulations (Mitra-Majumdar et al., 1998; Sanyal et al., 1999). The same can be said for axially-resolved and radially-resolved mass transfer data. Thus, in the short term validation of modeling approaches and exploration of submodels will be a major hurdle for researchers simulating bubble columns with CFD.

In simulating a bubble column via CFD, the major choices that must be made are:

- Treatment of two-phases (Eulerian-Eulerian, Lagrangian-Eulerian, Algebraic Mixture Model or Direct Numerical Simulation);
- Choice of steady or transient simulation;
- Choice of domain (2-dimensional or 3-dimensional);
- Turbulence model (κ-ε, κ-ω, large eddy simulation [LES] or perhaps others); and
- Choice of submodels for interphase momentum transfer and mass transfer (perhaps accounting for interactions of bubbles with each other), bubble size (perhaps accounting for coalescence) and turbulent dispersion enhancement due to bubbles.

Among the numerous papers in the literature describing CFD simulation of bubble contactors, several are reviewed below to illustrate these different approaches.

Ranade (1997) undertook CFD studies of bubble columns because, like Mitra-Majumdar et al., he felt one-dimensional approaches lack generality (are applicable only for designs and operating conditions for which experimentally-derived constants are

valid). Studies were performed for air-water systems with bubbles whose diameter varied from 3 mm to 8 mm. The objective of the work was to reproduce numerically the tendency of bubbles to migrate toward the center of a cylindrical bubble column in heterogeneous bubble flow. To account for this, the author resorted to an artificial, if effective, device – the imposition of the following condition on bubble drag:

$$F_D \propto \left[a - b\left(\frac{r}{R}\right)^{1/2} \right] \tag{35}$$

In the above relation F_D is the drag force on the bubble at radial coordinate r, R is the bubble column radius and a and b are constants equal to 2.2 and 1.7, respectively. The constants a and b were chosen to reproduce observed distribution of the gas phase in the reactor and are believed to account for bubble-bubble interactions. The ratio of bubble drag coefficient to diameter was chosen to be 290 m^{-1}. Not surprisingly, the author achieved good qualitative agreement with experimental values. The agreement was assessed via graphical comparison of axial mean velocity and turbulence intensity and radial gas phase holdup.

In a demonstration that CFD can be applied to increasingly complex bubble column flows, Mitra-Majumdar, Farouk et al. (1998) developed a CFD model of two and three-phase co-current flow of water, air bubbles and glass beads. An Eulerian-Eulerian treatment of the multiple phases was used and both the gas and solid phases were treated as dispersed phases. Both experiments and CFD simulations were performed and radial and axial gas and solid phase holdups were compared with experimental data. In general,

the two-phase CFD model predicted radial variation in gas phase holdup well, while the three-phase model did not fare as well, perhaps due to the choice of drag model in the three phase CFD simulations.

Pfleger, Gomes et al. (1999) performed CFD and experimental investigations of a bubble column with stagnant water and air bubbles sparged into a rectangular channel. The position of the sparger and gas flow rate were varied and two-dimensional and three-dimensional transient simulations were performed. The commercial CFD code CFX 4.2 was used for the CFD simulations and the two-phase system was modeled as Eulerian-Eulerian. Time steps were 0.01 seconds and the total simulated (real) time was 400 seconds. A fixed bubble diameter and drag coefficient were specified.

The authors noted a marked difference between two-dimensional and three-dimensional simulations, with the three-dimensional calculations far better estimating experimentally measured turbulence intensity and qualitative behavior (transient drift) of the bubble plume in the column. The authors determined that the keys to performing a tractable and realistic bubble column simulation were to use three dimensions and a fine length scale. The κ-ε turbulence model employed for the liquid phase appeared adequate for producing realistic results.

Eulerian-Eulerian and Algebraic slip mixture model two phase flow treatments were compared directly in a study performed by Sanyal, Vásquez et al (1999). The authors used the commercial CFD code FLUENT (Fluent, Inc., Lebanon, N.H., USA) to perform transient, two-dimensional simulations of a circular cylindrical bubble column in

which air was sparged into stagnant water. A single bubble diameter was chosen to represent the bubble size distribution and bubble drag was calculated via a relation for a single sphere dropping in an infinite fluid (the precise relation is not provided in the paper). Time steps were 0.01 seconds for Eulerian-Eulerian simulations and 0.005 seconds for simulations using an algebraic slip mixture model two-phase treatment. The turbulence model was κ-ε and a uniform grid (0.66 cm axial $\times$ 0.5 cm radial) approximated the geometry.

The authors found good agreement between results generated using both two-phase models when bubbly flow was simulated but found significant difference when churn turbulent flow was simulated (no mention is made of changes in bubble diameter or coalescence for heterogeneous bubble flow). Both models tended to over predict the centerline axial velocity. Though the authors did not draw this conclusion, this result is consistent with the experience of Pfleger et al. (1999) and indicates that two-dimensional bubble column simulations have limitations. However, Sanyal concluded that two-dimensional axisymmetric models provide "good engineering descriptions" of bubble column hydrodynamics and holdup. The authors indicated the need for better turbulence modeling and prediction of turbulent diffusivity.

In a CFD simulation of a bubble plume in a cylindrical column whose diameter is much greater than the plume diameter, Bernard, Maier et al. (2000) used a single-phase flow code, MAC3D (Army Corps of Engineers Waterways Experiment Station, Vicksburg, MS, USA) with source terms added to the momentum equation to simulate

vertically-rising bubbles. The authors dub this approach the drift-flux model. The advantages of this approach are obvious – single-phase calculations are much easier to perform and require less computational effort than multiphase codes. MAC3D is a finite volume code and a κ-ε turbulence model was employed for the liquid phase. Walls were modeled as no-slip boundaries and the free surface was approximated as a rigid lid. Bubbles were assumed to have a uniform diameter and plume geometry was imposed on the solution. The model reproduced steady velocities in the bubble plume within a factor of two and the authors believe the far-field mixing effects of a bubble plume in a reservoir were well characterized. The authors indicated their intent to perform future in which the model accounts for stratified liquids.

Large Eddy Simulation (LES) and κ-ε models were compared for Eulerian-Eulerian simulation of bubble column flow by Deen, Solberg et al. (2001). Results from CFD simulations were compared to experimental data and the two turbulence models were compared. The bubble column in that study was a rectangular cross-sectioned cylinder outfitted with a distributor plate with 49 holes of 1 mm diameter. Grid spacings for the κ-ε turbulence model simulations were 10×10×10 mm. Coarse (10×10×10 mm) and fine (4.7×10×4.7 mm) grid spacings were used in LES simulations. Transient flow was modeled and time steps of 0.01 sec and 0.005 seconds were used for the κ-ε and LES simulations, respectively. Bubble diameter was uniform and steady and set equal to 4 mm. The drag coefficient was chosen to be 1.0 based on the computed value of Eötvös number. The Sato model for enhanced turbulence (Sato and Sekoguchi 1975) was

employed.

Comparison of profiles of simulated and experimental liquid axial velocity profiles, axial gas velocity profiles, radial liquid velocity fluctuations and turbulent kinetic energy profiles showed clearly that the LES turbulence model produced better agreement between calculations and experiment. LES computations took 90 hours to complete on a 4-processor, high-end workstation. No data are provided on the computational requirements for the κ-ε simulations.

The Euler-Lagrange approach to two-phase modeling in a bubble column was employed by Laín, Bröder et al. (2002). A comparison of the Eulerian-Eulerian and Eulerian-Lagrangian approaches summarized from that paper is presented in Table 18.

Table 18: Comparison of Eulerian-Eulerian and Eulerian-Lagrangian Approaches

Approach	**Eulerian-Eulerian**	**Eulerian-Lagrangian**
Liquid phase	Navier-Stokes equations with source terms added for bubble momentum transfer	Navier-Stokes like equations coupled with Navier-Stokes like equation for gas phase
Gas phase	Newtonian equations of motion with bubble-bubble interactions via collision models	Navier-Stokes like equations coupled with Navier-Stokes like equations for liquid phase
Appropriate applications	Dilute two-phase flows and heterogeneous bubbly flows.	Dense flows. Validity is questionable for very dilute flows (Laín et al., 2002)
Advantages	Accounts for a spectrum of bubble sizes and allows modeling of bubble break-up and coalescence	Computational efficiency. May be used to predict bubble coalescence if bubbles are represented by multiple dispersed phases (Olmos et al., 2003)

CFD simulations and experimental results were compared for a bubble column (air-water) with stagnant water and a membrane aerator. Based upon previous experience, the authors used a distribution of bubble diameters (the precise distribution is not stated) and calculated drag coefficient as:

$$C_D = \begin{cases} 16R_e^{-1} & R_e < 1.5 \\ 14.9R_e^{-0.78} & 1.5 < R_e < 80 \\ 48R_e^{-1}\left(1 - 2.21R_e^{-0.5}\right) + 1.86\times 10^{-15} R_e^{4.756} & 80 < R_e < 1500 \\ 2.61 & R_e > 1500 \end{cases} \quad (36)$$

where R_e is Reynolds number based on the bubble diameter and magnitude of the velocity difference between the bubble and liquid. Transient, two-dimensional calculations were performed.

Time-averaged mean and fluctuating velocity profiles (axial and radial) were compared with experimental values and good agreement was claimed. In general, the authors determined that accurate modeling of bubble column flow with the Eulerian-Lagrangian approach requires:

- Inclusion of relevant bubble class sizes in the Lagrangian model;
- Use of an appropriate relation for drag coefficient that distinguished between Reynolds number regimes; and
- Application of appropriate source terms in a κ-ε turbulence model to account for interphase momentum transfer.

III EXPERIMENTAL METHODS

Two types of laboratory experiments were performed in a bubble column operated with countercurrent flow:

- Residence time distribution (RTD) studies and
- Ozone mass transfer visualization studies.

RTD studies generated data that allowed evaluation of column hydrodynamics and characterization of mixing. These data were used to relate mixing intensity to column operating conditions and in validation of the proposed CFD model. Ozone mass transfer visualization studies enabled quantification of spatial variations in mass transfer in the reactor and were also used in CFD model validation.

As described in the literature survey, numerous experimental methods for investigation of hydraulics and mass transfer in bubble column reactors have been employed in prior studies. None of these methods were deemed appropriate for generating data about mass transfer at the fidelity desired in the current study.

For example, in all prior ozone bubble column mass transfer studies (Scott et al., 1992; Tobiason et al., 1992; Mariñas et al., 1993; Owens et al., 1994; Saberi et al., 1995; Owens et al., 2000; Kim et al., 2002a; Kim et al., 2002b; Charlton 2003) ozone mass transfer rate was estimated based on discrete measurements of ozone residuals at the bottom and top of the reactor or at six or fewer intermediate positions along the reactor. These measurements allowed mass transfer rate estimates, but were not sufficiently

resolved to relate mass transfer to hydrodynamics and did not result in expressions for mass transfer that could be scaled. Other experimental studies such as those employing phase-Doppler anemometry (PAD) (Laín et al., 1999), particle image velocimetry (PIV) (Chen and Fan 1992; Delnoij et al., 1999; Liu et al., 2005) or computer-automated radioactive particle tracking (CARPT) (Chen et al., 1999; Degaleesan et al., 2001) provided highly-resolved data on distribution of bubbles or flow field, but did not yield information about mass transfer. Additionally, since the PIV and CARPT techniques require seed of particles in the liquid phase, they are generally performed for bubble columns with non-flowing liquid phase.

Because the techniques outlined above could not provide mass transfer data at the resolution desired, a novel technique for obtaining mass transfer data was developed. This technique is described in detail in III.3. The only prior study that employed a similar technique (image analysis of images taken of flow in a countercurrent flow bubble column reactor) (Rice and Littlefield 1987; Baird and Rao 1998) investigated dispersion, not mass transfer.

III.1 Experimental Apparatus

Experiments were performed in the 15.2 cm diameter, 1.83 m tall glass bubble column reactor shown in Figure 18 and depicted schematically in Figure 19 and Figure 20. As reported in the literature review of this dissertation, all pilot and laboratory continuous flow bubble column ozone contactors studies found in the literature employed circular cylindrical reactors (Roustan et al., 1987; Scott et al., 1992; Tobiason et al.,

1992; LeSauze et al., 1993; Mariñas et al., 1993; Kim et al., 2002a; Kim et al., 2002b; Charlton 2003). The reactors used in these prior studies differed only in their inlet and outlet configurations, diffuser type and location, and operating conditions. The reactor chosen for the current study was selected because it was similar to reactors used in prior pilot studies of ozonation in bubble columns (allowing easy comparison of performance with reactors used in prior studies) and because a suitable column was available for use at Drexel following relatively minor modifications.

Figure 18: Experimental Reactor Photograph

The column's liquid feed is a mixture of tap water and stock solution. For tracer studies the stock was a dilute solution of sodium chloride. In ozone visualization experiments the stock solution was a 100% dilution of potassium indigo trisulfonate dye reagent (described below). The tap water stream was metered via a rotameter and the stock solution stream was delivered by a metering peristaltic pump (Fisher Scientific [provide model number]). A 30 cm in-line helical static mixer mixes the two liquid streams approximately 60 cm upstream of the introduction of the liquid stream into the reactor. The liquid stream is introduced to the reactor through two ports (0.64 cm diameter) in the bottom of the reactor collar. The collar was packed with 7 mm beads that dissipate the inlet liquid stream momentum and promote uniform flow into the bubble column. Liquid flows downward in the bubble column, exiting the reactor via four symmetric discharge ports in the bottom of the reactor. The bottom of the reactor is packed with 7 mm glass beads to promote uniform flow and reduce the impact of discharge design on flow in the reactor.

Gas flows into the reactor via a 2.5 cm spherical fine bubble diffuser located approximately 5 cm above the reactor bottom, as depicted in Figure 21. In tracer experiments the gas feed is compressed air and in ozone mass transfer visualization experiments the gas feed is ozonated compressed air. A rotameter measures gas flow feed rate. Off gas is vented from the top of the reactor. For experiments in which ozonated air is bubbled in the reactor, the off-gas is bubbled in a closed flask under a chemical fume hood (to allow measurement of off-gas ozone concentration). Discharge

from the closed flask is then fed to a solution of sodium thiosulfate to ensure destruction of residual ozone.

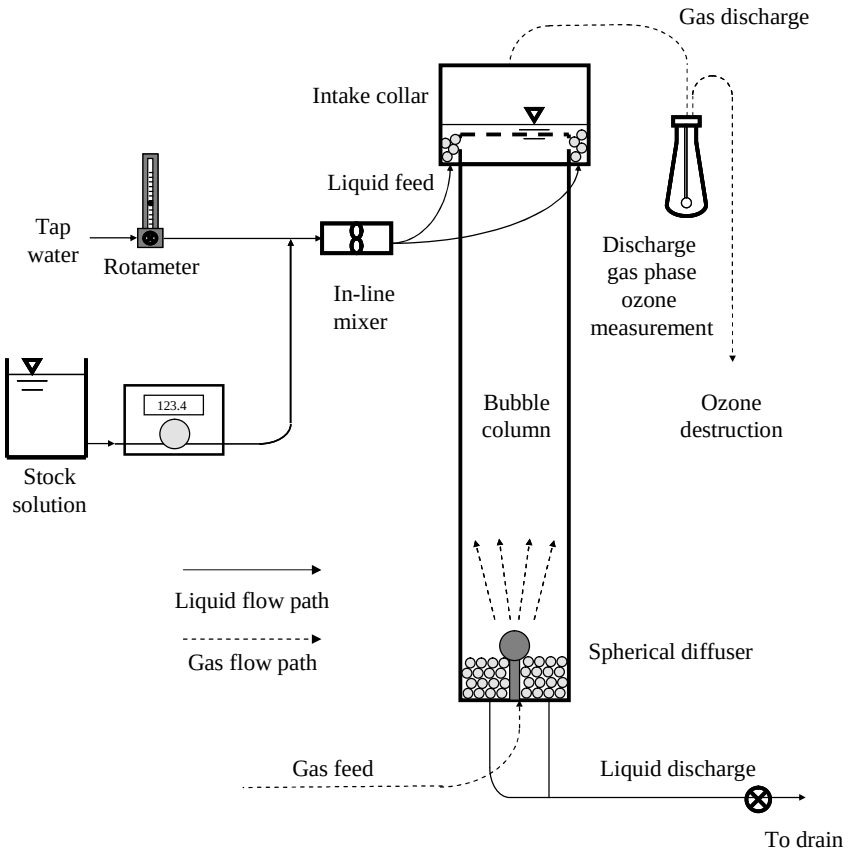

Figure 19: Laboratory Bubble Column Schematic Diagram (not to scale)

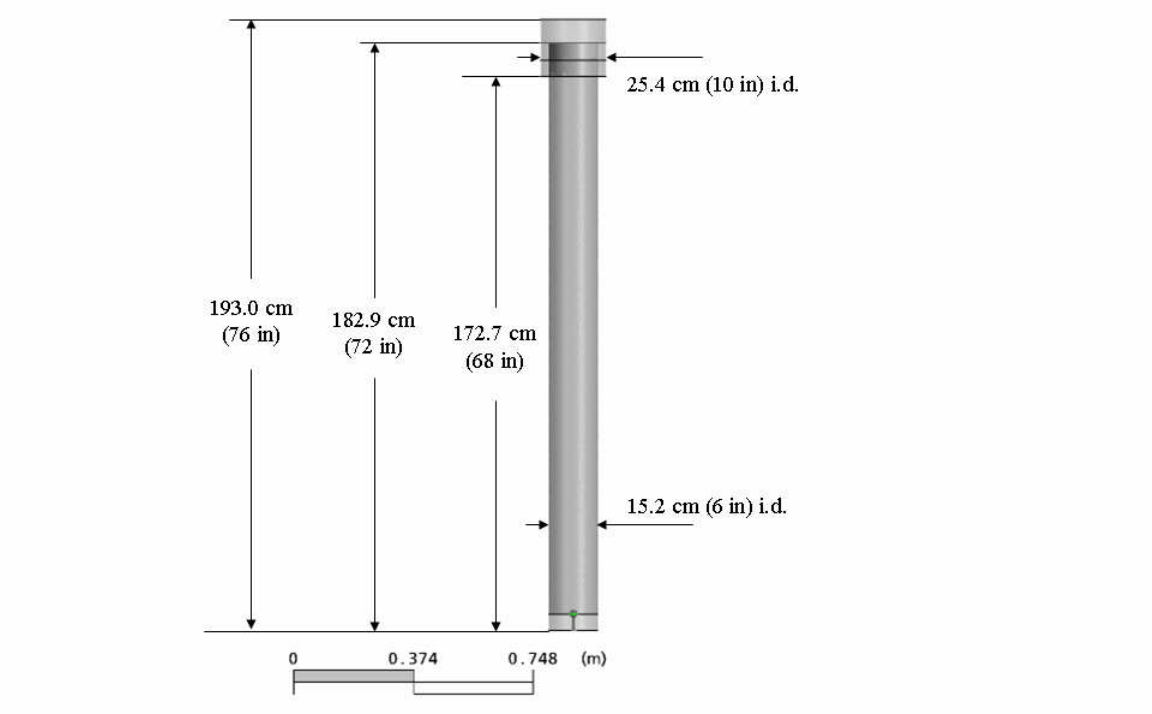

Figure 20: Reactor Schematic Diagram, Scale Drawing

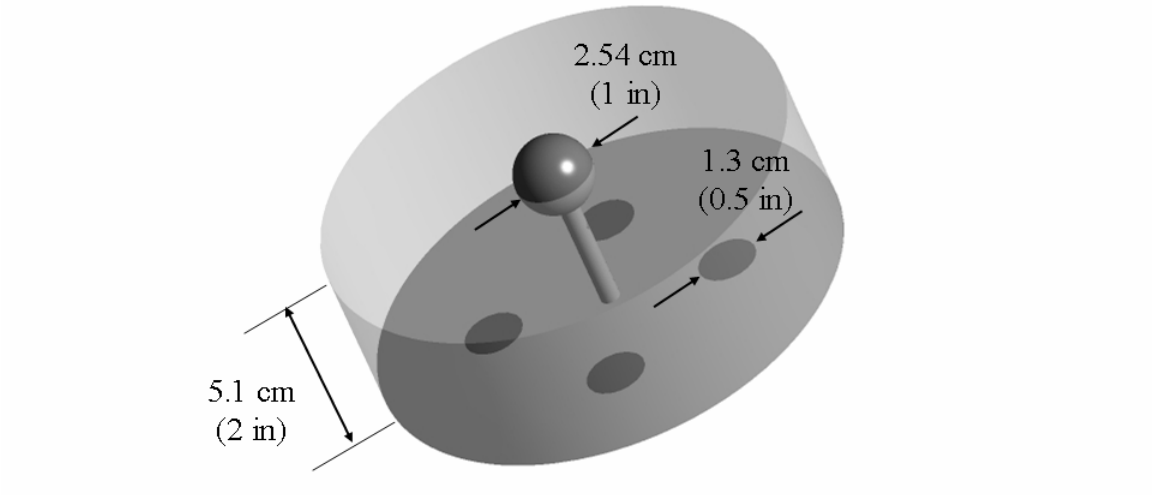

Figure 21: Scale Drawing of Laboratory Column Bottom

III.2 Residence Time Distribution Studies

Step tracer experiments were used to generate data for residence time distribution analyses. Stock solutions of sodium chloride tracer were mixed to provide a tracer concentration of 500 mg/L in the reactor liquid feed. This concentration was chosen because it provides a sufficient variation in liquid feed conductivity for accurate measurement of tracer breakthrough but does not have a large enough difference in density from that of tap water to influence hydrodynamics (Bartrand et al., 2005). Salt concentration was measured as conductivity with a VWR dip cell conductivity meter (model 2052). A plot showing conductivity measured by the conductivity probe as a function of salt concentration is presented in Figure 22. Because conductivity is a linear function of sodium chloride concentration over the concentration range used in tracer experiments, conductivity measurements were used instead of salt concentrations in residence time analyses.

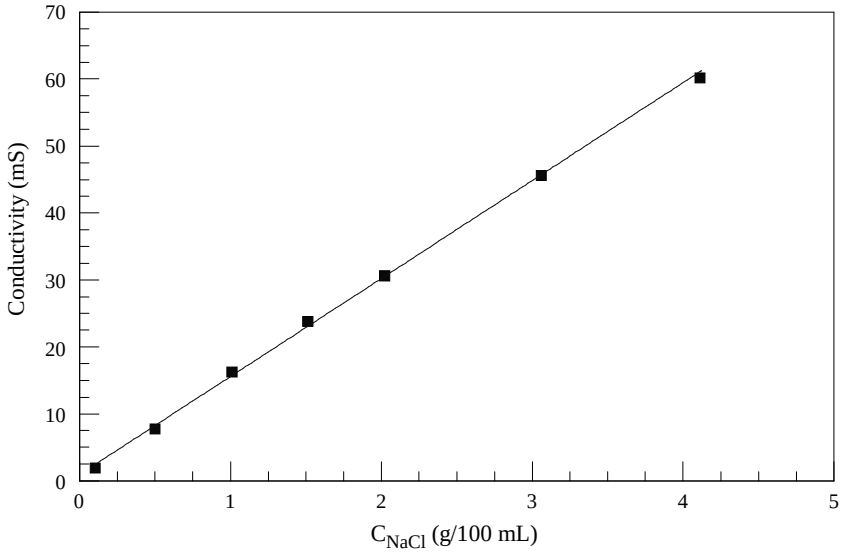

Figure 22: Conductivity Probe Calibration

Prior to step tracer experiments, the liquid stock was tap water and the reactor was operated at steady gas and liquid flows for at least 4 theoretical hydraulic residence times. At the beginning of tracer experiments (time = 0 sec) the liquid stock solution was changed from tap water to sodium chloride solution. Samples were taken from the liquid discharge line approximately 8 cm downstream of the reactor discharge at 15 second intervals. After approximately 4 theoretical hydraulic residence times, the stock solution was switched to tap water and samples were taken for an additional 4 theoretical hydraulic residence times. Both step-up and step-down experiments were performed so that effects of tracer density on the tracer curve might be identified. A typical tracer curve is shown in Figure 23.

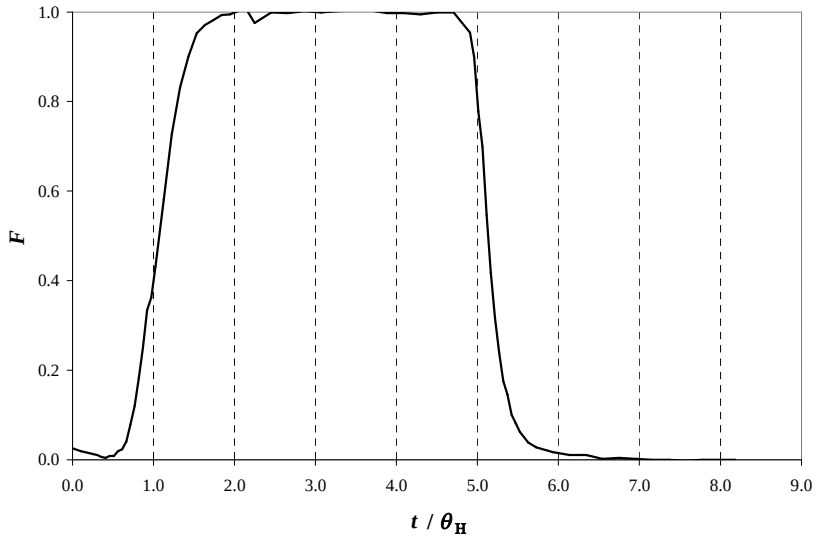

Figure 23: Typical Tracer Curve

In Figure 23, as in subsequent analyses, tracer data are normalized and presented as an "F" curve, where

$$F = \frac{C_{\text{tracer}} - C_{\text{background}}}{C_{\text{feed}} - C_{\text{background}}} \tag{37}$$

and time is non-dimensionalized by theoretical hydraulic residence time, t_H. In equation 35, C_{tracer} is the conductivity immediately downstream of the reactor discharge, C_{feed} is the conductivity at the reactor intake and $C_{\text{background}}$ is the background (tap water) conductivity.

Residence time distribution data (F, θ) were fit to the five residence time distribution models depicted in Figure 24. The single stream N-CSTR and 1-dimensional

ADR (advection dispersion reaction) models (Figure 24(a) and Figure 24 (c)) were chosen because of their widespread use in reactor analysis (e.g., LeSauze et al., 1993; e.g., Kim et al., 2002a). Parallel stream models (Figure 24(b) and Figure 24 (d)) were chosen to account for the presence of two streams in two-phase flow – one associated with downward flow of liquid outside the bubble plume and a second associated with downward flow of liquid within the bubble plume. The cell backflow model (Figure 24(e)) was chosen because entrainment of liquid into the bubble plume was observed during flow visualization and because of reported successes modeling two phase flow with the cell backflow model (Nauman and Buffham 1983; El-Din and Smith 2001(b)).

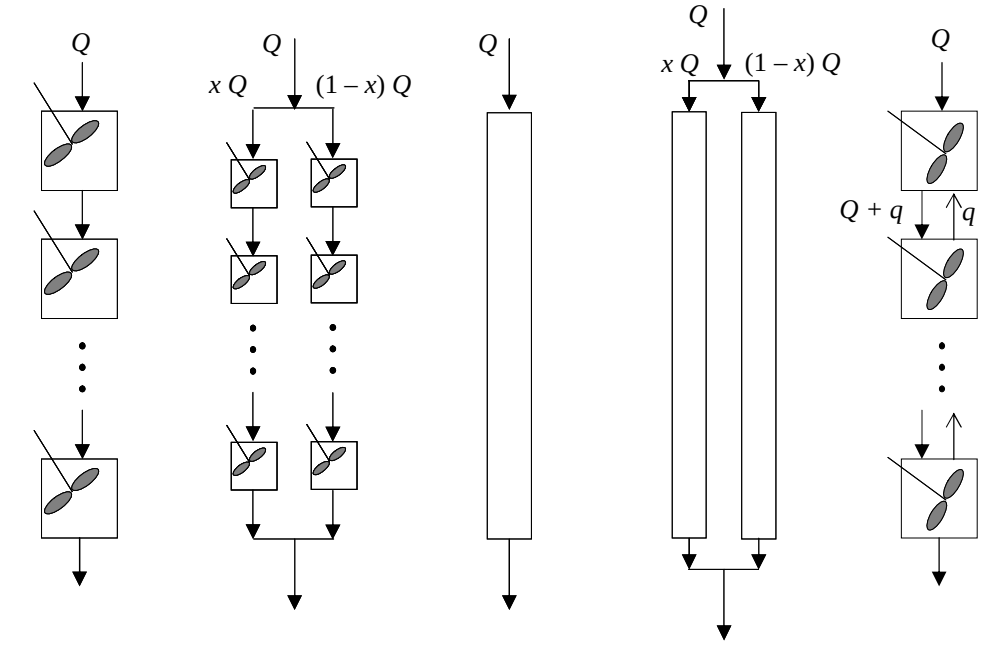

Figure 24: RTD Model Schematic Diagrams

It can be shown that the residence time distribution of a step tracer for an N-CSTR reactor model is given by the equation (Haas et al., 1997):

$$E(t) = \frac{1}{2\theta_H \sqrt{\frac{\pi t D}{\theta_H}}} \exp\left[\frac{\left(1 - \frac{t}{\theta_H}\right)^2}{4\frac{t}{\theta_H} D} \right] \tag{38}$$

where D is dispersion, θ_H is mean hydraulic residence time, and t is time. This distribution depends upon two parameters, D and θ_H. Rather than reporting dispersion directly, mixing is usually reported via the dimensionless parameter Peclet number, defined as

$$P_e = \frac{U_L L}{D} \tag{39}$$

where U_L is liquid superficial velocity (volumetric flow rate divided by reactor cross sectional area), and L is characteristic length (reactor height for bubble column reactors).

The inverse Gaussian function provides an approximation for the residence time distribution for the axial dispersion model. This distribution is a function of two parameters, mean hydraulic residence time and variance of the inverse Gaussian distribution, υ, and an approximation to the distribution is given by (Haas et al., 1997):

$$E(t) = \sqrt{\frac{\theta}{2\pi t^3 \nu}} \exp\left[-\frac{(t-\theta)^2}{2\theta t \nu} \right] \tag{40}$$

The parallel stream models are linear combinations of equations 38 and 40 of the

form

$$E(t) = \lambda E_1(t) + (1-\lambda)E_2(t) \tag{41}$$

where λ is an additional parameter that provides the distribution of mass flow in the parallel reactors. The parallel reactor distributions are functions of 5 parameters.

Although approximations to the cell backflow model have been proposed in the literature (Retallick 1965) they are accurate over small ranges in the number of cells and the amount of backflow between cells (q) and use of the full model equations for modeling two phase flow is recommended (Nauman and Buffham 1983). Consequently, best fit model parameters for the cell backflow model were determined by comparing numerical solutions of the cell backflow model equations to experimental measurements.

III.3 Ozone Mass Transfer Visualization Studies

III.3.1 Overview

The objective of ozone mass transfer visualization experiments was to establish steady flow conditions and obtain a digital photograph showing the distribution of a reactive dye in a reactor.

Ozone mass transfer studies proceeded as follows:

1. Air was sparged into the reactor at a steady rate and off-gas from the head space was vented through tubing and bubbled in water from a Milli-Q water system (Millipore Intertech, Bedford, MA).

2. A mixture of reactive dye (buffered solution of potassium indigo trisulfonate) and tap water was introduced to the reactor at a steady rate.

3. As dye filled the reactor, samples were taken from the reactor discharge at two minute intervals. Dye concentration was determined from these samples via a spectrophotometric measurement at 500 nm in a Barnstead/Thermoline Spectrophotometer, model 340.

4. After at least 4 theoretical hydraulic residence times, steady conditions were assumed to exist and the dye concentration was assumed uniform. While the reactor was being filled with dye solution, water samples were taken from a sample port approximately 8 cm downstream of the reactor discharge at 2 minute intervals. After the completion of experiments, the dye concentration in the samples was measured and used to confirm that steady conditions had been achieved.

5. The ozone generator (shown in Figure 19) was switched on at a chosen voltage. The voltage was chosen to ensure that enough ozone was supplied to the column to ensure a significant difference in dye color between the top and the bottom of the column, but not so much ozone that all the dye was decolored prior to discharge from the column.

6. The liquid feed rate, gas feed rate and ozone generator voltage were held steady for at least three reactor theoretical hydraulic residence times, during which time the ozone decolored the dye and a quasi-steady distribution of dye was established in the

reactor. The dye distribution was quasi-steady (rather than steady) because turbulence in the reactor liquid flow caused fluctuating dye concentrations throughout the reactor.

7. During the dye decoloration process, digital photographs were taken of the reactor at 2 minute intervals (details of the photographic setup are provided below) and samples were withdrawn from the sample port downstream of the reactor discharge at 2 minute intervals. The digital photographs were used for calculating ozone mass transfer rate and the samples were used to verify that quasi-steady conditions had been established.
8. The liquid discharge temperature was noted and the water feed, gas feed and ozone generator were turned off.
9. The ozone concentration in the water through which the off-gas was bubbled was determined using the indigo trisulfonate method (American Public Health Association 1998).
10. The reactor was refilled with tap water and digital images of the reactor (with no dye or bubbles) were taken. These images were used to remove variations in background lighting from the images taken of indigo dye at quasi-steady distribution.

Important components of these steps are described in detail below.

III.3.2 Indigo Dye Solution Composition and Preparation

The dye used in ozone mass transfer visualization experiments is a buffered

solution of indigo potassium trisulfonate. Indigo trisulfonate is shown in Figure 25. In solution, the carbon double bond of indigo trisulfonate reacts rapidly and preferentially with ozone, decoloring the molecule (Bader and Hoigné 1981). One mole of ozone is consumed per mole of indigo trisulfonate decolored. To determine whether tap water contained constituents that interfered with the ozone-indigo dye reaction the indigo dye method was used to measure the ozone concentration in a samples diluted with milli-Q water and tap water. Ozonated air was bubbled into mill-Q water for 15 minutes (until a steady ozone concentration was established) and 20 mL samples were transferred to 4 flasks containing 10 mL of indigo dye reagent. Two of the flasks were filled to 100 mL with milli-Q water and two were filled to 100 mL with tap water. Absorbance at 500 nm was determined via spectrophotometer. Experiments were conducted at 3 ozone residual concentrations. In all cases there was no difference between absorbance (and ozone concentration) between the samples diluted with tap water and those diluted with milli-Q water. This indicated that tap water consitutents did not interfere with the ozone-indigo reaction and that no treatment of tap water was necessary prior to use in ozone mass transfer visualization experiments.

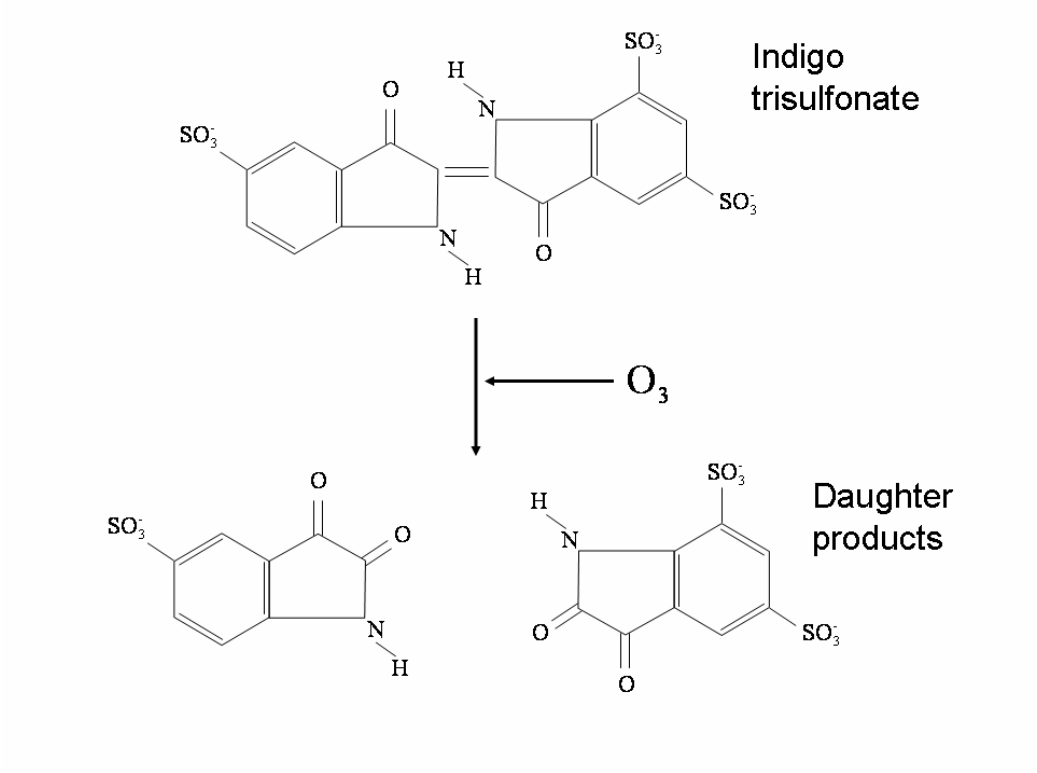

Figure 25: Indigo Trisulfonate Structure and Daughter Products

Prior to performing ozone mass transfer visualization experiments, test runs were performed in which indigo dye was fed to the reactor at known concentrations and flow rates and the ozone generator was operated at a range of voltages. These test experiments identified a range of indigo dye concentrations and ozone generator voltages that produced significant dye without causing complete decoloration anywhere in the reactor. decoloring was observed but the discharge water was not completely decolored.

III.3.3 Photography Methodology

The setup for recording digital images was developed to

- Provide uniform lighting of the reactor;
- Provide images that spanned as much of the reactor as possible while still providing high resolution;
- Ensure photographs taken in different experiments were taken under the same conditions.

Backlighting was used to provide uniform illumination of the reactor. The lighting setup is shown in Figure 26.

The light sources were two high-temperature fluorescent lamps, 2.44 m (8 ft) tall, mounted on the frame holding the bubble column. Because the lamps extended above and below the reactor, variations in lighting along the reactor length were relatively minor. The greatest variations in lighting occurred at the reactor top and bottom, where light was partially blocked by the horizontal PVC sheets supporting the column. The camera (Nikon Coolpix 8700, Nikon Corporation, Tokyo, Japan) was positioned 1.68 m (66 in) from the front of the reactor. This position was chosen to maximize the reactor height visible with zero zoom.

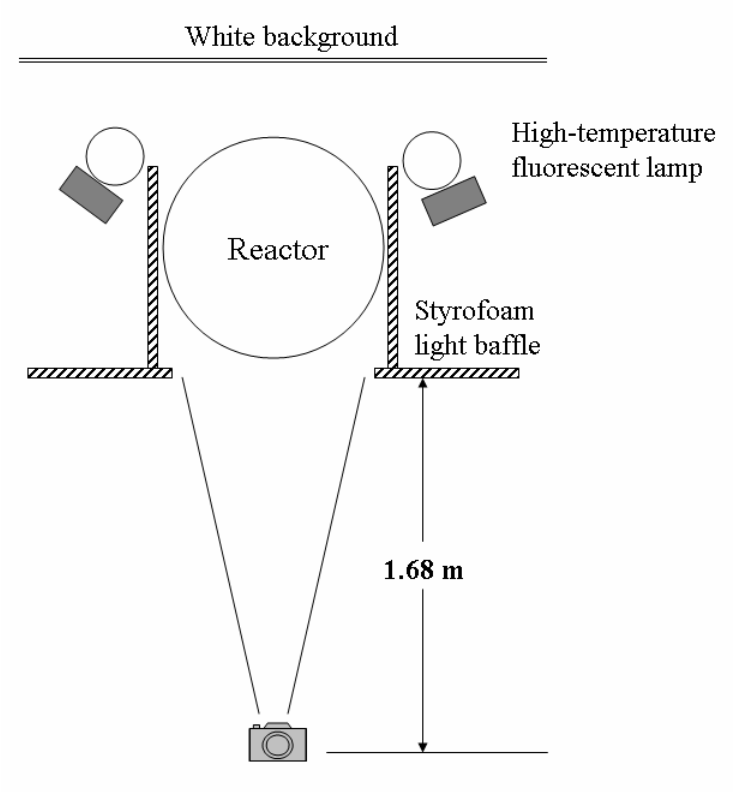

Figure 26: Mass Transfer Visualization Experiment Lighting

III.3.4 Development of Indigo Dye Color Calibration Curve

Prior to performing the steps outlined above, the relationship between the color recorded in digital images and the indigo dye concentration was established. This relationship was established by

- filling the reactor with solutions of indigo reagent diluted with tap water,
- taking samples and digital photographs of the reactor filled with dye,
- plotting the dye concentration against the absorbance of the dye (measured via

spectrophotometer at 500 nm),

- processing digital images to account for variations in background lighting and
- plotting mean color of digital images against indigo dye concentration.

Experiments were performed at 6 indigo trisulfonate concentrations. The highest concentration was chosen to be higher than any concentration that would be encountered during ozone mass transfer visualization experiments.

Image processing consisted of:

- Subtracting an image of the reactor filled with a known dye concentration from an image of the reactor filled with tap water (the background).
- Inverting the color of the resulting image.
- Cropping the image to include only the reactor.
- Removing the glass manufacturer's mark by "cloning" an area immediately above the mark over the black lettering.
- Converting the image from 32-bit RGB JPEG image to an 8-bit (grey scale) TIF (tagged image file) format.
- Determining the mean pixel value and mode pixel value for the 8-bit image.

Image processing was performed using the public domain image processing software ImageJ, version 1.34s (Rasband 2005). Processed digital images showing the dye color

at 6 dilutions are presented in Figure 27.

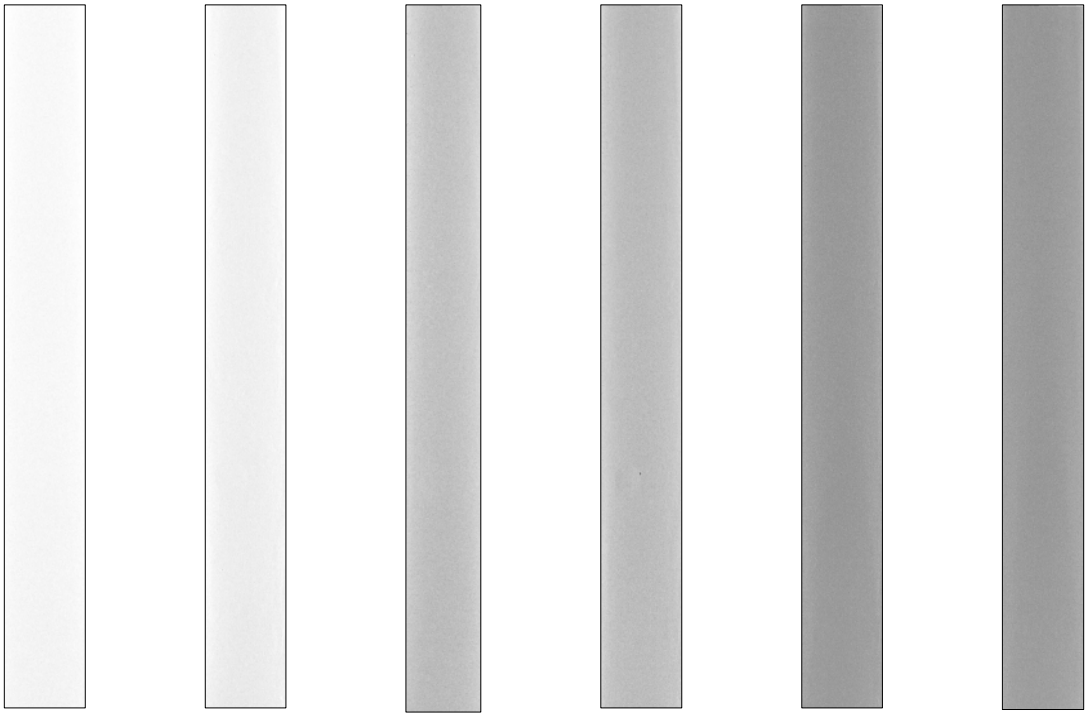

(a) 0.64 mg/L (b) 1.28 mg/L (c) 2.57 mg/L (d) 3.85 mg/L (e) 5.13 mg/L (f) 6.42 mg/L

Figure 27: Pixel Color Calibration Images

Histograms showing distribution of pixel color for the images shown above are shown in Figure 28. The abscissas of the plots in Figure 28 are the pixel color (in 8-bit grayscale). A pixel value of 0 indicates a completely black pixel and a pixel value of 256 indicates a completely white pixel. The histograms exhibit sharp peaks at distinctly different pixel values over the range of indigo dyes examined. These sharp peaks at

distinct colors indicate that pixel color is a reliable indicator of indigo dye concentration. Calibration of indigo dye concentration with pixel color is described below.

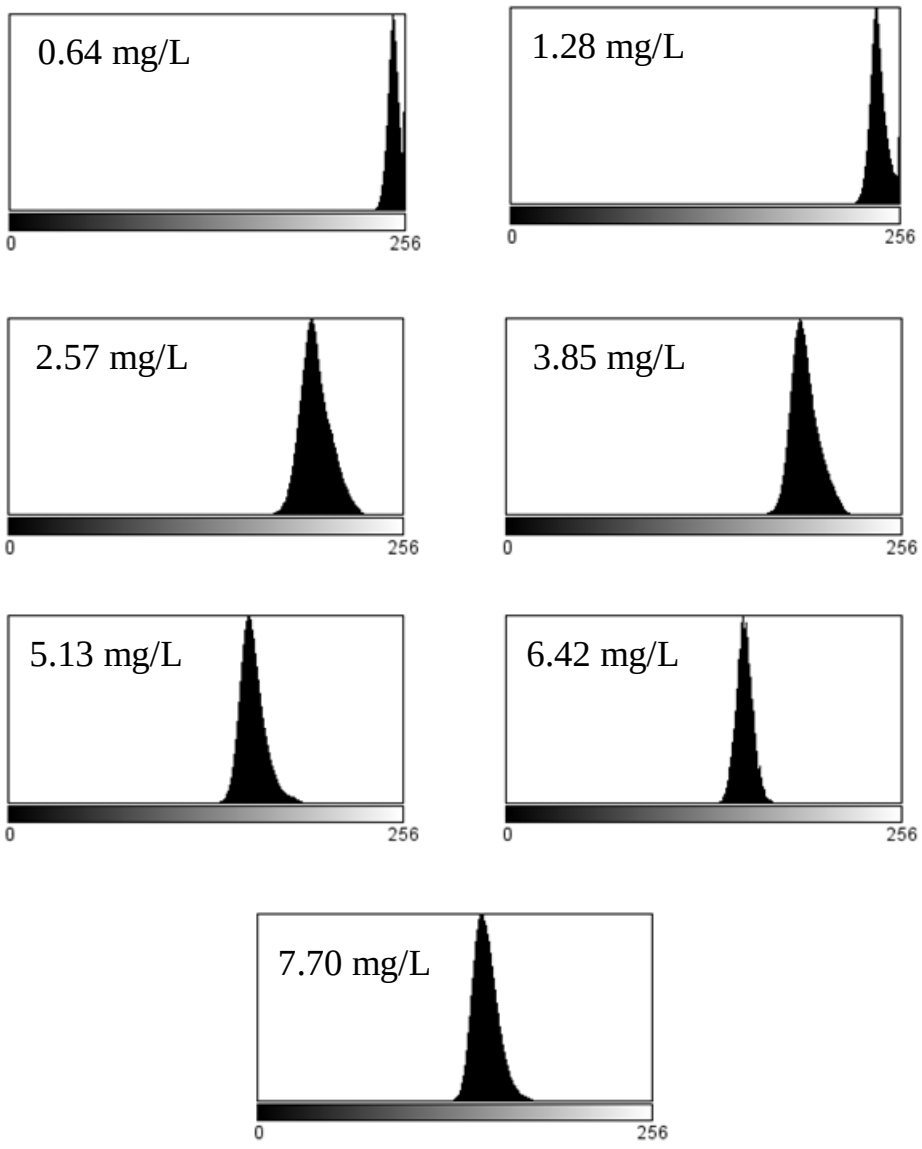

Figure 28: Calibration Image Histograms

A plot of absorbance at 600 nm versus indigo trisulfonate concentration for dilution of indigo reagent in tap water is presented in Figure 29. The linear dependence of absorption on indigo trisulfonate concentration indicates that:

- The constituents of tap water do not significantly alter the absorbance of solutions of indigo trisulfonate at 600 nm, and
- Absorbance at 600 nm is a linear function of indigo trisulfonate concentration.

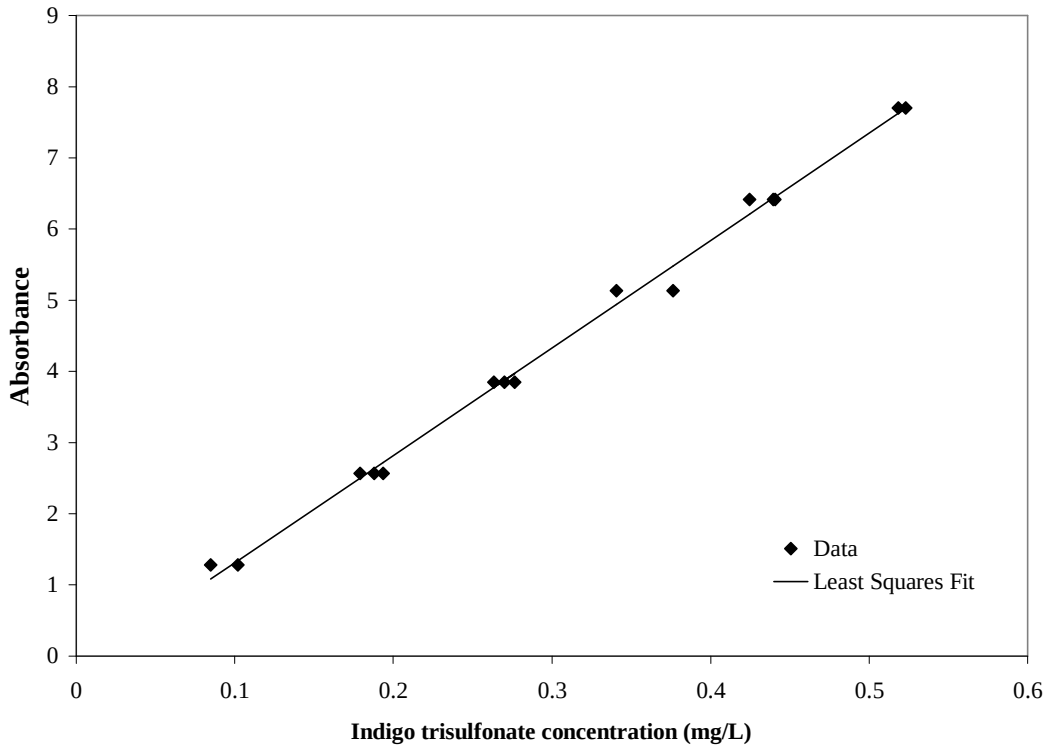

Figure 29: Variation of Absorbance with Indigo Concentration for Indigo Reagent Diluted with Tap Water

Plots showing pixel value mean and mode for the images shown in Figure 27 and Figure 28 versus known indigo dye concentration are presented in Figure 30. Curves were plotted for images with and without the background subtracted and for the mode and mean of the pixel values. Note that images are 8 bit gray scale. As such, pixel color ranges from 0 to 256, with 256 corresponding to white (0 indigo dye concentration) and 0 corresponding to black. The curves corresponding to images with the background subtracted are offset from those in which the background was not subtracted. This indicates that the subtraction of the background pixel color does not affect the final image color (monochromatic blue in RGB channels). Two important observations can be made based on Figure 30:

- For all curves, the variation in mean and mode of the pixel color is linear with indigo dye concentration and
- over the concentration range expected to span the concentrations during experiments, there is a significant change in pixel color intensity.

These observations indicate that the pixel color intensity is a sensitive indicator of indigo dye concentration and that a calibration curve relating pixel intensity to indigo dye concentration may be developed. The calibration curve based on mean pixel color with the background subtracted and is shown as a solid line in Figure 30.

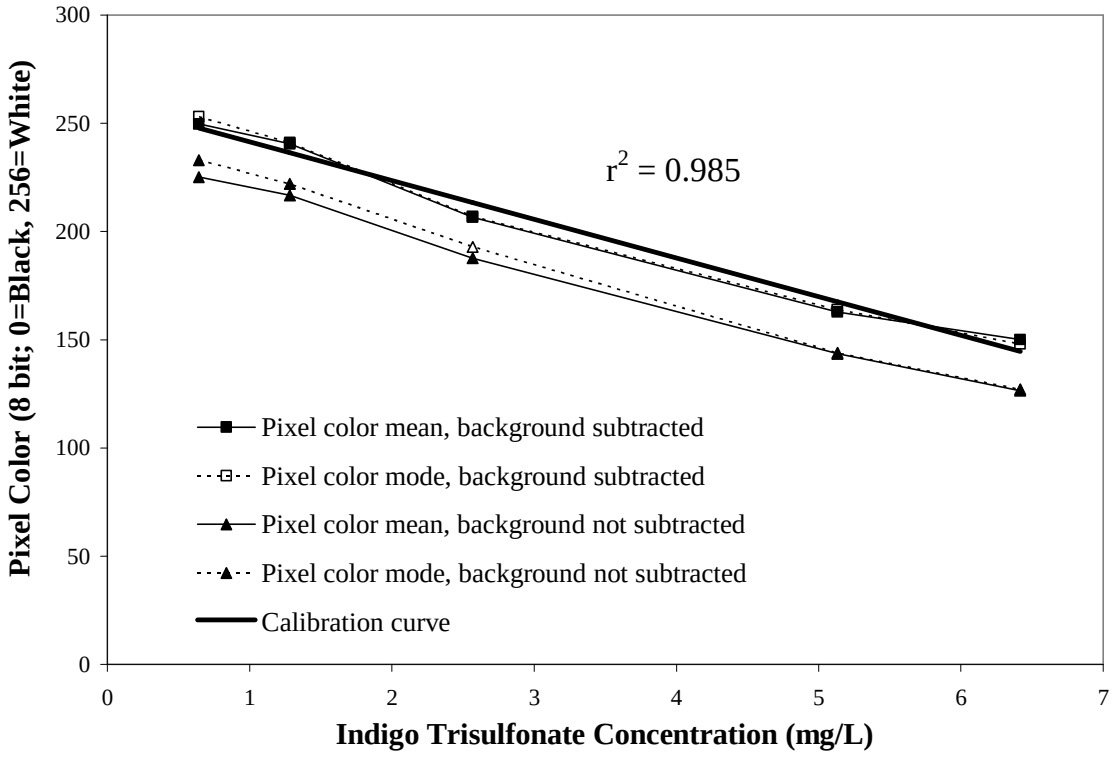

Figure 30: Pixel Color Calibration Curve

IV NUMERICAL METHODS

IV.1 Mathematical Model

A two-phase model (Eulerian-Eulerian) is employed for the numerical solution of the gas/liquid flowfields and phase distributions. In this model, the phases are modeled as uniformly mixed within a given mesh element and the volume occupied by phase α in that mesh element is denoted ϕ_α. In the current two phase study, ϕ_L is liquid volume fraction, ϕ_G is gas volume fraction and $\phi_G + \phi_L = 1.0$.

Assuming no source terms for the liquid and gas phases and no mass transfer between phases due to phase change, the two-phase model continuity and momentum equations are:

$$\frac{\partial}{\partial t}\left(\phi_\alpha \rho_\alpha\right) + \nabla \bullet \left(\phi_\alpha \rho_\alpha \vec{V}_\alpha\right) = 0 \tag{42}$$

and

$$\frac{\partial}{\partial t}\left(\phi_\alpha \rho_\alpha \vec{V}_\alpha\right) + \nabla \bullet \left[\phi_\alpha \left(\rho_\alpha \vec{V}_\alpha \times \vec{V}_\alpha\right)\right] = -\phi_\alpha \nabla P_\alpha + \nabla \bullet \left\{\phi_\alpha \mu_\alpha \left[\nabla \vec{V}_\alpha + \left(\nabla \vec{V}_\alpha\right)^T\right]\right\} + \vec{F}_\alpha \tag{43}$$

where ρ_α, V_α, P_α and μ_α are the density, velocity, pressure and viscosity of phase α, respectively, and F_α is the interfacial force acting on phase α due to the presence of the other phase. For the current problem, the only interfacial forces of significance are drag force and interphase turbulent dispersion force and

$$\vec{F}_\alpha = \vec{F}_\alpha^{\,D} + \vec{F}_\alpha^{\,T} \tag{44}$$

where $\vec{F}_{\alpha}^{\,D}$ is the interfacial force due to drag and $\vec{F}_{\alpha}^{\,T}$ is interfacial force due to turbulent dispersion.

The drag component of the interfacial force term is given as

$$\vec{F}_{\alpha}^{\,D} = \frac{C_D}{8} A_{\alpha\beta} \rho_{\alpha} \left(\vec{V}_{\beta} - \vec{V}_{\alpha} \right) \tag{45}$$

where C_D is drag coefficient, $A_{\alpha\beta}$ is the net interfacial area between the phases and $\vec{V}_{\beta}$ and $\vec{V}_{\alpha}$ are the velocities of phases α and β. The Grace relation was chosen for drag coefficient because bubbles were observed to be elliptical and dispersed. The Grace drag coefficient (Clift et al., 1978) is:

$$C_D = \frac{4}{3} \frac{g d_B}{U_T^2} \frac{\Delta\rho}{\rho_L} \tag{46}$$

where g is gravitational acceleration, d_B is mean bubble diameter, $\Delta\rho$ is the difference in density between the phases, ρ_L is liquid phase density and U_T is bubble terminal rise velocity, given by

$$U_T = \frac{\mu_L}{\rho_L d_B} \Lambda^{-0.149} \left(K - 0.857 \right) \tag{47}$$

In the terminal velocity expression, Λ is the Morton number (a fluid property) given by

$$\Lambda = \frac{\mu_L^4 g \Delta\rho}{\rho_L^2 \sigma^3} \tag{48}$$

where σ is surface tension and K is given by

$$K = \begin{cases} 0.94B^{0.751} & 2 < B \le 59.3 \\ 3.42B^{0.441} & B > 59.3 \end{cases} \tag{49}$$

In equation 20, B is given by

$$B = \frac{4}{3} Eo\, \Lambda^{-0.149} \left(\frac{\mu_L}{\mu_{ref}} \right)^{-0.14} \tag{50}$$

and Eo is the Eötvös number, given by

$$Eo = \frac{g\, \Delta\rho\, d_b^2}{\sigma} \tag{51}$$

Turbulent dispersion force is given by

$$\vec{F}_\alpha^{\,T} = C_{TD} C_d \frac{\nu_{t,L}}{\sigma_{t,L}} \left(\frac{\nabla \phi_G}{\phi_G} - \frac{\nabla \phi_L}{\phi_L} \right) \tag{52}$$

where C_{TD} is an empirical constant (taken to be 1.0 in the absence of data for turbulent dispersion force in countercurrent flow), C_d is drag coefficient (described above), $\nu_{t,L}$ is turbulent viscosity, $\sigma_{t,L}$ is liquid turbulent Schmidt number (taken to be 0.9) and ϕ_G and ϕ_L are the gas and liquid phase volume fractions, respectively.

The two equation turbulence model (κ-ω) for the continuous (liquid) phase is

$$\frac{\partial}{\partial t}\left(\phi_L\, \rho_L\, \kappa_L\right) + \nabla \bullet \left\{ \phi_L \left[\rho_L \vec{U}_L\, \kappa_L - \left(\mu + \frac{\mu_{t,L}}{\sigma_k} \right) \nabla k_L \right] \right\} = \phi_L \left(-P_{t,L} + \beta' \rho_L\, \kappa\, \omega \right) \tag{53}$$

$$\frac{\partial}{\partial t}(\phi_L\,\omega)+\nabla\bullet\left[\phi_L\,\rho_L\,\vec{U}_L\,\omega-\left(\mu+\frac{\mu_{t,L}}{\sigma_\omega}\right)\nabla\omega\right]=\phi_L\left(\lambda\frac{\omega}{\kappa}P_{t,L}-\beta\,\rho_L\,\omega^2\right) \tag{54}$$

In equations 46 and 47, κ is the turbulent kinetic energy, ω is the characteristic turbulence frequency, $\mu_{t,L}$ is the liquid phase turbulent viscosity and the constants β, β', σ_k, σ_ω and λ are 0.075, 0.09, 2, 2 and 5/9, respectively. The liquid phase turbulent viscosity is modeled using the Sato particle enhanced turbulence model (Sato and Sekoguchi 1975), given in equation 48:

$$\mu_{t,L}=\mu_{t,s}+\mu_{t,p} \tag{55}$$

where $\mu_{t,s}$ is the conventional shear-induced turbulent viscosity and $\mu_{t,p}$ is a particle induced component of turbulent viscosity given by

$$\mu_{t,p}=C_{\mu,p}\rho_L\phi_g d_b\left|\vec{U}_G-\vec{U}_L\right| \tag{56}$$

and $C_{\mu,p}$ is given a value of 0.6. The term $P_{t,L}$ in equations 46 and 47 is the turbulence production due to viscous forces, calculated as

$$P_{t,L}=\mu_t\,\nabla\vec{U}\bullet\left(\nabla\vec{U}+\nabla\vec{U}^T\right)-\frac{2}{3}\nabla\bullet\vec{U}\left(3\mu_t\nabla\bullet\vec{U}+\rho_L\kappa\right) \tag{57}$$

The dispersed (gas) phase turbulence is modelled using a zero equation model in which gas turbulent viscosity is proportional to liquid phase turbulent viscosity:

$$\mu_{t,G}=\frac{\rho_G}{\rho_L}\frac{\mu_{t,L}}{\sigma_{t,g}} \tag{58}$$

where $\sigma_{t,g}$ is a turbulent Prandtl number relating the dispersed phase kinematic eddy viscosity to the continuous phase kinematic eddy viscosity. In calculations, $\sigma_{t,g}$ was assumed to equal 1, the standard value used in the absence of detailed turbulent kinetic energy measurements.

The governing equation for transport of a conservative scalar quantity (tracer) in the continuous (liquid) phase is given as

$$\frac{\partial}{\partial t}\left(\phi_L C_T\right)+\nabla\bullet\left(\phi_L C_T \vec{U}_L\right)-\nabla\bullet\left[\phi_L\left(D_{T,L}+\frac{\nu_T}{Sc_T}\right)\nabla C_T\right] \tag{59}$$

where C_T is volumetric concentration of the tracer, $D_{T,L}$ is diffusivity of the tracer in the liquid phase and Sc_T is turbulent Schmidt number. Because there is no mass transfer of the tracer to the dispersed phase, there is no scalar transport equation for the dispersed phase.

Dirichlet inlet boundaries were specified for water (at the top) and air (at the bottom). A degassing boundary condition for the gas (no slip for the liquid phase, sink term for the gas phase) was specified at the top of the reactor. In the laboratory reactor the top of the reactor is a free surface and gas leaves the water at the free surface and flows through a sealed plenum and escapes the plenum at a port located in the center of the plenum top. Four pressure boundaries, located in the bottom of the column, make up the water discharge boundary. In the laboratory reactor, the region between the sparger and water discharge is packed with 7 mm glass beads. This volume is simulated in CFD

as a porous volume with transmissivity of 0.01 cm^2. The transmissivity was estimated using the Karman-Cozeny relation.

Simulations were started as steady state and results from steady simulations were used as initial conditions for transient simulations. It was found that the following initial conditions yielded a relatively fast (within 500 iterations) convergence to an rms (root mean square) residual of 1×10^{-4} for all variables:

- Uniform gas velocity equal to the predicted single bubble terminal rise velocity;
- Uniform downward liquid velocity equal to the water volumetric flow rate divided by the reactor cross sectional area.
- Small gas volume fraction, uniform throughout the reactor.

IV.2 Numerical Model

The governing equations described in the earlier sections were solved numerically for specified initial and boundary conditions with the commercial finite volume CFD package CFX (ANSYS Europe Ltd. 2004) on a 3-dimensional unstructured mesh. Mesh density was chosen based on a grid resolution study and generated to provide high resolution at column walls and near the diffuser.

To assess the grid resolution, gas volume fraction along the column diameter shown in Figure 31 was calculated at three mesh densities (coarse, medium and fine). In grid resolution studies, steady flow was assumed, the gas phase was monodisperse with a mean bubble diameter of 2.5 mm and a κ-ω turbulence model was employed. As

described below, steady flow is reasonable to assume when the bubble column is perfectly vertical. When a slight lean (< 0.5º from vertical) is included, the bubble plume is not steady in the center of the column and a transient simulation is required.

The coarse, medium and fine density grids had 140,000, 372,000 and 712,000 tetrahedral elements, respectively. In grid resolution studies the gas and liquid flow rates were 2 L/min and 6.6 L/min. Results from the grid resolution study are presented in Figure 32.

Because differences in the gas fraction profile were minor between the medium and fine meshes, the mesh used in the present study is a refinement of the medium density mesh. Prism elements were added to the medium mesh at the column walls and the grid was refined locally in the vicinity of the sparger, water intake and the top of the column (where water enters the column from the intake section). The resulting grid has a total of 470,000 tetrahedral and prismatic elements.

Figure 31: Diameter Along which Grid Resolution Study was Performed

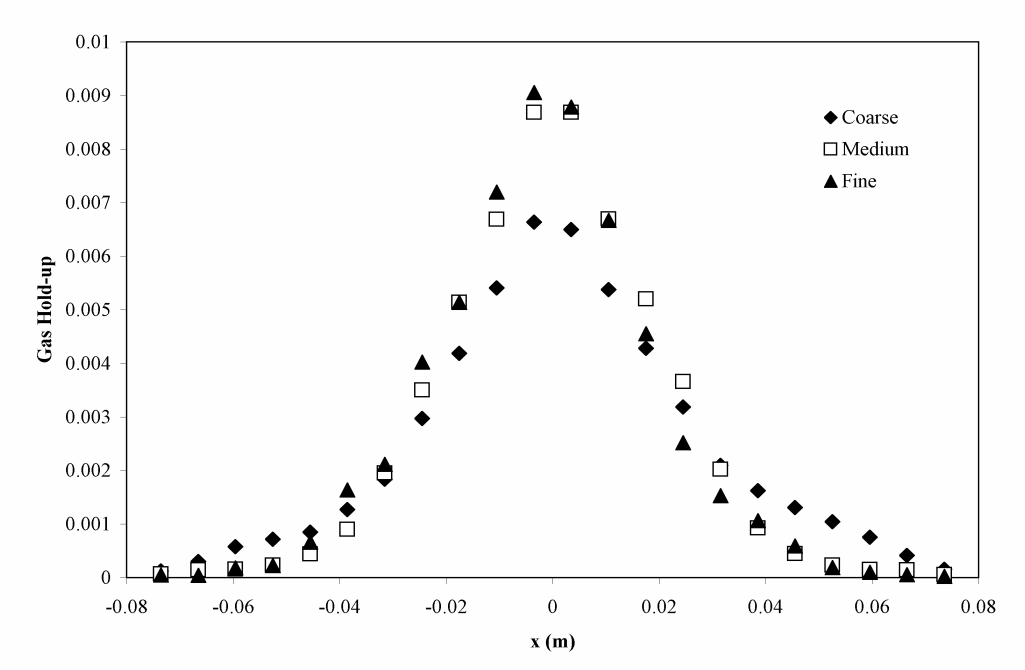

Figure 32: Gas Volume Fraction Profiles

A second-order upwind transient scheme with relatively small time steps (0.05 s) was required to achieve convergence to an RMS residual of 1×10^{-5} within 10 iterations per time step. To produce representative "quasi-steady" results, calculations were performed for approximately 10s of simulation time, after which variations in bubble plume shape became minor and bubble plume was seen to rotate in the column, though not with a fixed period.

IV.3 Model Validation

Based on the observations of Rice and Littlefield (1987) and observations in the laboratory, it was noted that minor misalignments of the column (of less than 0.5° off

vertical) or its components (e.g., sparger locations) can drastically change gas and liquid flow and mixing. Despite efforts at leveling the column, locating the diffuser in the column center and ensuring even flow through inlet and discharge ports, it was surmised that perfect alignment of the column was unlikely. So the CFD model included a slight (0.25°) vertical tilt. In the absence of this tilt, CFD predicted a perfectly symmetric bubble plume. When the tilt was included the plume exhibited the asymmetric plume rise observed in bubble column experiments. Specifically, the plume tended to migrate toward the column wall and spiral as it ascended.

The countercurrent flow model was validated using tracer data (described below). In the CFD model, a non-reactive, conservative tracer was introduced as a step feed in the liquid phase at time 0s and the concentration of the tracer at the reactor discharge was calculated at regular time intervals. The CFD model reactor discharge is shown in Figure 21. This study is referred to as a "virtual tracer study."

Gas flow rate and liquid flow rate for the virtual tracer study were 2 L/min and 6.6 L/min, respectively. A plot showing normalized experimental tracer concentration (F) and virtual tracer normalized concentration versus normalized time (t / t_H) is presented in Figure 33. The virtual tracer curve shown in Figure 33 is a plot of instantaneous tracer concentration, area-averaged at the reactor discharge. The definition of normalized tracer concentration is given in equation 37 (repeated below).

$$F = \frac{C_{Tracxer} - C_{Background}}{C_{Feed} - C_{Background}} \tag{37}$$

The CFD model reproduced measured residence time distribution data reasonably well, predicting a slightly earlier breakthrough than that experimentally observed and matching experimental data more closely at later times. In Figure 33, the CFD model (the solid line) shows greater variation than the experimental data (symbols). This is because the CFD model was "sampled" at 1 second intervals and via a point measurement, whereas the experimental tracer studies used samples taken at 15 second intervals and requiring approximately five seconds to draw. The agreement between observed and predicted RTDs is considered excellent given the complexity of the flow and the use of a two-equation turbulence model.

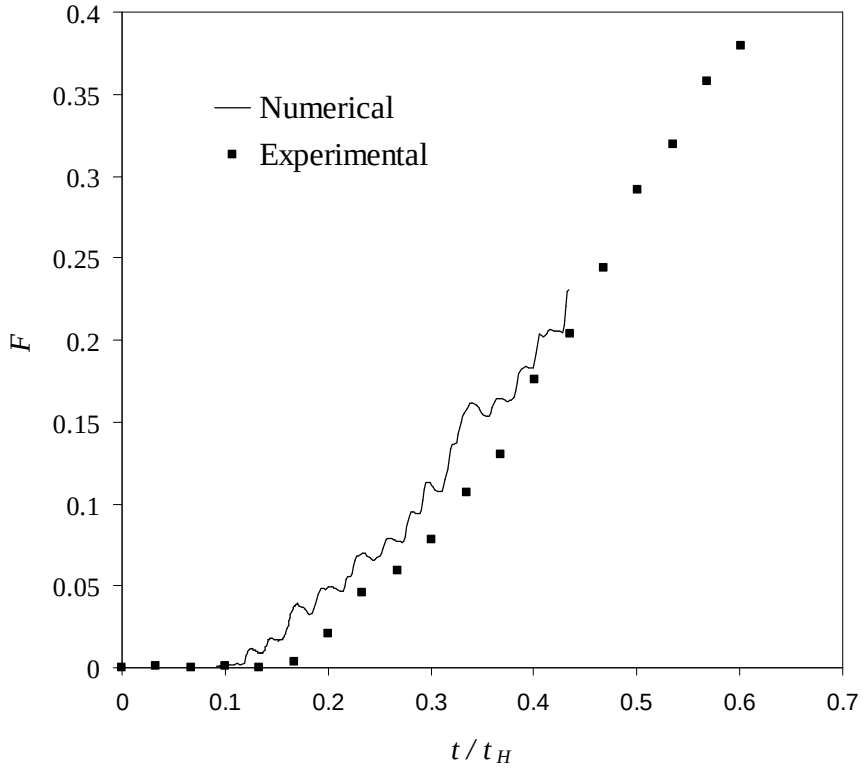

Figure 33: CFD Model Validation

V COUNTERCURRENT FLOW HYDRODYNAMICS INVESTIGATIONS

Experimental and numerical studies performed are summarized in Table 19. As described above, tracer studies entailed introduction of a step input of sodium chloride tracer at the reactor inlet and monitoring the conductivity of water at the reactor discharge. Conductivity is a linear function of salt concentration over the concentration range used in these studies. Tracer studies generated data for calculation of Peclet number and characterizing dispersion. Tracer studies were performed at a single liquid flow rate (6.6 L/min) and a range of gas flow rates chosen to span the ideal bubbly flow regime.

Table 19: Countercurrent Flow Hydrodynamics Experimental and Numerical Studies

Study	Liquid flow rate(s) (L/min)	Gas Flow Rate(s) (L/min)
Flow Visualization	6.6, 10.5, 13.5	0.4, 0.7
Experimental Tracer	6.6	0, 0.5, 1.0, 1.5, 2.0, 2.2, 2.4, 3.0, 3.5
CFD Studies	6.6, 13.5	0.4, 1.0, 1.5, 2.0, 2.5

In flow visualization studies, rather than a salt tracer, a non-reactive dye was introduced to the reactor as a step function. Flow visualization studies were performed at two gas flow rates (0.4 and 0.7 L/min) and liquid flow rates of 6.6, 9.0 and 12.0 L/min. Flow visualization studies showed phenomena related to early breakthrough of tracer.

V.1 Bubble Plume Behavior and Flow Visualization

As gas flow rate was increased, the behavior of the bubble plume changed significantly, though no increases in bubble break-up or collisions were observed. At a low gas flow rate (0.5 L/min) and a liquid flow rate of 6.6 L/min, the plume rises vertically and increases in diameter with height, as shown in Figure 34(a). Analysis of high-resolution digital images indicates bubbles range in shape from nearly spherical to oblate and bubbles tend to ascend in a spiral or zigzag path. At a higher gas flow rate (2.5 L/min), the bubble plume rotates while rising, tending to migrate away from the column centreline and toward the wall as shown in Figure 34(b). At some distance above the sparger (typically between 0.6 and 1 m), the plume expands to fill the entire column.

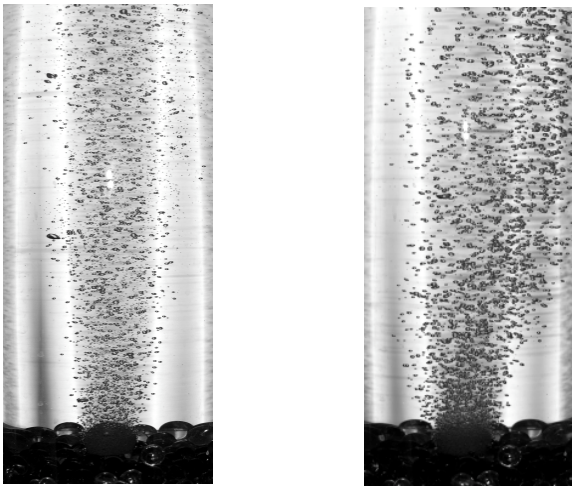

a) Low gas flow rate

b) High gas flow rate

Figure 34: Photographs of Bubble Plume Shapes

Flow visualization at a water flow rate of 6.6 L/min and a gas flow rate of 2.0 L/min is shown in Figure 3. The individual frames show the progress of the dye at 30 s, 1 min, 1 min 30 s and 2min after the start of dye injection. Digital image processing was used to remove variations in image color caused by uneven illumination. The black mark seen at approximately one third the reactor's height is the glass manufacturer's mark.

As with salt tracer studies, in flow visualization studies the reactor was operated at steady state for 4 theoretical hydraulic residence times prior to the introduction of the non-reactive dye (dilute solution of buffered sodium indigo trisulfonate) to the reactor. The dye was fed at a steady rate and concentration for 4 theoretical hydraulic residence times. The color (darkness) of the image is proportional to the concentration of the dye. The linear relationship between image color and dye concentration was ascertained through analysis of digital images of the reactor filled with uniform solution of dye at 7 dilutions as described in section 0.

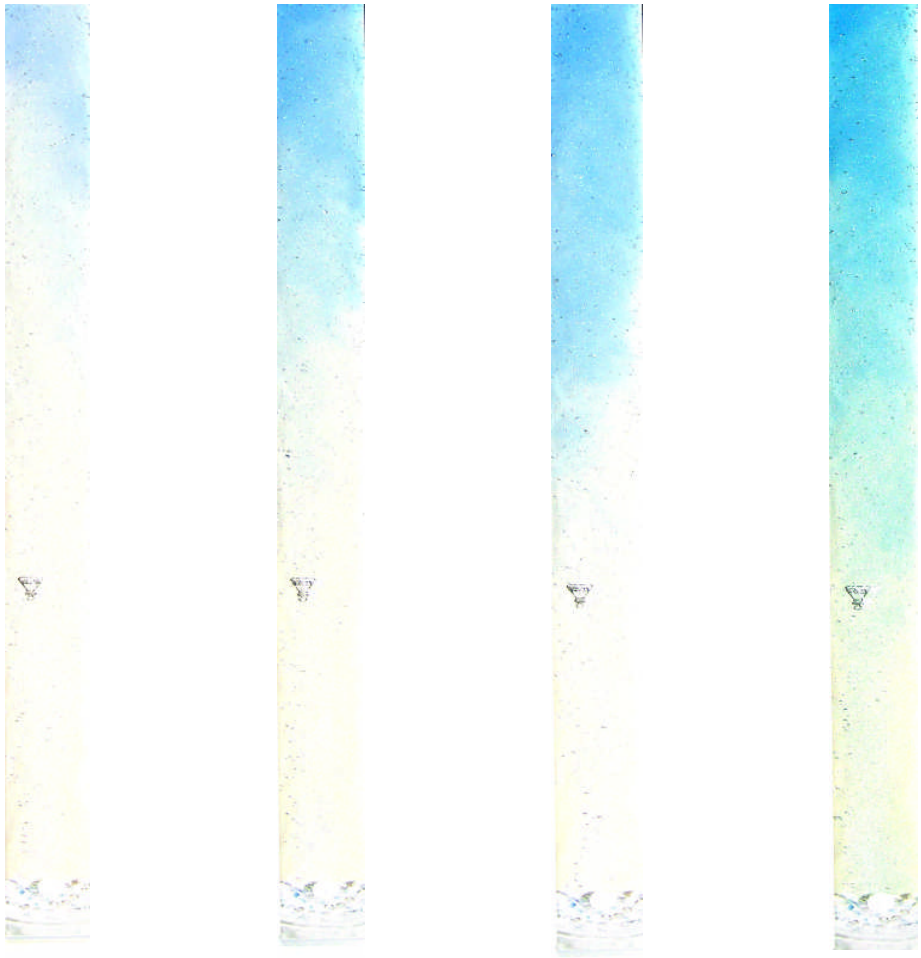

(a) 30 s (b) 1 min (c) 1 min 30 s (d) 2 min

Figure 35: Flow Visualization – Dye Progress at 30s, 1 min, 1 min 30s and 2 min (the Dark Triangle Approximately 1/3 the Reactor Height in Each Image is the Glass Maker's Manufacturer's Mark)

The liquid phase does not exhibit plug flow behavior; dye proceeds unevenly in the column, tending to flow faster near the column wall. Preferential flow of the dye near the column wall is seen in frames (a) – (c). As the dye plume proceeds down the column,

dye is entrained into the bubble plume (in the center of the column) and back-mixes with the down-flowing stream. This is seen in Figure 35(d). In that frame the front of the dye plume is better mixed than in the prior 3 frames. Based on these observations, one can expect early tracer breakthrough (due to the rapid progress of the dye near the column wall), and a long tail on the residence time distribution arising from back-mixing of the tracer into the bubble plume.

V.2 Residence Time Distribution Analysis

Experimental "*F*" curves corresponding to a liquid flow rate of 6.6 L/min and gas flow rates ranging from 0 to 3 L/min are presented in Figure 36. The parameters θ and F are the normalized time (t / t_H) and the normalized concentration, defined above in equation 37.

The early portions of the *F* curves in Figure 36 indicate that increased gas flow rates promote earlier breakthrough. This is due, in part, to upward flow of liquid phase in the bubble plume ("gulfstreaming") and reduction of the effective column cross sectional area through which downward-flowing liquid passes. Because the late portions of the *F* curves approach the value 1.0 very slowly, it is clear there is significant hold-back or back-mixing of the tracer in the reactor. This is likely due to entrainment of the tracer into the bubble plume and transport of the tracer upward in the reactor.

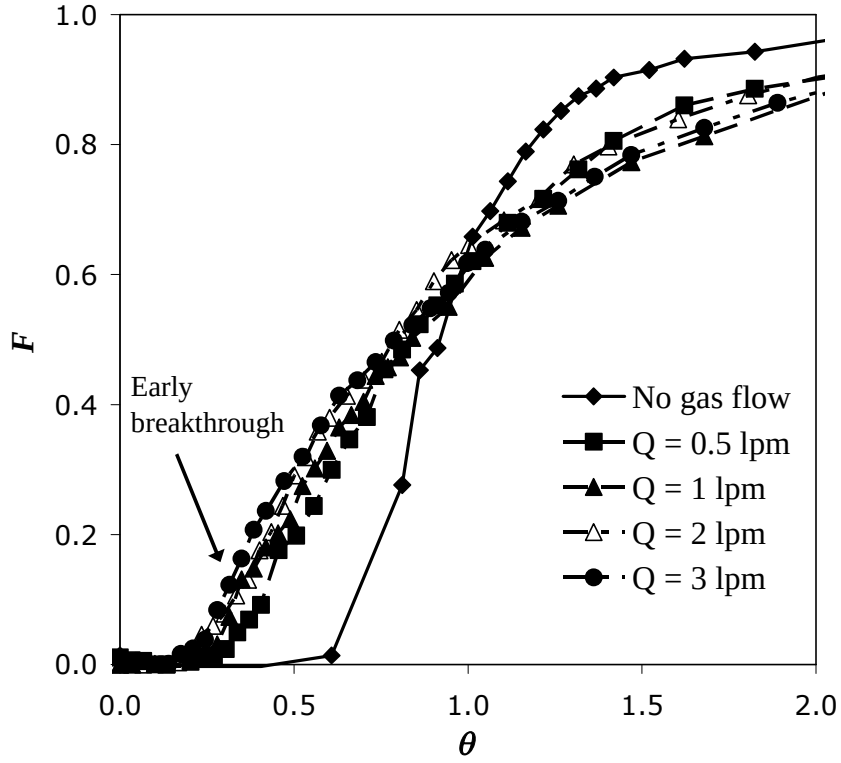

Figure 36: Experimental Residence Time Distributions (RTDs) for $0 < Q_g < 3$ L/min

As described above, nonlinear regression was used to fit candidate residence time distribution models to the experimentally measured residence distribution curves. The gamma function (an approximation to the solution of the transient *N*-CSTRs in series model) and the inverse Gaussian function (an approximation to the solution of the axial dispersion model) were fit to the data by varying their model parameters. Since both models have two parameters, the best fit model was the model yielding the lowest sum of squares of errors between the model prediction and the experimental data. For all gas

flow rates the inverse Gaussian model provided the best fit to experimental data.

Peclet number, in environmental engineering applications, is defined in equation 53 (repeated below) (Weber 2001)

$$P_e = R_e S_{c,t} = \frac{U_L H}{E_L}$$

where R_e is Reynolds number, $S_{c,t}$ is turbulent Schmidt number, U_L is liquid phase superficial velocity, H is reactor height and E_L is turbulent dispersion. Peclet number was calculated from the variance of the inverse Gaussian distribution fitted to the tracer data using equation 4 (repeated below)

$$\nu = 2P_e^{-1} - 2P_e^{-2}\left(1 - e^{-P_e}\right) \tag{60}$$

where ν is the dimensionless variance ratio.

Experimental relations found in the literature for Peclet number in countercurrent bubble columns are presented in Table 20. With the exception of that of Baird and Rice, all the relations presented in Table 20 were developed based residence time distribution analysis of tracer. Baird and Rice developed their relation using analysis of images captured on video cassette. In their work, they followed the mixing of two solutions of different pH by tracking the front of a pH sensitive dye.

Table 20: Countercurrent Flow Peclet Number Relations

Relation	Study
$E_L \propto \frac{u_g^2 d_c}{v_b}$	Bischoff and Phillips (1966)[a]
$P_e = \frac{\left(2u_G + v_b\right) d_c}{E_L} = 3.0 \pm 0.3$	Reith et al. (1968)[b]
$P_e = \frac{u_G H}{0.35\left(u_G\, g\right)^{1/3} d_C^{4/3}}$	Baird and Rice (1975)[c]
$P_e^{-1} = \frac{4.88}{H}\left[0.00185 + 9.7 \frac{u_G^{1/2}}{u_L^{5/3}}\left(\frac{\nu_L}{d_b}\right)^{7/6}\right]$	(Kim et al., 2002a)[d]

[a] Based on analysis of data from numerous small diameter cocorruent, countercurrent and nonflowing liquid phase bubble columns. Only valid in the ideal bubbly flow regime.
[b] Based on experimental data taken in 5 cm and 14 cm cocurrent and countercurrent bubble columns in which air was sparged into tap water. The term $2u_g + v_b$ is the relative velocity between phases.
[c] Developed using dispersion data collected from several studies and under the assumption of isotropic turbulence and turbulent energy dissipation rate equal to ($u_g\, g$).
[d] Developed for co- and countercurrent flow in a 15 cm circular bubble column. Units of H is in m and all other units must be dimensionally consistent.

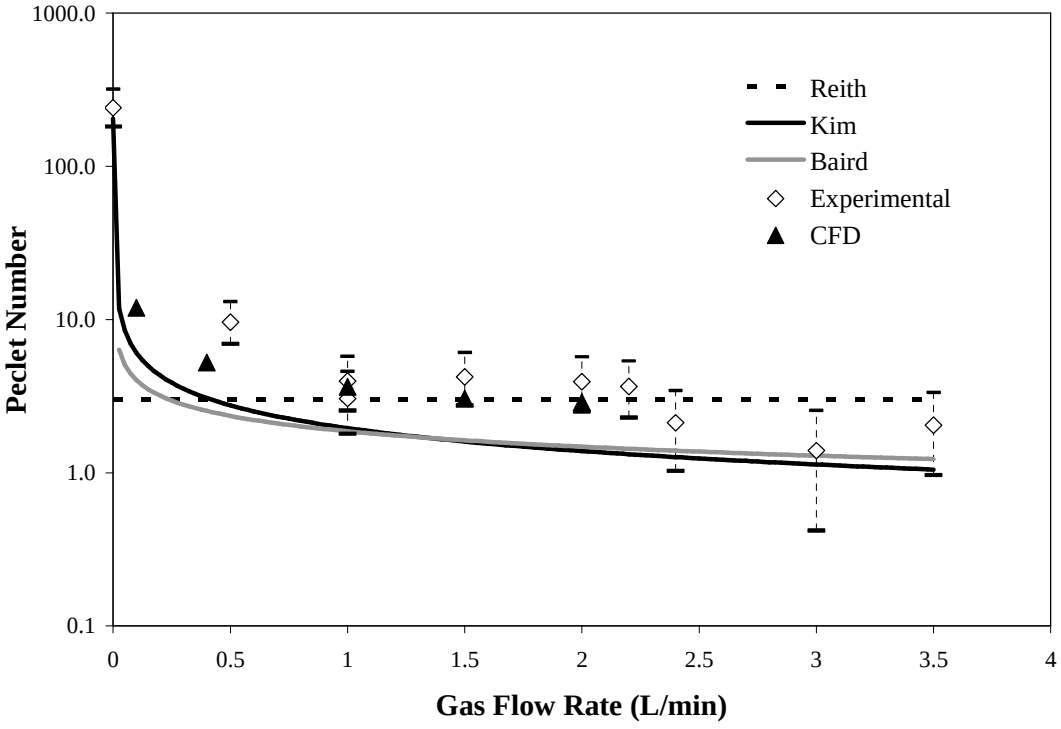

Figure 37: Experimental and Predicted Peclet Number

Figure 37 shows Peclet number calculated from experimental data (as described above) plotted along with Peclet number estimates from relations for countercurrent bubble column Peclet number found in the literature and with estimates made using CFD calculations. The experimental estimates of Peclet number are shown with a 90% confidence interval. To estimate Peclet number from CFD calculations, the volume averaged specific turbulence energy dissipation rate, $\bar{\varepsilon}$, was calculated for each gas flow rate and used in the expression proposed by Baird and Rice (1975) to calculate axial

dispersion

$$E_L = 0.35 d_c^{4/3} \bar{\varepsilon}^{1/3} \quad (62)$$

The corresponding Peclet number was calculated using equation 53. Note that although the parameter E_L is usually called "axially dispersion" in environmental and chemical engineering literature, the dispersion in the reactor is not uniform in the axial direction and the term E_L would be more aptly referred to as the average turbulent dispersion.

Peclet number falls sharply as gas flow increases from 0 to 0.5 L/min, is relatively constant (around 3.0) for moderate gas flow rate and falls as gas flow rate increases above 2 L/min. The Kim expression (listed in Table 20) fits experimental data well at low and high gas flow rates. Reith estimate (listed in Table 20) fits the data at moderate gas flow rate. Baird and Rice's approximation to equation 31 ($\varepsilon = U_G d_c$) consistently underpredicts Peclet number.

CFD estimates for Peclet number offer the best match to experimental data, falling within a 90% confidence interval around experimental values at intermediate gas flow rates. Like experimental values, CFD estimate of Peclet number does not vary significantly at intermediate gas flow rates. This agreement indicates that the CFD model accounts for the important hydrodynamics in this regime.

Summarizing experimental observations, RTD analyses indicate three flow regimes encountered over the range of gas flows. At low gas flow rate (1 L/min and below) there is very little backmixing and the Peclet number falls sharply with increasing gas flow

rate. At intermediate gas flow rates (1.5 L/min $\leq Q_{gas} \leq$ 2.5 L/min), the Peclet number is relatively constant. In this regime the bubble plume rises asymmetrically in the column and rotates as a function of time near the sparger. At high gas flow rates Peclet number falls slightly and backmixing increases significantly. Churn turbulent behaviour (significant bubble break-up and coalescence) was not observed during any experiment.

V.3 Numerical Studies

Numerical studies were performed to develop a detailed understanding of the mixing phenomena and trends identified in experimental studies. Specifically, details were sought on the variation in mixing over the axial extent of the reactor. Transient simulations, summarized in Table 19, were performed at a liquid flow rate of 6.6 L/min and gas flow rates ranging from 0.4 to 2.0 L/min. These cases were used to estimate Peclet number (shown in Figure 37) and to generate velocity vector diagrams for exploration of the changes in flowfield that occur with increasing gas flow rate.

A “virtual tracer study” was also performed in which the step feed and passage of a conservative tracer through the reactor was simulated. Gas and liquid flow rates for the virtual tracer study were 2.0 L/min and 6.6 L/min, respectively. Figure 38 shows contours of virtual tracer concentration at 20, 40 and 60 s after introduction of the tracer. Red indicates the tracer concentration is equal to the feed concentration and blue indicates zero tracer concentration. The images in Figure 38 compare favorably with the experimental flow visualization images found in Figure 35. As seen in experiments, the CFD model predicts that the tracer projects downward into the reactor along the reactor

sides, swirling as it progresses.

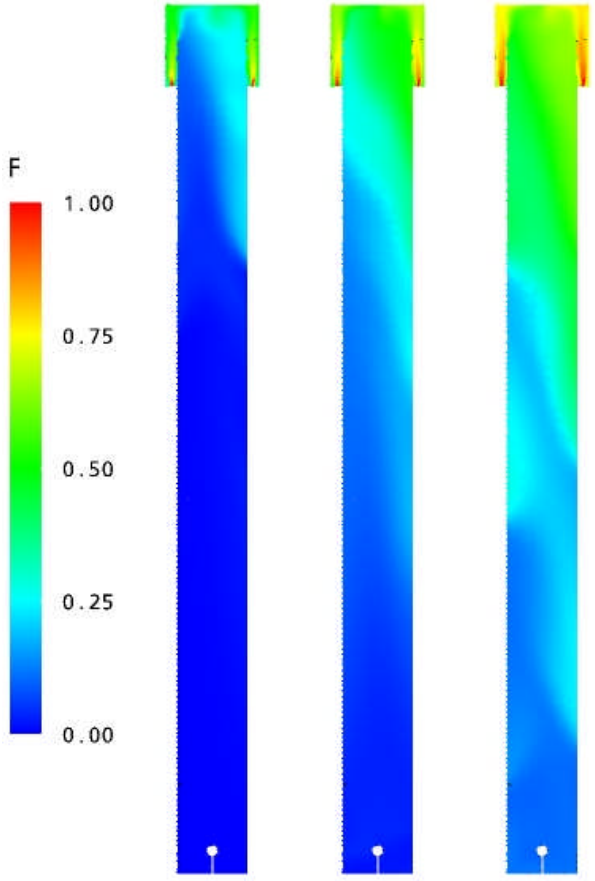

Figure 38: Virtual Tracer Concentration at 20s, 40s and 60s after Step Input

Contours of gas volume fraction, ϕ_g, predicted at a gas flow rate of 2 L/min are shown in Figure 39(a). The plume does not rise symmetrically, but migrates in the column and finally migrates to the wall near the top of the column. The plume region, shown in Figure 39 (b) is defined as the region within which the liquid phase velocity is

upward. The surface shown in Figure 39 (b) is an isosurface where liquid vertical velocity, w_L, is equal to zero. Note that there is upflow of liquid in the bubble plume over the entire reactor height and that the plume twists as it rises in the column. These figures illustrate non-axisymmetric plume rise and significantly different plume shape near the sparger compared with higher locations. In drinking water treatment, non-asymmetric flow as illustrated in Figure 39 creates the potential for short-circuiting of raw water and retards ozone mass transfer via poor mixing in the bubble plume and reduced contact of bubbles with raw water. The uneven distribution of the phases seen in Figure 39 provide an explanation for the great difference prior researchers have noted in Peclet number for perfectly vertical columns and slightly tilted columns. The slight column misalignment introduced into CFD calculations causes the bubble plume to migrate toward the wall and contributes to the non-uniform distribution of phases.

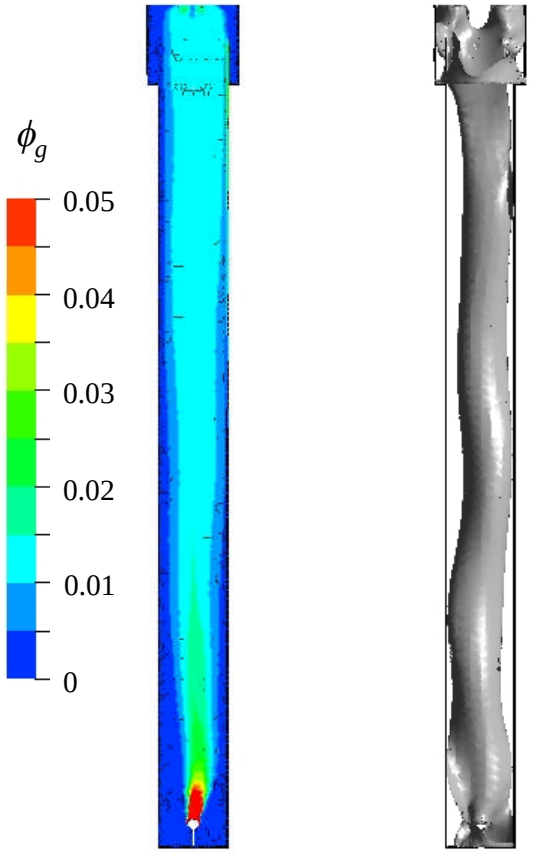

(a) Gas volume fraction (b) Plume shape

Figure 39: Phase Distribution

Liquid superficial velocity vectors in the near-sparger region (the bottom 75 cm of the reactor) at 4 gas flow rates are shown in Figure 40. At low gas flow rate (Q_G = 0.4 L/min) large recirculation regions appear on alternate sides of the plume, causing the plume to rise in a wavy path. When gas flow rate is increased to 1.0 L/min, the bubble plume diameter increases, squeezing the recirculation regions and resulting in faster

down-flow of liquid near the column wall. Increasing gas flow rate to 1.5 L/min further increases the velocity of the down-flowing liquid near the column wall. At a gas flow rate of 2.0 L/min, distinct recirculating regions similar to those seen at a gas flow rate of 0.5 L/min appear, though somewhat smaller and with greater rotational speed.

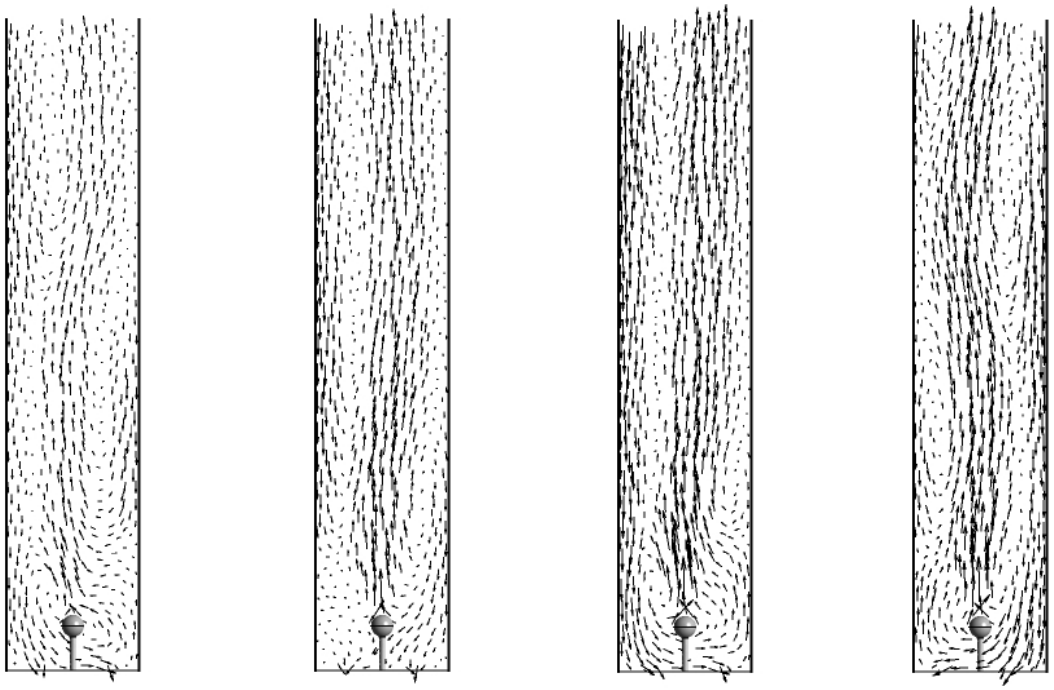

(a) Q_G = 0.4 L/min (b) Q_G = 1.0 L/min (c) Q_G = 1.5 L/min (d) Q_G = 2.0 L/min

Figure 40: Water Velocity Vectors near the Diffuser

The recirculating regions seen in Figure 40 explain the asymmetric plume rise observed during laboratory experiments – these large structures, once established, deflect the bubble plume. These recirculation regions differ from those typically found in bubble column reactors with non-flowing liquid phase. In countercurrent flow, the large scale

flow structures move downward with the liquid flow, tending to swirl around the reactor as they proceed. As these fluid structures progress, the bubble plume is deflected, resulting in a chaotic bubble plume motion. The shapes and locations of large fluid structures are strongly dependent on reactor geometry and the interaction between downflowing liquid and bubble plume is also expected to be influenced by reactor geometry. The boundary between the bubble plume and down-flowing liquid and the preferential flow path for liquid are clearly seen in Figure 40. This segregation between the phases is an impediment to mass transfer and provides a "Short-circuit" by which some of the liquid phase passes quickly out of the reactor. In disinfection, this short circuiting provides a path for pathogenic organisms to elude treatment.

Axial variation in mixing in the column is shown in Figure 41. Neglecting large-scale fluid motion, local mixing intensity is approximately proportional to the square root of the rate of turbulent energy dissipation (Droste 1997). Figure 41(a) shows contours of turbulent kinetic energy dissipation on a column midplane and Figure 41(b) is a plot of mean dissipation as a function of axial location. Average turbulent dissipation, $\overline{\dot{P}}_k$, at axial location *k*, is calculated by:

$$\overline{\dot{P}}_k = \frac{\sum_{i=1}^{\#\text{elemnts}} \left(\phi_g\right)_{i,k} \left(\dot{P}\right)_{i,k} A_{i,k}}{\sum_{i=1} \left(\phi_g\right)_{i,k} A_{i,k}} \tag{63}$$

where $A_{i,k}$ is area of element *i* at axial location *k.* Mixing is non-uniform both axially and radially. Mixing is highest near the sparger (z < 0.5 m) and uniform in the rest of the column, except near the top where entrance effects dominate the flow. Mixing intensity is

high inside the bubble plume; poorly mixed regions are observed outside the bubble plume. These results provide an explanation for early breakthrough of tracer at high gas flow rates (seen in Figure 36) – the flow field is partitioned into a well-mixed portion rising in the bubble plume and a poorly mixed stream flowing downward.

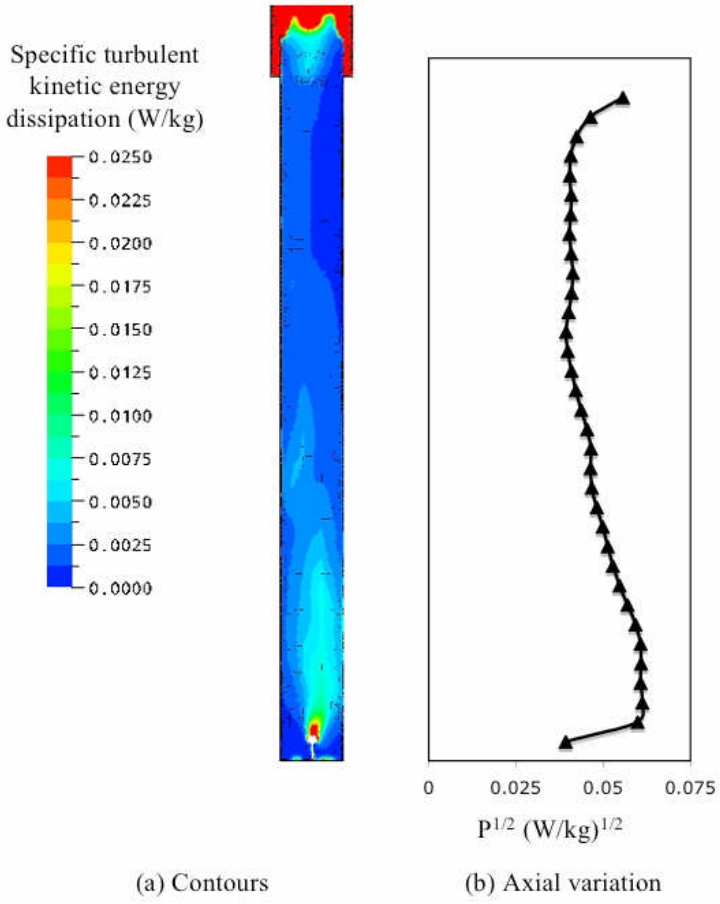

Figure 41: Spatial Variations in Mixing

The observed variations in mixing along the axial extent of the reactor have mass transfer implications. Near the sparger, though mixing in the bubble plume is intense, liquid is rising in the bubble plume and has relatively high dissolved gas concentration; the concentration gradient is low and mass transfer rate is low, despite intense mixing. Away from the sparger mixing is uniform and the bubble plume is distributed more evenly in the column. Based on these observations, local mass transfer rate near the sparger is expected to be different from that away from the sparger. Currently, most bubble column designs are based on an assumption that mass transfer is relatively uniform in the reactor.

V.4 Influences of Inlet and Discharge Configurations

Most often in industrial and pilot scale ozone bubble contactors, liquid does not enter the reactor opposing gas flow. Rather, it flows into the pilot reactor or chamber of a full scale reactor perpendicular to the gas rise direction, as illustrated in Figure 42, a schematic diagram of a full-scale ozonation reactor in current use in the Netherlands (Smeets et al., 2006). Inlet hydrodynamics can exert a strong influence on the behavior of the bubble plume(s) and the degree of mixing in the reactor. For example, for the configuration shown in Figure 42, the cross-flowing water entering the dissolution chamber is expected to deflect the bubble plume top toward the baffle wall and to generate a large circulation in the dissolution chamber.

The impact of inlet and discharge configuration on the flow field in a countercurrent flow bubble column was investigated via CFD modeling of a pilot scale

ozone bubble column reactor operated by the Philadelphia Water Department (Charlton 2003). The Philadelphia Water Department evaluated ozone disinfection as an alternative to chlorine for improved inactivation of *Cryptosporidium parvum* and reduced formation of disinfection by-products (DBPs). The pilot study indicated that bromide concentrations observed in Schuylkill River water gave rise to unacceptable bromate concentrations when treated with ozone and alternative means for DBP control were adopted.

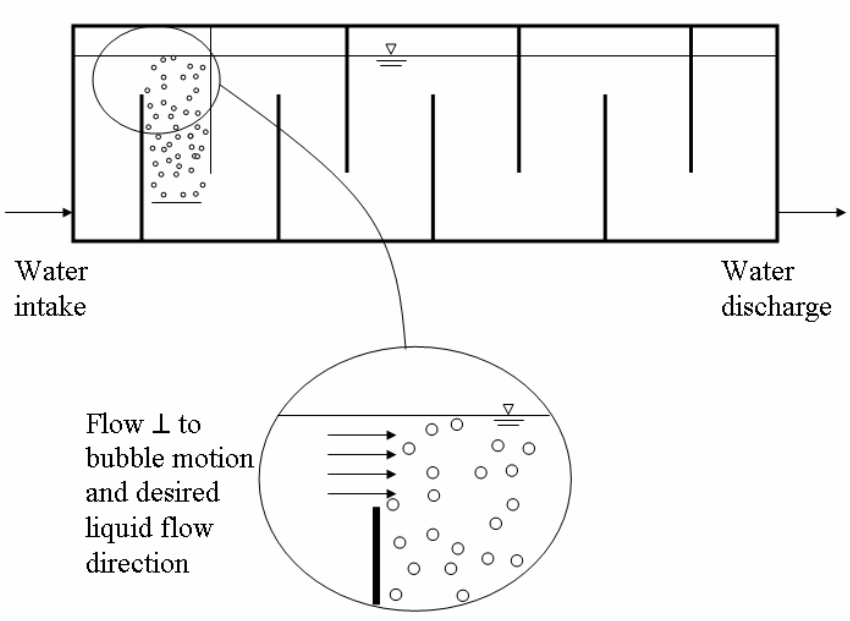

Figure 42: Typical Intake Configuration for Countercurrent Full Scale Ozonation

V.4.1 Philadelphia Water Department Pilot Disinfection Unit

The PWD pilot disinfection operation was comprised of 9 right circular cylindrical reactors, each 15.2 cm (6 inches) in diameter arranged in series. Each column was plumbed to allow operation in either cocurrent or countercurrent mode. Air or ozonated air could be introduced into any of the first 4 columns in the pilot plant. Air or ozonated air was sparged into the bottom of bubbled columns via a distributor plate. Flow entered and was discharged from the columns via 6.4 cm (2.5 in) pipes, as seen in Figure 43. In Co-current flow mode, the water entered the column perpendicular to the column centerline approximately 10 cm above the sparger and exited the column approximately 10 cm below the water surface. In countercurrent flow, the water entered the reactor at the top and exited at the bottom.

Results of CFD analysis of the PWD pilot reactor are presented in Figure 43 - Figure 45. In Figure 43, color contour plots of the gas volume fraction are shown for a plane that passes through the reactor centerline. The water and gas flow rates for this simulation were 37 L/min and 3.5 L/min. The CFD model of the first bubble column in the PWD pilot reactor employed a mesh of 208,044 tetrahedral elements, with mesh clustering near the intake and discharge ports, uniform bubble diameter of 2 mm and specified medium turbulence intensity at the reactor water intake. All other model components were the same as those described for the laboratory reactor model.

The inlet and discharge configurations result in deflection of the bubble plume toward the discharge (at the reactor bottom) and away from the intake (at the top of the

reactor). At the intake and discharge the distribution of phases is much less uniform than in the middle of the reactor. This poor distribution of phases results in lower mass transfer than is the phases were more evenly distributed, despite relatively energetic gas phase. Velocity vectors showing superficial liquid velocity near the reactor intake and discharge are plotted in Figure 44. A large vortex is present in the reactor in the portion of the reactor opposite the discharge port. This vortex results in significant back-mixing of the liquid phase and high dispersion, even though the phases are poorly distributed. The water intake configuration promotes a strong flow of liquid along the column wall directly opposite the intake.

Results of a virtual tracer study of the PWD pilot reactor operated in countercurrent mode are presented in Figure 45. As expected based on the velocity vectors plotted in Figure 44, the tracer flows quickly down the reactor wall opposite the intake and discharge side until the tracer front reaches the large vortex in the bottom of the reactor. In the bottom of the reactor, the vigorous back-mixing results in a region of uniform tracer concentration, despite poor distribution of phases.

The importance of inlet and discharge configuration in determining the residence time distribution and hydrodynamics of bubble column contactors is not unique to tall, cylindrical columns such as those used by the Philadelphia Water Department – Ta and Hague (2004) found that inlet and discharge configurations were the dominant factor in the flow field for a right rectangular cylindrical bubble contactor with the inlet transverse to the flow direction and with a much lower aspect ratio than the Philadelphia Water

Department contactor. Since full scale reactors typically employ inlets and discharges perpendicular to the flow direction, care should be taken in accounting for inlet and discharge hydrodynamics in scaling from pilot to full scale.

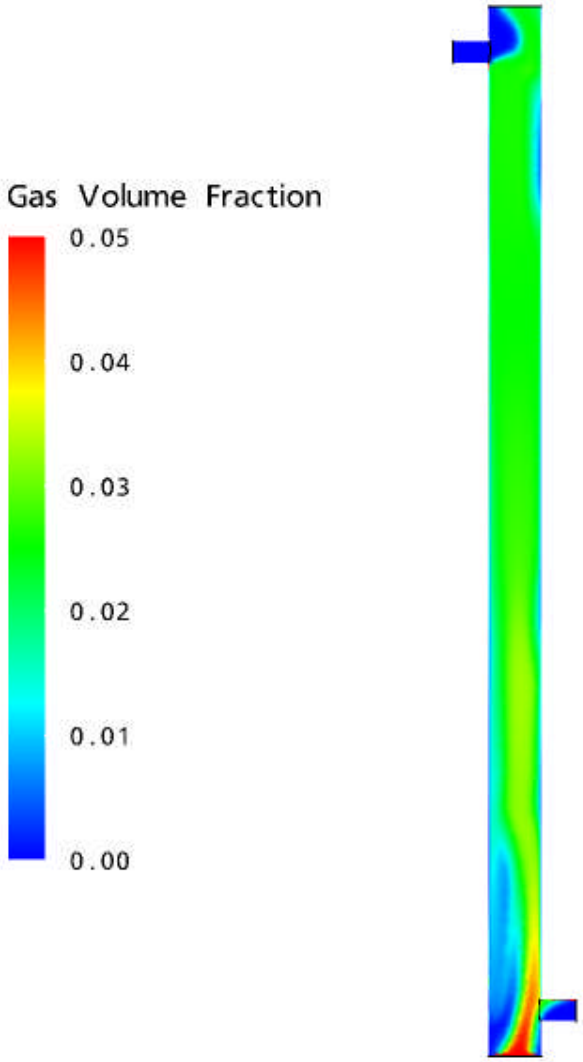

Figure 43: Philadelphia Water Department Pilot Column Phase Distribution

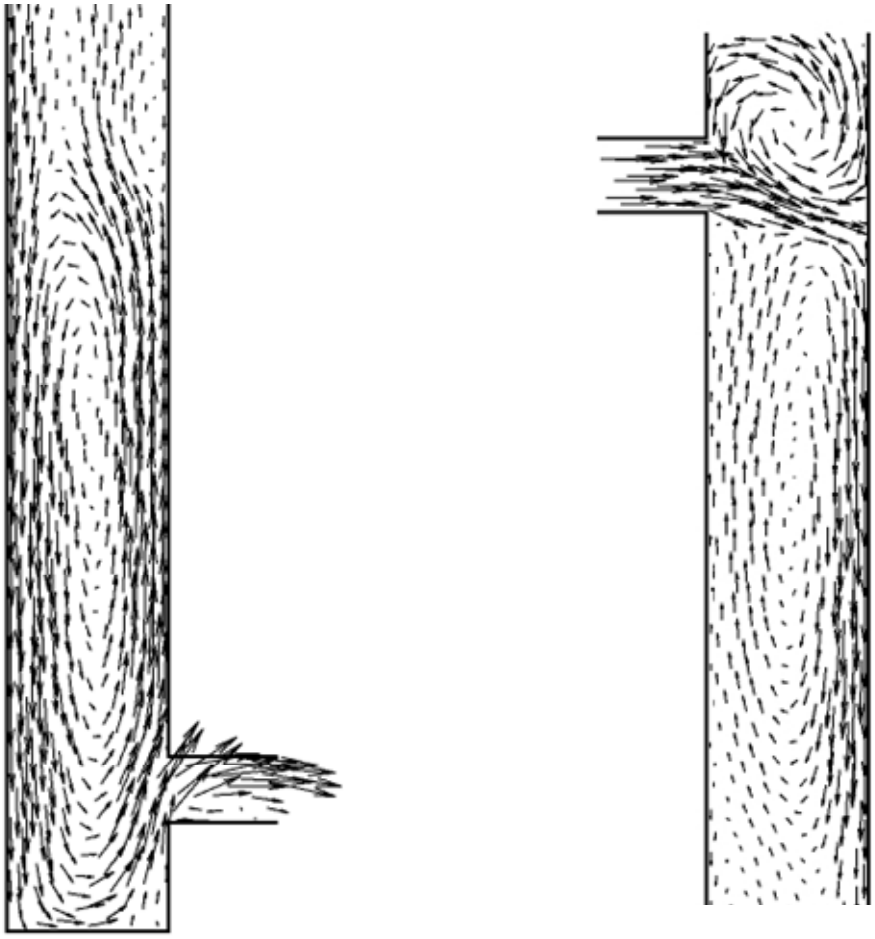

(a) Reactor Discharge Region (a) Reactor Intake Region

Figure 44: PWD Pilot Reactor Intake and Discharge Region Velocity Vectors

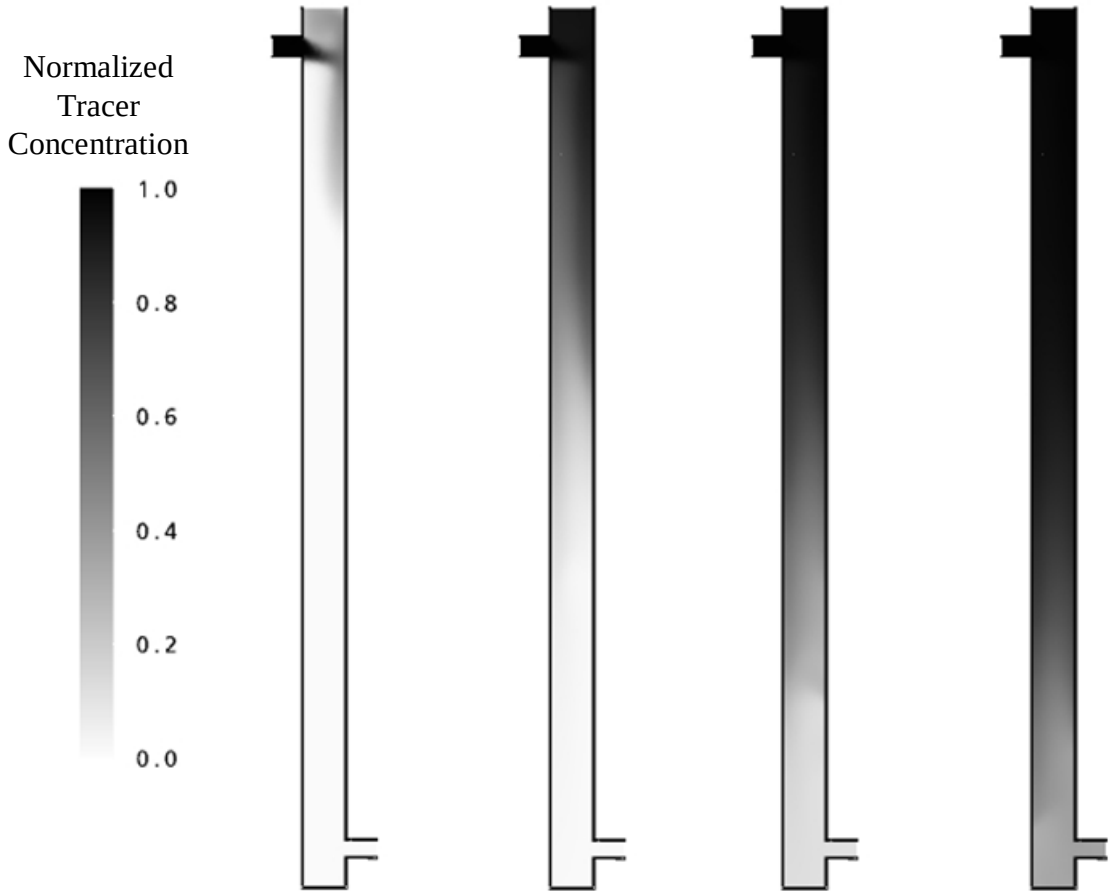

Figure 45: PWD Virtual Tracer Study

VI MASS TRANSFER STUDIES

Flow visualization and computational fluid dynamic studies were performed of mass transfer in the laboratory bubble column reactor. These studies allowed quantification of spatial variations in mass transfer in a simple cylindrical bubble column reactor. The studies also demonstrated that, without a priori knowledge of mass transfer coefficient and without calibration, a computational fluid dynamic model can be used to predict phase distribution and mass transfer in countercurrent bubble column flow. Thus CFD should be considered more reliable than currently-used models for scale-up of bubble column reactors from pilot scale to full scale.

In this chapter, results from the ozone mass transfer visualization technique described above are presented and a qualitative description of countercurrent hydrodynamics and mass transfer in a cylindrical column is provided. Processed images of indigo dye are then used for estimation of mass transfer rate, dispersion and entrance region length for the bubble column operating at three liquid flow rates and two gas flow rates. Images of indigo dye are compared with images generated using CFD and CFD is compared to other countercurrent flow models. Finally, the impact of choice of mass transfer submodel in a CFD model is quantified.

VI.1 Matrix of Mass Transfer Studies

Mass transfer visualization experiments were conducted at three gas flow rates and three liquid flow rates. In all but one experiment, ozone generator voltage was chosen to provide a wide variation in indigo dye concentration in the reactor while

ensuring the indigo was not decolored anywhere in the reactor. In the single experiment conducted at the highest gas flow rate, the indigo dye was decolored above the bottom of the reactor. Though the images taken of that case could not be used in the estimation of mass transfer rate or mixing, they did allow visualization of entrainment of indigo dye into the bubble plume.

The mass transfer visualization experiments conducted are summarized in Table 21. Experiments run at the same gas and liquid flow rates are designated case A and case B. The range of gas to liquid flow ratios used in experiments are typical of those used in prior pilot studies and in full scale facilities (Mariñas et al., 1993; Owens et al., 2000).

Table 21: Mass Transfer Visualization Experiments

Tap water flow rate (lpm)	Indigo stock flow rate (lpm)	Net liquid flow rate, Q_L (lpm)	Gas flow rate, Q_G, (slpm)	Q_G / Q_L	Case	Ozone generator voltage	Discharge water temperature (°C)
6	1	7	0.4	0.057	A	60	22
6	1	7	0.4	0.057	B	65	16
9	1.5	10.5	0.4	0.038	A	60	20
9	1.5	10.5	0.4	0.038	B	65	12
12	1.5	13.5	0.4	0.030	A	65	9
12	1.5	13.5	0.4	0.030	B	70	4.5
6	1	7	0.7	0.100		65	17
9	1.5	10.5	0.7	0.067		65	20
12	1.5	13.5	0.7	0.052		70	20
9	1.5	10.5	0.9	0.087		70	22

VI.2 Ozone Mass Transfer Visualization Results

The indigo dye ozone mass transfer visualization technique allowed qualitative and quantitative observations of the mass transfer process. In this section, images from the mass transfer visualization technique are presented and the hydrodynamics of mass transfer are described. Next, estimates of Peclet number and Stanton number are made using radially-averaged indigo dye color data and the variation in these parameters with column gas to liquid flow ratio is documented.

VI.2.1 Observations

The indigo dye mass transfer visualization technique yielded vivid images that allowed direct observation of mixing and mass transfer in the laboratory reactor. As described above, the influent indigo dye concentration and gas phase ozone concentration were chosen to provide the widest possible variation in indigo dye color between the reactor top and bottom but to ensure indigo dye was present in the reactor discharge.

Images showing indigo dye decoloration at gas to liquid flow rates of 0.06 and 0.03 are presented in Figure 46. The only processing performed on the two images in Figure 46 was elimination of background variations in lighting. The light triangular mark approximately 1/3 of the axial distance between the reactor bottom and top is the manufacturer's mark (physically present on the laboratory reactor wall). The sparger and glass bead packing appear white in the images because there was no difference in color between the indigo dye image and the background image from which it was subtracted.

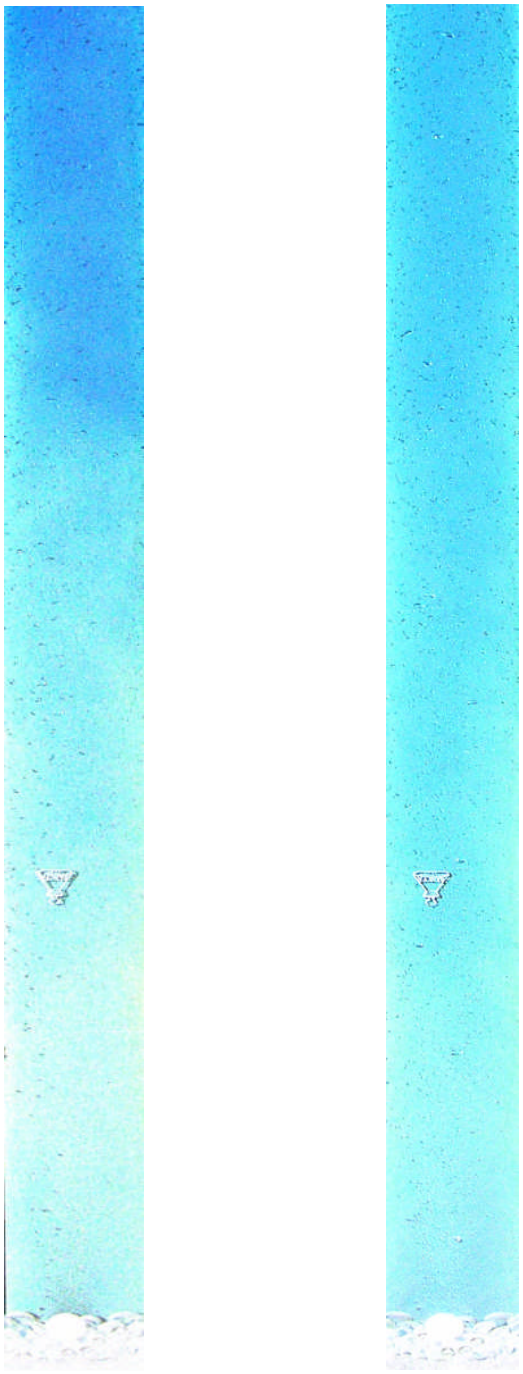

(a) Q_g/Q_L= 0.06 (b) Q_g/Q_L= 0.03

Figure 46: Indigo Dye Decoloration Images

Both of the images shown in Figure 46 were taken while ozone was being fed to the reactor and after the reactor reached quasi-steady state (as described in Chapter III). Image (a) was taken at gas and liquid flow rates of 0.4 slpm and 7.0 lpm (gas to liquid flow rate of 0.06), ozone generator voltage of 65 V and indigo dye inlet concentration of 5.5 mg/L. Image (b) was taken at gas and liquid flow rates of 0.4 slpm and 13.5 lpm (gas to liquid flow ratio of 0.03), ozone generator voltage of 65 V and indigo dye inlet concentration of 4.3 mg/L.

There are significant differences in the pattern of indigo dye decoloration observed in Figure 46 (a) and Figure 46 (b). At high gas to liquid flow rate (Figure 46 (a)), there is a relatively sharp decline in indigo dye concentration near the top of the reactor. Asymmetric flow of the indigo dye downward can be observed at the top of the reactor and slightly below the manufacturer's mark. Large swirls of dye (length scale on the order of the column diameter) are observed throughout the reactor, particularly in the bottom half of the reactor. At high gas-to-liquid flow ratios, in the bottom half of the reactor, dye projected downward along the column wall and large eddies of dye-rich liquid were entrained into the bubble plume, decoloring rapidly after entrainment. At a low gas to liquid flow ratio (Figure 46 (b)), the decoloration of indigo dye is more uniform in the liquid flow direction than at the high gas to liquid flow ratio.

In both images, the concentration of indigo dye appears to increase at the very bottom of the reactor. This increase is more pronounced in the high gas-to-liquid flow ratio and was observed in most of the images obtained during mass transfer visualization

experiments. It is hypothesized that this increase is a result of the entrainment of indigo dye-rich liquid outside the bubble plume into the large recirculating regions near the sparger shown in Figure 40.

The progress of dye-rich eddies downward is shown more clearly in Figure 47. In that figure, images 1 and 2 were both taken at quasi-steady state, approximately 20 seconds apart. Images were converted to grayscale and contrast was enhanced to accentuate the indigo dye color. For the images in Figure 47, gas and liquid flow rates were 0.9 slpm and 10.5 lpm, respectively, the ozone generator was operated at a voltage of 70 V, and indigo dye intake concentration was 5.5 mg/L. These operating conditions resulted in near complete discolorization of the indigo dye upstream of the discharge. Complete discolorization produced images that show flow details very well.

Large eddies with high indigo dye concentration and with length scale on the order of column diameter appear to flow downward outside the bubble plume core, spiraling around the reactor as they proceed. As they descend these eddies are entrained into the bubble plume and decolored rapidly. The images in Figure 47 indicate two important mixing length scales: mass transfer from bubbles to liquid depends upon mixing on the length scale of the order of the bubble diameter. Transport of “fresh” liquid to the bubble plume from the bulk liquid phase depends on mixing on the length scale of the column diameter. Figure 47 also indicates that even within the dispersed bubble flow regime, discharge indigo dye concentration is unsteady, because the transport of the large indigo-rich eddies is a time dependent random process. This

observation is constituent with measurements of effluent ozone concentration in full-scale ozone fine bubble contactors (Schulz and Bellamy 2000) and should be considered when evaluating sample ozone residual concentration data for making *Ct* estimates.

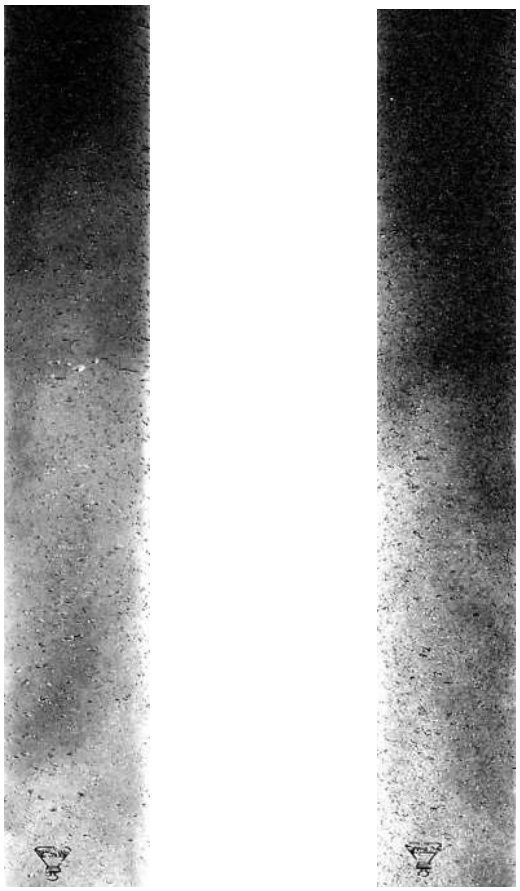

(a) Image 1 (b) Image 2

Figure 47: Eddy Transport during Ozonation

VI.2.2 Parameter Estimates

Images from mass transfer visualization studies were used to estimate mass transfer rate and dispersion. The steps in this process were:

- Processing of indigo dye images (subtraction of background and conversion to greyscale);
- Calculating radially averaged indigo dye concentration data from processed indigo dye images;
- Application of non-linear regression to determine the parameters of candidate models for the fate and transport of indigo dye that produce the best fit of data from indigo dye images; and
- Comparison of fitted models to determine the model that best fit the data.

VI.2.2.1 One-Dimensional Indigo Dye Decoloration Models

As described above and observed by prior researchers (Rice and Littlefield 1987; LeSauze et al., 1993), in the top portion of the laboratory reactor, indigo dye was decolored more or less monotonically as the dye flowed downward. Near the sparger, however, the dye concentration was nearly uniform, exception where large eddies of dye-rich water flowing near the walls were entrained into the bubble plume. This tendency is illustrated in Figure 48, which shows an image of indigo dye concentration along with a plot of radially-averaged indigo dye concentration.

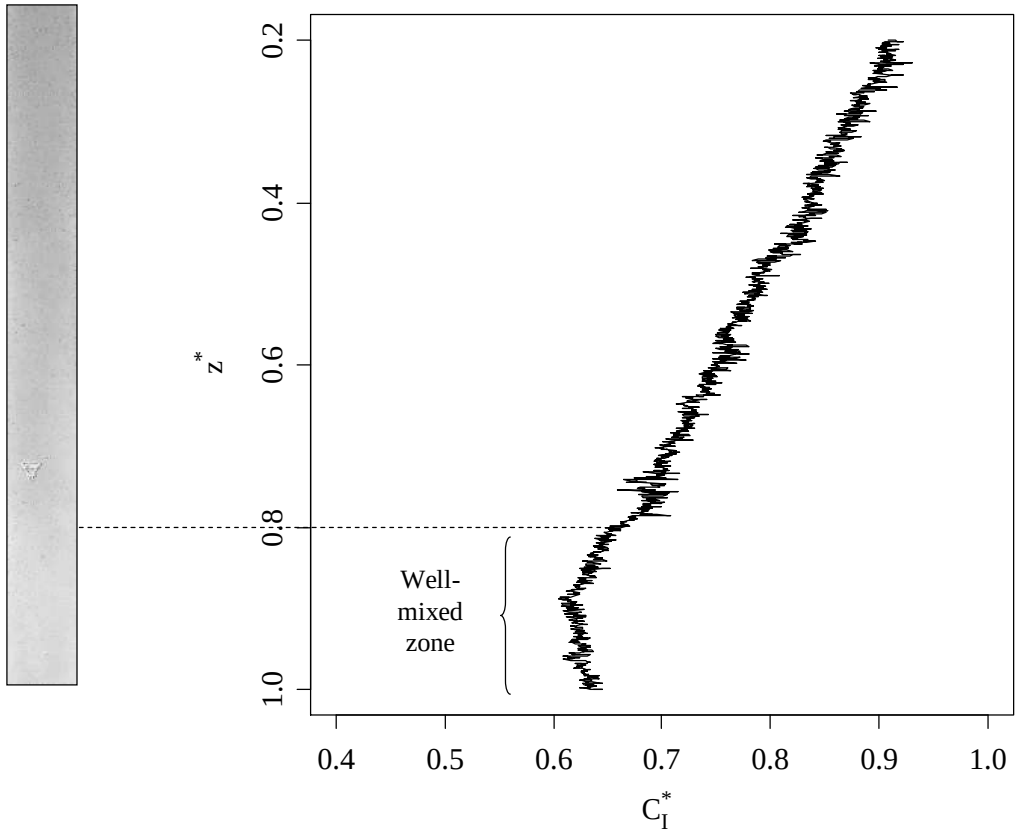

Figure 48: Illustration of Well-Mixed Zone and Radially-Averaged Concentration

The gas and liquid flow rates corresponding to Figure 48 were 0.4 slpm and 13.5 lpm, respectively. The terms z^* and C_I^* are nondimensional depth and dimensionless indigo dye concentration, given by

$$z^* = \frac{z}{H} \tag{64}$$

and

$$C_I^* = \frac{C_I}{C_{I,0}} \tag{65}$$

where z is depth from the water free surface, H is reactor height (from the discharge ports to the water free surface), C_I is indigo dye mass concentration and $C_{I,0}$ is indigo dye concentration at the liquid inlet.

Based on this observation, two models for indigo dye decoloration were proposed:

- a single-zone model in which the dispersion and mass transfer coefficient were assumed uniform in the reactor and
- a two-zone model in which the portion of the reactor near the sparger was modeled as a continuously stirred tank reactor (CSTR) and the rest of the reactor was modeled using the 1-dimensional advection-dispersion-reaction (ADR) model.

Detailed derivation of expressions for indigo dye concentration for the one- and two-zone models are provided in Appendix B and summarized below.

For the single-zone model, normalized indigo dye concentration is given by

$$C_I^* = 1 - \left(\frac{\psi}{(N_S/S) - P_e} \right) \left[P_e \, e^{-(N_S/S)} \left(1 - e^{(N_S/S)z^*} \right) - (N_S/S) e^{-P_e} \left(1 - e^{P_e z^*} \right) \right] \tag{66}$$

where N_S is Stanton number, given by

$$N_S = \frac{k_L \, a \, H}{U_L}; \tag{67}$$

S is stripping factor, given by

$$S = \frac{mU_G}{U_L}; \tag{68}$$

P_e is Peclet number, defined in equation 39 (repeated below)

$$P_e = \frac{U_L H}{D} \tag{39}$$

and the parameter ψ is given by

$$\psi = \frac{M_I}{M_{O_3}} \frac{C_{O_3(g)0}}{C_{I,0}} S = \frac{M_I}{M_{O_3}} \frac{mQ_G}{Q_L} \frac{C_{O_3(g)0}}{C_{I,0}} \tag{69}$$

In equations 37, 59 - 61, k_L is liquid side mass transfer coefficient, a is specific surface area, m is Henry's law constant (dimensionless ratio of mass concentration in gas phase to mass concentration in liquid phase), U_G and U_L are superficial gas and liquid flow rates, M_I and M_{O_3} are molecular weights of potassium indigo trisulfonate and ozone, $C_{O_3(g)0}$ is gas ozone concentration at the sparger, and $C_{I,0}$ is indigo trisulfonate concentration at the water intake. Measured water temperature ranged from 4.9° C to 22° C over the course of mass transfer visualization experiments and Henry's law constant was calculated via the expression (Perry and Chilton 1973)

$$\log(m) = \begin{cases} 3.25 - \dfrac{840}{T} & 5^\circ\mathrm{C} \le T \le 5^\circ\mathrm{C} \\ 6.2 - \dfrac{1687}{T} & 5^\circ\mathrm{C} \le T \le 5^\circ\mathrm{C} \end{cases} \tag{70}$$

In the limit of $N_S \to P_e$, the single zone expression for normalized indigo dye concentration becomes

$$\underset{\lim\left(\frac{N_S}{S}\right)\to P_e}{C_I^*} = 1-\psi\left[\left(P_e - P_e z^* + 1\right)e^{-P_e\left(1-z^*\right)} - e^{-P_e}\left(1+P_e\right)\right] \tag{71}$$

Two versions of the two-zone model were fit to experimental data. In one version the Stanton number was assumed the same in zones 1 and 2 and only mixing differed between the two zones. The indigo dye concentration for this model is given by

$$C_I^* = e^{P_e z^*} + \left(C_{I,2}^* + \psi\right)\left(1 - e^{P_e z^*}\right) + \left(\frac{\psi P_e}{\left(N_S/S\right) - P_e}\right)\left(\frac{1}{1+\left(N_S/S\right)\left(1-z_c^*\right)}\right)\left(e^{-\left(N_S/S\right)\left(z_c^* - z^*\right)} - e^{P_e z^* - \left(N_S/S\right)z_c^*}\right) \tag{72}$$

where P_e refers to the Peclet number in zone 1 (the top of the reactor), z_c^* is the nondimensionalized critical depth and $C_{I,2}^*$ is the dimensionless indigo dye concentration in zone 2 (the well mixed zone) given by

$$C_{I,2}^* = \frac{1}{C_{I,0}}\frac{1}{n_{data} - n_c}\sum_{i=n_c}^{n_{data}} C_{I,i} \tag{73}$$

where n_{data} is the number of (pixels) in the indigo dye image and n_c is the row corresponding to the critical depth.

For the two-zone model in which different Stanton numbers were allowed in zones 1 and 2, the expression for indigo dye concentration is

$$C_I^* = e^{P_e z^*} + \left(C_{I,2}^* + \psi\right)\left(1 - e^{P_e z^*}\right) + \left(\frac{\psi P_e}{\left(N_{S1}/S\right) - P_e}\right)\left(\frac{1}{1 + \left(N_{S2}/S\right)\left(1 - z_c^*\right)}\right)\left(e^{-\left(N_{S1}/S\right)\left(z_c^* - z^*\right)} - e^{P_e z^* - \left(N_{S1}/S\right) z_c^*}\right) \quad (74)$$

where N_{S1} and N_{S2} are the zone 1 and zone 2 Stanton numbers. In the limit $\left(N_{S1}/S\right) \to P_e$, the expression for indigo dye concentration becomes

$$C_I^* = e^{P_e z^*} + \left(C_{I,2}^* + \psi\right)\left(1 - e^{P_e z^*}\right) + \left(\frac{\psi P_e z^* e^{P_e\left(z^* - z_c^*\right)}}{1 + \left(N_{S2}/S\right)\left(1 - z_c^*\right)}\right) \quad (75)$$

VI.2.2.2 Methodology for Determining Model Parameters

Model equations 58, 62, 65 and 66 were fit to radially-averaged indigo dye concentration data from digital photographs of mass transfer visualization experiments. Fits were made using the nls (nonlinear least squares) utility in the R programming language (The R Foundation 2006). After models were fit to data, independence was assessed via runs tests (Manly 1997). Data were considered independent unless independence could be rejected with 95% confidence.

When dependency was encountered, a subset of data was taken from the original data set, best fit parameters were again determined and independence was again assessed. Two sampling methodologies were assessed when selecting subsets from the original data set. In one, a random sample of n_{data}/j points was taken from the original data set, where n_{data} was the number of data points (rows) in the original data set and j took the values 2, 4, 8, 16, 20, 24, 28, 32, 36, 40, 44, 48, 52, 56, 60 and 64. In the second

sampling methodology a systematic sample was taken in which the subset consisted of each *j*th data point where *j* took the values 2, 4, 8, 16, 20, 24, 28, 32, 36, 40, 44, 48, 52, 56, 60 and 64. In all cases the systematic sampling resulted in elimination of dependence at lower values of *j* than the random sampling. Reducing the number of data points did not result in significant changes in parameter estimates. In all cases, independence could be demonstrated for the two-zone model (usually after the number of data points in the sample was 20 times less than that in the original data set). Independence could not be demonstrated for any cases for the single-zone model. Thus, the two zone model was considered the more appropriate model and parameter estimates were taken from the two-zone model.

In two zone models, the critical depth, z_c^*, was determined as follows. The best fit parameters and sum of the squares of the errors were determined for all $z_c^* \in (0.5, 1.0)$. The critical depth was taken to be the value that gave the lowest sum of squares of errors. The minimum sum of the squares of the errors was usually readily identifiable. A typical plot of sum of the squares as a function of index of critical depth is provided in Figure 49. In digital images, each row of pixels corresponds to a value of z^*, so in Figure 49, the index n_c is the row number corresponding to the critical depth z_c. For the plot shown, there was a total of 60 data points and the critical depth was determined to be at the 44th data point.

An R-language script used for determination of two-zone model best fit parameters and for performing a runs test of the fitted model is provided in Appendix D:

Similar scripts were written for the one zone model and for versions of the models in which the Peclet and Stanton numbers were equal.

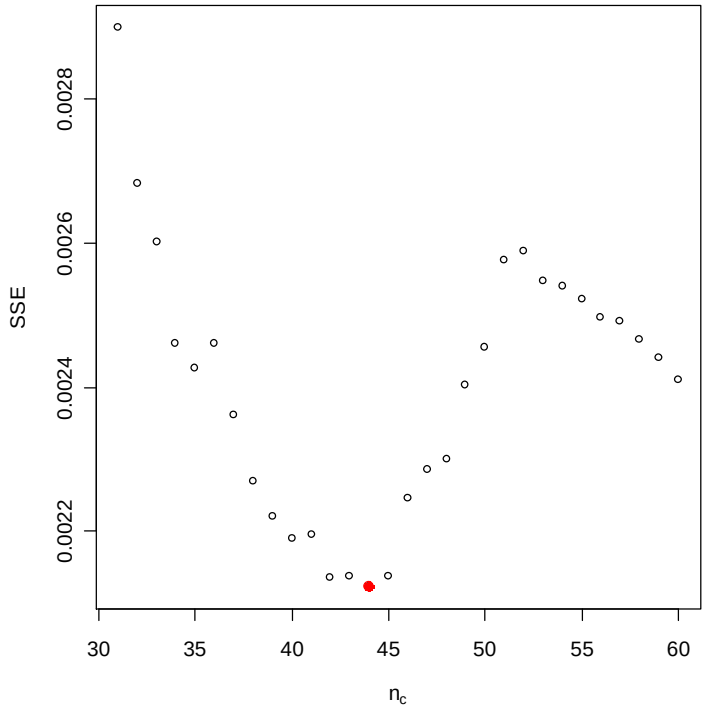

Figure 49: Identification of Best Fit Critical Depth

VI.2.2.3 Parameter Estimates

Processed images, best-fit models and parameters corresponding to best fit models for each mass transfer visualization experiment are presented below. For each of the indigo dye experiments, two images and plots showing 1- and 2-zone best fit models are shown in Figure 51 - Figure 59. Both color (blue) and grayscale images are provided,

since the color images provide greater detail in the variation of indigo dye color. Along with reactor images, plots of best fit 1-zone and 2-zone models are provided. In all cases, independence could not be demonstrated for the one-zone model; the one-zone plots are included in Figure 51 - Figure 59 for contrast with best fits of the two-zone model and to document the trends in data that gave rise to data dependence. Data dependence is manifested in either periodic variation of the data around the model (such as seen in Figure 53 (c)) or significant deviation of the model from the data at the top and bottom of the reactor (such as seen in Figure 52 (c)).

Several general observations can be made based on Figure 51 - Figure 59. First, in all cases, in the top of the reactor the indigo dye concentration decreases steadily as the water progresses downward. Second, the rate of decrease of indigo dye in the bottom of the reactor is always less than that in the top of the reactor (though not necessarily zero, as would be observed in a true CSTR). Third, in several cases (Figure 53, Figure 56, Figure 58 and Figure 59) there is an upturn in indigo dye concentration at the very bottom of the reactor. One explanation for this upturn is that dye-rich water flowing along the column walls is backmixed into the column as the water is entrained into the large eddies near the sparger (as seen in Figure 40). As seen later in this chapter, CFD also predicts there is a region of high indigo concentration at and below the sparger depth. Finally, the inability to demonstrate independence for the single zone model is related to large length scale oscillations in indigo dye concentration around the trend line. These oscillations are not surprising, given the observation of large dye-rich eddies flowing downward in the

reactor, and indicate that time series analysis of radially-averaged indigo dye concentration data might yield quantitative data on large scale mixing processes.

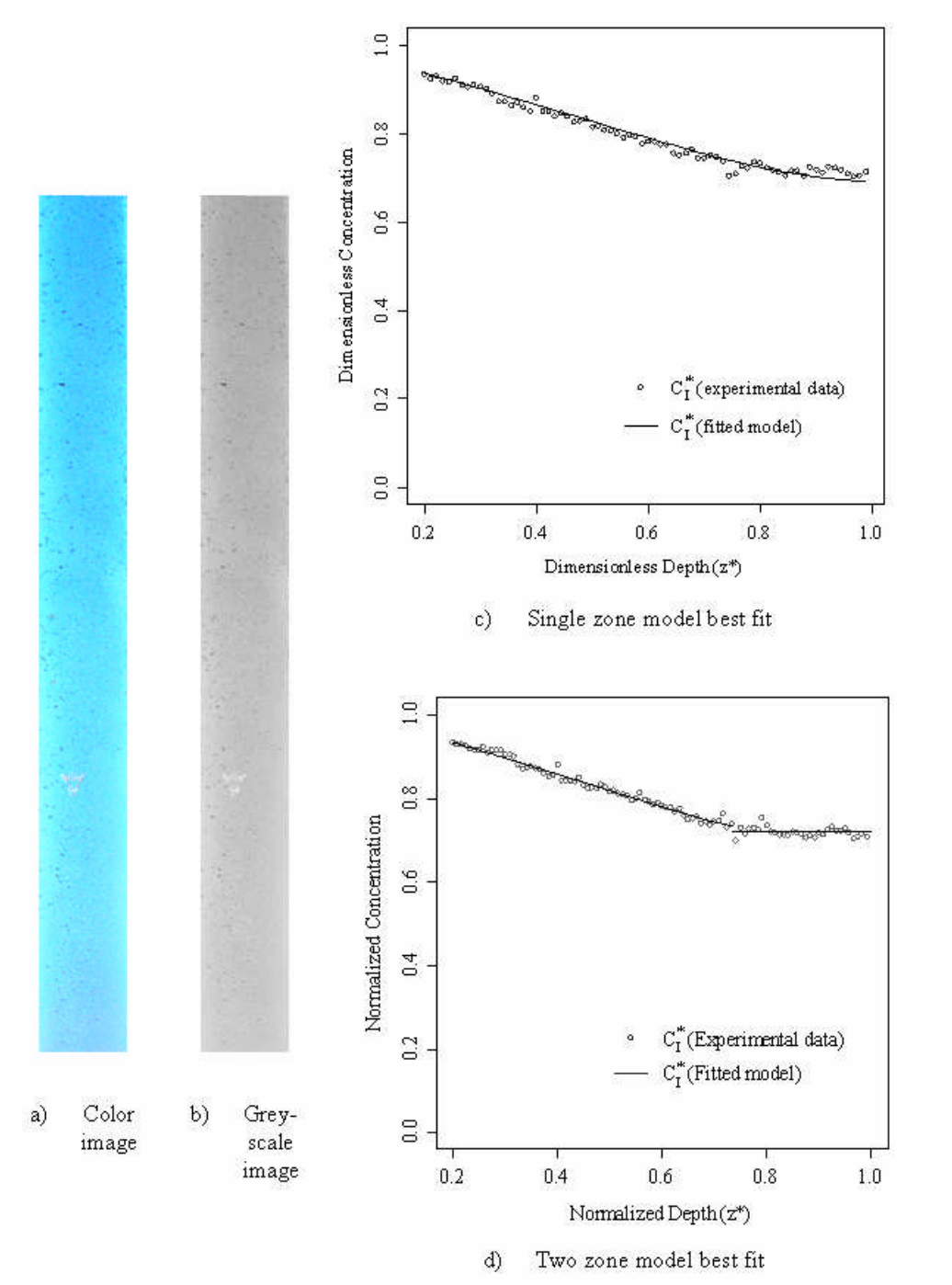

Figure 50: Mass Transfer Visualization, Q_{gas} = 0.4 slpm, Q_L = 7.0 lpm, Case A

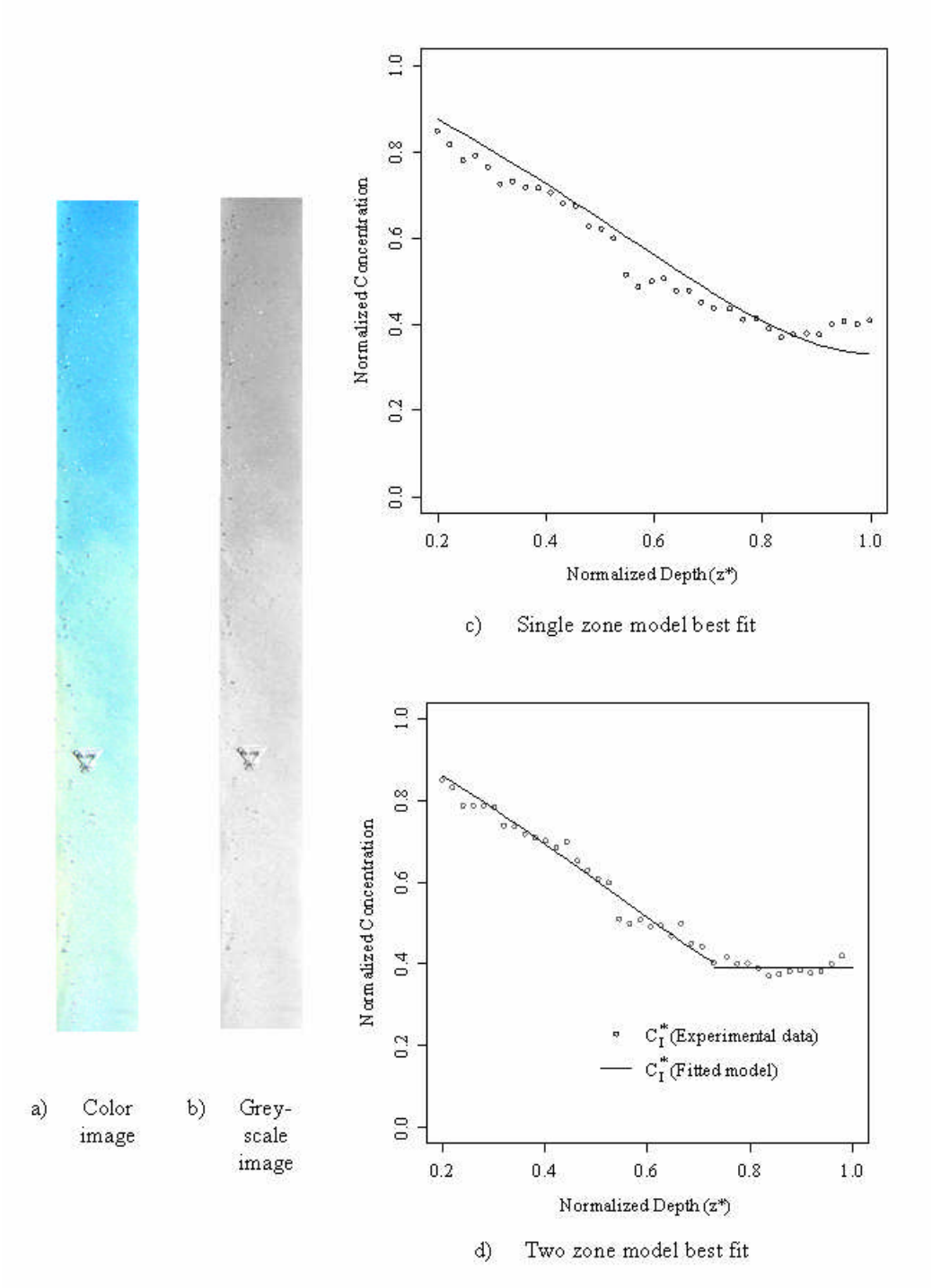

Figure 52: Mass Transfer Visualization, Q_{gas} = 0.4 slpm, Q_L = 7.0 lpm, Case B

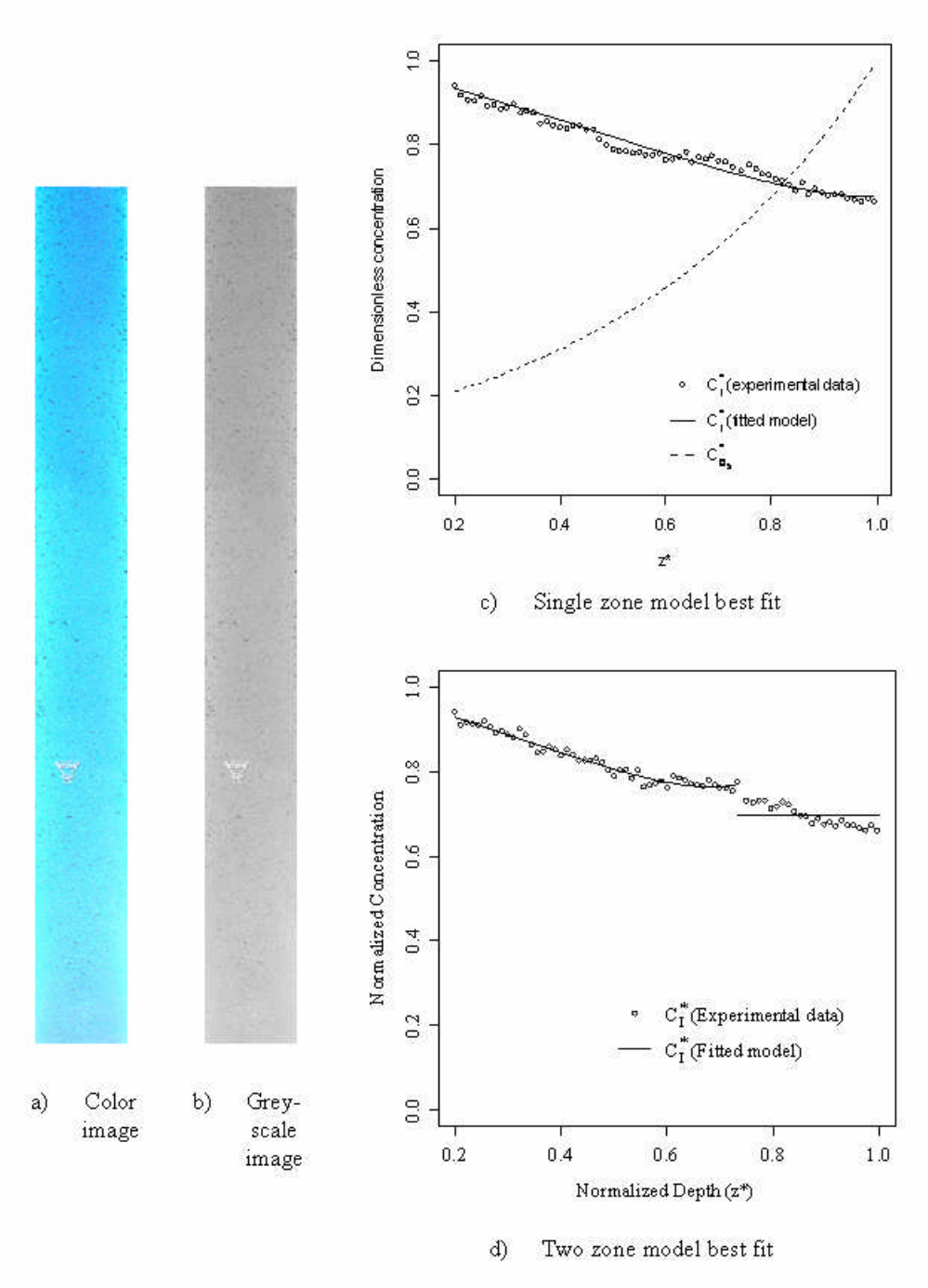

Figure 53: Mass Transfer Visualization, Q_{gas} = 0.4 slpm, Q_L = 10.5 lpm, Case A

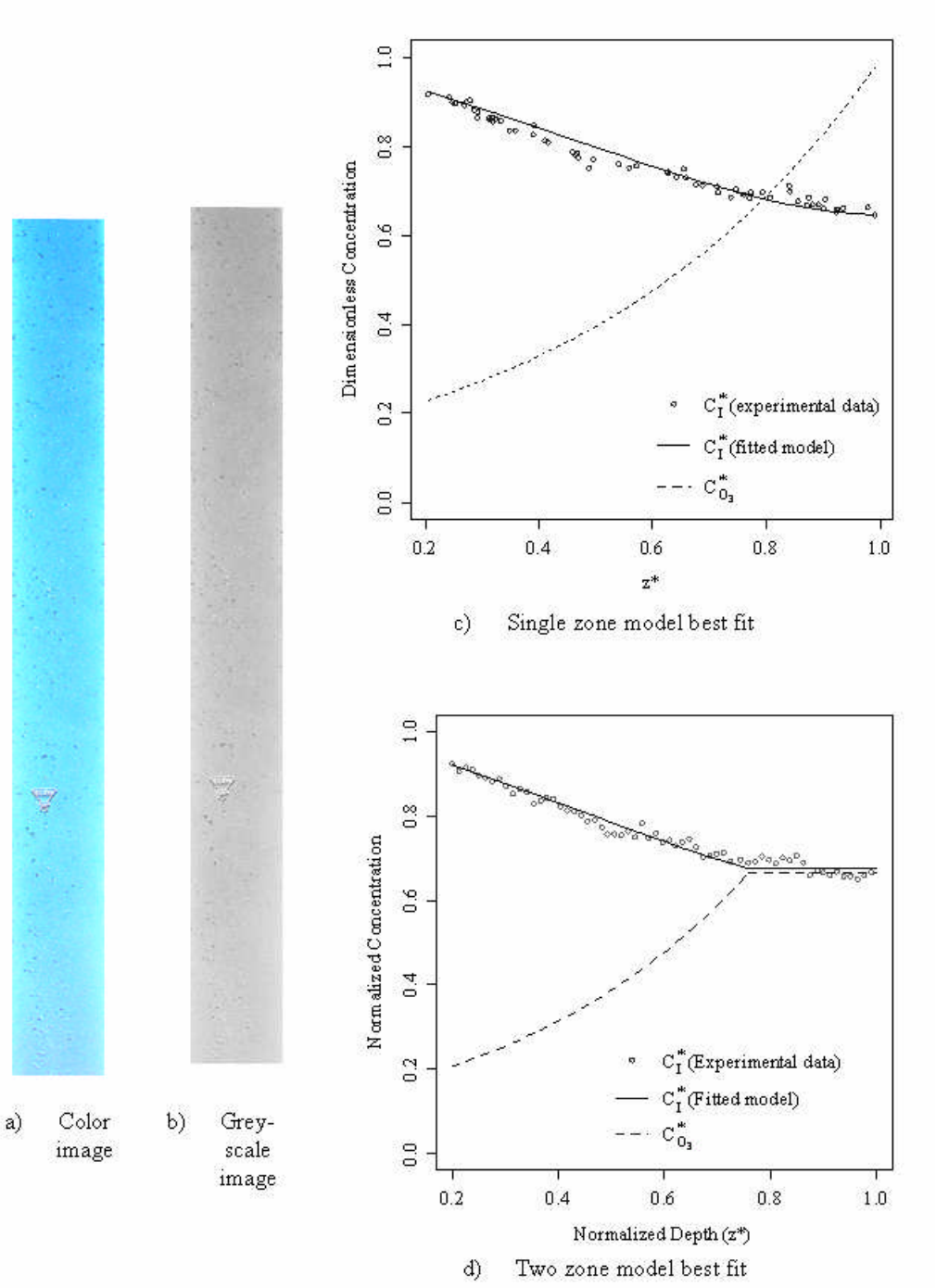

Figure 54: Mass Transfer Visualization, Q_{gas} = 0.4 slpm, Q_L = 10.5 lpm, Case B

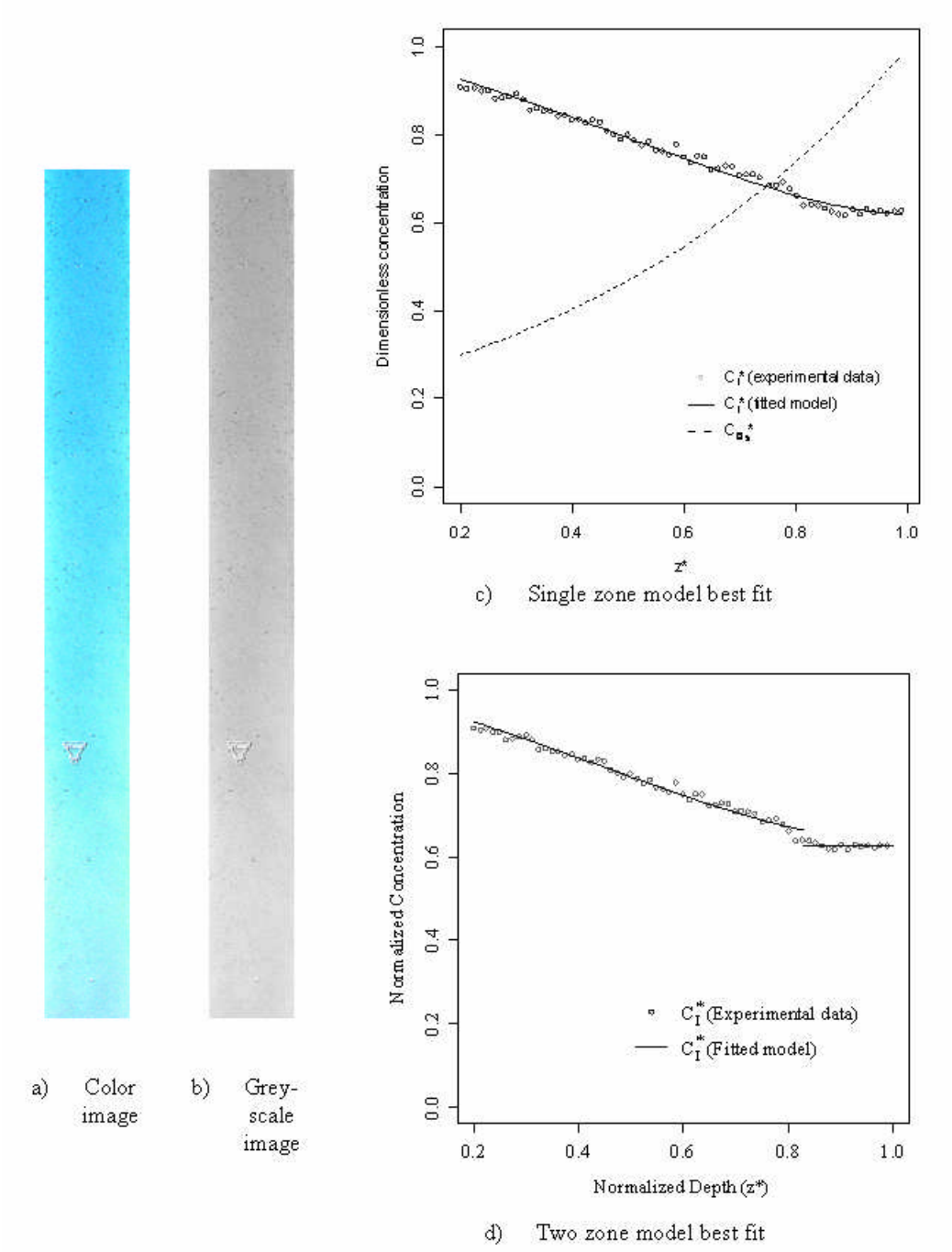

Figure 55: Mass Transfer Visualization, Q_{gas} = 0.4 slpm, Q_L = 13.5 lpm, Case A

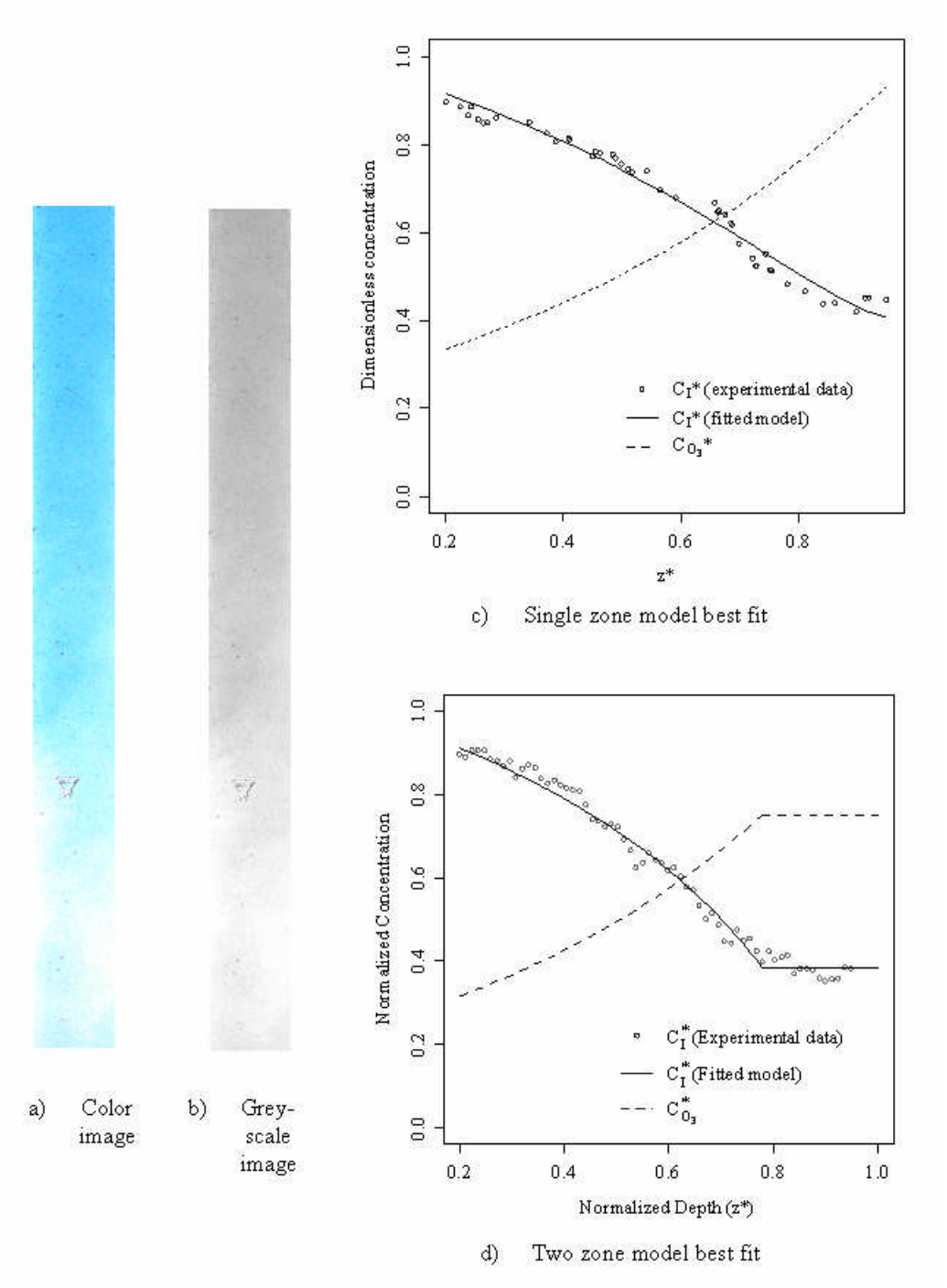

Figure 56: Mass Transfer Visualization, Q_{gas} = 0.4 slpm, Q_L = 13.5 lpm, Case B

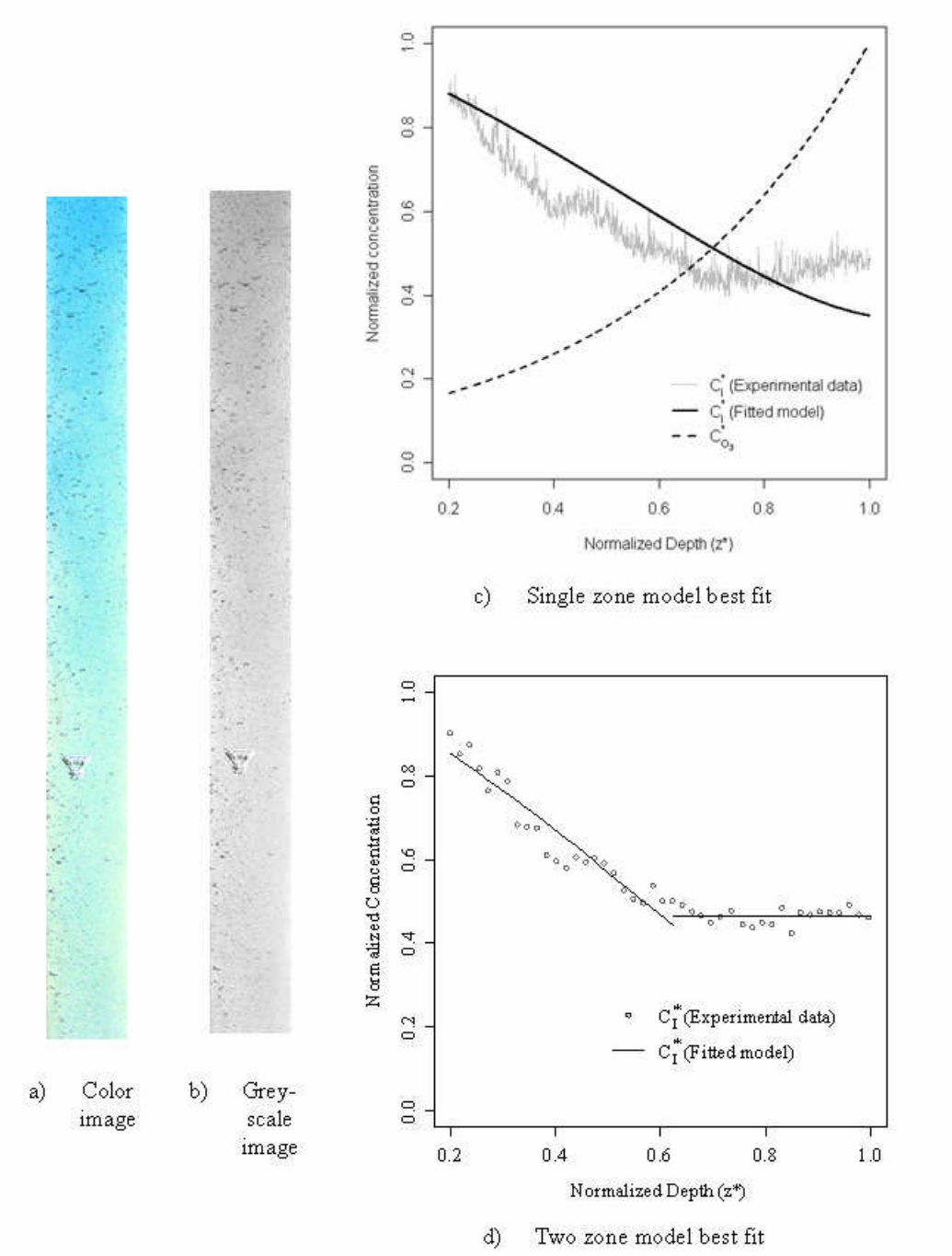

Figure 57: Mass Transfer Visualization, Q_{gas} = 0.7 slpm, Q_L = 7.0 lpm

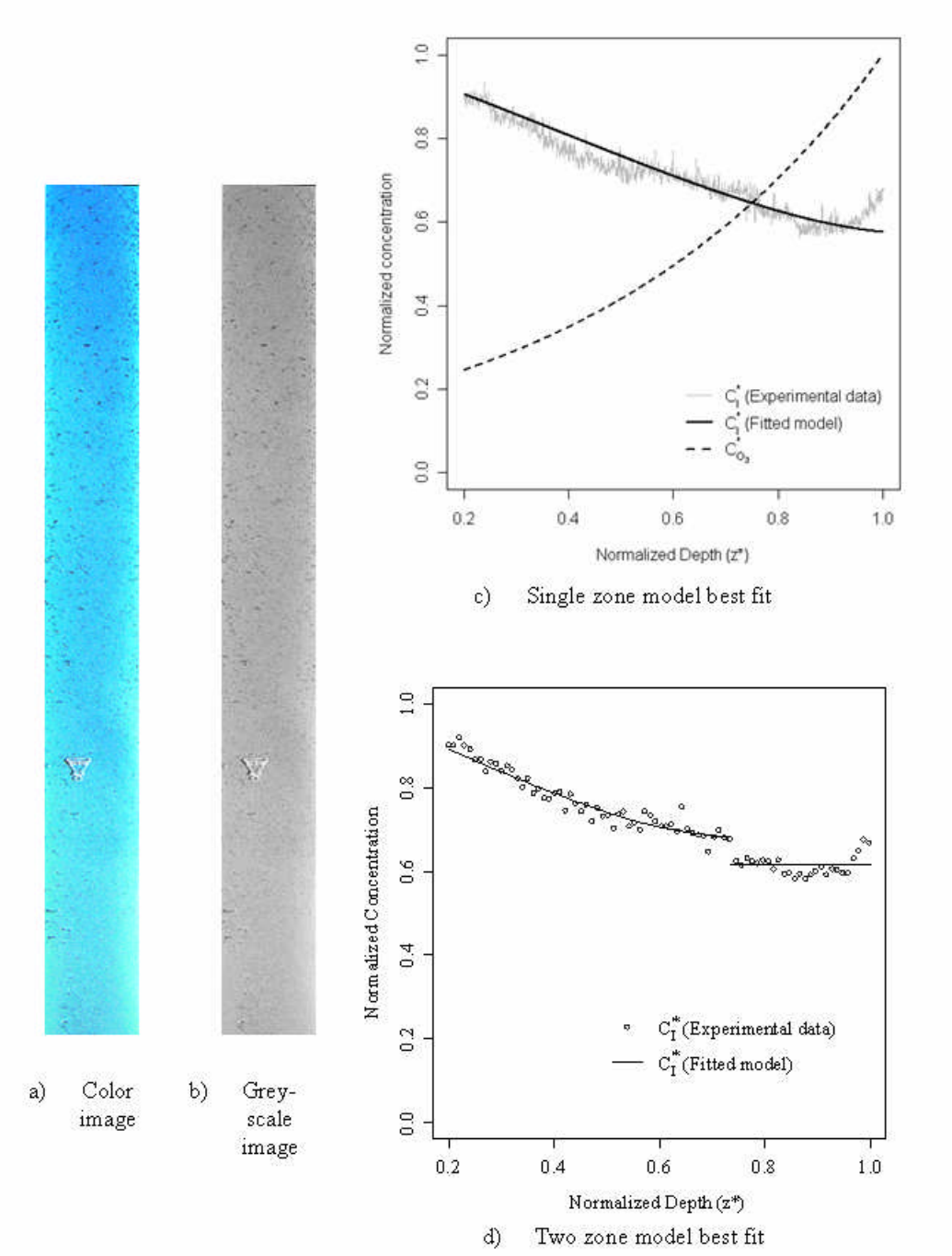

Figure 58: Mass Transfer Visualization, Q_{gas} = 0.7 slpm, Q_L = 10.5 lpm

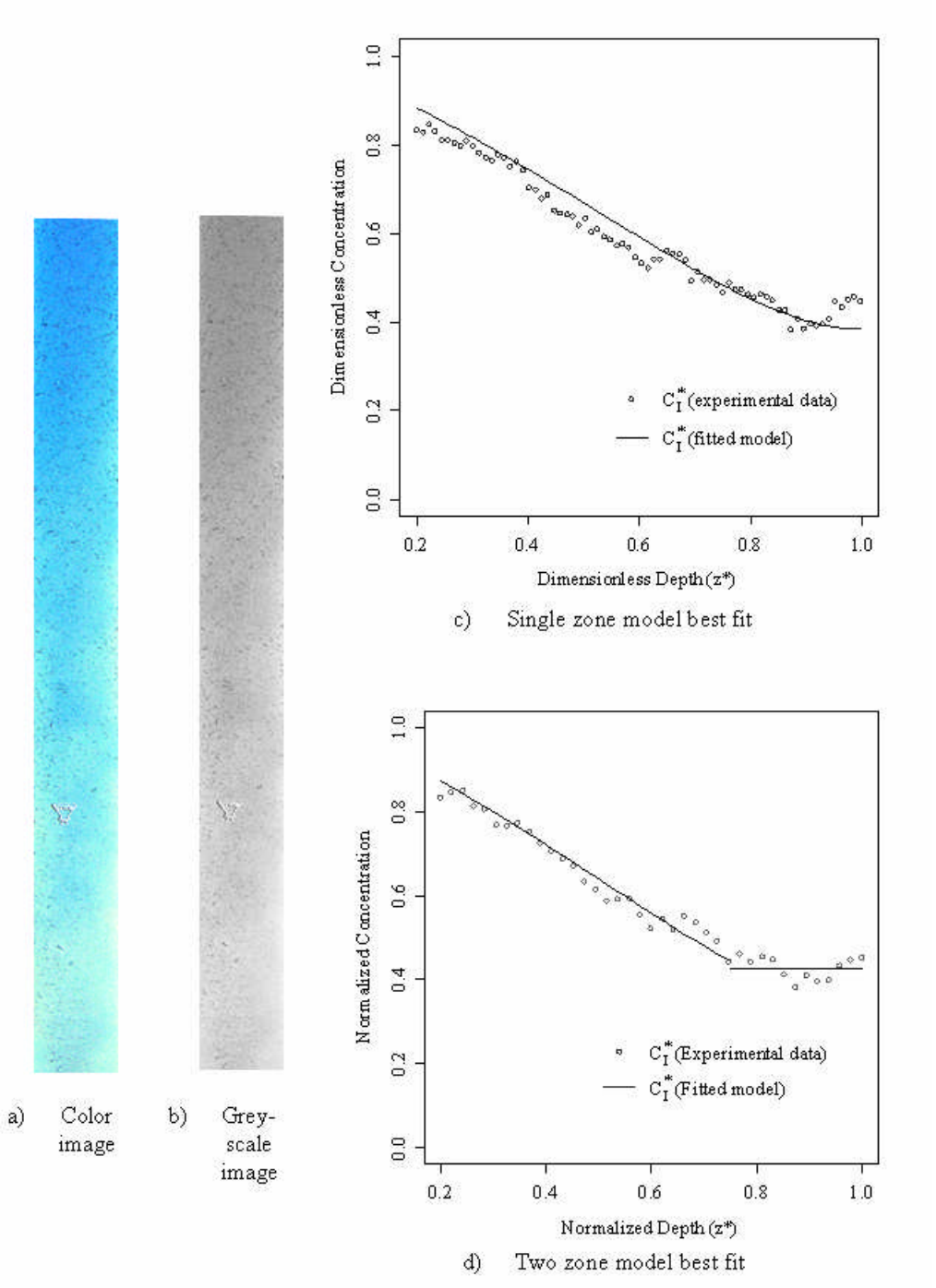

Figure 59: Mass Transfer Visualization, Q_{gas} = 0.7 slpm, Q_L = 13.5 lpm

Best fit parameters for each mass transfer visualization experiment are presented in Table 22. In Table 22, the sample size at which independence could not be rejected with 95% confidence was n_{data} / j where n_{data} is the number of data points in the full data set. In general, Peclet number estimates were found to vary more widely than estimates for Stanton number and length of the entrance region. In one case (gas flow rate of 0.4 slpm, liquid flow rate rate of 10.5 lpm, case B) the zone 2 Stanton number was estimated to be zero. This indicates that the change in indigo color observed in the top of the reactor can be attributed solely to mixing and that all significant mass transfer takes place in the well-mixed zone in the bottom of the reactor.

Table 22: Best Fit Parameters

Q_g (slpm)	Q_L (lpm)	Case	j	P_e	N_{S1}	N_{S2}	z_c^*
0.4	7.0	A	24	1.49	0.29	0.29	0.266
0.4	7.0	B	56	1.93	0.43	0.43	0.282
0.4	10.5	A	32	5.77	0.16	0.025	0.226
0.4	10.5	B	16	1.66	0.19	0.00	0.240
0.4	13.5	A	16	2.04	0.14	0.14	0.173
0.4	13.5	B	36	7.76	0.10	0.10	0.216
0.7	7.0		24	1.91	0.96	0.96	0.396
0.7	10.5		28	1.52	0.35	0.35	0.266
0.7	13.5		24	1.93	0.38	0.38	0.219

Peclet number, Stanton number and critical depth were found to correlate with the ratio of gas to liquid flow rates. Figure 60 shows the variation in entrance region length ($1 - z_c^*$) with gas to liquid flow ratio. Estimates based on data from experiments conducted at a gas flow rate of 0.4 slpm are shown as solid diamonds and those based on experiments at a gas flow rate of 0.7 slpm are shown as unfilled squares. Entrance region length increases steadily with increasing gas to liquid flow ratio for the gas and liquid flow rates used in this study. This result indicates that high gas to liquid flow rates result in greater mixing of the liquid phase (primarily through the formation of large vortices in the vicinity of the sparger and attendant backmixing of the liquid phase) but less uniform distribution of the phases. In a more complex reactor geometry than that of the laboratory rector used in this study, uneven distribution of phases creates the potential for short-circuiting of the liquid phase in the bubble column and could result in significant variations in ozone residuals, as has been observed in full-scale ozonation reactors (Schulz and Bellamy 2000).

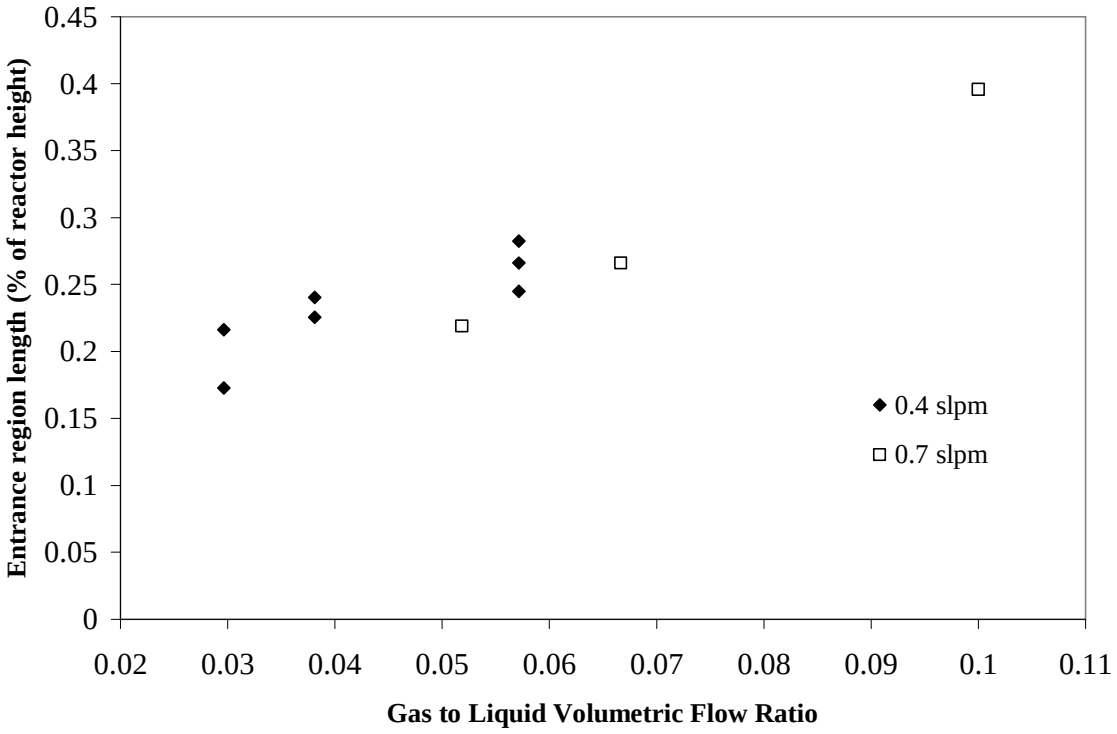

Figure 60: Variation of Entrance Region Length with Gas to Liquid Flow Ratio

As expected, zone 1 Stanton number increases with gas to liquid flow ratio, as seen in Figure 61. Higher gas flow rates produce more bubbles, resulting in greater dispersion (in the bubble wakes) and higher specific surface area (*a*). Had gas phase holdup been measured during mass transfer visualization studies, the relative importance of these two changes (increased dispersion and increased specific surface area) could have been ascertained.

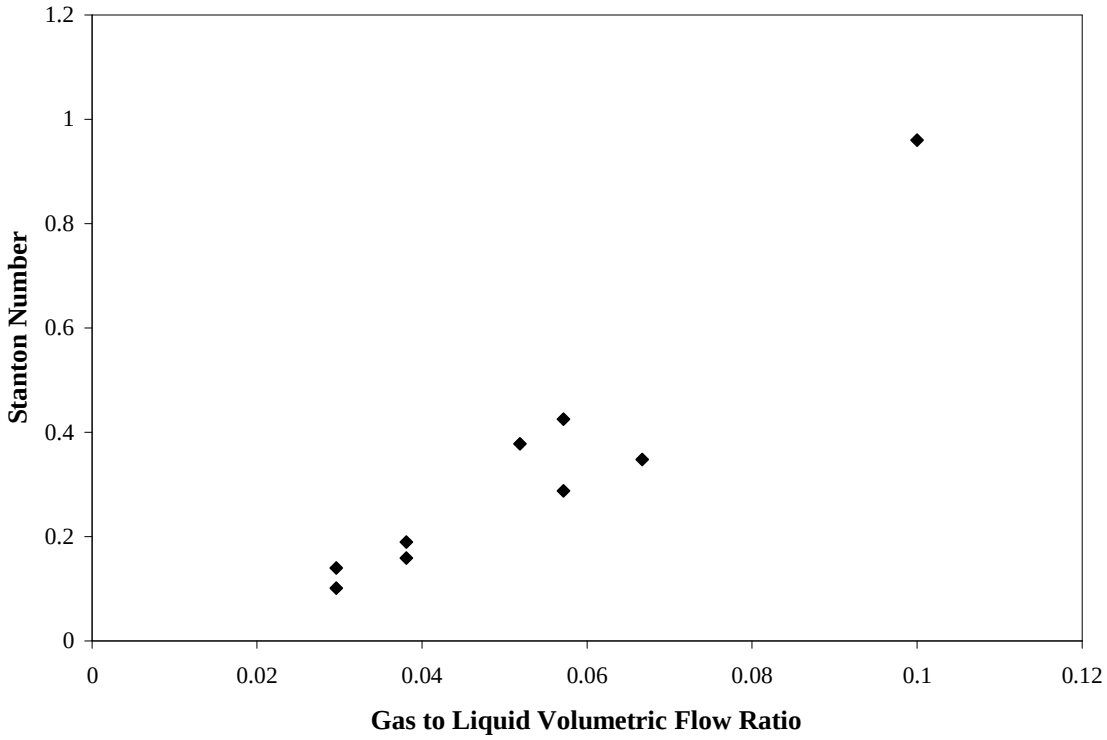

Figure 61: Variation of Zone 1 Stanton Number with Gas to Liquid Flow Ratio

The variation of zone 1 Peclet number with gas to liquid flow ratio is shown in Figure 62. As noted in Table 22, there was wide variation in Peclet number estimates from indigo dye image analysis, indicating high uncertainty in Peclet number estimates, especially at low gas-liquid flow ratios. In general, data follow the trends in Peclet number determined via RTD studies and CFD analyses shown in Figure 37, except for one estimate of Peclet number at the lowest gas to liquid flow rate. Images and best fit model for the case with the unexpectedly low Peclet number are found in Figure 56. Images and best fit model for the other case at the lowest gas to liquid flow ratio are

found in Figure 55. The only difference in operating conditions between the two cases is the ozone generator voltage: the voltage for the low Peclet number case was 70 V and that for the other case was 65 V. Based on the images in Figure 56, it is possible that some of the liquid phase was completely decolored for the case run at the higher ozone generator voltage and this may have made the Peclet number estimate less accurate.

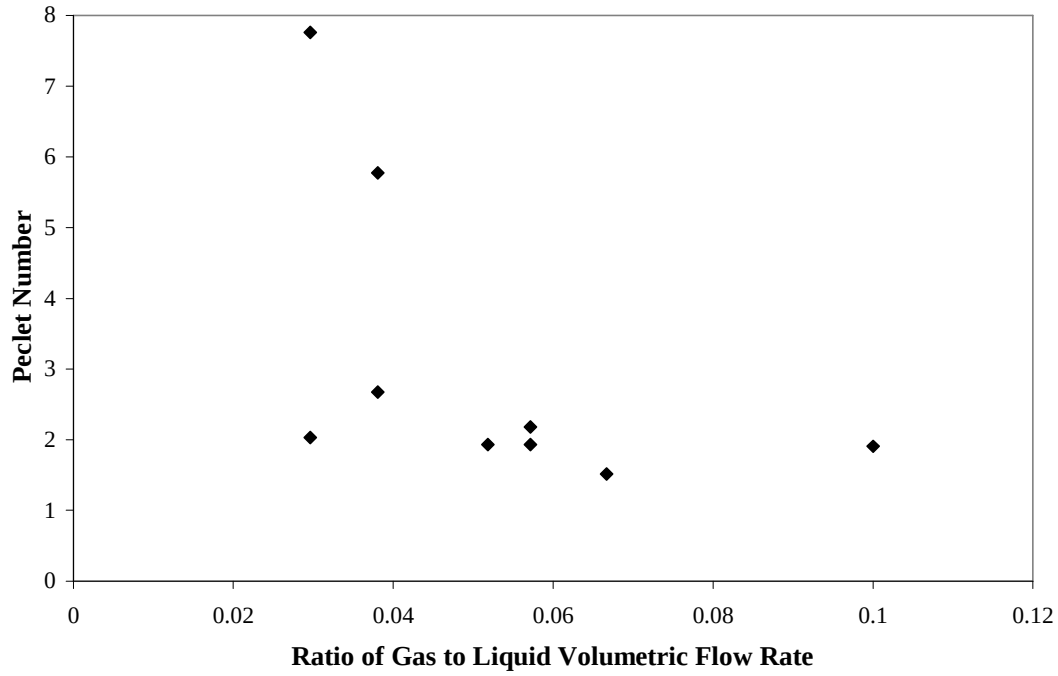

Figure 62: Variation of Zone 1 Peclet Number with Gas to Liquid Flow Ratio

The most significant findings and observations from the experimental mass transfer studies are that:

- The mass transfer and mixing near the sparger (in the "entrance region") differ from

those in the rest of the reactor.

- The entrance region length can be determined using the indigo dye mass transfer visualization technique.
- The entrance length increases with increasing gas to liquid flow ratio.
- Although the entrance region liquid phase is well-mixed, distribution of phases in the entrance region is poor.
- Stanton number increases with increasing gas to liquid flow ratio, likely because of specific surface area and turbulent dispersion increases.
- Peclet number trend is similar to that measured in RTD studies and predicted in CFD studies.

VI.3 CFD Mass Transfer Modeling Results

As described above, CFD was used to predict ozone mass transfer and fate and transport of indigo dye. Recapping important CFD model features, bubbles were assumed monodisperse with a diameter of 2.5 mm, bubble drag was estimated using the Grace drag model (Clift et al., 1978), mass transfer rate was estimated using the Kawase mass transfer relation (Kawase and Moo-Young 1992) and the indigo-ozone reaction was assumed sufficiently fast that there was no accumulation of dissolved ozone. The CFD model was run to allow comparison of predictions with results of four mass transfer visualization experiments:

- Q_G = 0.4 slpm, Q_L = 7.0 lpm, case A
- Q_G = 0.4 slpm, Q_L = 13.5 lpm, case A
- Q_G = 0.7 slpm, Q_L = 7.0 lpm, and
- Q_G = 0.7 slpm, Q_L = 13.5 lpm.

Direct comparison was made between indigo dye concentrations predicted by CFD and measured concentrations from samples drawn from the reactor. Samples were drawn from the reactor centerline from regularly spaced sample ports on the laboratory bubble column. The sample ports were sealed with Teflon seals held in place by fittings that allowed samples to be drawn from the sample centerline by 25 cc glass syringes outfitted with 3 inch (7.62 cm) hypodermic needles. Sample locations are shown in Figure 63.

Prior to sampling, the reactor was run at steady water and gas flow rates and ozone dose for more than three hydraulic residence times. Samples were drawn from one sample port at a time, beginning with the top port and proceeding to the bottom. Individual samples required up to 20 seconds to draw and the entire sampling process took approximately 2 minutes. Sample sizes were small (between 11 and 15 cc). Samples were diluted with enough milli-Q water to make the total sample volume 40 cc (the minimum sample volume for the 1 inch diameter (2.5 cm) spectrophotometer cells used) and absorbance was measured using a spectrophotometer. Absorbance of samples was measured at 500 nm and indigo concentration was calculated for samples using the

calibration curve described in Chapter III and accounting for dilution.

Figure 63: Sample Locations

Sample and CFD normalized indigo dye concentrations are compared in Figure 64. CFD results agree very well with sample concentrations at the bottom and top of the reactor, but are consistently lower in the center of the reactor. It is difficult to assess the CFD model based on this comparison. As described above, flow in the reactor is decidedly three dimensional and transient

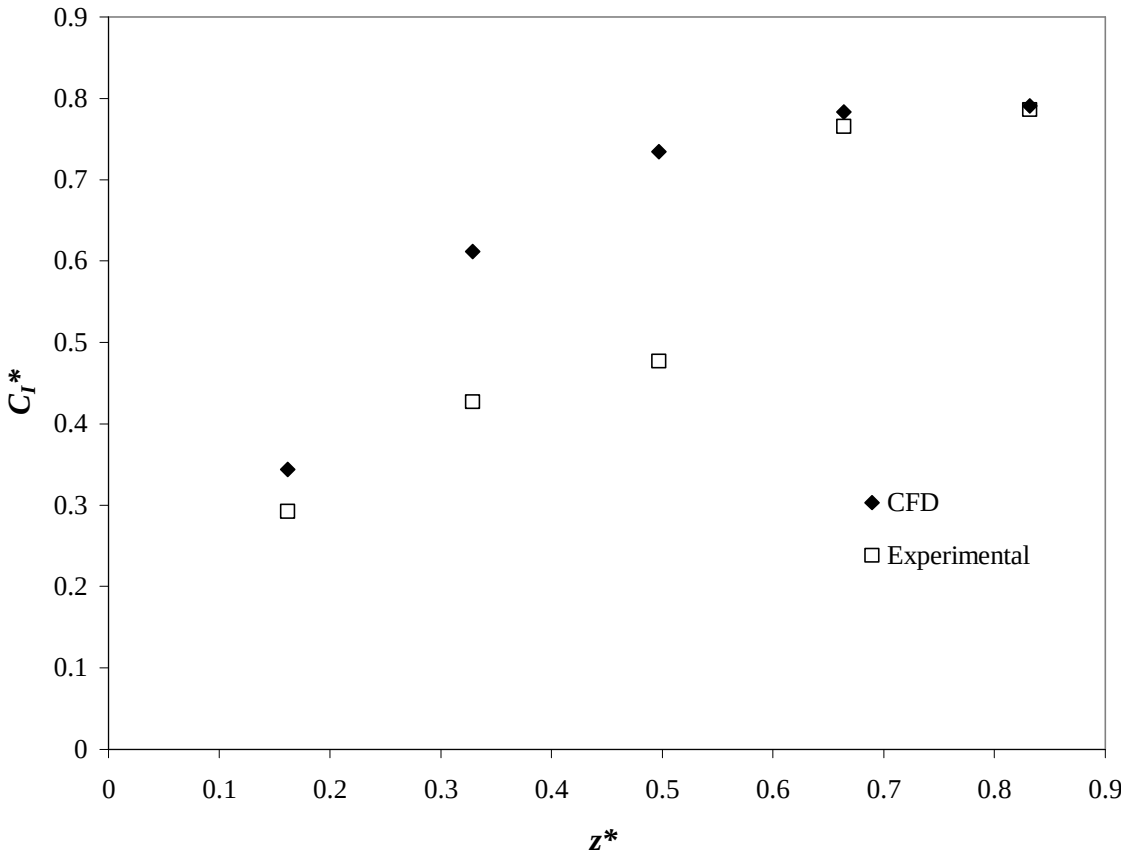

Figure 64: Predicted and Measured Indigo Dye Concentrations

Color contours and grayscale contours from CFD analyses are presented next to processed experimental indigo dye images in Figure 66 - Figure 69. Qualitatively, the consumption of indigo dye in the CFD images is very close to that of the experimental image. Differences in indigo dye concentration radial distribution between the experimental and CFD are related to differences between how the CFD image and the image captured on camera were generated. The experimental image is a two dimensional

image of the average indigo concentration at a particular location (r, z) on the image background, as illustrated in Figure 65. The CFD image shows indigo contours at a plane passing through the centerline of the reactor. Additionally, portions of bubble surfaces appear as dark spots in the experimental image, making the bubble plume look slightly darker than it should. As described in the experimental methods indigo dye concentration calibration portion of this thesis (section III.3.4), the indigo dye calibration curve (relating indigo dye concentration to image pixel color) was developed for images with bubbles. In CFD images, no bubbles are present and this difference results in minor differences between CFD and experimental images of indigo concentration.

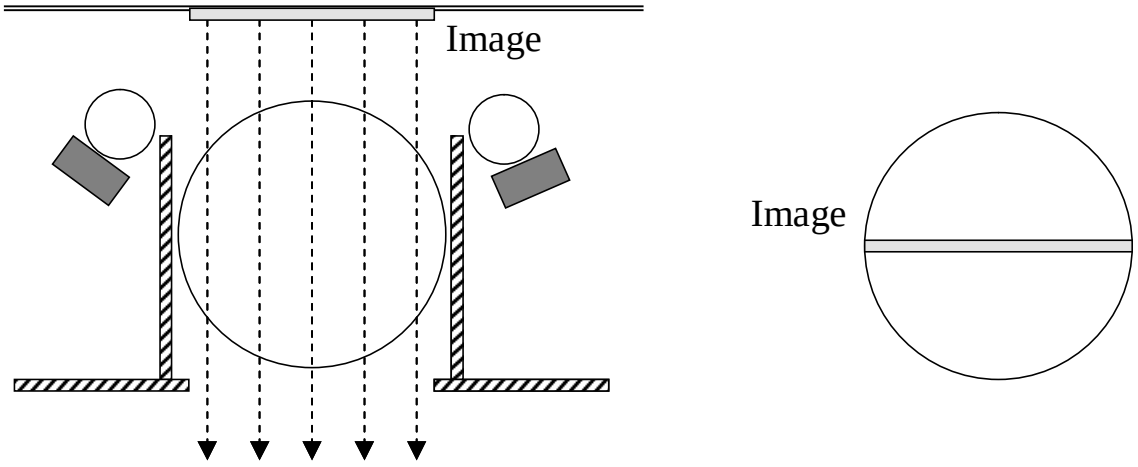

(a) Image Location, Experimental Image (b) Image Location, CFD

Figure 65: Image Location, Experimental Images and CFD

The impact liquid flow rate has on spatial distribution of mass transfer can be seen through comparison of Figure 66 and Figure 67. The gas flow rate was the same for both cases (0.4 slpm) and the liquid flow rates are 7.0 lpm and 13.5 lpm, respectively. In the high gas to liquid flow ratio case (Figure 66), indigo dye is decolored nearly to the top of the reactor, with the lowest indigo concentration water found in the bubble plume slightly above the sparger. At high liquid flow rate, the region in which indigo dye is decolored is much shorter, reaching only the reactor mid-height. In the high liquid flow case, there is vigorous backmixing of the liquid phase near the sparger and ozone is stripped from the gas phase rapidly near the sparger as a result of this mixing. At a gas flow rate of 0.7 slpm, the trend of mass transfer occurring over a greater portion of the reactor at the low liquid flow rate (Figure 68) than at high liquid flow rate (Figure 69) is again observed.

Comparing the CFD and experimental images, some of the flow structure observed in the experimental images is not seen in the CFD images. For example, Figure 69, large swirls of high indigo dye concentration water are observed in the bottom half of the reactor. The absence of these eddies in the CFD results is a result of the choice of turbulence model. Had a LES (large eddy simulation) model been chosen instead of the κ - ω implemented, these eddies might have been identified, though a finer mesh and smaller time step would have been required.

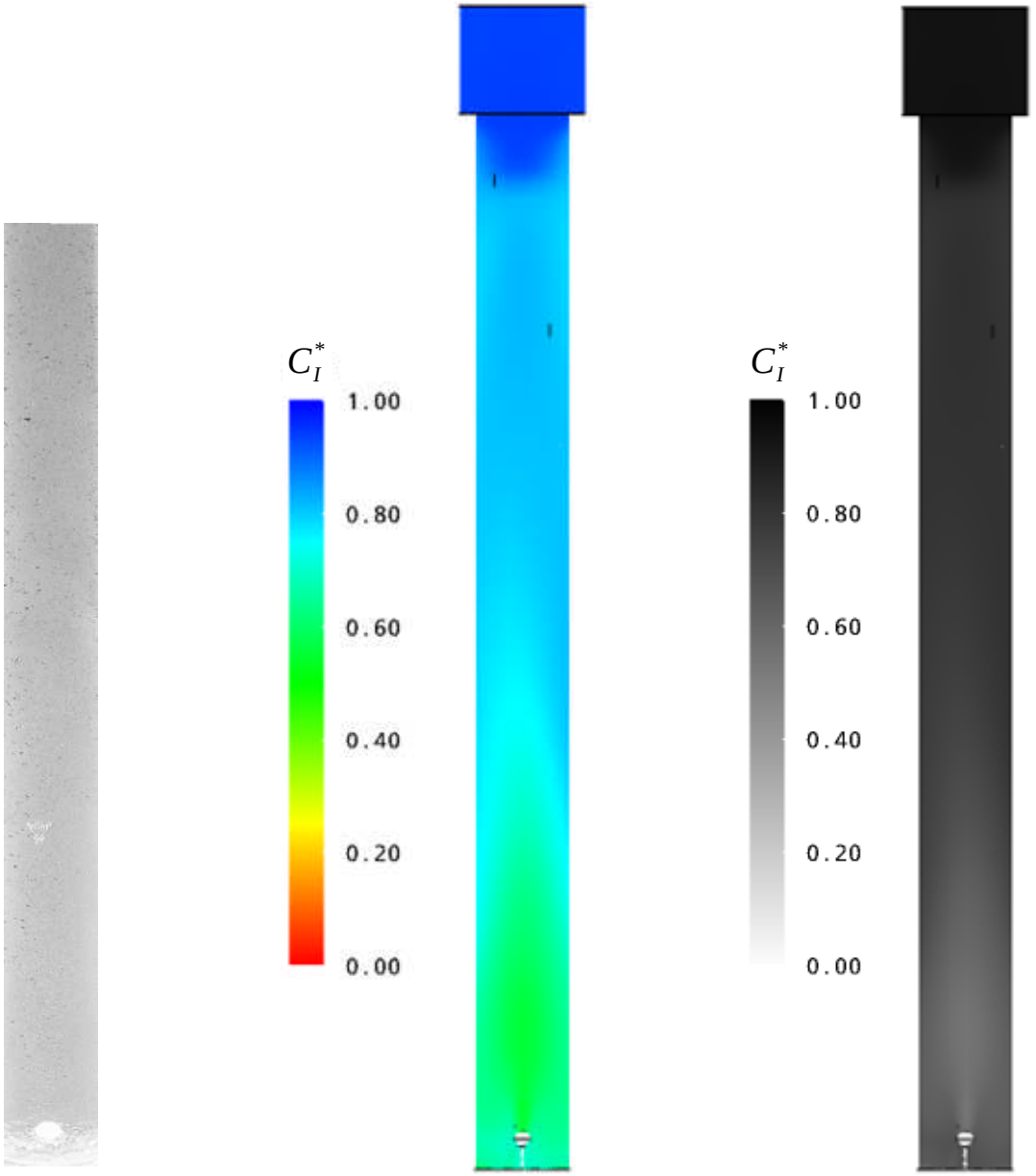

(a) Experiment (b) CFD, Color Contours (c) CFD, Grayscale

Figure 66: Experimental and CFD Indigo Dye Image, Q_L = 7.0 lpm, Q_G = 0.4 slpm

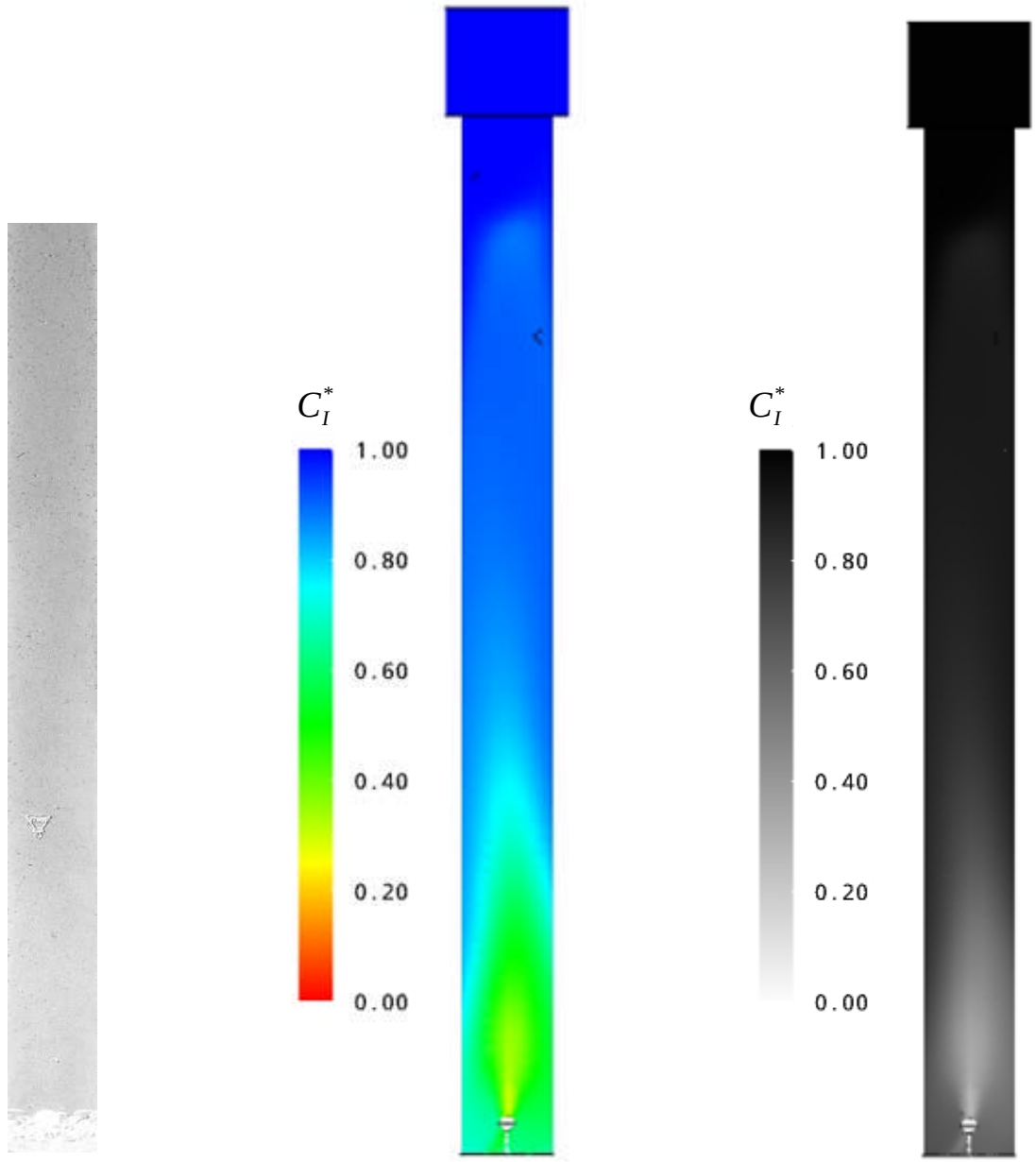

(a) Experiment (b) CFD, Color Contours (c) CFD, Grayscale

Figure 67: Experimental and CFD Indigo Dye Image, Q_L = 13.5 lpm, Q_G = 0.4 slpm

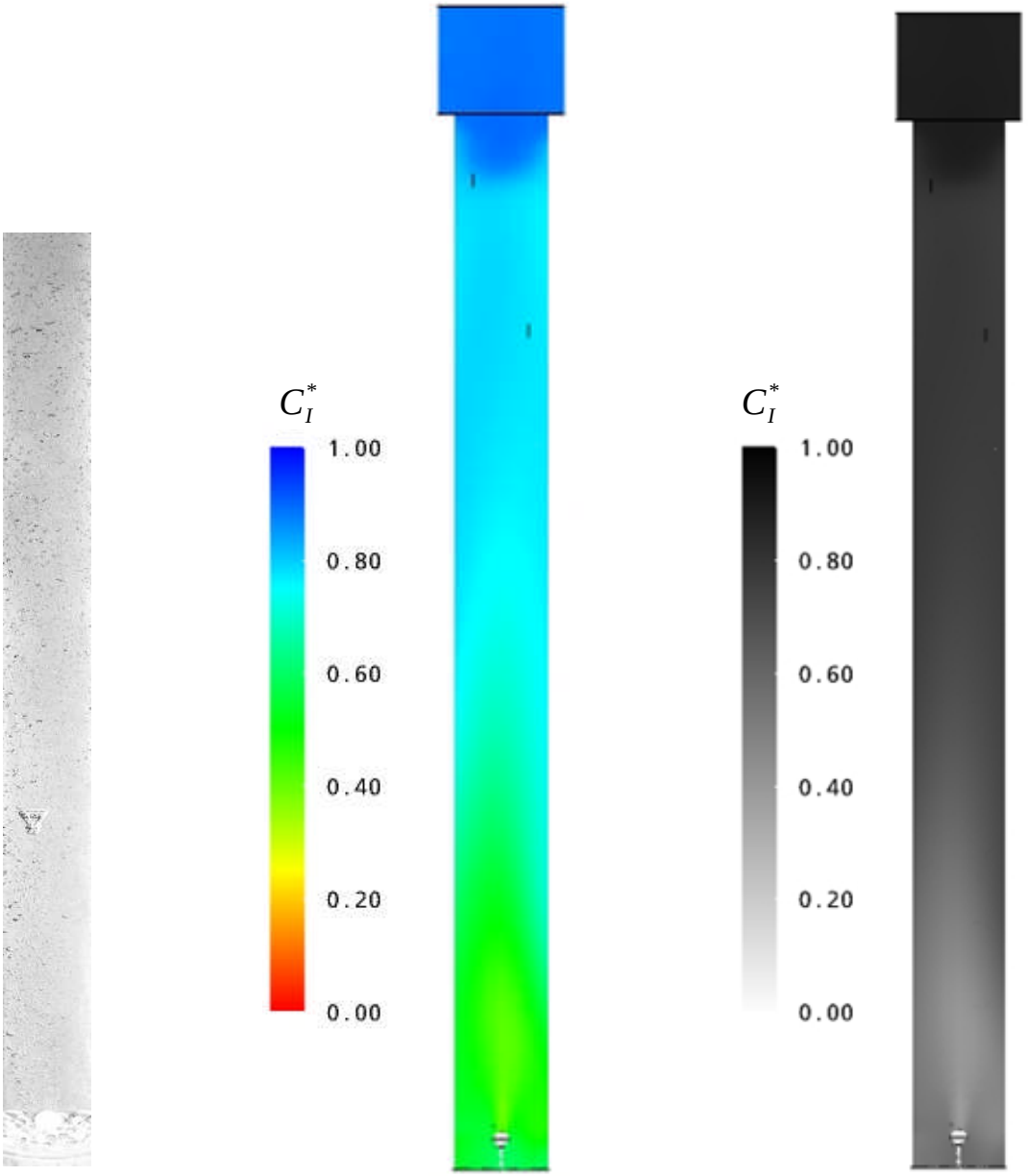

(a) Experiment (b) CFD, Color Contours (c) CFD, Grayscale

Figure 68: Experimental and CFD Indigo Dye Image, Q_L = 7.0 lpm, Q_G = 0.7 slpm

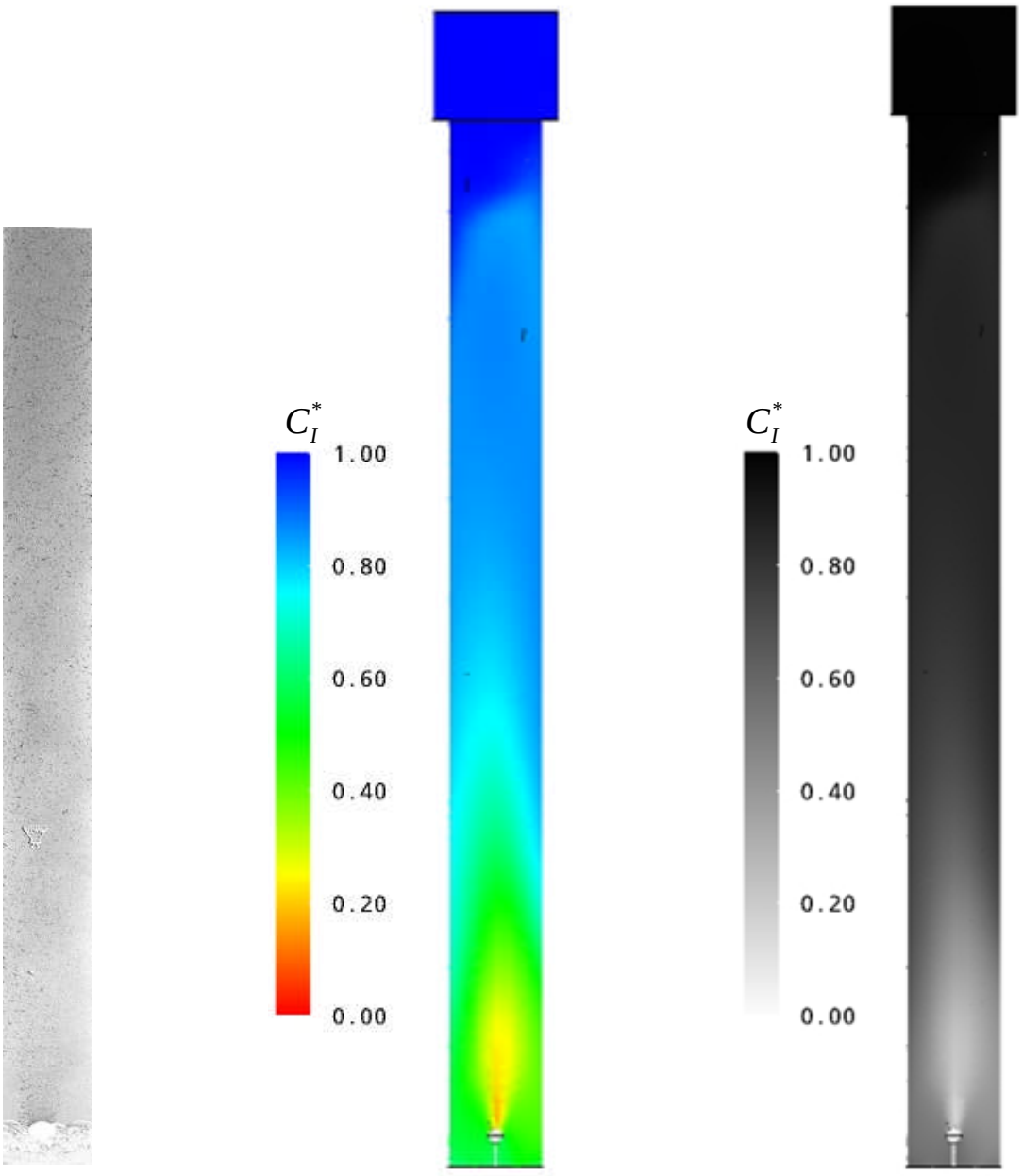

(a) Experiment (b) CFD, Color Contours (c) CFD, Grayscale

Figure 69: Experimental and CFD Indigo Dye Image, Q_L = 13.5 lpm, Q_G = 0.7 slpm

To allow direct comparison of CFD predictions with data from mass transfer visualization images, CFD predictions for indigo dye concentration were averaged on horizontal planes (area-weighted averaging) and plotted along with radially-average indigo dye data. The results of this comparison are plotted in Figure 70- Figure 73. Figure 70 shows a plot of CFD and experimental average indigo dye concentrations measured/calculated at a gas flow rate of 0.4 slpm and a liquid flow rate of 7.0 lpm. The CFD model predicts the slope of the experimental indigo dye curve quite well, though the CFD results are off-set from the experimental results. Figure 71 compares measured and predicted indigo dye concentration at a gas flow rate of 0.4 slpm and a liquid flow rate of 13.5 lpm. Again, the CFD results have the same slope as the experimental results, but are significantly off-set from the experimental values. Figure 72 compares measured and predicted indigo dye concentration at a gas flow rate of 0.7 slpm and a liquid flow rate of 7.0 lpm. The CFD predictions are in worse agreement with experimental values at these operating conditions than for any other cases, though the CFD model predicts the net indigo dye consumption in the reactor fairly accurately. It appears the CFD model does not adequately model the mixing zone near the sparger. Finally, Figure 73 compares measured and predicted indigo dye concentration at a gas flow rate of 0.7 slpm and a liquid flow rate of 13.5 lpm. Again, the CFD model predictions appear offset from the experimental values.

One plausible explanation for the offset observed between observed and predicted indigo dye concentrations is uncertainty in reactor influent indigo dye concentration.

Indigo dye solution was delivered to the influent plumbing via a peristaltic metering pump. Prior to experiments, the pump was calibrated via measurement of water flow rate and comparison with pump read-out. These measurements were made with the pump discharging to atmospheric pressure through a short length of tubing. It is possible that, with the pump delivering water to the column, the pump delivery rate differed from that measured during calibration studies or that the pump delivery rate varied during experiments due to chaffing of the tube through indigo dye solution was delivered.

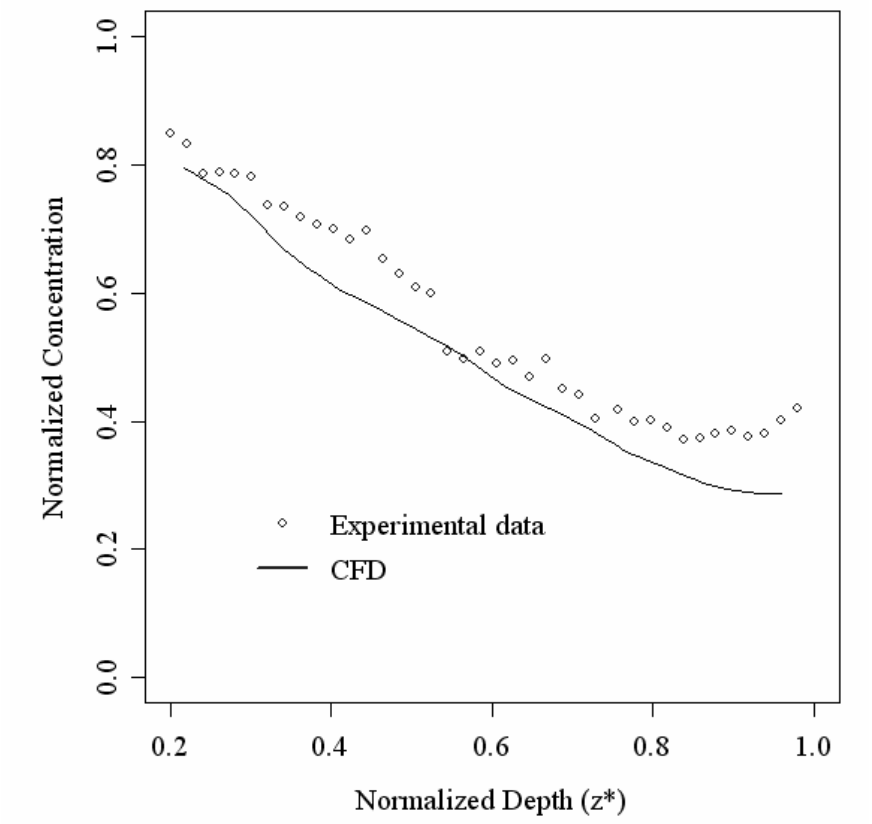

Figure 70: Comparison of CFD and Experimental Indigo Dye Concentration Data, Q_6=0.4 slpm, Q_L=7.0 lpm

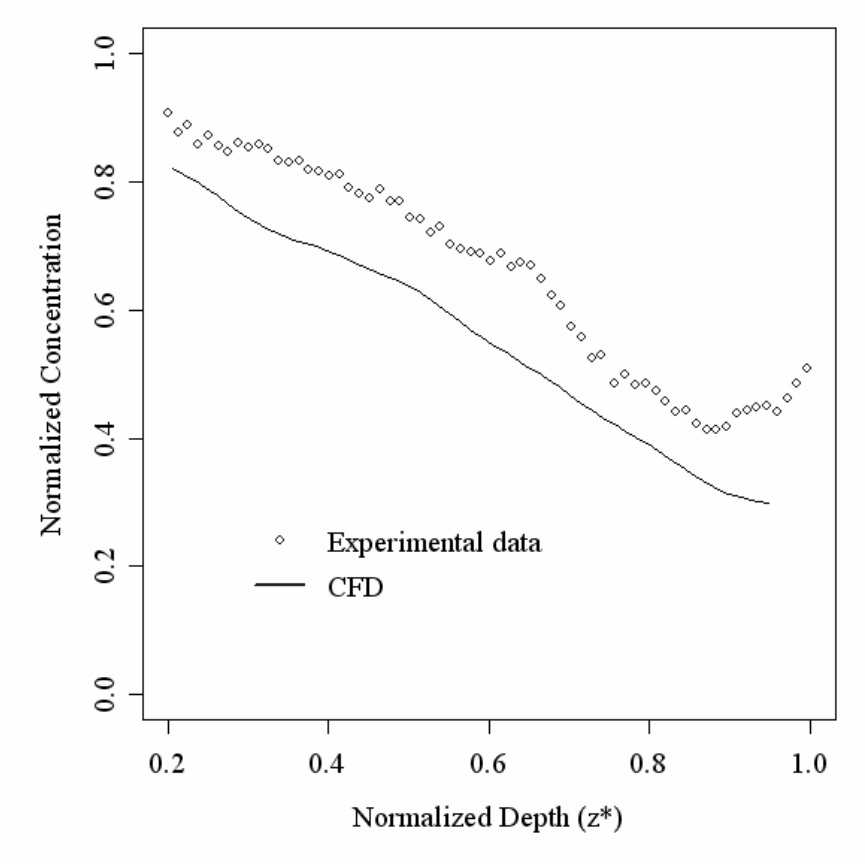

Figure 71: Comparison of CFD and Experimental Indigo Dye Concentration Data, Q_6=0.4 slpm, Q_L=13.5 lpm

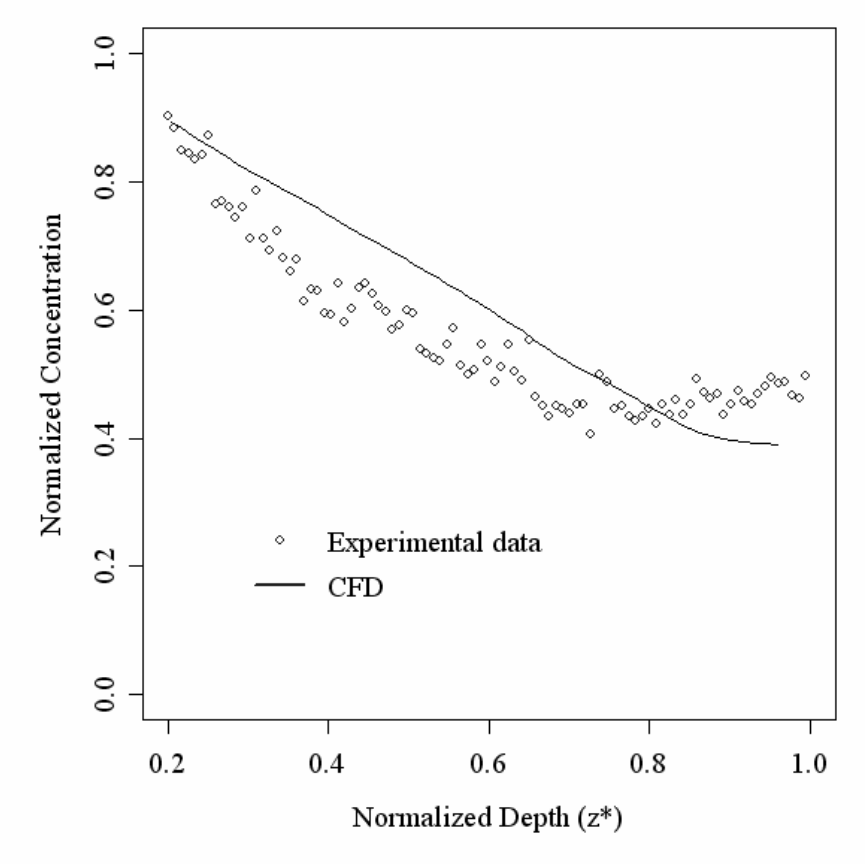

Figure 72: Comparison of CFD and Experimental Indigo Dye Concentration Data, Q_6=0.7 slpm, Q_L=7.0 lpm

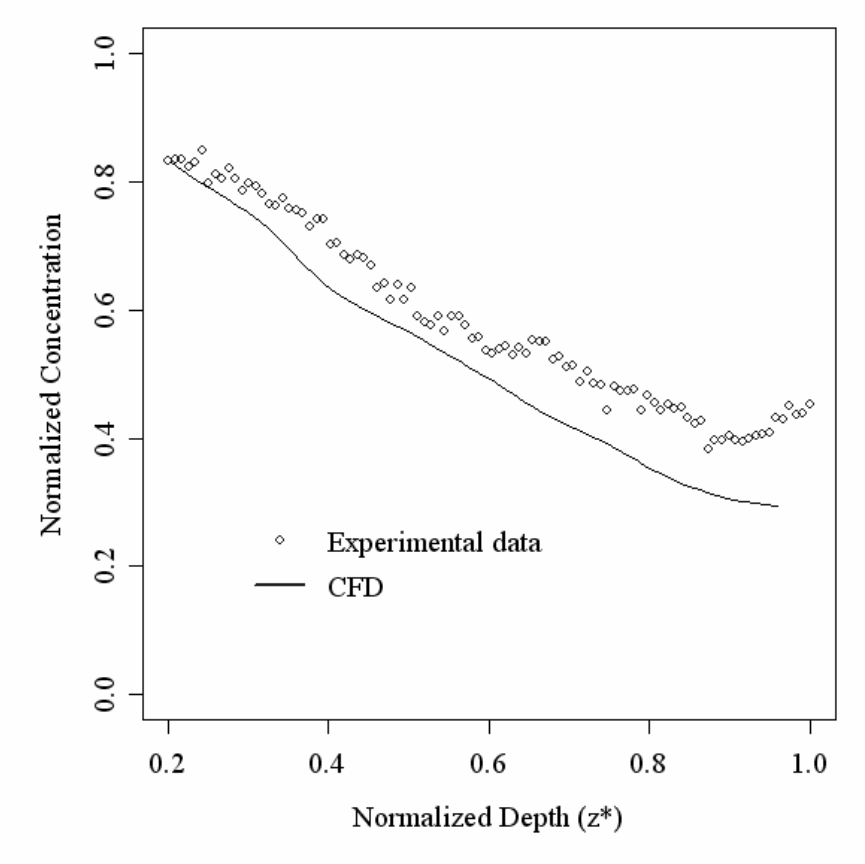

Figure 73: Comparison of CFD and Experimental Indigo Dye Concentration Data, Q_6=0.7 slpm, Q_L13.5 lpm

VII CRYPTOSPORIDIUM INACTIVATION AND BROMATE FORMATION IN A FULL-SCALE REACTOR

A rough CFD model was developed to demonstrate CFD prediction of mass transfer, *Cryptopsoridium parvum* inactivation, bromate formation and ozone decay in a full scale reactor. Here, rough means 2-dimensional and with a relatively coarse mesh. Because the intent of the full scale modeling effort was demonstration and not rigorous prediction, the rough model was deemed adequate. Had more accurate results been required, a more detailed CFD study would have been conducted more methodically and would have included a mesh sensitivity analysis and validation with experimental data.

VII.1 Description of Full Scale Reactor

The full-scale reactor modeled in this demonstration is the Alameda County Water District (ACWD) ozone contactor located in Fremont, CA. Design and operating condition details for the reactor were drawn from the study by Tang et al. (2005). In that study, the authors assessed the ability of the one-dimensional advection-dispersion-reaction model (ADR) to predict *Cryptosporidium parvum* inactivation and bromate formation in a full scale reactor. The authors determined that the ADR model, when calibrated with dispersion data from tracer studies, provided "good" agreement with experimental data (calculated v. predicted ozone residual, *Cryptosporidium parvum* surrogate concentration and bromate concentration) for most cases, though for at least two operating conditions predicted ozone residual was significantly different from measured residual. The authors suggested poor agreement in those cases might have

been the result of variation in water quality during experiments or might have been related to their model's simplifying assumptions. They also suggested that backmixing strongly influences bromate formation, which suggests the ADR model, which does not formally incorporate backmixing, may not be the optimal model for use in predicting bromate formation in full scale reactors.

A schematic diagram showing the full-scale contactor is provided in Figure 74. Reactor dimensions and other design data were taken from a published study of the hydrodynamics and disinfection efficiency of the full scale reactor (Mariñas et al., 1999). The two, two-phase chambers are operated in countercurrent mode. Based on data presented in one study of the full scale reactor (Tang et al., 2005), the ozone generator feed gas is dried air and gas to liquid flow ratio in the reactor varied between 0.083 and 1.4. Gas was injected through fine pore diffusers. The shape and spacing of the diffusers were not reported.

In the rough (two dimensional) CFD model developed for the reactor shown in Figure 74, several simplifications of reactor geometry were made. The simplifications were made because detailed design data were not available. Had these data been available, developing a more accurate model geometry and improved mesh would have been straightforward and would not have resulted in significant increases in the CPU time required to generate solutions.

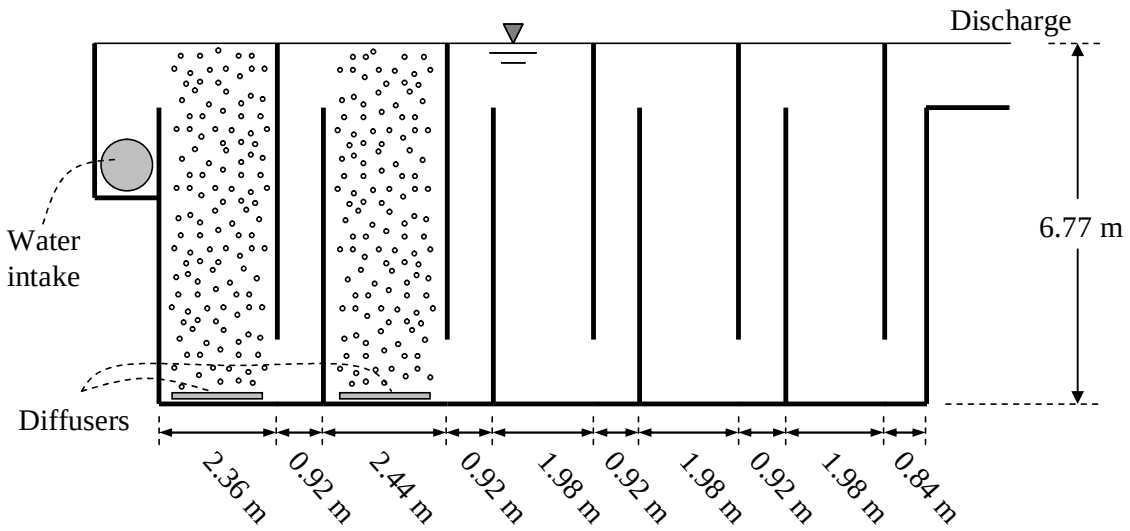

Figure 74: ACWD Full Scale Reactor Schematic Diagram

VII.2 Full Scale Reactor CFD Model

VII.2.1 CFD Model General Features

The major features of the full scale reactor CFD model were largely the same as those of the laboratory reactor CFD model:

- Two phase flow was modeled using an Eulerian-Eulerian treatment.
- Bubbles were assumed monodisperse with a bubble diameter of 2.5 mm.
- Bubble drag was calculated using the Grace drag model and ozone mass transfer was calculated using the Higbie mass transfer model.
- Dirichlet (specified normal velocity) boundary conditions were used for the water and

gas intakes; a pressure boundary condition was applied at the water discharge. The water free surface was specified as a "degassing" boundary (free-slip boundary for the liquid flow, zero gradient boundary for the gas phase).

A schematic diagram showing the CFD model is presented in Figure 75.

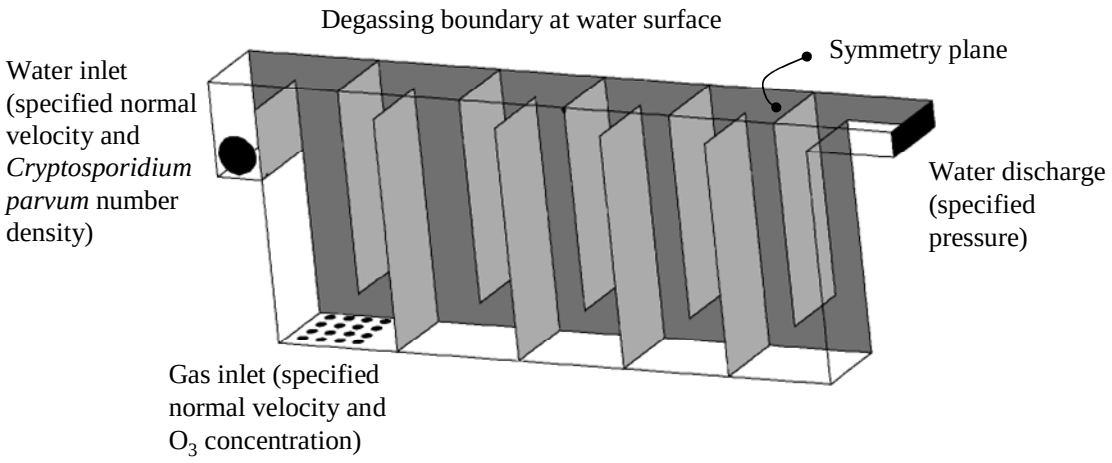

Figure 75: Full Scale Reactor CFD Model Schematic Diagram

To reduce computation time, only half the reactor was modelled and a symmetry boundary condition was imposed at the reactor midplane, as shown in Figure 75. A relatively coarse unstructured mesh with a total of 704,200 elements was employed. Elements were clustered near the inlet, the spargers and the underflows/overflows of the baffles.

VII.2.2 Cryptosporidium Inactivation and Bromate Formation Submodels

In the CFD model, scalar transport and reaction rate expressions were included for ozone decay, ozone demand (by natural organic matter [NOM]), bromate formation and *Cryptosporidium parvum* inactivation. Reaction rate expressions for all of these constituents were those reported by Tang (2005) and presented below.

Ozone demand was modeled with first-order kinetics and, based on batch ozone decay studies, the decay constant was $k_{O_3} = 0.011 \pm 0.001\ s^{-1}$. The authors modeled bromate formation as first order with respect to ozone concentration. Based on semi-batch ozonation studies, the rate constant for bromate formation was estimated to be $9.4 \times 10^{-5}\ s^{-1}$. Though the bromate formation model and rate constant are consistent with data collected in batch experiments, their utility for waters other than those tested seems unlikely, since the bromate formation rate is not dependent on raw water bromide or ammonia concentrations.

C parvum inactivation was assumed to follow Chick kinetics (overall second order, first order in both ozone concentration and *C parvum* oocyst density). Based on *Ct* values in the LT2ESWTR (Table 1), the rate constant was $k_N = 0.0917 \times 1.097^T$, where T is temperature in °C.

Rate expressions for ozone decay, ozone demand, bromate formation and *C. parvum* inactivation are summarized in Table 23.

Table 23: Rate Expressions and Constants, Full Scale CFD Model

Reaction	Rate expression	Rate constant	Notes
Ozone decay	$\frac{dC_{O_3}}{dt} = k_{O_3} C_{O_3}$	$k_{O_3} = 0.011 \pm 0.001\ \text{s}^{-1}$	Batch experiments performed at 20°C
Ozone demand	$\frac{dC_{O_3}}{dt} = k_{\text{NOM}} C_{O_3} C_{\text{NOM}}$	$k_{\text{NOM}} = 3.20 \pm 0.16\ \text{L / mg - s}$	Approximation developed to ensure demand occurs much faster than decay and inactivation
Bromate formation	$\frac{dC_{\text{BrO}_3}}{dt} = k_{\text{BrO}_3} C_{O_3}$	$k_{\text{BrO}_3} = 9.4 \times 10^{-5}\ \text{s}^{-1}$	Developed based on batch experiments. Initial bromide concentration not reported
C. parvum inactivation	$\frac{d\,N}{dt} = k_N C_{O_3} N$	$k_N = 0.0917 \times 1.097^T\ \text{L / mg}_{O_3}\text{ - min}$	Based on *Ct* tables rather than batch experiments

VII.3 Phase Distribution and Flow Field

Gas volume fraction contours predicted by the CFD model for the reactor operating at a gas flow rate of 404 standard cubic meters per hour and a liquid flow rate of 15.5 MGD (2.01 m^3/s) are presented in Figure 76 -Figure 78. Gas volume fraction is the volume occupied by gas within a given reactor volume. Figure 76 shows gas volume fraction on a vertical plane at the midsection of the computational domain. The bubble plumes from the individual diffusers do not rise straight upward. Rather, they are drawn

toward the reactor headwall and coalesce as they rise. The tendency of bubble plumes to be drawn toward walls and coalesce is consistent with the experimental observations of Freire et al. (2002). Another factor in the deflection of the bubble plume toward the headwall is the large clockwise circulation generated in the dissolution chamber by the horizontal introduction of water to the chamber. This phenomenon is illustrated below.

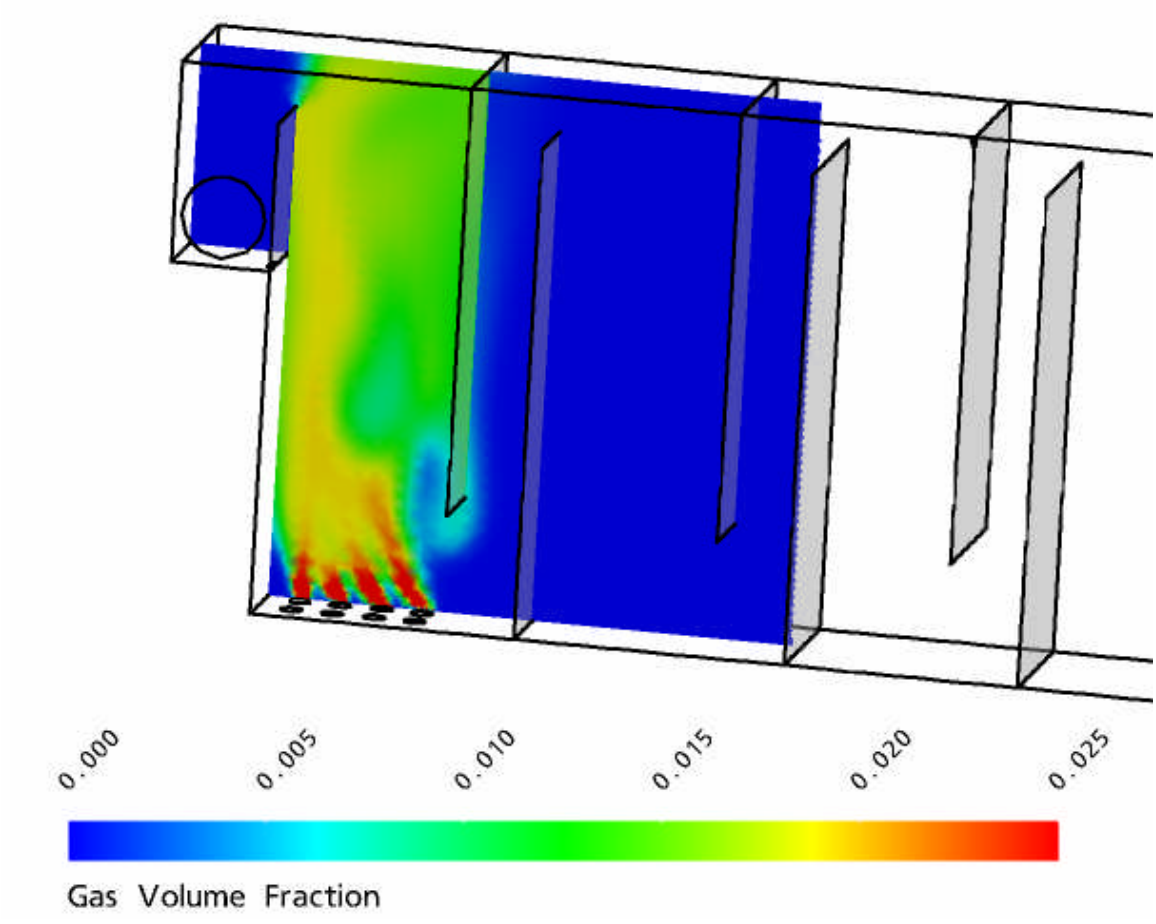

Figure 76: Gas Volume Fraction Contours, Full Scale Reactor, Vertical Plane

The distribution of gas on a horizontal plane near the sparger and on a horizontal

plane at the midheight of the reactor are shown in Figure 77 and Figure 78, respectively. These figures show the migration of the bubble plume toward the center of the reactor (due to coalescence of bubble plumes) and the presence of large vortices (diameter on the order of the chamber length) in the dissolution chamber. The gas volume fraction contours show a non-uniform and three dimensional distribution of gas in the reactor.

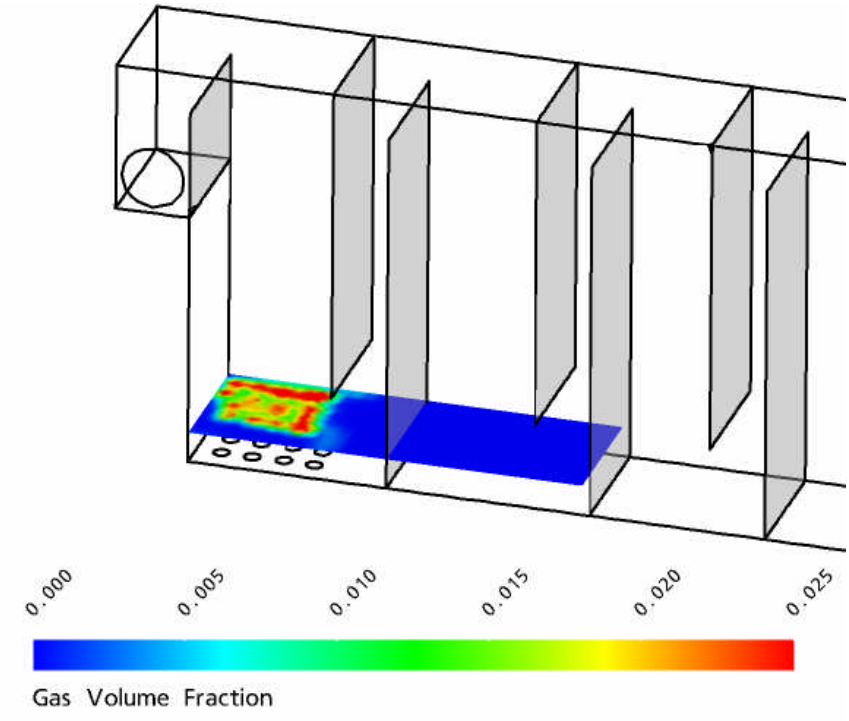

Figure 77: Gas Volume Fraction Contours, Full Scale Reactor, Horizontal Plane near the Spargers

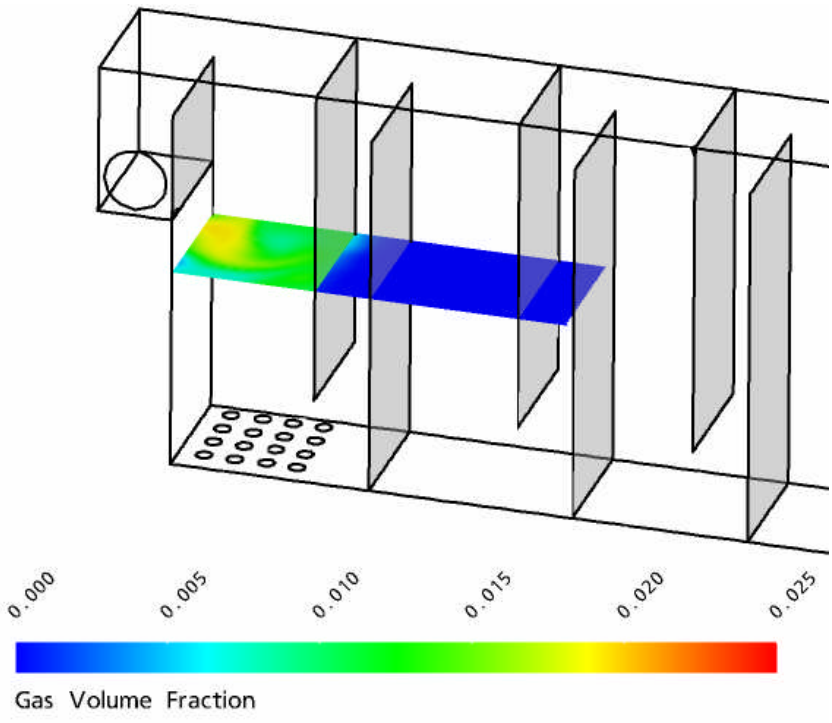

Figure 78: Gas Volume Fraction Contours, Full Scale Reactor, Horizontal Plane at the Reactor Mid-height

Superficial velocity vectors on a vertical plane in the first 6 and last 6 chambers of the reactors are shown in Figure 79 and Figure 80, respectively. In the vector plots, the magnitude of the vector is indicated by its color and vectors were not projected onto the plane.

In the ozone dissolution chamber (with the diffusers on the bottom, the momentum of the influent water stream creates several large recirculations whose length scales are on the order of the chamber width, as seen in Figure 79. There is a strong upward flow along the reactor headwall and a strong downward flow of liquid at the

upstream face of the first baffle. In the second large chamber, circulation is also pronounced and water follows a serpentine path as it traverses the reactor. In subsequent chambers (shown in Figure 80) the water flow path becomes better defined, tending to flow preferentially at the upstream face of each baffle. The hydrodynamics illustrated in Figure 80 deviate significantly from plug flow. In the final 5 chambers the main water flow path occupies less than half the available cross sectional area and there are large recirculating regions present in each chamber. As shown below, the presence of the preferential flow path results in short circuiting of pathogens past treatment and the presence of recirculating regions results in prolonged contact between bromide and ozone and contributes to bromate formation.

Tracer studies performed by Tang et al. indicate that in the AWCD ozone bubble contactor, the ozone dissolution chambers behave as CSTRs. This result supports the approach proposed by Lev and Regli (1992b) of treating bubbled chambers as CSTRs in assigning *Ct* credit. This result also indicates that conditions conducive to higher than expected bromate formation exist (Tang et al., 2005), though in the prior study no rigorous modeling or experimental work provided conclusive evidence that these recirculating regions are indeed bromate formation “hot spots.”. The fluid recirculating in the center of the dissolution chambers has a high residence time and potentially a high ozone concentration.

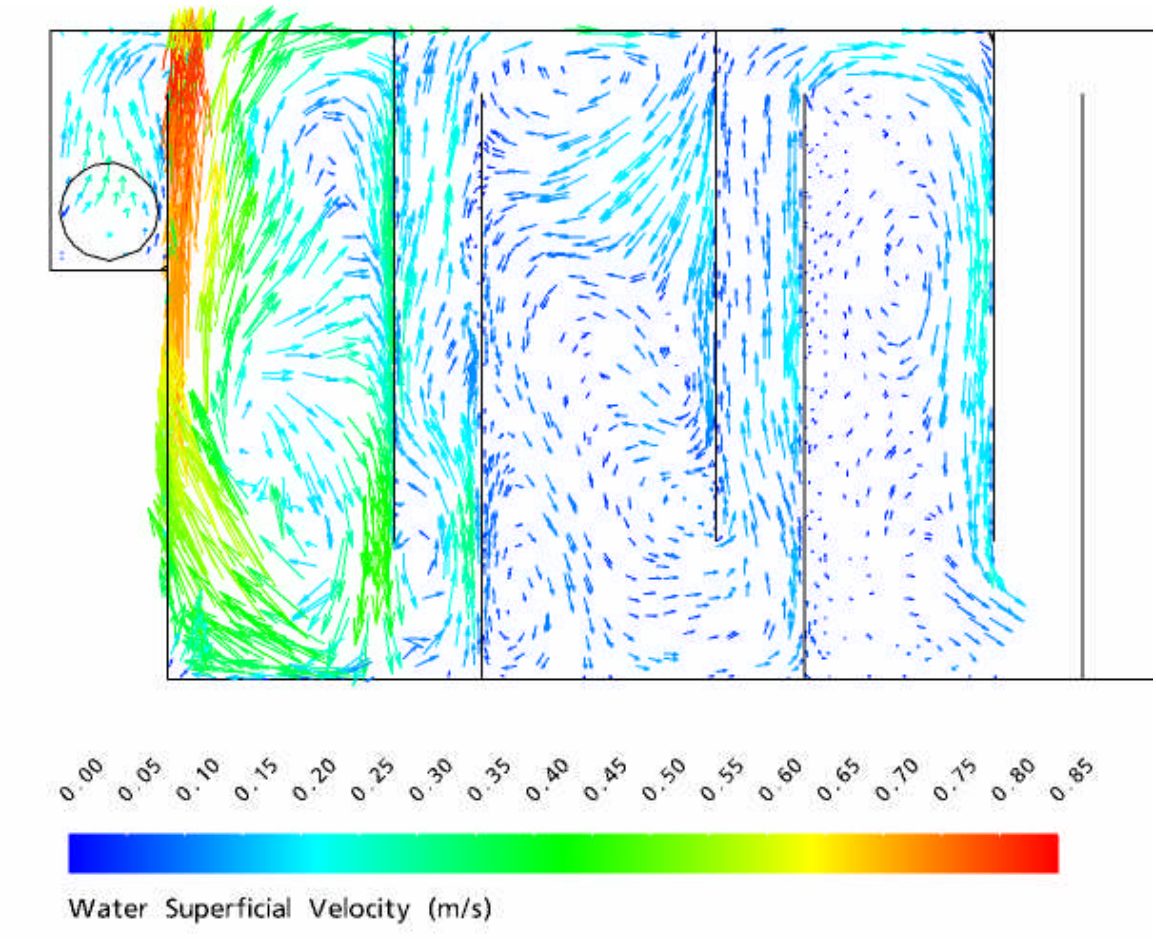

Figure 79: Water Superficial Velocity Vectors, Chambers 1 - 5, Full Scale Reactor

Like serpentine horizontal reactors, the 180° turns employed in the full scale reactor design produce dead zones and large recirculations that reduce the effective chamber cross sectional area and cause flow to deviate from plug flow, even in the narrow chambers in which net water flow is upward. To improve non-ideal hydrodynamics such as those seen in Figure 79 and Figure 80, engineers usually modify

under-over baffle reactors by modifying baffle spacing (Cockx et al., 1999; Do-Quang et al., 1999), modifying baffle gap distance (between the baffle and reactor floor) (Henry and Freeman 1995), or by adding partial baffles that may be solid or perforated (Heathcote and Drage 1995).

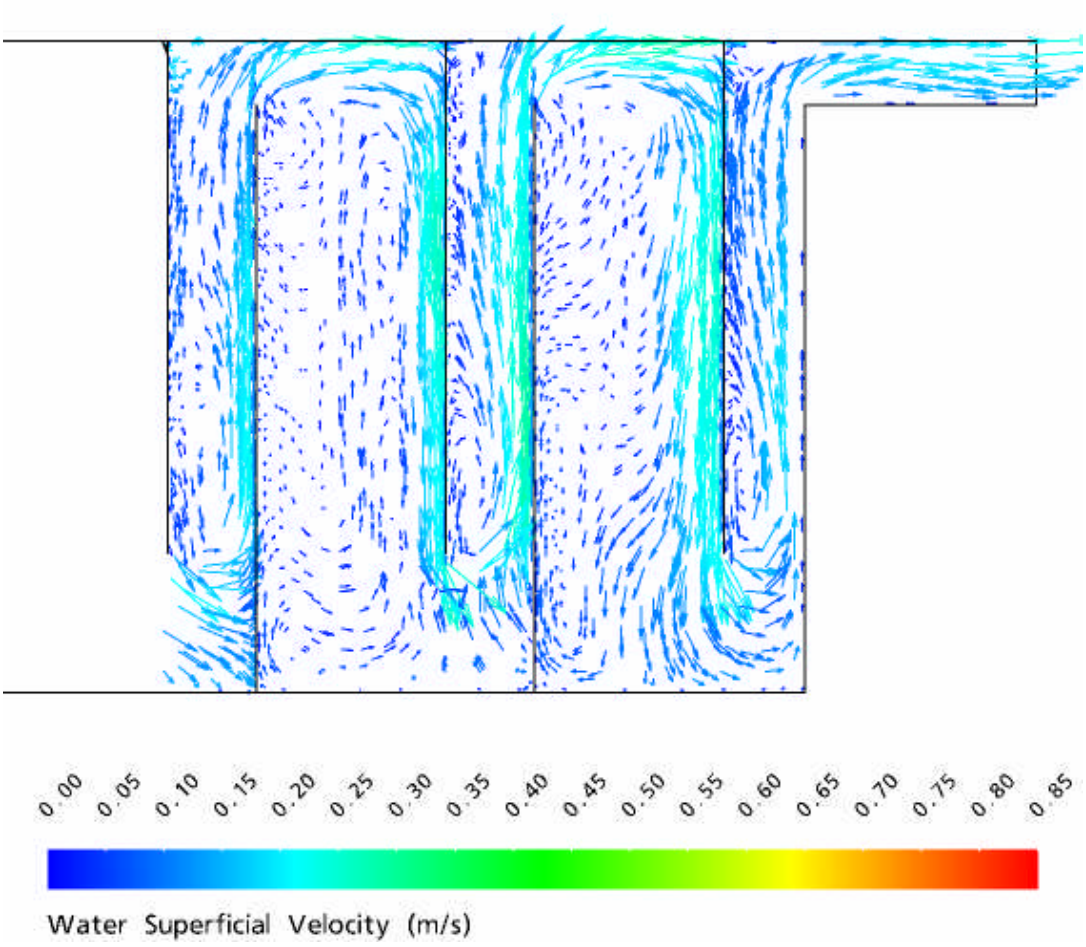

Figure 80: Water Superficial Velocity Vectors, Chambers 6 - 10, Full Scale Reactor

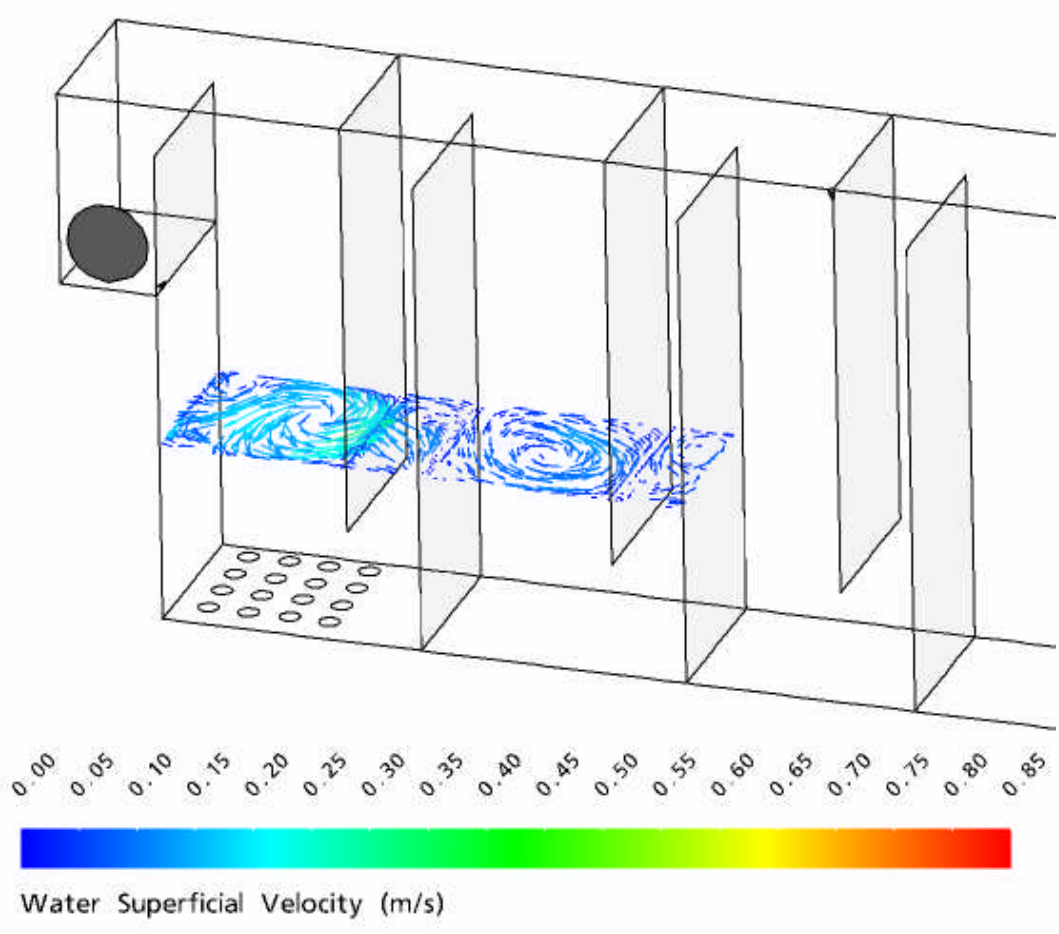

Figure 81: Water Superficial Velocity Vectors, Full Scale Reactor, Horizontal Plane, Chambers 1 – 4, Projection Tangential to Plane

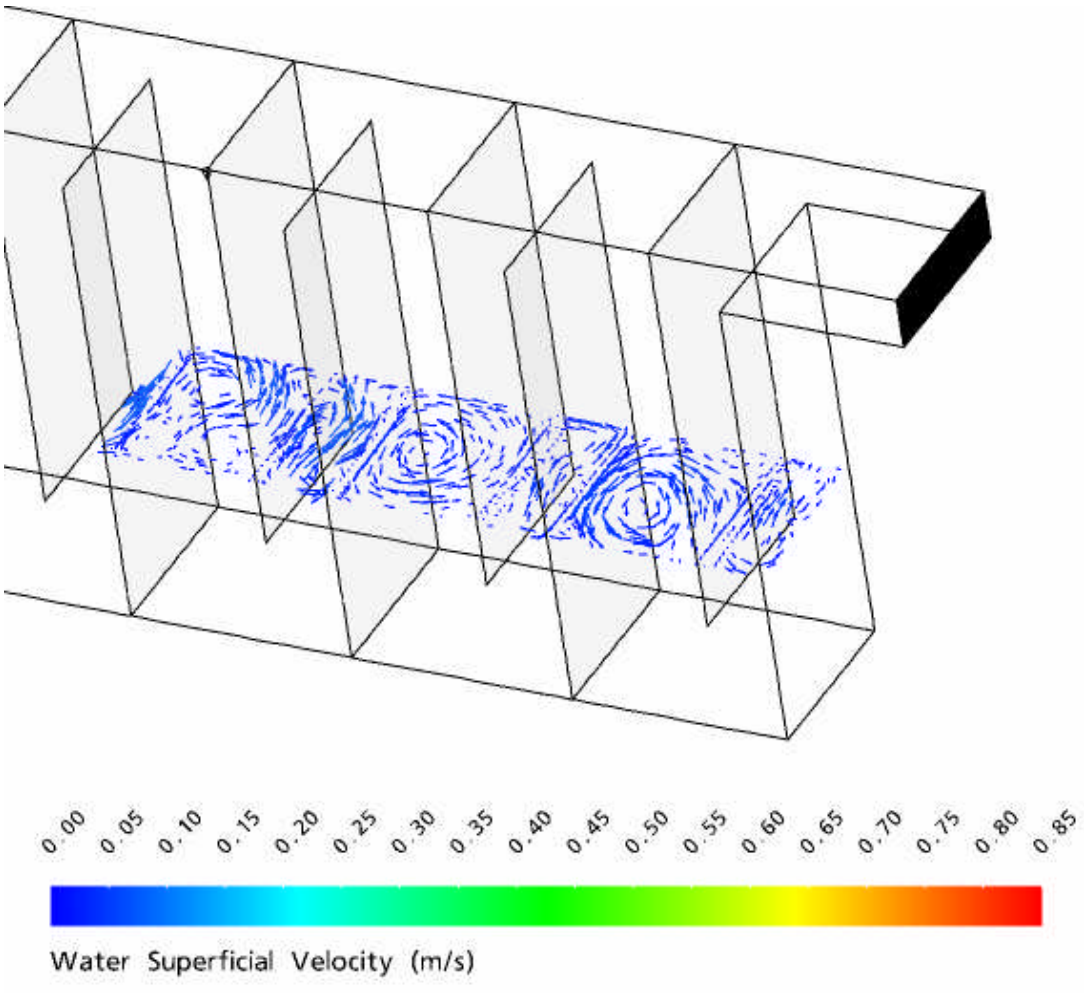

Figure 82: Water Superficial Velocity Vectors, Full Scale Reactor, Horizontal Plane, Chambers 5 – 10, Projection Tangential to Plane

VII.4 Inactivation and Comparison to Log Credits from Ct Models

CFD predictions for ozone residual, bromate concentration and *Cryptosporidium oocyst* number are presented in Figure 83, Figure 84 and Figure 85, respectively.

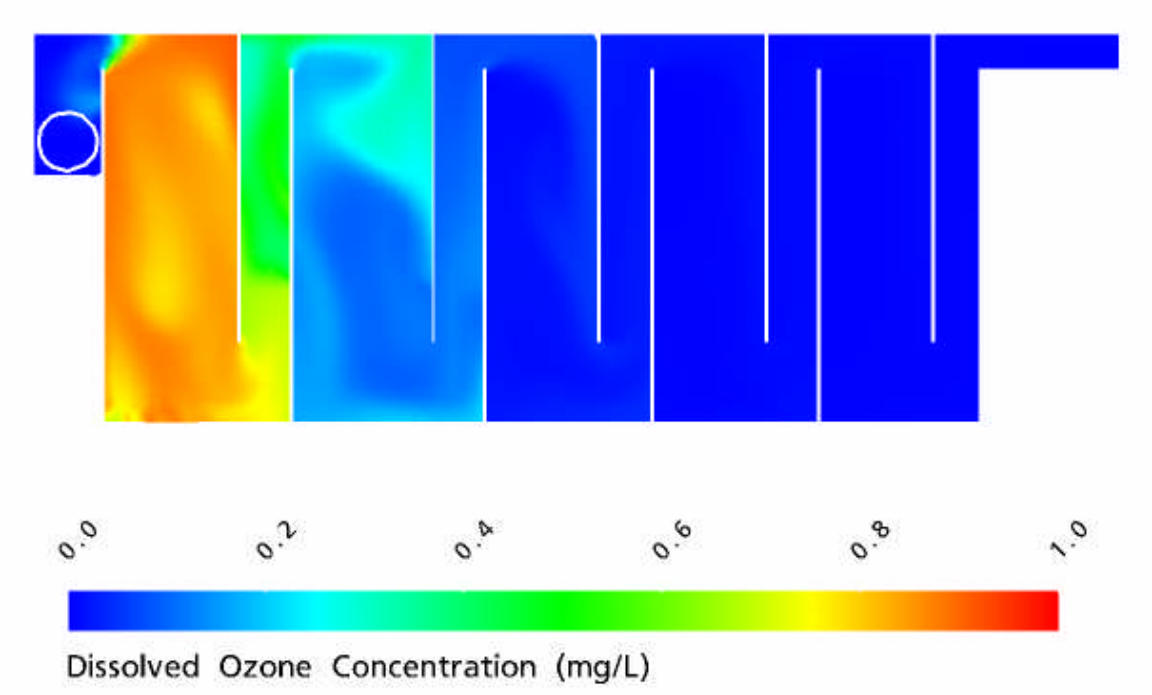

Figure 83: Dissolved Ozone Concentration Contours, Full Scale Reactor

As measured in the full scale contactor (Tang et al., 2005), ozone residual at the reactor discharge is less then 0.05 mg/L. The predicted ozone residual profile seen in Figure 83 indicates that full advantage is not being used of the reactor volume. Because no *Ct* credit is awarded for the first chamber (the only chamber with a high discharge ozone residual), the only chamber contributing significantly to *Ct* is the second chamber in which ozonated air is bubbled. From a *Ct* credit standpoint, a better operating condition would be application of only enough ozone to overcome fast demand in the first chamber and increasing ozone application in the second bubbled chamber. This approach would result in higher ozone residual in the last 6 chambers of the reactor. For

the first ozone dissolution chamber, the regulatory approach of not allowing any disinfection credit presents a disincentive to good design (i.e., ozone application in the two chambers that maximizes transferred dose and mixing) and is inconsistent with the observation that significant disinfection can take place in a chamber that has low or no measurable ozone residual in its effluent (Xu et al., 2002). Regardless of the point of application of ozone, ozone decay is a serious problem in this reactor.

Because bromate formation rate was modeled as first order with respect to ozone residual, bromate contours, shown in Figure 84, are similar to ozone contours. The small region of low bromate concentration water in the discharge pipe is a result of the choice of an entrainment boundary condition. For an entrainment boundary, pressure gradient is set equal to zero and concentration of scalar species for fluid flowing into the boundary is specified (in this case, influent bromate concentration was set equal to zero). Because the low bromate concentration is confined to the discharge pipe, the boundary condition does not influence conditions within the reactor and is considered adequate.

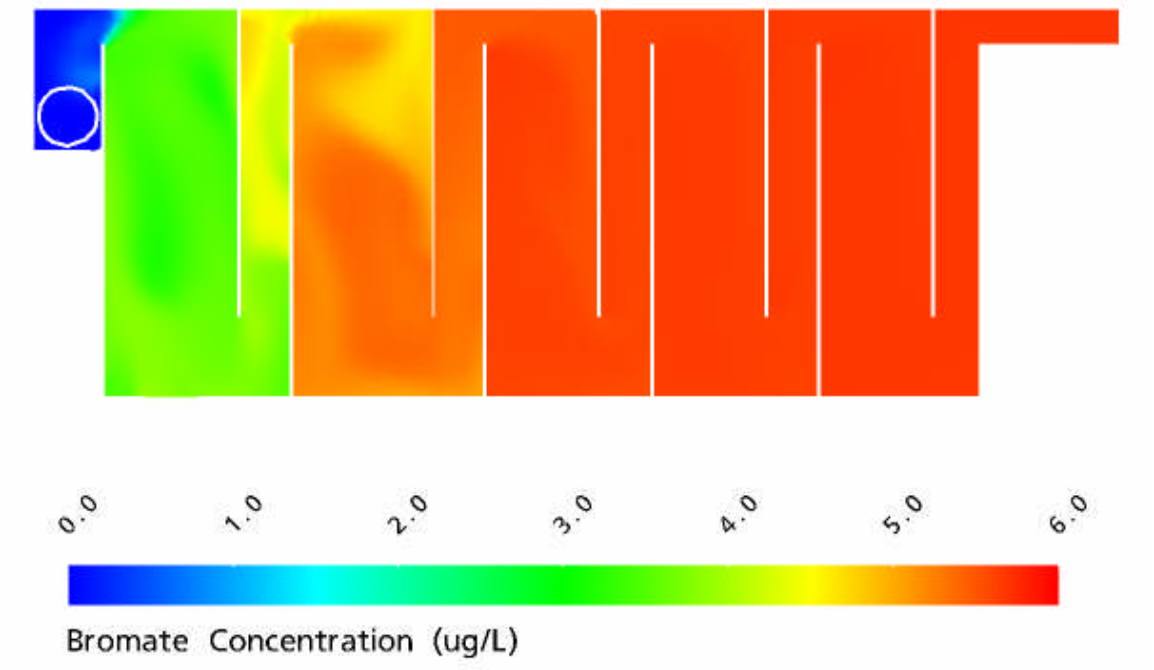

Figure 84: Bromate Concentration Contours, Full Scale Reactor

Recirculating regions are bromate-formation hot spots. This is evident in the bubbled chambers, both of which have large high bromate concentration regions in their centers. Bromate formation in the last 5 chambers of the reactor is minimal, because ozone residual is low. Predicted bromate formation does not exceed the MCL of 10 μg/L, though if higher ozone residual were realized in the reactor, the production of bromate would be higher.

Cryptosporidium parvum density contours, seen in Figure 85, indicate that

- log removal of microorganisms is high for water detained in recirculations in the two

bubbled chambers and

- significant short circuiting exists non-bubbled chambers.

The first observation is consistent with the assumptions used in development of methodology for determining reactor *Ct*. The second observation indicates that, despite their common use, under-over baffled reactors employing 180° turns are prone to dead zones in the corners of the turns and large recirculations in all chambers. These dead zones and recirculations reduce the volume of reactor available for the main liquid flow and promote short circuiting. Short-circuiting, in turn, reduces contact time between microorganisms and disinfectant.

Suboptimal hydrodynamics related to flow through 180° turns occurs in single-phase serpentine chlorine contactors and other chemical disinfection processes as well as in ozone bubble contactors. Systematic study of design modifications that improve hydraulics in such arrangements would be a general benefit to the water treatment industry.

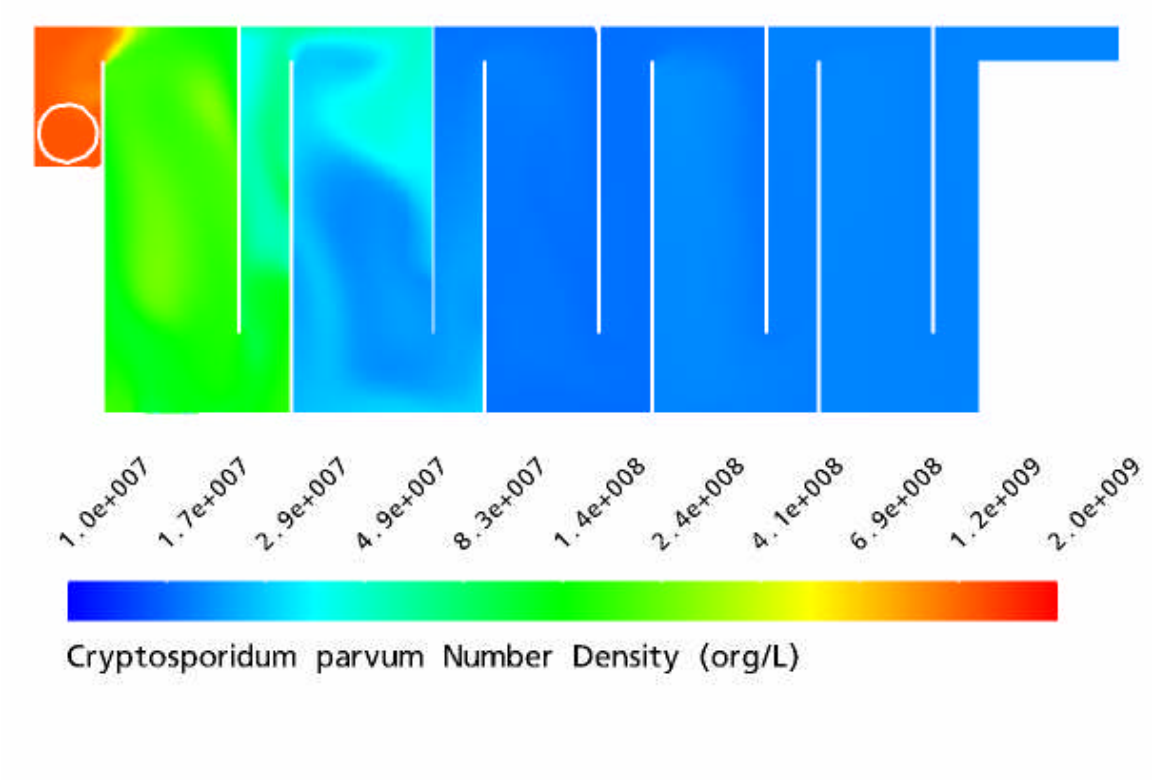

Figure 85: *Cryptosporidium parvum* Density Contours, Full Scale Reactor

VIII CONCLUSIONS AND DISCUSSIONS

VIII.1 Summary of Major Findings

- Three gas flow rate ranges within the ideal bubbly flow regime were identified in which the variation in Peclet number with gas flow rate differed. At low gas flow rates, Peclet number falls sharply with gas flow rate. At intermediate gas flow rates Peclet number does not vary with gas flow rate. At high gas flow rate Peclet number falls with increasing gas flow rate.
- CFD "virtual tracer" studies agreed very well with measured tracer concentrations. CFD analyses predict large vortices are present at the column walls in the vicinity of the sparger. These vortices cause back-mixing of the liquid stream and elongate as gas-to-liquid flow ratio is increased.
- CFD and mass transfer visualization experiments demonstrated that mixing is non-uniform in the column. High-intensity mixing occurs at the bottom of the reactor, which may be regarded as a completely mixed reactor. The length of this well-mixed region increases with increasing gas-to-liquid flow ratio.
- Outside the well-mixed zone, Stanton number increases with increasing gas-to-liquid flow ratio.

VIII.2 Details of Major Findings

Two series of experiments were conducted to quantify mixing in countercurrent bubbly flow, investigate spatial variations in mixing and mass transfer and explore the

advantages of CFD over lower fidelity models such as the ADR and CSTR reactor models for adequately reproducing phenomena observed in experiments. The anticipated benefits associated with these goals were improved bubble contactor designs more consistent with countercurrent hydrodynamics and better modeling leading to informed management of acute and chronic health risks associated with drinking water contaminants.

Tracer studies performed over a range of gas flow rates identified three gas flow rate ranges in which mixing (Peclet number) variation with gas flow rate differed. For gas flow rate below 1.0 slpm, Peclet number fell sharply with increasing gas flow rate. In the gas flow range 1.0 to 2.25 slpm, Peclet number remained constant at 3.0. This finding was consistent with that of one prior study of mixing in countercurrent flow bubbly flow. Above gas flows of 2.25 slpm, Peclet number fell with increasing gas flow rate, following trends predicted by two other prior researchers.

CFD “virtual tracer studies” agreed well with experimental tracer studies and mixing intensity predicted in CFD analyses of countercurrent flow also matched dispersion estimates made in residence time distribution analyses. Peclet number predicted in CFD analyses for the same range of gas flow rates as tracer studies agreed very well with experimental data, especially for gas flow rates at and above 0.5 slpm. CFD analyses also provided insights into the flow field and variation of mixing intensity with height. In the vicinity of the sparger, large vortices are produced by the shear of the down-flowing liquid by the up-flowing bubble plume. As gas flow rate is increased,

these vortices elongate and the bubble plume changes from relatively straight and wide to wavy and narrow as it rises in the column. The large vortices near the sparger back-mix the liquid phase, making the region near the sparger well-mixed, despite poor distribution of phases.

CFD showed the variation in mixing in the reactor to be non-uniform, with much more intense mixing in the bottom of the reactor (near the sparger) than in the top of the reactor. This distribution of mixing intensity would be changed significantly if inlet and discharge configuration were different than those of the laboratory reactor. There are two implications related to the importance of inlet and discharge configurations. First, in addition to other scale-up laws, the influence of inlet and discharge configuration on pilot column hydrodynamics must be considered when scaling to full scale. Second, if poor hydraulic performance is realized in an ozone bubble contactor (e.g., T_{10} / θ is very low or large fluctuations in ozone residuals occur at the reactor discharge), modifications to inlets and discharges for chambers within the reactor offer relatively low-cost means of improvement. Assessment of alternative modifications with a validated CFD model prior to implementation could provide quantitative data on the effect of the alternatives faster, cheaper and with more detail than experiments such as tracer studies or flow visualization experiments.

A technique employing a reactive dye (indigo dye) and digital photography was devised for allowing visualization of mass transfer and investigation of spatial variations in mixing and mass transfer in the reactor. Inspection of images produced using this

technique produced the following observations:

- Indigo dye concentration and ozone dose can be selected to yield wide variation in indigo dye concentration in the reactor.
- In images of indigo dye flowing in the reactor, digital image pixel color varies linearly with indigo dye concentration for indigo dye in the concentration range 0.5 to 6.5 mg/L.
- Indigo dye decolors steadily and uniformly as water flows downward in the top of the reactor.
- Lower in the reactor, there are significant variations in indigo dye concentration at a given reactor axial location.
- Throughout the reactor, liquid flow occurs in two zones – upward flow in the bubble plume and downward flow near the cylinder walls. Flow in the reactor is three dimensional and unsteady, swirling and exhibiting chaotic motions. In the bottom of the reactor, decoloration of indigo dye occurs as eddies of dye-rich water from the downward flow are entrained into the bubble plume and decolored. Had aqueous ozone not been immediately consumed by indigo dye, ozone concentration in the bubble plume (and driving force for ozone mass transfer) would have been higher and mass transfer in the vicinity of the bubbles would have been retarded.
- Near the bottom of the reactor (near the sparger), there is a zone in which indigo dye color is more or less uniform, indicating the liquid contents of that zone are well

mixed. This zone is referred to as the entrance zone and its length increases with gas to liquid flow ratio. As seen in CFD studies, this entrance zone is comprised of a central upward flowing region (the bubble plume) driving large vortices between the bubble plume and reactor walls.

To allow estimation of Peclet number, Stanton number and entrance zone length, indigo concentration data from digital images were radially-averaged and the results were fit using two models: a one-zone model in which the entire reactor was modeled using the ADR model and a two-zone model in which the zone near the sparger was modeled as a CSTR and in the upper zone the ADR model was used. Because data dependence could not be disproved when the radially-averaged data were fit with the single zone model, it was demonstrated that there are two distinct zones of different dispersion and perhaps different mass transfer coefficient in the reactor. This finding is significant given the use of single zone ADR or CSTR models for bubble column flows in pilot studies, full scale reactor analyses and regulatory compliance.

Entrance region length increases with gas to liquid flow ratio. This finding is consistent with CFD predictions that increasing gas flow rate stretches the large vortices present in the vicinity of the sparger. At a gas to liquid flow ratio of 0.1, the entrance region occupies nearly 40% of the reactor height. Future experiments should be directed at determining the dependence of entrance length on water depth in the reactor. It is hypothesized that entrance region length should be independent of water depth; since momentum exchange between the bubble plume and downward flowing liquid

establishes the vortices that define the entrance region, the entrance length should be dependent on gas and liquid flow rates (momentum) and independent of water depth in the reactor.

Stanton number increases with increasing gas to liquid flow ratio. Two phenomena likely play roles in this trend. Higher gas flow rates result in both higher specific surface area and increased turbulence and dispersion generated in bubbles' wakes. In order to determine the roles these phenomena play in dependence of mass transfer on gas to liquid flow ratio, the gas phase holdup must be measured. For the reactor used in the current study, gas phase holdup at 5 points in the reactor could be made using a differential pressure sensor. For a two dimensional reactor, gas phase holdup could be estimated through analysis of digital photographs. Such an analysis would involve bubble identification using particle identification techniques and summing of bubble volumes within regions of the reactor.

Trends of Peclet number with gas to liquid flow ratio could not be determined conclusively. All Peclet number estimates from indigo dye experiments followed trends observed in RTD analyses except a single, low gas to liquid ratio datum at which Peclet number was significantly less than expected. Indigo dye may have been completely depleted in portions of the reactor in the experiment from which the anomalous Peclet number was estimated.

As with mixing investigations, CFD analyses yielded details and insights into countercurrent flow mass transfer. Most important, using an uncalibrated mass transfer

model, the CFD model was able to accurately predict the variation in indigo dye concentration in the reactor over the entire range of liquid and gas flow rates studied. This agreement indicates that despite use of a two-equation turbulence model prone to numerical dispersion, the CFD model predicted mixing of the main liquid flow with the bubble plume sufficiently. Improvement in mass transfer and mixing predictions can be expected if a higher-resolution turbulence model such as LES (large eddy simulation) were used.

CFD simulations predicted and explained an increase in indigo concentration in the vicinity of the sparger observed in numerous mass transfer visualization images. Near the sparger, indigo dye rich water from the reactor walls is back-mixed into the middle of the reactor, resulted in an apparent increase in indigo dye concentration.

VIII.3 Using CFD in Design and Scale-up of Ozone Bubble Contactors

Common use of the advection-dispersion-reaction (ADR) model (LeSauze et al., 1993; Zhou and Smith 1994; El-Din and Smith 2001(a); Kim et al., 2002b; Kim et al., 2005) and the CSTR model (US EPA Office of Drinking Water 1991; LeSauze et al., 1993; Roustan et al., 1996; US EPA Office of Water 2003) for pilot and full scale ozone bubble contactors implies that in countercurrent flow, phases are uniformly distributed and contact between phases is uniform. The current study has shown that this is not the case, even in the relatively simple tall cylindrical bubble column in which experiments were performed. This discrepancy between models and hydrodynamics is significant – modeling reactors as CSTRs provides a conservative estimate of inactivation in full scale

ozone bubble contactors (Lev and Regli 1992a; Lev and Regli 1992b) but leads to designs prone to unnecessary bromate production (Tang et al., 2005).

As an alternative to the ADR and CSTR models, CFD can deliver realistic estimates for microbial inactivation and for chemical species whose rate of production can be dependably represented by a set of elementary reactions or a global reaction expression. These CFD models can be developed using mass transfer and bubble transport submodels drawn from empirical and semi-empirical studies and using batch kinetic data for chemical species and microorganisms. Unlike models such as the ADR which are calibrated using data from pilot studies, CFD models are based on first-principles submodels and have validity for reactors of virtually any geometry.

Application of CFD should no longer be limited to modeling and design of unit process operations in very high production plants, as has been the tendency in the past. The resources for producing the CFD models for this thesis (one student under the direction of knowledgeable managers, a desktop computer and a software license) are modest, making CFD accessible, either in-house or through subcontracts, to small utilities in need of improved hydrodynamics, bromate production or design of new disinfection unit operations.

Incorporation of CFD into pilot studies will allow improved scale-up to full scale. As demonstrated in this study, RTD analyses, the most common technique used in pilot reactor hydrodynamics characterization, is not suited to identifying important flowfield features such as the well mixed zone in the reactor bottom, the large recirculating flows

in the vicinity of the sparger, or the flow structures associated with inlets and outlets. The inlet and outlet configuration may dominate pilot reactor hydrodynamics, as seen in the Philadelphia Water Department pilot reactor. Given the importance of inlet and discharge configuration, it would be advisable to perform CFD analysis as a part of the pilot reactor design process.

Accurate depiction of hydrodynamics is important for accurate prediction of the progress of chemical reactions in continuous flow reactors (Hermanowicz et al., 1999; Tang et al., 2005). When chemical reactions are modeled as a sequence of elementary reactions and the fate and transport of intermediate species is included in a CFD model, CFD more accurately predicts the production/consumption of chemical species than lower-fidelity models because chemical reactions occur based on the *local* concentration of all species. There is a limit to the ability of CFD to incorporate species into a chemical reaction model – each species adds to CPU time requirements of a solution and very short-lived species or species whose reaction rate is very fast require very small time steps to avoid numerical instability or overflows.

Finally, it is noted that most ozone bubble column reactors are similar in design. Nearly all ozone contactors have over-under baffle arrangements and similar density of spargers on the reactor floors. CFD could be used in a general exploration of the influence of reactor geometry and operating conditions on hydraulic and disinfection performance of reactors with different chamber aspect ratios, sparger spacings, baffle configurations, gap widths, etc. A systematic study of these design parameters might

yield guidelines for preliminary reactor designs and information helpful in scale-up from cylindrical pilot reactors to full scale.

A specific design modification that should be investigated is exploration of the impact of minor tilts in reactor walls on mixing in ozone contact chambers. As seen in the current work and a prior study (Rice and Littlefield 1987), minor misalignment of a tall cylindrical bubble column away from vertical can increase mixing by an order of magnitude. A reactor designed to take advantage of this phenomenon would be a significant improvement of existing reactors because vigorous mixing would promote more even distribution of phases which, in turn, would result in greater mass transfer rates and less propensity for the liquid phase to short circuit in ozone dissolution chambers.

VIII.4 Critical Review of Ozone Mass Transfer Visualization Technique

The mass transfer visualization technique demonstrated in this study allowed observation of spatial variation in mass transfer rate at a resolution heretofore unreported in the literature and permitted estimation of a gas entrance length region.

Subsequent studies employing the mass transfer visualization technique can benefit from several modifications.

- *Use of a two-dimensional reactor*. The reactor used in this study was designed to be comparable to pilot ozone bubble contactors used in prior studies and to promote, as nearly as possible, axisymmetric flow. Though these goals were met in the reactor

design, the curvature of the reactor distorted color near the reactor walls. Subsequent studies might employ a tall, thin right rectangular cylindrical reactor. In such a reactor, a rod sparger or different numbers and spacings of spherical spargers could be employed. In addition to yielding better digital images, this design could be modeled with a simpler CFD mesh (multi-block structured grid) and would allow easier comparison of CFD results with images from mass transfer visualization experiments.

- Improved background lighting. An alternative lighting scheme that might provide more intense, uniform lighting is shown in Figure 86. Optimization of this scheme will require experimentation with the number and spacing of fluorescent tubes and the thickness and material of the translucent plastic sheet.

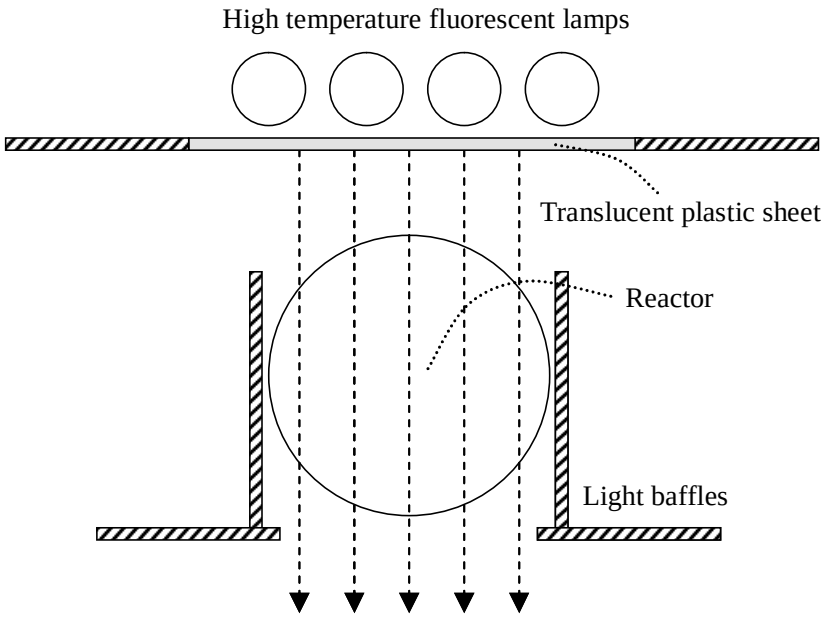

Figure 86: Alternate Lighting Scheme

- Performing all experiments at a single ozone generator voltage and indigo dye concentration. The rationale for choosing the ozone voltage used in the experiments in this study were achieving the greatest change in indigo dye color without completely decoloring the dye within the reactor. Since the optimal voltage was not known precisely for each experiment, multiple cases were run at different voltages for some operating conditions. Influent indigo dye concentration also varied between experiments. These variations in ozone dose and intake indigo dye concentration made direct comparison of mass transfer (indigo consumption) from case to case difficult. Based on the results of the indigo dye mass transfer visualization method reported in this dissertation, future researchers should be able to select an adequate

ozone generator voltage and indigo dye concentration for all experiments.

VIII.5 Balancing Acute and Chronic Risks

As outlined in section Chapter I, it is difficult to design reactors that afford a high level of disinfection while not producing a harmful concentration of disinfection by-products. Relatively long detention times provide a factor of safety and ensure disinfection occurs to a desired level; relatively short residence times diminish disinfection by-product formation. Balancing the acute microbial risks with chronic risks from by-products may require more detailed understanding of the interaction of hydrodynamics, chemistry and microbiology than has traditionally been established prior to design of ozone bubble columns. Here, balancing means designing reactors with a distribution of residence times that are long enough to ensure sufficient disinfection, but not so long that excessive disinfection by-product formation occurs.

Hydrodynamics in bubble column reactors are complex and have a strong influence on both microbial inactivation and disinfection byproduct formation. The preceding work demonstrated that, because bubbled chambers tend to behave as CSTRs, the US EPA's approach of assigning *Ct* credit assuming CSTR behavior is justified and does provide a conservative estimate of microbial inactivation. It also demonstrated that in regard to bromate formation, producing reactors whose chambers behave as CSTRs is not a conservative approach and is not protective of chronic risks from chemical contaminants.

The first step in balancing acute (microbial) and chronic (DBP) risks in fine bubble ozone contactors is improved modeling and identification of hydrodynamics and reactor designs that promote DBP formation. CFD is the only analysis available today that incorporates all necessary processes with the level of detail needed to accurately predict microbial inactivation and disinfection byproduct formation.

The second step is to design reactors with hydraulics in contact chambers closer to plug flow. Developing such reactors will require experimentation. Tracer studies have been used effectively in analysis of reactor hydraulics, but do not provide definitive or specific information about the direction fluids flow in a given region in a reactor, so it is recommended that experimentation be accompanied by CFD analyses. CFD modeling can be less expensive than experimentation and could enable a wider range of design alternatives.

Finally, current regulations and guidelines favor design of reactors that behave as CSTRs. This approach is protective of acute risk but not chronic risk. Allowing use of alternative models (beyond those permitted in the LT2ESWTR) for assessing disinfection efficiency could encourage development of reactors designed to promote disinfection and minimize DBP formation.

LIST OF REFERENCES

Adams, E. W. and W. Rodi (1990). "Modeling Flow and Mixing in Sedimentation Tanks." Journal of Hydraulic Engineering **116**(7): 895-913.

Akita, K. and F. Yoshida (1973). "Gas Hold-up and Volumetric Mass Transfer Coefficients in Bubble Columns." Industrial and Engineering Chemistry; Process Design and Development **12**: 76-80.

Akita, K. and F. Yoshida (1974). "Bubble Size, Interfacial Area, and Liquid-Phase Mass Transfer Coefficient in Bubble Columns." Industrial and Engineering Chemistry; Process Design and Development **13**(1): 84-90.

Alves, S. S., S. P. Orvhalho and J. M. T. Vasconcelos (2005). "Effect of Bubble Contamination on Rise Velocity and Mass Transfer." Chemical Engineering Science **60**: 1-9.

American Public Health Association (1998). Standard Methods for the Examination of Water and Wastewater. Washington, DC, American Public Health Association.

Anderson, J. L. and J. A. Quinn (1970). "Bubble Columns: Flow Transitions in the Presence of Trace Contaminants." Chemical Engineering Science **25**(3): 373-80.

Anderson, K. G. and R. G. Rice (1989). "Local Turbulence Model for Predicting Circulation Rates in Bubble Columns." AIChE Journal **35**(3): 514-8.

ANSYS Europe Ltd. (2004) CFX-5.7.1 5.7.1 Abingdon, UK http://www.ansys.com/cfx

ANSYS Inc. (2004) CFX 5.7 Canonsburg, PA

Bader, H. and J. Hoigné (1981). "Determination of Ozone in Water by the Indigo Method." Water Research **15**(4): 449-56.

Baird, M. H. I. and N. V. R. Rao (1998). "Axial Mixing in a 15 cm Diameter Reciprocating Plate Bubble Column." The Canadian Journal of Chemical Engineering **76**(2-3): 370-378.

Baird, M. H. I. and R. G. Rice (1975). "Axial Dispersion in Large Unbaffled Columns." The Chemical Engineering Journal **9**(1): 171-174.

Bartrand, T. A., D. Santoro, B. Farouk, L. Liberti, M. Notarnicola and C. N. Haas (2005). Effects of Tracer Density on the Hydrodynamics of Two Disinfection Reactors.

Disinfection 2005. Sharing Disinfection Technologies: Water, Wastewater, Water Reuse and Biosolids, Phoenix, AZ, USA.

Benitez, J. (2002). Principles and Modern Applications of Mass Transfer Operations. New York, New York, Wiley-Interscience.

Bernard, R. S., R. S. Maier and H. T. Flavey (2000). "A Simple Computational Model for Bubble Plumes." Applied Mathematical Modelling **24**(3): 215-33.

Bín, A. K. (1995). "Application of a Single-Bubble Model in Estimation of Ozone-Transfer Efficiency in Water." Ozone: Science and Engineering **17**(5): 469-82.

Bín, A. K., B. Duczmal and P. Machniewski (2001). "Hydrodynamics and Ozone Mass Transfer in a Tall Bubble Column." Chemical Engineering Science **56**(21-22): 6233-6240.

Bischoff, K. B. and J. B. Phillips (1966). "Longitudinal Mixing in Orifice Plate Gas-Liquid Reactors." Industrial and Engineering Chemistry Process Design and Development **5**(4): 416-21.

Blanchard, D. C. (1970). "Mechanisms for the Water to Air Transfer and Concentration of Bacteria." Science **170**(3958): 626-8.

Bouaifi, M., G. Hebrard, D. Bastoul and M. Roustan (2001). "A Comparative Study of Gas Hold-up, Bubble Size, Interfacial Area, and Mass Transfer Coefficients in Stirred Gas-Liquid Reactors and Bubble Columns." Chemical Engineering and Processing **40**(1): 97-111.

Brouckaert, C. J. and C. A. Buckley (1999). "The Use of Computational Fluid Dynamics for Improving the Design and Operation of Water and Wastewater Treatment Plants." Water Science and Technology **40**(4-5): 81-9.

Burns, L. F. and R. G. Rice (1997). "Circulation in Bubble Columns." AIChE Journal **43**(6): 1390-1402.

Calderbank, P. H. and M. Moo-Young (1961). "The Continuous Phase Heat and Mass-Transfer Properties of Dispersions." Chemical Engineering Science **16**(1-2): 39-54.

Camarasa, E., C. Vial, S. Poncin, G. Wild, N. Midoux and J. Bouillard (1999). "Influence of Coalescence Behavior of the Liquid and of Gas Sparging on Hydrodynamics and Bubble Characteristics in a Bubble Column." Chemical Engineering and Processing **38**(4-6): 329-44.

Charlton, N. (2003). personal communication. T. Bartrand. Philadelphia, PA.

Chen, J., A. Kemoun, M. H. Al-Dahhan, M. Dudokovic, D. J. Lee and L.-S. Fan (1999). "Comparative Hydrodynamics Study in a Bubble Column Using Computer-Automated Radioactive Particle Tracking (CARPT)/Computer Tomography (CT) and Particle Image Velocimetry (PIV)." Chemical Engineering Science **54**: 2199-2207.

Chen, R. C. and L.-S. Fan (1992). "Particle Image Velocimetry for Characterizing the Flow Structure in Three-Dimensional Gas-Liquid-Solid Fluidized Beds." Chemical Engineering Science **47**(13/14): 3615-22.

Clark, R. M. and B. K. Boutin (2001) Controlling Disinfection By-Products and Microbial Contaminants in Drinking Water. EPA/600/R-01/110. US EPA National Center for Environmental Assessment Cincinnati, OH, USA

Clift, R., J. R. Grace and M. E. Weber (1978). Bubbles, Drops and Particles. New Nork, NY, Academic Press.

Cockx, A., Z. Do-Quang, J. M. Audic, A. Liné and M. Roustan (2001). "Global and Local Mass Transfer Coefficients in Waste Water Treatment Processes by Computational Fluid Dynamics." Chemical Engineering and Processing **40**: 187-94.

Cockx, A., Z. Do-Quang, A. Liné and M. Roustan (1999). "Use of Computational Fluid Dynamics for Simulating Hydrodynamics and Mass Transfer in Industrial Ozonation Towers." Chemical Engineering Science **54**: 5085-90.

Craig, K., C. De Traversay, B. Bowen, K. Essemiani, C. Levecq and R. Naylor (2002). "Hydraulic Study and Optimisation of Water Treatment Processes Using Numerical Simulation." Water Science and Technology: Water Supply **2**(5-6): 135-42.

Danckwerts, P. V. (1951). "Significance of Liquid-Film Coefficients in Gas Absorption." Industrial and Engineering Chemistry **43**(6): 1460-67.

Danckwerts, P. V. (1953). "Continuous Flow Systems. Distribution of Residence Times." Chemical Engineering Science **2**(1): 13-.

Deckwer, W.-D., R. Burckhart and G. Zoll (1974). "Mixing and Mass Transfer in Tall Bubble Columns." Chemical Engineering Science **29**: 2177-88.

Deckwer, W.-D. and A. Schumpe (1993). "Improved Tools for Bubble Column Reactor Design and Scale-up." Chemical Engineering Science **48**(5): 889-911.

Deen, N. G., T. Solberg and B. H. Hjertager (2001). "Large Eddy Simulation of the Gas-

Liquid Flow in a Square Cross-Sectioned Bubble Column." Chemical Engineering Science **56**: 6341-9.

Degaleesan, S., M. Dudokovic and Y. Pan (2001). "Experimental Study of Gas-Induced Liquid-Flow Structures in Bubble Columns." AIChE Journal **47**(9): 1913-31.

Delnoij, E., J. Westerweel, N. G. Deen, J. A. M. Kuipers and W. P. M. van Swaaij (1999). "Ensemble Correlation PIV Applied to Bubble Plumes Rising in a Bubble Column." Chemical Engineering Science **54**: 5159-71.

Do-Quang, Z., A. Cockx and J.-M. Laine (1999). Innovative Design for Enhanced *Cryptosporidium* Removal in a 60 MGC WTP: Use of CFD Modelling and Full-Scale Data. Water Quality Technology Conference, Tampa, FL, American Water Works Association.

Do-Quang, Z., C. C. Ramirez and M. Roustan (2000). "Influence of Geometrical Characteristics and Operating Conditions on the Effectiveness of Ozone Contacting in Fine-Bubbles Conventional Diffusion Reactors." Ozone Science and Engineering **22**(4): 369-78.

Drahos, J., J. Zahradník, M. Fialová and F. Bradka (1992). "Identification and Modeling of Liquid Flow Structures in Bubble Column Reactors." Chemical Engineering Science **47**(13/14): 3313-20.

Driedger, A., E. Staub, U. Pinkernell, B. J. Mariñas, W. Koster and U. Von Gunten (2001). "Inactivation of *Bacillus subtilis* Spores and Formation of Bromate During Ozonation." Water Research **35**(12): 2950-60.

Droste, R. L. (1997). Theory and Practice of Water and Wastewater Treatment. New York, J. Wiley and Sons.

Ducoste, J. J. and M. M. Clark (1999). "Turbulence in Flocculators: Comparison of Measurements and CFD Simulations." AIChE Journal **45**(2): 432-6.

Dudley, J. (1995). "Mass Transfer in Bubble Columns: A Comparison of Correlations." Water Research **29**(4): 1129-38.

El-Din, M. G. and D. W. Smith (2001(a)). "Designing Ozone Bubble Columns: A Spreadsheet Approach to Axial Dispersion Model." Ozone Science and Engineering **23**(5): 369-84.

El-Din, M. G. and D. W. Smith (2001(b)). "Development of Transient Back Flow Cell Model (TBCM) for Bubble Columns." Ozone Science and Engineering **23**(4): 313-26.

Falconer, R. A. and A. I. B. M. Ismail (1997). "Numerical Modeling of Tracer Transport in a Contact Tank." Environment International **23**(6): 763-73.

Field, R. W. and J. F. Davidson (1980). "Axial Dispersion in Bubble Columns." Transactions of the Institution of Chemical Engineers **58**(4): 228-36.

Finch, G. R., C. N. Haas, J. A. Oppenheimer, G. Gordon and R. R. Trussell (2001). "Design Criteria for Inactivation of *Cryptosporidium* by Ozone in Drinking Water." Ozone Science and Engineering **23**: 259-84.

Freire, A. P. S., D. D. E. Miranda, L. M. S. Luz and G. F. M. França (2002). "Bubble Plumes and the Coanda Effect." Intenational Journal of Multiphase Flow **28**(8): 1293-1310.

Gaddis, E. S. (1999). "Mass Transfer in Gas-Liquid contactors." Chemical Engineering and Processing **38**: 503-10.

Goodridge, F. and I. D. Robb (1965). "Mechanism of Interfacial Resistance in Gas Absorption." Industrial and Engineering Chemistry Fundamentals **4**(1): 49-55.

Greene, D. J. (2003). Numerical Simulation of Chlorine Disinfection Processes in Non-Ideal Reactors. School of Environmental Science, Engineering and Policy. Philadelphia, PA, Drexel University**:** 231.

Greene, D. J., C. N. Haas and B. Farouk (2001). "Numerical Simulation of Chlorine Disinfection Process." Water Science and Technology: Water Supply **2**(3): 167-73.

Grevet, J. H., J. Szekely and N. El-Kaddah (1982). "An Experimental and Theoretical Study of Gas Bubble Driven Circulation Systems." International Journal of Heat and Mass Transfer **25**(4): 487-97.

Gyürék, L. L. and G. R. Finch (1998). "Modeling Water Treatment Chemical Disinfection Kinetics." Journal of Environmental Engineering **124**(9): 783-93.

Haas, C. N., J. Joffe, M. Heath, J. Jacangelo and U. Anmangandla (1998). "Predicting Disinfection Performance in Continuous Systems from Batch Disinfection Kinetics." Water Science and Technology **38**(6): 171-9.

Haas, C. N., J. Joffe, M. S. Heath and J. Jacangelo (1997). "Continuous Flow Residence Time Distribution Function Characterization." Journal of Environmental Engineering **123**(2): 107-14.

Harriott, P. (1962). "A Random Eddy Modification of the Penetration Theory." Chemical Engineering Science **17**: 149-54.

Heathcote, G. R. and B. E. Drage (1995). "Development of an Ozone Disinfection Contactor Using a Physical Scale Model." Ozone Science and Engineering **17**(1): 15-24.

Heijnen, J. J. and K. Van't Riet (1984). "Mass Transfer, Mixing and Heat Transfer Phenomena in Low Viscosity Bubble Column Reactors." The Chemical Engineering Journal **28**(2): B21-B42.

Henry, D. J. and E. M. Freeman (1995). "Finite Element Analysis and T_{10} Optimization of Ozone Contactors." Ozone Science and Engineering **17**(6): 587-606.

Hermanowicz, S. W., W. D. Bellamy and L. C. Fung (1999). "Variability of Ozone Reaction Kinetics in Batch and Continuous Flow Reactors." Water Research **33**(9): 2130-8.

Higbie, R. (1935). Transactions of the American Institutes of Chemical Engineers **31**: 65.

Hikita, H., S. Asai, K. Tanigawa, K. Segawa and M. Kitao (1980). "Gas Hold-ups in Bubble Columns." Chemical Engineering Journal **20**: 59-67.

Huang, T., C. J. Brouckaert, M. Docrat and M. Pryor (2002). "A Computational Fluid Dynamic Model and Experimental Study of an Ozone Contactor." Water Science and Technology **46**(9): 87-93.

Hughmark, G. A. (1967a). "Holdup and Mass Transfer in Bubble Columns." I&EC Process Design and Development **6**(2): 218-20.

Hughmark, G. A. (1967b). "Mass and Heat Transfer from Rigid Spheres." AIChE Journal **13**(6): 1219-21.

Ishii, M. and N. Zuber (1979). "Drag Coefficient and Relatively Velocity in Bubbly, Droplet or Particulate Flows." AIChE Journal **25**(5): 843-55.

Jackson, M. L. and C.-C. Shen (1978). "Aeration and Mixing in Deep Tank Fermentation Systems." AIChE Journal **24**(1): 63-71.

Johnson, P. N. and R. A. Davis (1996). "Diffusivity of Ozone in Water." Journal of Chemical Engineering Data **41**(6): 1485-7.

Jones, S. C., F. Sotiropoulos and A. Amirtharajah (2002). "Numerical Modeling of Helical Static Mixers for Water Treatment." Journal of Environmental Engineering

128(5): 431-40.

Kawase, Y. and M. Moo-Young (1987). "Theoretical Prediction of Gas Hold-up in Bubble Columns with Newtonian and non-Newtonian Fluids." Industrial and Engineering Chemistry Research **26**(5): 933-7.

Kawase, Y. and M. Moo-Young (1992). "Correlations for Liquid Phase Mass Transfer Coefficients in Bubble Column Reactors with Newtonian and Non-Newtonian Fluids." The Canadian Journal of Chemical Engineering **70**(Feb. '92): 48-54.

Khudenko, B. M. and E. Shpirt (1986). "Hydrodynamic Parameters of Diffused Air Systems." Water Research **20**(7): 905-15.

Kim, J.-H., J. L. Rennecker, R. B. Tomiak, B. J. Mariñas, R. J. Miltner and J. H. Owens (2002b). "Inactivation of *Cryptosporidium* Oocysts in a Pilot-Scale Ozone Bubble-Diffuser Contactor. II: Model Validation and Application." Journal of Environmental Engineering **128**(6): 522-32.

Kim, J.-H., R. B. Tomiak and B. J. Mariñas (2002a). "Inactivation of *Cryptosporidium* Oocysts in a Pilot-Scale Ozone Bubble-Diffuser Contactor. I: Model Development." Journal of Environmental Engineering **128**(6): 514-21.

Laín, S., D. Bröder and M. Sommerfeld (1999). "Experimental and Numerical Studies of the Hydrodynamics in a Bubble Column." Chemical Engineering Science **54**: 4913-20.

Laín, S., D. Bröder and M. Sommerfeld (2002). "Modeling Hydrodynamics and Turbulence in a Bubble Column Using the Euler-Lagrange Procedure." Intenational Journal of Multiphase Flow **28**(8): 1381-1407.

Lainé, J.-M., L. Phan, P. Pellarin and P. Robert (1999). "Operating Diagnostics on a Flocculator-Settling Tank Using FLUENT CFD Software." Water Science and Technology **40**(4-5): 155-62.

Langlais, B., D. A. Reckhow and D. R. Brink, Eds. (1991). Ozone in Water Treatment: Application and Engineering. Chelsea, MI, Lewis Publishers, Inc.

Lapin, A., T. Paaschen, K. Junghans and A. Lübbert (2002). "Bubble Column fluid dynamics, Flow Structures in Slender Columns with Large-Diameter Ring-Spargers." Chemical Engineering Science **57**: 1419-24.

Lehrer, I. H. (1984). "Turbulent Axial Dispersion Coefficients in the Liquid in a Two-Phase Bubble Column." AIChE Journal **30**(4): 654-7.

LeSauze, N., A. LaPlanche and N. Martin (1993). "Modeling of Ozone Transfer in a Bubble Column." Water Research **27**(6): 1071-83.

Lev, O. and S. Regli (1992a). "Evaluation of Ozone Disinfection Systems: Characteristic C." Journal of Environmental Engineering **118**(July/Aug 1992): 477-94.

Lev, O. and S. Regli (1992b). "Evaluation of Ozone Disinfection Systems: Characteristic Time, T." Journal of Environmental Engineering **118**(March/April 1992): 268-85.

Liu, J., M. Crapper and G. L. McConnachie (2004). "An Accurate Approach to the Design of Channel Hydraulic Flocculators." Water Research **38**: 857-86.

Liu, Z., Y. Zheng, L. Jia and Q. Zhang (2005). "Study of Bubble Induced Flow Structure Using PIV." Chemical Engineering Science **60**: 3537-52.

Lochiel, A. C. and P. H. Calderbank (1964). "Mass Transfer in the Continuous Phase Around Axisymmetric bodies of Revolution." Chemical Engineering Science **19**: 471-84.

Lockett, M. J. and D. Kirkpatrick (1975). "Ideal Bubbly Flow and Actual Flow in Bubble Columns." Transactions of the Institution of Chemical Engineers **53**: 267-73.

Lyn, D. A., A. I. Stamou and W. Rodi (1992). "Density Currents and Shear-Induced Flocculation in Sedimentation Tanks." Journal of Hydraulic Engineering **118**(6): 849-67.

Manly, B. F. J. (1997). Randomization, Bootstrap and Monte Carlo Methods in Biology. London, Chapman and Hall.

Mariñas, B. J., S. Liang and E. M. Aieto (1993). "Modeling Hydrodynamics of Ozone Residual Distribution in a Pilot-Scale Ozone Bubble-Diffuser Contactor." Journal AWWA **85**(3): 90-9.

Mariñas, B. J., J. L. Renneker and S. Teefy (1999). "Assessing Ozone Disinfection with Non-Biological Surrogates." Journal AWWA **91**(9): 79-89.

Mitra-Majumdar, D., B. Farouk and Y. T. Shah (1998). "Two- and Three-Phase Flows in Bubble Columns: Numerical Predictions and Measurements." Industrial and Engineering Chemistry Research **37**(6): 2284-92.

Moore, D. W. (1959). "The Rise of a Gas Bubble in a Viscous Liquid." Journal of Fluid Mechanics **6**: 113-30.

Motarjemi, M. and G. J. Jameson (1978). "Mass Transfer from Very Small Bubbles - the Optimum Bubble Size for Aeration." Chemical Engineering Science **33**(11): 1415-23.

Moustiri, S., G. Hebrard, S. S. Thakre and M. Roustan (2001). "A Unified Correlation for Predicitng Liquid Axial Dispersion Coefficient in Bubble Columns." Chemical Engineering Science **56**: 1041-7.

Murrer, J., J. Gunstead and S. Lo (1995). "The Development of an Ozone Contact Tank Simulation Model." Ozone Science and Engineering **17**(6): 607-17.

Nauman, E. B. (2001). Chemical Reactor Design, Optimization and Scaleup. New York, NY, McGraw-Hill.

Nauman, E. B. and B. A. Buffham (1983). Mixing in Continuous Flow Systems. New York, John Wiley and Sons.

Nieminski, E. C. (1990). "Ozone contactor Hydraulic Considerations i Meeting "Ct" Disinfection Requirements." Ozone Science and Engineering **12**(2): 133-142.

Olmos, E., C. Gentric and N. Midoux (2003). "Numerical Description of Flow Regime Transition in Bubble Column Reactors by a Multiple Gas Phase Model." Chemical Engineering Science **58**: 2113-21.

Owens, J. H., R. J. Miltner, E. W. Rice, C. H. Johnson, D. R. Dahling, F. W. Schaefer III and H. M. Shukairy (2000). "Pilot-Scale Ozone Inactivation of *Cryptosporidium* and Other Microorganisms in Natural Water." Ozone Science and Engineering **22**: 501-17.

Owens, J. H., R. J. Miltner, F. W. I. Schaefer and E. W. Rice (1994). "Pilot-Scale Ozone Inactivation of *Cryptosporidium*." Journal of Eukaryotic Microbiology **41**(5): 56S-57S.

Öztürk, S. S., A. Schumpe and W.-D. Deckwer (1987). "Organic Liquids in a Bubble Column: Holdups and Mass Transfer Coefficients." AIChE Journal **23**(9): 1473-80.

Peebles, F. N. and H. J. Garber (1953). "Studies on the Motion of Gas Bubbles in Liquids." Chemical Engineering Progress **49**(2): 88-97.

Perry, R. H. and C. H. Chilton (1973). Chemical Engineer's Handbook. New York, McGraw-Hill.

Pfleger, D., S. Gomes, N. Gilbert and H.-G. Wagner (1999). "Hydrodynamic Simulations of Laboratory Scale Bubble Columns Fundamental Studies of the Eulerian-Eulerian Modeling Approach." Chemical Engineering Science **54**: 5091-99.

Pinkernell, U. and U. Von Gunten (2001). "Bromate Minimization during Ozonation: Mechanistic Considerations." Environmental Science and Technology **35**(12): 2525-31.

Rakness, K. L. (2005). Ozone in Drinking Water Treatment. Denver, CO, American Water Works Association.

Rakness, K. L., R. C. Renner, B. A. Hegg and A. G. Hill IV (1988). "Practical Design Model for Calculating Bubble Diffuser Contactor Ozone Transfer Efficiency." Ozone Science and Engineering **10**(2): 173-214.

Ranade, V. V. (1997). "Modeling of Turbulent Flow in a Bubble Column Reactor." Chemical Engineering Research and Design **75**(1): 14-23.

Rasband, W. (2005) ImageJ 1.34s National Institutes of Health Atlanta http://rsb.info.nih.gov/ij/

Reith, T., S. Renken and B. A. Israël (1968). "Gas Hold-up and Axial Mixing in the Fluid Phase of Bubble Columns." Chemical Engineering Science **23**: 619-29.

Retallick, W. B. (1965). "Distribution of Residence Times in a Cascade of Mixed Vessels with Backmixing." Industrial and Engineering Chemistry Fundamentals **4**(1): 88-90.

Rice, G. R. and M. A. Littlefield (1987). "Dispersion Coefficients for Ideal Bubbly Flow in Truly Vertical Bubble Columns." Chemical Engineering Science **42**(8): 2045-53.

Roustan, M., J.-P. Duguet, B. Brette, E. Brodard and J. Mallevialle (1987). "Mass Balance Analysis of Ozone in Conventional Bubble Contactors." Ozone Science and Engineering **9**: 289-97.

Roustan, M., J.-P. Duguet, J.-M. Laine, Z. Do-Quang and J. Mallevialle (1996). "Bromate Ion Formation: Impact of Ozone Contactor Hydraulics and Operating Conditions." Ozone Science and Engineering **18**(1): 87-97.

Roustan, M., R. Y. Wang and D. Wolbert (1996). "Modeling Hydrodynamics and Mass Trasnfer Parameters in a Continuous Ozone Bubble Column." Ozone: Science and Engineering **18**(2): 99-115.

Ruzicka, M. C., J. Drahos, M. Fialova and N. H. Thomas (2001). "Effect of Bubble Column Dimensions on Flow Regime Transition." Chemical Engineering Science **56**: 6117-24.

Saberi, S., K. Shakourzadeh and D. Bastoul (1995). "Bubble Size and Velocity Measurement in Gas-Liquid Systems: Application of Fiber-Optic Technique to Pilot Plant Scale." The Canadian Journal of Chemical Engineering **73**(April, 1995): 253-7.

Sanyal, J., S. Vásquez, S. Roy and M. P. Dudukovic (1999). "Numerical Simulation of Gas-Liquid Dynamics in Cylindrical Bubble Column Reactors." Chemical Engineering Science **54**: 5071-83.

Sardeing, R., P. Painmanakul and G. Hébrard (2006). "Effects of Surfactants on Liquid-Side Mass Transfer Coefficients in Gas-Liquid Systems: A First Step to Modeling." Chemical Engineering Science **61**(9): 6249-60.

Sarrot, V., P. Guiraud and D. Legendre (2005). "Determination of the Collision Frequency Between Bubbles and Particles in Flotation." Chemical Engineering Science **60**: 6107-17.

Sato, Y. and K. Sekoguchi (1975). "Liquid Velocity Distribution in Two-Phase Bubble Flow." International Journal of Multiphase Flow **2**(1): 79-95.

Schulz, C. R. and W. D. Bellamy (2000). "The Role of Mixing in Ozone Dissolution Systems." Ozone Science and Engineering **22**(4): 329-50.

Schulz, C. R., C. C. Davis, T. Bonacquisti and R. Navratil (2003). Designing Ozone Systems for *Cryptosporidium* Inactivation: Evaluating Impacts of New EPA CT Requirements. AWWA Water Quality and Technology Conference, Philadelphia, PA, AWWA.

Scott, K. N., R. L. Wolfe and M. H. Stewart (1992). "Pilot-Plant-Scale Ozone and PEROXONE Disinfection of *Giardia muris* Seeded into Surface Water Supplies." Ozone Science and Engineering **14**: 71-90.

Shah, Y. T., B. G. Kelkar, S. P. Godbole and W.-D. Deckwer (1982). "Design Parameters Estimations for Bubble Column Reactors." AIChE Journal **28**(3): 353-79.

Smeets, P. W. M. H., A. W. C. van der Helm, Y. J. Dullemont, L. C. Rietveld, J. C. van Dijk and G. J. Medema (2006). "Inactivation of *Escherichia coli* by Ozone under Bench-Scale Plug Flow and Full-Scale Hydraulic Conditions." Water Research **40**(17): 3239-3248.

Song, R., C. Donohoe, R. Minear, P. Westerhoff, K. Ozekin and G. Amy (1996). "Empirical Modeling of Bromate Formation During Ozonation of Bromide-Containing Waters." Water Research **30**(5): 1161-8.

Song, R., P. Westerhoff, R. Minear and G. Amy (1997). "Bromate Minimization During Ozonation." American Water Works Association Journal **89**(6): 69-78.

Ta, C. T. and W. J. Brignal (1998). "Application of Computation Fluid Dynamics

Technique to Storage Reservoir Studies." Water Science and Technology **37**(2): 219-26.

Ta, C. T. and J. Hague (2004). "A Two-Phase Computational Fluid Dynamics Model for OzoneTank Design and Troubleshooting in Water Treatment." Ozone: Science and Engineering **26**: 403-11.

Tang, G., K. Adu-Sarkodie, D. Kim, J.-H. Kim, S. Teefy, H. M. Shukairy and B. Mariñas (2005). "Modeling *Cryptosporidium parvum* Oocyst Inactivation and Bromate Formation in a Full-Scale Ozone Contactor." Environmental Science and Technology **39**(23): 9343-50.

Teefy, S. M. and P. C. Singer (1990). "Performance and Analysis of Trace Tests to Determine Compliance of a Disinfection Scheme with the SWTR." Journal AWWA **82**(12): 88-98.

The R Foundation (2006). The R Project. **2006**.

Tobiason, J. E., J. K. Edzwald, O. D. Schneider, M. B. Fox and H. J. Dunn (1992). "Pilot Study ofthe Effects of Ozone and PEROXONE on In-Line Direct Filtration." American Water Works Association Journal **84**(12): 72-84.

Trussell, R. R. and J.-L. Chao (1977). "Rational Design of Chlorine Contact Chambers." Journal of the Water Pollution Control Federation **49**(4): 659-667.

U.S. EPA Office of Drinking Water (1991) Guidance Manual for Compliance with the Filtration and Disinfection Requirements for Public Systems Using Surface Water Sources. Prepared under contract number 68-01-6989. Washington DC

Uchida, S., S. Tsuyutani and T. Seno (1989). "Flow Regimes and Mass Transfer in Counter-Current Bubble Columns." The Canadian Journal of Chemical Engineering **67**(5): 866-9.

US EPA (2005) FACTOIDS: Drinking Water and Ground Water Statistics for 2004. EPA 816-K-05-001. United States Environmental Protection Agency Washington D.C.

US EPA Office of Drinking Water (1991) Guidance Manual for Compliance with the Filtration and Disinfection Requirements for Public Systems Using Surface Water Sources. Prepared under contract number 68-01-6989. Washington DC

US EPA Office of Water (1999) Alternative Disinfectants and Oxidants Guidance Manual. EPA 815-R-99-014. United States Environmental Protection Agency Washington DC

US EPA Office of Water (2001) Stage 1 Disinfectants and Disinfection Byproducts Rule. EPA 816-F-01-014. United States Environmental Protection Agency Washington DC

US EPA Office of Water (2003) Long Term 2 Enhanced Surface Water Treatment Rule - Toolbox Guidance Manual. EPA 815-D-03-009. United States Environmental Protection Agency Washington DC

Valade, M., D. Rokjer, R. Peters, D. Kessler and M. Borsykowsky (2003). Development of Alternate Means for Validation of UV Reactors. Water Quality Technology Conference, Philadelphia, PA, AWWA.

Vasconcelos, J. M. T., S. P. Orvalho and S. S. Alves (2002). "Gas-Liquid Mass Transfer to Single Bubbles: Effect of Surface Contamination." AIChE Journal **48**(6): 1145-54.

von Gunten, U. (2003a). "Ozonation of Drinking Water: Part 1. Oxidation Kinetics and Product Formation." Water Research **37**(7): 1443-67.

von Gunten, U. (2003b). "Ozonation of Drinking Water: Part 2. Disinfection and By-Product Formation in Presence of Bromide, Iodide or Chlorine." Water Research **37**(7): 1469-87.

Wang, H. and R. A. Falconer (1998). "Simulating Disinfection Processes in Chlorine Contact Tanks Under Various Turbulence Models and High-Order Accurate Difference Schemes." Water Research **32**(5): 1529-43.

Weber, J. W. J. (2001). Environmental Systems and Processes. NY, NY, John Wiley and Sons.

Westerhoff, P., R. Song, G. Amy and R. Minear (1998). "NOM's Role in Bromine and Bromate Formation During Ozonation." American Water Works Association Journal **89**(11): 82-94.

Wozniak, D., M. Kiwak, C. Cahoon and R. H. Edgerton (1976). "Water to Air Bacterial Transfer by Bacterial Bubbles." Journal of the Environmental Division, Proceedings of the ASCE **102**(EE3): 567-70.

Xu, P., M.-L. Janex, P. Savoye, A. Cockx and V. Lazarova (2002). "Wastewater Disinfection by Ozone: Main Parameters for Process Design." Water Research **36**: 1043-55.

Zhou, H. and D. W. Smith (1994). "Modeling of Dissolved Ozone Concentration Profiles in Bubble Columns." Journal of Environmental Engineering **120**(4): 821-40.

Zhou, S., J. A. McCorquodale and A. M. Godo (1994). "Short Circuiting and Density Interface in Primary Clarifiers." Journal of Hydraulic Engineering **120**(9): 1060-80.

APPENDIX A: LIST OF SYMBOLS

Variable	Description
a	Specific interfacial area
A	Area
Bo	Bond number
C_D	Drag coefficient
C_I	Indigo dye mass concentration
C_{O_3}	Dissolved ozone mass concentration
d_B	Bubble diameter
D_i	Binary diffusion coefficient of species i
E	Axial dispersion (L^2/T)
$E(t)$	Expectation
Eo	Eotvos number
F	Normalized tracer concentration
g	Gravitational acceleration
G_a	Galileo number
H	Reactor height
I_T	Turbulent kinetic energy intensity
k_{BrO_3}	Bromate reaction rate coefficient
k_L	Liquid side mass transfer coefficient
k_N	Microbial inactivation rate coefficient
k_{O_3}	Ozone autodecomposition reaction rate coefficient
m	Henry's law constant (dimensionless)
M_o	Morton number
N	Microorganism number density
N_S	Stanton number
P	Pressure
P_e	Peclet number

Variable	Description
$\dot{P}_T$	Turbulent kinetic energy dissipation rate
Q	Volumetric flow rate
R_e	Reynolds number
S	Stripping factor
S_c	Schmidt number
S_h	Sherwood number
t	Time
T_{10}	Time for passage of 10% of pulse of conservative tracer
U_G	Gas superficial velocity
U_L	Liquid superficial velocity
$\vec{U}$	Velocity
V	Volume
v_B	Bubble terminal rise velocity
W_e	Weber number
z	Depth
z^*	Normalized depth
ε_G	Gas hold-up
σ	Surface tension
ρ	Density
ν	Kinematic viscosity
μ	Dynamic viscosity
μ_T	Turbulent viscosity
ϕ_G	Gas volume fraction

APPENDIX B: LIST OF ABBREVIATIONS AND ACRONYMS

Variable	Description
ADR	Advection-Dispersion-Reaction
CFD	Computational Fluid Dynamics
CSTR	Completely Stirred Tank Reactor
Ct	Product of ozone residual concentration and time
DBP	Disinfection Byproduct
HAA	Haloacetic Acid
HDT	Hydraulic Detention Time
LT2ESWTR`	Long Term 2 Enhanced Surface Water Treatment Rule
NOM	Natural Organic Matter
SWTR	Surface Water Treatment Rule
TA	Total Alkalinity
TOC	Total Organic Carbon
USEPA	United States Environmental ProtectionAgency

APPENDIX C: ANALYSIS OF RADIALLY-AVERAGED IMAGE DATA

Radially-averaged indigo dye image data were used to estimate dispersion and mass transfer rate in the column. The presence or absence of multiple zones was determined via comparison of fit of single- and multiple-zone models to data.

Several models were formulated based on observed trends in indigo dye consumption. At relatively high gas to liquid flow ratios, indigo dye concentration reduced monotonically in the top of the reactor and was constant in the bottom of the reactor. This observation prompted the formulation of the one-zone and two-zone models described below. In the one-zone models, the mass transfer rate and dispersion are assumed uniform in the reactor. In two-zone models, the bottom of the reactor is assumed to behave as a continuously stirred tank reactor (CSTR) and it is assumed the top of the reactor can be modeled as a 1-dimensional axial flow with dispersion and reaction (1-D ADR) reactor. In one formulation of the two-zone model, the mass transfer rate in the CSTR portion of the reactor is assumed to be different from that in the top half of the reactor. In a second formulation, the mass transfer rate is assumed the same in the top and bottom of the reactor and the difference in observed mass transfer in the two regions is attributed wholly to difference in mixing.

Derivation of the single-zone and two-zone models follows.

Single-zone model

Conservation of gas phase ozone and aqueous indigo dye are depicted in Figure

87. Gas phase dispersion (back-mixing of bubbles) is assumed to be negligible and dissolved ozone is assumed to react very quickly with indigo dye.

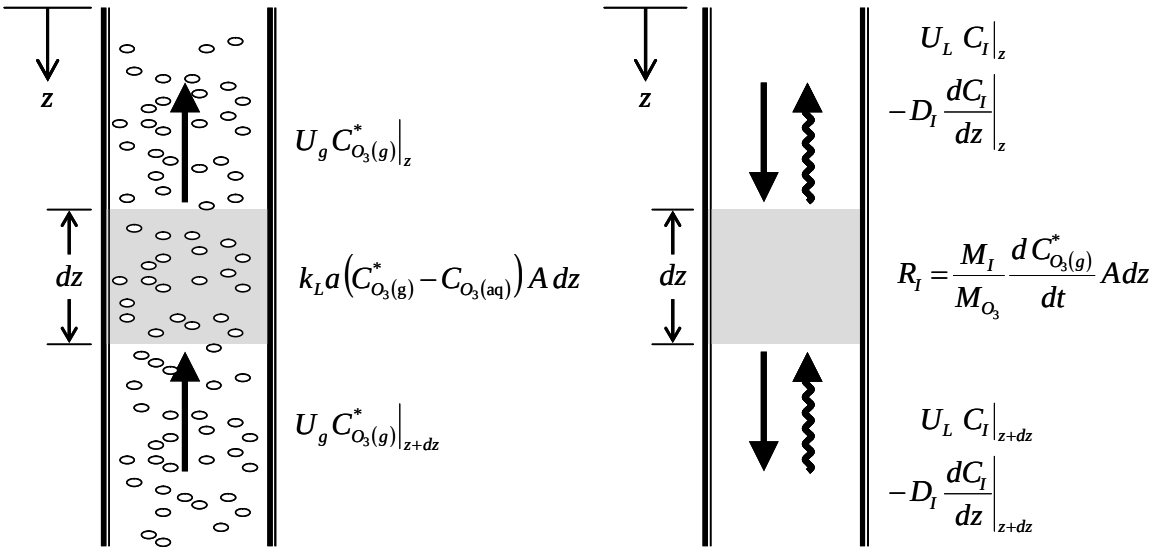

(a) Conservation of gas phase ozone (b) Conservation of aqueous indigo dye

Figure 87: Conservation of Gas Phase Ozone and Aqueous Indigo Dye

Conservation of gas phase ozone

Conservation of mass about the control volume depicted in Figure 87(a) can be written

$$\left(-Q_G\ C_{O_3(G)}\big|_z + Q_G\ C_{O_3(G)}\big|_{z+dz}\right) = \left[k_L\ a\left(mC_{O_3(G)} - C_{O_3(aq)}\right)\right] dz$$

where A is the column cross sectional area, Q_G is gas volumetric flow rate (positive upward), k_L is mass transfer coefficient (dimensions L/T), a is specific surface

area (surface area per unit volume of reactor; dimensions L^{-1}), $C_{O_3(G)}$ is gas phase ozone mass concentration, $C_{O_3(aq)}$ is aqueous phase ozone mass concentration and *m* is the Henry's law constant (equilibrium gaseous ozone concentration ÷ equilibrium aqueous ozone concentration). Henry's law constant is calculated via the relation (Perry and Chilton 1973) in equation 70 (repeated below)

$$\log(m) = \begin{cases} 3.25 - \dfrac{840}{T} & 5^{\circ}\mathrm{C} \le T \le 5^{\circ}\mathrm{C} \\ 6.2 - \dfrac{1687}{T} & 5^{\circ}\mathrm{C} \le T \le 5^{\circ}\mathrm{C} \end{cases} \tag{70}$$

where *T* is temperature in degrees Kelvin and *m* is dimensionless.

Since the ozone-indigo dye reaction is very fast, aqueous ozone does not accumulate and the conservation equation becomes

$$\frac{C_{O_3(G)}\Big|_{z+dz} - C_{O_3(G)}\Big|_{z}}{dz} = \frac{k_L a}{m U_G} C_{O_3(G)}$$

$$\frac{d\,C_{O_3(G)}}{dz} = \frac{k_L a}{m U_G} C_{O_3(G)} \tag{A-1}$$

Define Stanton number, stripping factor and dimensionless height as

$$N_S = \frac{k_L\, a\, H}{U_L}; \tag{A-2}$$

$$S = \frac{m U_G}{U_L}; \text{ and} \tag{A-3}$$

$$z^* = \frac{z}{H}. \tag{A-4}$$

Equation A-1 becomes

$$\frac{d\,C_{O_3(G)}}{C_{O_3(G)}} = \frac{N_S}{S}\,dz^* \tag{A-5}$$

Equation A-5 is integrated from z^* to the reactor bottom ($z^* = 1$; gas injection point). Denoting the gas injection ozone concentration as $C_{O_3(G)\,0}$, the integration of equation A-3 proceeds as follows:

$$\ln\left(C_{O_3(G)}\right)\Big|_{C_{O_3(G)}}^{C_{O_3(G)0}} = \frac{N_S}{S}\,z^*\Big|_{z^*}^{1}$$

$$\ln\left(\frac{C_{O_3(G)0}}{C_{O_3(G)}}\right) = \frac{N_S}{S}\left(1 - z^*\right)$$

$$C_{O_3(G)} = C_{O_3(G)0}\,e^{-\frac{N_S}{S}\left(1-z^*\right)}$$

and

$$C^*_{O_3(G)} = C^*_{O_3(G)0}\,e^{-\frac{N_S}{S}\left(1-z^*\right)} \tag{A-6}$$

where

$$C^*_{O_3(G)} = \frac{C_{O_3(G)}}{m} \tag{A-7}$$

Conservation of aqueous indigo dye

Conservation of indigo dye, depicted in Figure 87(b), can be written

$$\frac{\partial C_I}{\partial t} A dz = - AD \frac{\partial C_I}{\partial z}\bigg|_z + Q_L C_I\big|_z + AD \frac{\partial C_I}{\partial z}\bigg|_{z+dz} - Q_L C_I\big|_{z+dz} - R_I A\, dz$$

where Q_L is liquid volumetric flow rate, C_I is indigo trisulfonate concentration, D is dispersion and R_I is rate of indigo consumption. Assuming steady state conditions in the column and that the ozone-indigo reaction is fast enough that rate of consumption of indigo dye is equal to the mass transfer rate of ozone and noting that liquid superficial velocity, U_L, is equal to Q_L/A, the conservation of indigo dye can be written

$$D\left(\frac{\left.\frac{dC_I}{dz}\right|_{z+dz} - \left.\frac{dC_I}{dz}\right|_z}{dz} \right) - U_L \left(\frac{C_I\big|_{z+dz} - C_I\big|_z}{dz} \right) = \frac{M_I}{M_{O_3}} k_L a\, C^*_{O_3(G)}\, dz$$

Substitute the expression from equation A-6 for $C^*_{O_3(G)}$ and, as $dz \to 0$, the conservation of indigo dye becomes

$$D \frac{d^2 C_I}{dz^2} - U_L \frac{dC_I}{dz} = \frac{M_I}{M_{O_3}} (k_L a) C^*_{O_3(G)0}\, e^{-\left(\frac{N_S}{S}\right)(1-z^*)}$$

Introduce the dimensionless parameters $z^* = z / H$ and $C_I^* = C_I / C_{I0}$, where C_{I0} is indigo dye concentration in the reactor feed. The nondimensionalized conservation of aqueous indigo dye becomes

$$\frac{d^2 C_I^*}{\left(d z^*\right)^2} - \frac{U_L H}{D}\frac{d C_I^*}{d z^*} = \frac{M_I}{M_{O_3}}\frac{C^*_{O_3(G)0}}{C_{I0}}\left(\frac{N_S}{S}\right)S\left(\frac{U_L H}{D}\right)e^{-\frac{N_S}{S}\left(1-z^*\right)}$$

Define Peclet number and the parameter ψ as

$$P_e = \frac{U_L H}{D} \tag{A-8}$$

$$\psi = \frac{M_I}{M_{O_3}}\frac{C_{O_3(g)0}}{C_{I,0}}S = \frac{M_I}{M_{O_3}}\frac{mQ_G}{Q_L}\frac{C_{O_3(g)0}}{C_{I,0}} \tag{A-9}$$

Conservation of aqueous indigo dye becomes

$$\frac{d^2 C_I^*}{\left(d z^*\right)^2} - P_e\frac{d C_I^*}{d z^*} = \psi\left(\frac{N_S}{S}\right)P_e\, e^{-\frac{N_S}{S}\left(1-z^*\right)} \tag{A-10}$$

Equation A-10 is integrated as follows.

$$\frac{d}{d z^*}\left(\frac{d C_I^*}{d z^*} - P_e C_I^*\right) = \psi\left(\frac{N_S}{S}\right)P_e\, e^{-\left(\frac{N_S}{S}\right)\left(1-z^*\right)}$$

$$\frac{d C_I^*}{d z^*} - P_e C_I^* = \psi\, P_e\, e^{-\frac{N_S}{S}\left(1-z^*\right)} + \alpha \tag{A-11}$$

where α is an integration constant. Equation A-11 is solved using an integrating factor:

$$p = e^{\int -P_e\, dz^*} = e^{-P_e z^*}$$

$$\frac{d}{dz^*}\left(p C_i^*\right) = p\left(\psi\, P_e\, e^{-\frac{N_S}{S}\left(1-z^*\right)} + \alpha\right)$$

$$\frac{d}{dz^*}\left(e^{-P_e z^*}\, C_I^*\right) = e^{-P_e z^*}\left(\psi\, P_e\, e^{-\frac{N_S}{S}\left(1-z^*\right)} + \alpha\right)$$

$$e^{-P_e z^*}\, C_I^* = \psi\left(\frac{P_e}{\left(N_S/S\right)-P_e}\right) e^{-P_e z^* - \left(\frac{N_S}{S}\right)\left(1-z^*\right)} - \frac{\alpha}{P_e}\, e^{-P_e z^*} + \beta$$

$$C_I^* = \psi\left(\frac{P_e}{\left(N_S/S\right)-P_e}\right) e^{-\left(N_S/S\right)\left(1-z^*\right)} - \frac{\alpha}{P_e} + \beta\, e^{P_e z^*} \tag{A-12}$$

and the rate of change of indigo dye concentration with respect to axial location is:

$$\frac{dC_I^*}{dz^*} = \psi\left(\frac{\left(N_S/S\right)P_e}{\left(N_S/S\right)-P_e}\right) e^{-\left(N_S/S\right)\left(1-z^*\right)} + \beta\, P_e\, e^{P_e z^*} \tag{A-13}$$

Determining integration constants for single zone model

Equation 11 is solved subject to a Dirichlet inlet boundary condition ($C_I = C_{I,0}$ at $z^* = 0$) and Danckwerts boundary condition at the outlet ($dC_I / dz^*|_{z=1}=0$) (Nauman and Buffham 1983; Teefy and Singer 1990; Haas et al., 1998). At the reactor discharge,

$$\left.\frac{dC_I^*}{dz^*}\right|_{z^*=1} = 0$$

$$0 = \psi\left(\frac{\left(N_S/S\right)P_e}{\left(N_S/S\right)-P_e}\right) + \beta\, P_e\, e^{P_e}$$

$$\beta = -\psi\left(\frac{\left(N_S/S\right)}{\left(N_S/S\right)-P_e}\right) e^{-P_e}$$

Substitute β into the expression for indigo dye concentration (equation A-11) and simplify.

$$C_I^* = \psi\left(\frac{P_e}{(N_S/S)-P_e}\right)e^{-(N_S/S)(1-z^*)} - \frac{\alpha}{P_e} - \psi\left(\frac{(N_S/S)}{(N_S/S)-P_e}\right)e^{-P_e}e^{P_e z^*}$$

$$C_I^* = \left(\frac{\psi}{(N_S/S)-P_e}\right)\left(P_e\, e^{-(N_S/S)(1-z^*)} - (N_S/S)\, e^{-P_e(1-z^*)}\right) - \frac{\alpha}{P_e} \qquad \text{(A-14)}$$

A Dirichlet boundary condition is applied at the top of the reactor ($z^* = 0$):

$$C_I^*\Big|_{z^*=0} = 1 \qquad \text{(A-15)}$$

$$1 = \left(\frac{\psi}{(N_S/S)-P_e}\right)\left(P_e\, e^{-(N_S/S)} - (N_S/S)e^{-P_e}\right) - \frac{\alpha}{P_e}$$

$$-\frac{\alpha}{P_e} = 1 - \left(\frac{\psi}{(N_S/S)-P_e}\right)\left(P_e\, e^{-(N_S/S)} - (N_S/S)e^{-P_e}\right)$$

Substitute the expression for α into equation 15 for the final expression for aqueous indigo dye concentration.

$$C_I^* = 1 - \left(\frac{\psi}{(N_S/S)-P_e}\right)\left(-P_e\, e^{-S(1-z^*)} + (N_S/S)e^{-P_e(1-z^*)} + P_e\, e^{-(N_S/S)} - (N_S/S)e^{-P_e}\right)$$

$$C_I^* = 1 - \left(\frac{\psi}{(N_S/S)-P_e}\right)\left[P_e\, e^{-(N_S/S)}\left(1 - e^{(N_S/S)z^*}\right) - (N_S/S)e^{-P_e}\left(1 - e^{P_e z^*}\right)\right] \qquad \text{(A-16)}$$

In the limit $(N_S/S) \to P_e$, equation A-16 becomes indeterminate and an expression for

dimensionless indigo dye concentration is determined using L'Hopital's rule.

$$\lim_{(N_S/S)\to P_e}\left[\frac{P_e\, e^{-(N_S/S)}\left(1-e^{(N_S/S)z^*}\right)-(N_S/S)e^{-P_e}\left(1-e^{P_e z^*}\right)}{(N_S/S)-P_e}\right]$$
$$=\lim_{(N_S/S)\to P_e}\left[\frac{P_e\, e^{-(N_S/S)}+\left(1-z^*\right)P_e e^{-(N_S/S)(1-z^*)}-e^{-P_e}\left(1-e^{P_e z^*}\right)}{1}\right]$$

Substituting this result into equation A-16 yields the final expression for dimensionless indigo dye concentration in the limit $(N_S/S)\to P_e$:

$$C_{I\,\lim\left(\frac{N_S}{S}\right)\to P_e}^{*}=1-\psi\left[\left(P_e-P_e z^*+1\right)e^{-P_e(1-z^*)}-e^{-P_e}\left(1+P_e\right)\right] \qquad \text{(A-17)}$$

Derivation of Governing Equations, Two Zone Model

The two-zone model, depicted in Figure 88, was developed based on observations from ozone mass transfer visualization experiments that the near-sparger region (zone 2 [$z^* > z_c^*$]) has a uniform indigo dye concentration whereas the in the top of the reactor (zone 1 [$z^* < z_c^*$]), indigo dye concentration increases monotonically with height. In the two-zone model, zone 2 is modeled as well mixed (CSTR) and zone 1 is modeled using the advection-dispersion-reaction model, as in the single-zone model described above. The term z_c^* is the "critical" depth separating the two zones.

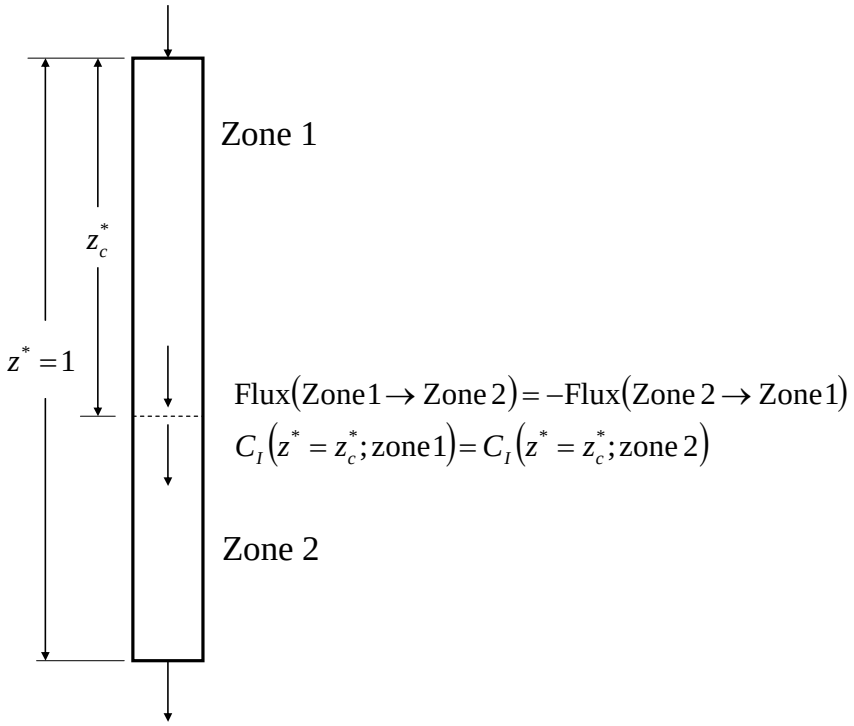

Figure 88: Schematic Diagram, Two-Zone Model

Two-zone models were formulated assuming:

- Equal Stanton number in zones 1 and 2
- Different Stanton numbers in zones 1 and 2.

The derivation of these models is provided below.

Two Zone Model, Equal Stanton Numbers in Zones 1 and 2

Conservation of gaseous ozone in zone 2 is given as

$$U_G m C^*_{O_3(0)} - U_G m C^*_{O_3} = k_L a\, C^*_{O_3} (H - z_c)$$

$$C^*_{O_3(0)} - C^*_{O_3} = \frac{k_L a H}{m U_G} C^*_{O_3}\left(1 - z_c / H\right)$$

Recalling that Stanton number, stripping factor and dimensionless height are given by

$$N_S = \frac{k_L a H}{U_L}$$

$$S = \frac{m U_G}{U_L}$$

and

$$z^* = \frac{z}{H}$$

Gaseous ozone concentration in zone 2 becomes

$$C^*_{O_3} = \frac{C^*_{O_3(0)}}{1 + \left(N_S / S\right)\left(1 - z^*_c\right)} \tag{A-18}$$

Conservation of gaseous ozone in zone 1 is determined by integrating equation A-2 from z^* to $z_c{}^*$

$$\ln\left(C^*_{O_3}\right)\Big|_{C^*_{O_3}\left(z^*\right)}^{C^*_{O_3}\left(z^*_c\right)} = \left(N_S / S\right) z^*\Big|_{z^*}^{z^*_c}$$

$$\ln\left(\frac{C^*_{O_3(0)}}{1 + S\left(1 - z^*_c\right)}\right) - \ln\left(C^*_{O_3}\right) = \left(N_S / S\right)\left(z^*_c - z^*\right)$$

$$C_{O_3}^* = \frac{C_{O_3(0)}^*}{1+\left(N_S/S\right)\left(1-z_c^*\right)} e^{-\left(N_S/S\right)\left(z_c^*-z^*\right)} \tag{A-19}$$

Conservation of aqueous indigo dye in zone 2 is:

$$\left(Q_L C_I - DA\frac{dC_I}{dz}\right)\Bigg|_{z^*=z_c^*} - Q_L C_{I,2} = \frac{M_I}{M_{O_3}} k_L a \left(H - z_c\right) C_{O_3}^* A$$

Substitute for $C_{O_3(0)}^*$ from equation A-19 and nondimensionalize using $C_I^* = C_I/C_{I,0}$ and $z^* = z/H$.

$$\left(U_L C_{I,0} C_I^* - \frac{D C_{I,0}}{H}\frac{dC_I^*}{dz^*}\right)\Bigg|_{z^*=z_c^*} - U_L C_{I,2} = \frac{M_I}{M_{O_3}}\frac{k_L a H}{U_L} U_L \left(1-z_c^*\right)\frac{C_{O_3(0)}^*}{1+\left(N_S/S\right)\left(1-z_c^*\right)}$$

$$\left(\frac{dC_I^*}{dz^*} - \frac{U_L H}{D} C_I^*\right)\Bigg|_{z^*=z_c^*} = -\frac{U_L H}{D} C_{I,2} - \frac{M_I}{M_{O_3}}\frac{k_L a H}{U_L}\frac{U_L H}{D}\frac{C_{O_3(0)}^*}{C_I^*}\frac{\left(1-z_c^*\right)}{1+\left(N_S/S\right)\left(1-z_c^*\right)}$$

Recall that $N_S = k_L a H/U_L$, $S = mU_G/U_L$ and $P_e = U_L H/D$ and define

$$\psi = \frac{M_I}{M_{O_3}}\frac{mU_G}{U_L}\frac{C_{O_3(0)}^*}{C_{I,0}} = \frac{M_I}{M_{O_3}} S \frac{C_{O_3(0)}^*}{C_{I,0}} \tag{A-20}$$

$$\left(\frac{dC_I^*}{dz^*} - P_e C_I^*\right)\Bigg|_{z^*=z_c^*} = -P_e C_{I,2}^* - \psi\left(N_S/S\right) P_e \frac{\left(1-z_c^*\right)}{1+\left(N_S/S\right)\left(1-z_c^*\right)} \tag{A-21}$$

where

$$C_{I,2}^* = \frac{1}{C_{I,0}}\frac{1}{n_{data}-n_c}\sum_{i=n_c}^{n_{data}} C_{I,i} \tag{A-22}$$

Conservation of aqueous indigo dye in zone 1 is given by

$$D\frac{d^2C_I}{dz^2} - U_L\frac{dC_I}{dz} = \frac{M_I}{M_{O_3}}k_L a\, C^*_{O_3}$$

Nondimensionalize this expression and substitute for ozone concentration from equation A-19:

$$D\frac{d^2C_I}{dz^2} - U_L\frac{dC_I}{dz} = \frac{M_I}{M_{O_3}}k_L a\left[\frac{C^*_{O_3(0)}}{1+(N_S/S)(1-z^*_c)}\right]e^{-(N_S/S)(z^*_c - z^*)}$$

Rearranging this equation and introducing Stanton number, N_S, Peclet number, P_e, stripping factor, S, dimensionless height, z^*, and dimensionless indigo dye concentration, C_I^* yields the final expression for indigo dye concentration in zone 1.

$$\frac{d^2C^*_I}{dz^2} - P_e\frac{dC^*_I}{dz} = \psi\ P_e\left(\frac{N_S}{S}\right)\left[\frac{1}{1+(N_S/S)(1-z^*_c)}\right]e^{-(N_S/S)(z^*_c - z^*)} \qquad \text{(A-23)}$$

Equation A-23 is integrated as follows.

$$\frac{d}{dz^*}\left(\frac{dC^*_I}{dz} - P_e C^*_I\right) = \psi\ P_e\left(\frac{N_S}{S}\right)\left[\frac{1}{1+(N_S/S)(1-z^*_c)}\right]e^{-(N_S/S)(z^*_c - z^*)}$$

$$\frac{dC^*_I}{dz} - P_e C^*_I = \psi\ P_e\left[\frac{1}{1+(N_S/S)(1-z^*_c)}\right]e^{-(N_S/S)(z^*_c - z^*)} + \alpha \qquad \text{(A-24)}$$

The right hand side (RHS) of equation 20 is evaluated at $z^* = z_c^*$ and equated with the RHS of equation 17 to determine an expression for the integration constant:

$$\alpha = -P_e\, C^*_{I,2} - \psi\ P_e$$

Substitute the result into equation A-24.

$$\frac{dC^*_I}{d\,z} - P_e\, C^*_I = -P_e\,\left(C^*_{I,2} + \psi\right) + \psi\ P_e\left[\frac{1}{1+\left(N_S/S\right)\left(1-z^*_c\right)}\right] e^{-\left(N_S/S\right)\left(z^*_c - z^*\right)} \tag{A-25}$$

Equation A-25 is integrated using an integrating factor, yielding

$$\frac{d}{d\,z^*}\left(e^{-P_e z^*}\, C^*_I\right) = e^{-P_e z^*}\left[-P_e\left(C^*_{I,2} + \psi\right) + \psi\ P_e\,\frac{1}{1+\left(N_S/S\right)\left(1-z^*_c\right)}\, e^{-\left(N_S/S\right)\left(z^*_c - z^*\right)}\right]$$

$$C^*_I = \left(C^*_{I,2} + \psi\right) + \left(\frac{\psi\ P_e}{\left(N_S/S\right) - P_e}\right)\left(\frac{1}{1+\left(N_S/S\right)\left(1-z^*_c\right)}\right) e^{-\left(N_S/S\right)\left(z^*_c - z^*\right)} + \beta\, e^{P_e z^*} \tag{A-26}$$

where β is an integration constant. The integration constant is determined using the inlet boundary condition.

$$\beta = 1 - \left(C^*_{I,2} + \psi\right) + \left(\frac{\psi\ P_e}{\left(N_S/S\right) - P_e}\right)\left(\frac{1}{1+\left(N_S/S\right)\left(1-z^*_c\right)}\right) e^{-\left(N_S/S\right) z^*_c}$$

Substitute the integration constant into equation 22 and rearrange for the final expression for indigo dye concentration in zone 1.

$$\begin{aligned} C^*_I = {} & e^{P_e z^*} + \left(C^*_{I,2} + \psi\right)\left(1 - e^{P_e z^*}\right) + \\ & \left(\frac{\psi\ P_e}{\left(N_S/S\right) - P_e}\right)\left(\frac{1}{1+\left(N_S/S\right)\left(1-z^*_c\right)}\right)\left(e^{-\left(N_S/S\right)\left(z^*_c - z^*\right)} - e^{P_e z^* - \left(N_S/S\right) z^*_c}\right) \end{aligned} \tag{A-27}$$

Two Zone Model, Differing Stanton Numbers in Zones 1 and 2

In the two zone model in which Stanton number is allowed to differ in the zones,

Stanton number in zones 1 and 2 are designated N_{S1} and N_{S2}. Proceeding in a manner similar to that used in the two-zone, single Stanton number model, gaseous ozone concentration in zone 2 is given by

$$C_{O_3}^* = \frac{C_{O_3(0)}^*}{1+\left(N_{S2}/S\right)\left(1-z_c^*\right)} \tag{A-28}$$

and concentration of gaseous ozone in zone 1 is given by

$$C_{O_3}^* = \frac{C_{O_3(0)}^*}{1+\left(N_{S2}/S\right)\left(1-z_c^*\right)} e^{-\left(N_{S1}/S\right)\left(z_c^*-z^*\right)}$$

Conservation of aqueous indigo dye in zone 2 results in

$$\left(\frac{dC_I^*}{dz^*} - P_e C_I^*\right)\Bigg|_{z^*=z_c^*} = -P_e C_{I,2}^* - \psi\left(N_{S2}/S\right) P_e \frac{\left(1-z_c^*\right)}{1+\left(N_{S2}/S\right)\left(1-z_c^*\right)} \tag{A-29}$$

and the conservation of indigo dye in zone 1 is given by

$$\frac{d^2 C_I^*}{d z^2} - P_e \frac{d C_I^*}{d z} = \psi\ P_e\left(\frac{N_{S1}}{S}\right)\left[\frac{1}{1+\left(N_{S2}/S\right)\left(1-z_c^*\right)}\right] e^{-\left(N_{S1}/S\right)\left(z_c^*-z^*\right)} \tag{A-30}$$

Equation A-30 is integrated twice and integration constants are determined using a Dirichlet boundary condition at the inlet to zone 1 $\left(C_I^*\Big|_{z^*=0} = 1\right)$ and, at the discharge of zone 1 (into zone 2) using the boundary condition

$$\left(\frac{dC_I^*}{dz^*} - P_e C_I^*\right)\Bigg|_{z^*=z_c^*+} = \left(\frac{dC_I^*}{dz^*} - P_e C_I^*\right)\Bigg|_{z^*=z_c^*-}$$

The resulting expression for indigo dye concentration in zone 1 is

$$C_I^* = e^{P_e z^*} + \left(C_{I,2}^* + \psi\right)\left(1 - e^{P_e z^*}\right) + \left(\frac{\psi P_e}{\left(N_{S1}/S\right) - P_e}\right)\left(\frac{1}{1 + \left(N_{S2}/S\right)\left(1 - z_c^*\right)}\right)\left(e^{-\left(N_{S1}/S\right)\left(z_c^* - z^*\right)} - e^{P_e z^* - \left(N_{S1}/S\right) z_c^*}\right) \tag{A-31}$$

In the limit $\left(N_S/S\right) \to P_e$, the expression for indigo dye concentration becomes

$$C_I^* = e^{P_e z^*} + \left(C_{I,2}^* + \psi\right)\left(1 - e^{P_e z^*}\right) + \left(\frac{\psi P_e z^* e^{P_e\left(z^* - z_c^*\right)}}{1 + \left(N_{S2}/S\right)\left(1 - z_c^*\right)}\right) \tag{A-32}$$

APPENDIX D: R SCRIPT FOR BEST FIT PARAMETERS ESTIMATION

```
cIndigo <- function(S1Hat, PeHat, S2Hat)
      {exp(PeHat*Exp_Data2$zstar) +
       PeHat*psi*(exp(-S1Hat*(zc-Exp_Data2$zstar))-exp(-
S1Hat*zc+PeHat*Exp_Data2$zstar))/
       (S1Hat-PeHat)/(1+S2Hat*(1-zc)) +
       (CI2+psi)*(1-exp(PeHat*Exp_Data2$zstar))}
CIndigo <- function(p) {
    -sum((Exp_Data$MEAN - cIndigo(p[1],p[2]))^2)}

Exp_Data <- read.table("C:/Documents and Settings/Carolyn/My
Documents/TBFiles/O3/IndigoPics/Finals/05_25_06/MEANS2_by16_Gurian.DAT"
,header=TRUE)

par(fig=c(0.025,0.975,0.025,0.975),mai=c(0.85,0.85,0.05,0.05))
plot(Exp_Data$zstar,Exp_Data$MEAN,type="l",xlab=expression(z^a),ylab=ex
pression(C[O[3]]^2),ylim=c(0,1))
psi <- 1.1926

PeGuess <- 4
S1Guess <- 1
S2Guess <- 0

##
## Plot model line using initial gueses
##

ndata <- length(Exp_Data$zstar)
nmin <- round(3*ndata/5)
nmax <- ndata-1

nc <- nmin
zc <- Exp_Data$zstar[nc]

CI2 <- sum(Exp_Data$MEAN[nc:ndata])/(ndata - nc+1)
SSE2 <- sum((Exp_Data$MEAN[nc:ndata]-CI2)^2)
SSE2

MEAND <- Exp_Data$MEAN[1:nc]
ZD <- Exp_Data$zstar[1:nc]
Exp_Data2 <- data.frame(zstar=ZD, MEAN=MEAND)
CI2min <- min(Exp_Data$MEAN)
DCI2 <- MEAND[nc]-CI2min
DCI2
S2GuessX <- DCI2/(1-zc)/(psi-DCI2)
S2Guess <- max(0,S2GuessX)
S2Guess
C <- cIndigo(S1Guess,PeGuess, S2Guess)
lines(Exp_Data2$zstar,C,col="red")

Errs <- seq(length=ndata, from=-1e+6,by=0.000001)
```

```
PeEstS <- seq(length=ndata, from=-1e+6,by=0.000001)
S1EstS <- seq(length=ndata, from=-1e+6,by=0.000001)
S2EstS <- seq(length=ndata, from=-1e+6,by=0.000001)

for (i in nmax:nmin) {
nc <- i
zc <- Exp_Data$zstar[nc]
ndata <- length(Exp_Data$zstar)

CI2 <- sum(Exp_Data$MEAN[nc:ndata])/(ndata - nc+1)
SSE2 <- sum((Exp_Data$MEAN[nc:ndata]-CI2)^2)
SSE2

MEAND <- Exp_Data$MEAN[1:nc]
ZD <- Exp_Data$zstar[1:nc]
Exp_Data2 <- data.frame(zstar=ZD, MEAN=MEAND)
CI2min <- min(Exp_Data$MEAN)
DCI2 <- MEAND[nc]-CI2min
DCI2

genga <- nls.control(maxiter=10000,tol=1e-6,minFactor=0.000488281/128)
outIndigo <- nls(MEAND ~ cIndigo(S1Est,PeEst, S2Est),Exp_Data2,start=
        list(S1Est=S1Guess,PeEst=PeGuess,S2Est=S2Guess),genga,
        lower=c(0,0,0),algorithm="port")

AA <- coef(outIndigo)
BB <- residuals(outIndigo)
CC <- fitted.values(outIndigo)
SSE1 <- sqrt(sum(BB^2))
SSE1
SSE2
SSE <- SSE1 + SSE2
SSE

S1Est <- AA[1]
S1Guess <- S1Est
PeEst <- AA[2]
PeGuess <- PeEst
S2Est <- AA[3]
S2Guess <- S2Est
i
PeGuess
S1Guess
S2Guess

## CI <- cIndigo(S1Est,PeEst,S2Est)

lines(Exp_Data2$zstar,CC,col="blue")

zz <- Exp_Data$zstar[1:nc]
CO31 <- exp(-S1Est*(zc-zz))/(1+S2Est*(1-zc))
lines(zz,CO31,col="orange")
```

```
z2line <- c(zc,1)
CI2line <- c(CI2,CI2)
CO32 <- 1/(1+S2Est*(1-zc))
CO3Line <- c(CO32,CO32)
lines(z2line,CI2line,col="blue")
lines(z2line,CO3Line,col="orange")

Errs[i] <- SSE
S1EstS[i] <- S1Est
S2EstS[i] <- S2Est
PeEstS[i] <- PeEst
}

ii <- seq(length=(nmax-nmin+1),from=nmin,by=1)
imin <- which.min(abs(Errs))
imin
Errmin <- Errs[imin]
Errmin
Errmin <- min(abs(Errs))
Errmin
Errmax <- max(Errs)
Errmax
plot(ii,Errs[nmin:nmax],xlab=expression(n[c]),ylab="SSE",ylim=c(Errmin,
Errmax))
points(imin,Errmin,col="red",cex=1.3,pch=19)


## Make a pretty plot showing fitted curves (indigo and ozone) and data

windows()
par(fig=c(0.025,0.975,0.025,0.975),mai=c(0.85,0.85,0.05,0.05),family="s
erif",xaxs="r")
gc <- grey(0:8 / 8)
plot(Exp_Data$zstar,Exp_Data$MEAN,type="p",xlab="Normalized Depth
(z*)",
    ylab="Normalized Concentration",ylim=c(0,1),

xlim=c(0.2,1.0),col=gc[2],family="serif",cex.axis=1.25,cex.lab=1.25)

nc <- imin
nc
zc <- Exp_Data$zstar[nc]
zc

S1Guess <- S1EstS[imin]
S1Guess
S2Guess <- S2EstS[imin]
S2Guess
PeGuess <- PeEstS[imin]
PeGuess

CI2 <- sum(Exp_Data$MEAN[nc:ndata])/(ndata - nc + 1)
SSE2 <- sum((Exp_Data$MEAN[nc:ndata]-CI2)^2)
```

```
SSE2

MEAND <- Exp_Data$MEAN[1:nc]
ZD <- Exp_Data$zstar[1:nc]
Exp_Data2 <- data.frame(zstar=ZD, MEAN=MEAND)
genga <- nls.control(maxiter=100000,tol=1e-5)
outIndigo <- nls(MEAND ~ cIndigo(S1Est,PeEst,S2Est),Exp_Data2,

start=list(S1Est=S1Guess,PeEst=PeGuess,S2Est=S2Guess),genga,lower=c(0,0
,0),algorithm="port")

summary(outIndigo)
imin
Exp_Data$zstar[imin]

AA <- coef(outIndigo)
BB <- residuals(outIndigo)
CC <- fitted.values(outIndigo)

S1Est <- AA[1]
PeEst <- AA[2]
S2Est <- AA[3]

SSE1 <- sqrt(sum(BB^2))
SSE1
SSE2
SSE <- SSE1 + SSE2
SSE

CI <- cIndigo(S1Est,PeEst,S2Est)

lines(Exp_Data2$zstar,CC,col="black",lwd=2)

zz <- Exp_Data$zstar[1:nc]
CO31 <- exp(-S1Est*(zc-zz))/(1+S2Est*(1-zc))

z2line <- c(zc,1)
CI2line <- c(CI2,CI2)
CO32 <- 1/(1+S2Est*(1-zc))
CO3Line <- c(CO32,CO32)
lines(z2line,CI2line,col="black",lwd=2)
legend(0.5,0.3,legend=c(expression(C[I]^"\*"*"\ "*"(Experimental
data)"),expression(C[I]^"\*"*"\ "*"(Fitted model)")),
col=c(gc[2],gc[0]),lty=c(0,1),lwd=c(1,2),bty="n",pch=c(1,26),y.intersp=
1.3,cex=1.25,pt.cex=0.75)

##
## Perform runs test on the residuals.  Convert residuals to binary
array and
## factor, then perform the runs test
##

ResBi <- sign(BB)
```

```
ErrB <- seq(length=nc, from=-1e+6,by=0.000001)
for (i in 1:nc) {
ErrB[i] <- max(0,ResBi[i]) }
ErrBF <- factor(ErrB)
runs.test(ErrBF,alternative="two.sided")
```

Vita

Timothy Allen Bartrand was born in Muskegon, Michigan, USA, on Octboer 19th, 1961 to Loren L. Bartrand and Donna Hickey Bartrand. Mr. Bartrand attended Rogers High School, Wyoming, MI, graduating the class valedictorian. Upon graduation from high school Mr. Bartrand undertook undergraduate studies at the University of Notre Dame, Notre Dame, IN, earning a bachelor's degree in aerospace engineering in May, 1983. In June, 1983, Mr. Bartrand began service as a Peace Corps volunteer, teaching mathematics and physics at the Union Comprehensive Secondary School in Bachuo Akagbe, Manyu Division, Southwest Province, Cameroon. He is married to Carolyn Davis and they have one daughter, Olivia Davis Bartrand.

Mr. Bartrand has earned two masters degrees: a master of science in mechanical engineering from the University of Tennessee (awarded 12/87, thesis title "A Study of Low-Frequency Combustion Instability in Rocket Engine Preburners using a Heterogeneous Stirred Tank Reactor Model") and a master of science in civil engineering from Ohio University (awarded 12/97, thesis title "Experimental Investigation of a Vacuum Apparatus for Zebra Mussel Control in Closed Conduits").

Mr. Bartrand's professional experience includes eight years as a research engineer working as a NASA Lewis Research Center on-site contractor, three years experience developing water and sanitation facilities in relief settings and one year as an environmental regulator for the Ohio EPA.